Universidade do Minho
Escola de Engenharia

João Carlos Pacheco Barbosa

Development of three component solid-polymer electrolytes for energy storage applications

julho de 2023

Development of three component solid-polymer electrolytes for energy storage applications

João Barbosa

UMinho | 2023

Universidade do Minho
Escola de Engenharia

João Carlos Pacheco Barbosa

Development of three component solid-polymer electrolytes for energy storage applications

Tese de doutoramento

Engenharia de Materiais

Trabalho efetuado sob orientação de

Doutor Carlos Costa

Professora Doutora Verónica de Zea Bermudez

Professor Doutor Senentxu Lanceros-Mendez

julho 2023

DIREITOS DE AUTOR E CONDIÇÕES DE UTILIZAÇÃO DO TRABALHO POR TERCEIROS

Acknowledgements

First, I would like to thank to the European Union, Portuguese Government and Portuguese Foundation for Science and Technology for the funding (SFRH/BD/140842/2018 and COVID/BD/152990/2022) and the opportunity to work on my PhD thesis, in the scope of the Portugal 2020 and Norte 2020 programs.

To the Centre of Physics of University of Minho and Centre of Chemistry of Vila Real, for being my host institutions during these years. Also to the Institute for Bio sustainability, Centre of Chemistry of University of Minho, and to the Basque Centre for Materials, for allowing me to do significant parts of my work in their facilities.

To professor Senentxu Lanceros-Mendez, professor Verónica Bermudez, and Doctor Carlos Costa for being my supervisors and sharing their experience and knowledge in all the fields related to my work. To Bruno Ameduri and the Institute Charles Gerhardt, Montepllier, that warmly welcomed me during my stay, and made me feel at home.

To my colleagues in the Electroactive Smart Materials Group that helped in these years. In particular, a special thanks to Renato Gonçalves, Daniela Correia, Rafael Pinto and João Serra, which have closely accompanied all my work with dedication and friendship, during many hours at the laboratory.

Finally, thanks to my family, my parents Olinda and António and my sister Joana, for always believing and supporting me, and to Raquel, for being there in the good and difficult times with unconditional support and dedication.

STATEMENT OF INTEGRITY

I hereby declare having conducted this academic work with integrity. I confirm that I have not used plagiarism or any form of undue use of information or falsification of results along the process leading to its elaboration.

I further declare that I have fully acknowledged the Code of Ethical Conduct of the University of Minho.

Resumo

À medida que a sociedade moderna enfrenta um aumento industrial e populacional, as questões associadas à escassez, impacto ambiental e custos de energia tornam-se numa preocupação cada vez mais significativa, levando a que o armazenamento de energia tenha um papel crítico para a segurança energética e revolução digital, fortemente associada a mobilidade. No entanto existe ainda a necessidade de resolver alguns problemas relacionados com as baterias de ião-lítio, como segurança e durabilidade. Neste contexto, os eletrólitos sólidos poliméricos (SPE) são considerados uma tecnologia promissora para superar esses problemas num futuro próximo.

Neste trabalho é proposto um novo sistema ternário composto por uma matriz polimérica de base fluorinada de poli(fluoreto de vinilideno co-hexafluoropropileno) (PVDF-HFP), um líquido iónico (IL) e um zeólito. Durante o trabalho foram incorporados na matriz de PVDF-HFP diferentes tipos de ILs e zeólitos, e as suas propriedades foram avaliadas a fim de otimizar o desempenho em baterias. O efeito das condições de processamento dos compósitos (ordem de adição dos componentes e temperatura de evaporação de solvente) também foi estudado por forma a avaliar a sua influência nas propriedades do SPE. Os materiais e condições de processamento com melhores desempenhos foram então combinados para maximizar a otimização do eletrólito.

Os resultados obtidos demonstram potencial, tendo-se observado que a incorporação de zeólitos em SPEs, reportada pela primeira vez neste trabalho, aumenta a estabilidade térmica, mecânica e eletroquímica do sistema, resultando em baterias de longa vida útil. Além disso, foi alcançada uma excelente capacidade da bateria com valores máximos de 150 mAh g^{-1} à taxa C/10 para as amostras otimizadas, comprovando a relevância da escolha dos materiais e procedimentos para otimizar o desempenho. Finalmente, a aplicação do polímero poli(fluoreto de vinilideno-trifluoroetileno-clorofluoretileno) pela primeira vez em SPEs resultou numa alta capacidade de descarga para altas taxas, inferindo o papel de uma alta constante dielétrica na melhoria do desempenho da bateria.

Este trabalho representa um importante contributo na área de SPEs, visto que demonstra a relevância da constante dielétrica do polímero e a aplicação de zeólitos como agente estabilizador numa bateria, permitindo alcançar excelentes capacidades e durabilidade, mesmo a altas taxas de descarga e à temperatura ambiente, o que comprova a adequação deste sistema ternário para aplicação na próxima geração de baterias de ião-lítio de estado sólido.

Palavras-chave: energia, baterias de ião-lítio, eletrólitos sólidos poliméricos, zeólitos, líquidos iónicos

Abstract

As the modern society faces a growing population and industrialization, the issues associated energy scarcity, environmental impact and costs are becoming a more significant concern, which makes the energy storage a critical step towards the energy security and the digital revolution implementation, associated with an increasing mobility. Despite their widespread use, lithium-ion batteries still present both of safety and durability issues that need to be addressed. Solid polymer electrolytes (SPE) represent a promising technology to overcome those issues in the near future.

In this work, a novel ternary system comprising a fluorinated polymer matrix based on poly(vinylidene fluoride-co-hexafluoropropylene) (PVDF-HFP), an ionic liquid (IL) and a zeolite is proposed. Different kinds of zeolites and ILs were incorporated in the PVDF-HFP matrix and their properties were evaluated in order to optimize the system to maximize battery performance. The impact of the composites' processing conditions (component addition order and solvent evaporation temperature) were also studied to assess their influence SPE properties. The best materials and processing conditions were then combined to obtain the most optimized electrolyte.

The obtained results have shown to be promising, with the first ever application of zeolites in SPEs proving to improve the overall stability of the system, resulting in long lifecycle batteries. Excellent battery capacity was also achieved with values up to 150 mAh g^{-1} at C/10 rate (where C corresponds to the theoretical capacity of 170 mAh g^{-1}) for the optimized samples, which proves the relevance of choosing the right materials and procedures for the best performance. Finally, the application of the poly(vinylidene fluoride-trifluoroethylene-chlorofluoroethylene) polymer for the first time in solid polymer electrolytes resulted in high discharge capacity at high discharge rates, highlighting the role of a high dielectric constant in improving the battery performance.

This work represents a relevant contribution in the area of solid polymer electrolytes, as it highlights the relevance of the dielectric constant of the polymer and shows the application of zeolites as a stabilization agent in batteries, allowing to achieve excellent capacity and durability even at high discharge rates and room temperature, which proves the suitability of this ternary system for next generation solid-state lithium-ion batteries.

Keywords: energy, lithium-ion batteries, solid polymer electrolytes, zeolites, ionic liquids

Table of Contents

List of Figures

List of Tables

List of Abbreviations

AFM	Atomic Force Microscopy
ATR	Attenuated Total Reflection
CA	Cellulose acetate
CPT	Clinoptilolite
CTA	Cellulose thioacetate
CV	Cyclic voltammetry
DC	Direct current
DMC	Dimethyl carbonate
DMF	N,N-dimethylformamide
DSC	Differential scanning calorimetry
EC	Ethylene carbonate
EDTA	Ethylene diamine tetra-acetic acid
EIS	Electrochemical impedance spectroscopy
FTIR	Fourier Transform infrared
GO	Graphene oxide
GPE	Gel polymer electrolyte
HNT	Halloysite nanotube
HRTEM	High resolution transmission electron microscopy
ICP-AES	Inductively coupled plasma atomic emission spectroscopy
IE	Ion exchange
IL	Ionic liquid
IUPAC	International Union of Pure and Applied Chemistry
LATP	Lithium aluminum titanium phosphate
LCO	Lithium cobalt oxide
LFP	Lithium iron phosphate
LGPS	$Li_{10}GeP_2S_{12}$
LIB	Lithium-ion battery
LiBOB	Lithium bis(oxalato)borate
LiFSI	Lithium bis(fluoromethylsulfonyl)imide
LIPON	Lithium phosphorous oxynitride
LISICON	Lithium super ionic conductor
LiTFSI	Lithium bis(trifluoromethylsulfonyl)imide
LLTO	Lithium lanthanum titanate
LLZO	Lithium lanthanum zirconium oxide
LLZTO	$Li_{6.4}La_3Zr_{1.4}Ta_{0.6}O_{12}$
LMO	Lithium manganese oxide
MEEP	poly(bis((methoxyethoxy)ethoxy)phosphazene
MMT	Montmorillonite
MOF	Metal-organic framework
NASICON	Sodium super ionic conductor
NMP	N-methyl-2-pyrrolidone
P(VDF-TrFE-CFE)	Poly(vinylidene fluoride-trifluoroethylene-chlorofluoroethylene)
PAES-co-PEG	Poly(arylene ether sulfone)-co-poly(ethylene glycol)
PAN	Poly(acrylonitrile)
PANI	Poly(aniline)
PDADMA	Poly(diallyldimethylammonium)

PEBA	Poly(ether block amide)
PEC	Poly(ethylene carbonate)
PEG	Poly(ethylene glycol)
PEGDA	Poly(ethylene glycol) diacrylate
PEGMA	Poly(ethylene glycol) methacrylate
PEO	Poly(ethylene oxide)
PET	Poly(ethylene)
PGCN	Porous graphitic carbon nitride
PHEMO	Poly(3-{2-[2-(2-hydroxyethoxy)ethoxy]ethoxy}methyl-3'-methoxyloxetane))
PI	Poly(imide)
PIL	Polymerized ionic liquid
PMHS	Polymethylhydrosiloxane
PMMA	Poly(methyl methacrylate)
POSS	Polyhedral oligomeric silsesquioxanes
PP	Poly(propylene)
PPO	Poly(propylene oxide)
PTMEG	Poly(tetrahydrofuran)
PVAc	Poly(vinyl acetate)
PVC	Poly(vinyl chloride)
PVDF	Poly(vinylidene fluoride)
PVDF-HFP	Poly(vinylidene fluoride-co-hexafluoropropylene)
SEI	Solid electrolyte interphase
SEM	Scanning Electron Microscopy
SPE	Solid polymer electrolyte
SSB	Solid-state battery
TGA	Thermogravimetric analysis
UV	Ultraviolet
VTF	Vogel-Tamman-Fulcher
XPS	X-ray Photoelectron Spectroscopy
ZIF	Zeolitic imidazolate framework

List of ionic liquids

[BMIM][Cl]	1-butyl-3-methylimidazolium chloride
[BMIM][N(CN)$_2$]	1-butyl-3-methylimidazolium dicyanamide
[BMIM][SCN]	1-butyl-3-methylimidazolium thiocyanate
[BMIM][TFSI]	1-butyl-3-methylimidazolium bis(trifluoromethylsulfonyl)imide
[BMIM]$_2$[(SCN)$_4$Co]	1-butyl-3-methylimidazolium tetracyanatocobalate
[C$_2$mpyr][BF$_4$]	N-ethyl-N-methylpyrrolidinium tetrafluoroborate
[DEIM][TFSI]	1,2-dimethyl-3-ethoxyethyl-imidazolium bis(trifluoromethylsulfonyl)imide
[DEME][TFSI]	diethylmethyl(2-methoxyethyl)ammonium bis(trifluoromethylsulfonyl)imide
[EMIM][BF$_4$]	1-ethyl-3-methylimidazolium tetrafluoroborate
[EMIM][N(CN)$_2$]	1-ethyl-3-methylimidazolium dicyanamide
[EMIM][SCN]	1-ethyl-3-methylimidazolium thiocyanate
[EMIM][TFSI]	1-ethyl-3-methylimidazolium bis(trifluoromethylsulfonyl)imide
[HACC][TFSI]	hydroxypropyl trimethylammonium bis(trifluoromethylsulfonyl)imide
[PP][TFSI]	N-butyl-N-ethyl-piperidinium bis(trifluoromethylsulfonyl)imide
[PMPYR][TFSI]	N-propyl-N-methylpyrrolidinium bis(trifluoromethylsulfonyl)imide
[VBIM][TFSI]	1-vinyl-3-butylimidazolium bis(trifluoromethylsulfonyl)imide
[VEIM][TFSI]	1-vinyl-3-ethylimidazolium bis(trifluoromethylsulfonyl)imide
[VMIM][TFSI]	1-vinyl-3-methylimidazolium bis(trifluoromethylsulfonyl)imide
IL-CN	1-vinyl-3-cyanopropylimidazolium bis(trifluoromethylsulfonyl)imide
N$_{1222}$FSI	Triethylmethylammonium bis(fluorosulfonyl)imide
VIm(1O2) (TFSI)	1-vinyl-3-methoxyl-ethyl-imidazolium bis(trifluoromethylsulfonyl)imide

1. Introduction

The current state of the world's energy situation calls for a revolution in the energy supply and distribution. The bet in renewable energies is the key to a greener economy that must be integrated with convenient storage systems to overcome their irregularity supply issues. However, better storage systems must be developed in order to warrant safety, durability and performance. The current state of the art of lithium-ion batteries (LIBs), which are the most used energy storage system worldwide, still lacks advancements in some areas, particularly safety and durability. Solid polymer electrolytes (SPEs) are a suitable technology to overcome these issues, with a growing research and development efforts every year. These research efforts aim to improve the properties of the SPEs, namely at the level of conduction mechanisms and interfacial compatibility, which are the main concerns of the currently developed SPEs. Several strategies are being studied and applied with this purpose, by selecting and combining different materials, as well as by tuning the experimental procedures in order to optimize the SPE properties.

1.1. Objectives and methodology

The focus of this work is the development of a new generation of high performance SPEs for LIBs. The solid polymer electrolyte development will be based on the implementation of a three-component polymer composite approach. The three-component approach has the potential to improve the cyclability and stability of solid-state batteries (SSBs). This approach focuses on the use of the different properties of passive and active fillers with the objective of directly improve the performance through the ionic conductivity (active) and enhancing other battery properties, such as cycling stability (passive), which will also improve the battery operation. A judicious selection of the used materials and a fine tuning of their ratios is essential to provide maximum performance in a SPE.

In this regard, the main objective of this work consists in the production of three-component SPEs for solid-state batteries using zeolites as passive fillers and ionic liquids, ILs, as active fillers, assessing their properties and testing their cycling performance. The choice of the right materials as well as the tuning of the experimental procedure was studied in detail in order to maximize the performance of the SPE, with the purpose of achieving high performance and battery cycling stability at room temperature.

At the materials level, ILs seem to be the most effective approach for the active role of improving ionic conductivity, while simultaneously having positive effects in the polymer matrix, such as the reduction of the crystalline phase and the increase in the electroactive phase content. Regarding passive fillers, microporous materials are a very promising option, due to their high stability, porous structure and encapsulation properties, as well as the outstanding number of contact points they possess, which allow for a high number of interactions with the other SPE components. However, this approach is still in the early research stages, particularly regarding zeolites, meaning that a considerable amount of work is still needed to optimize this technology.

1.2. Methodology and Thesis structure

In order to achieve the main goal, the methodology of the work focus on the development and optimization of a system composed by a polymer matrix, a zeolite structure as passive filler and an IL as active filler. The methodological steps are well reflected in the structure of the thesis, which precisely follows the developed research strategy. First of all, the state of the art of the SPE development is approached in **section 2**, with particular focus on the use of fluorinated polymers (**section 2.1**), ILs (**section 2.2**) and microporous materials (**section 2.3**). The analysis of the state-of-the-art limitations allowed to develop strategies for the development of this work, which are described in **section 3**. Different studies were performed in order to optimize this system, starting at the materials level. The selection of different zeolites was studied in **section 4.1** by comparing 3 distinct zeolite structures and evaluating the effect of ion exchange (IE) on battery performance. The most adequate IL was selected in **section 4.2** with a study on the effect of IL cation chain length and anion type. After the materials selection, some experimental parameters were adjusted, namely the SPE solvent evaporation temperature (**section 4.3**) and the preparation method, in particular with respect to the order of addition of the different components (**section 4.4**). These works emphasize the importance of the materials processing conditions, which can have a significant impact on the performance.

Finally, after the parameters optimization, the obtained results in each one of these works were combined in a single SPE to achieve an optimized battery performance, and some variations at the level of active fillers and polymer matrix were also introduced, based on works reported in the literature (**section 4.5**). Finally, the main conclusions and some perspectives for future work are presented in **section 5**.

2. State of the art

The contextualization of the thesis thematic is presented, stating the relevance of lithium-ion batteries, as well as of solid polymer electrolytes, in the modern society. The main advances in the field of SPEs, with particular focus on the use of fluorinated polymers, ionic liquids and microporous materials, are reported, stating the most relevant results and the main limitations and challenges.

Based on "Metal–organic frameworks and zeolite materials as active fillers for lithium-ion battery solid polymer electrolytes"; João C. Barbosa et al., Materials Advances", 2021. 2(12): p. 3790-3805.

Nowadays, the world is facing relevant issues associated with the continuous growth of the population and the increasing living standards. These factors lead to the increasing use of resources and energy consumption, which in turn leads to an increased pressure on natural resources due to over exploration and environmental damage, particularly climate change, that is closely associated to the world's reliance on fossil fuels to run the economies [1]. The transition to highly efficient and environmental friendlier systems for energy production is needed to constrain climate change and to support sustainable population growth, warranting reliable and affordable energy for everyone without compromising the environment. The United Nations is one of the main drivers of this transition since they created their 2030 agenda for sustainable development with 17 distinct objectives, in which two of them are directly related to this thematic (7 – affordable and clean energy; 13 – climate action) [2]. The decarbonization of the economies, with reliance in renewable energy sources is one of the main strategies adopted by the to overcome the dependence on fossil fuels. However, renewable energies, such as wind or sun, are intermittent, since they are dependent on time or weather conditions to be effective [3]. This leads to the necessity of developing efficient and environmentally friendlier energy storage systems in the upcoming years, to store the energy that is not used during the high production hours, and that can be used later, in the hours of higher demand [4]. In this context, batteries emerge as an effective solution for these issues.

A battery can be defined as a device able to convert chemical energy into electrical energy, and vice-versa, in a closed system [5]. The first battery was developed by Alessandro Volta in 1800, using zinc and silver electrodes, and brine-soaked cloth as separator [6]. Lithium technology only started to be developed in the 20th century [7]. Early in 1972, in parallel to Brian Steele's presentation on titanium disulfide (TiS_2), Michel Armand [8] mentioned in the same conference the general properties needed for an intercalation electrode and provided the first report on a SSB. The performance of a metallic lithium and titanium disulfide ($Li(0)||TiS_2$) cell was confirmed simultaneously by Michael Stanley Whittingham [9] and Steele et al. [10] in 1976. The safety problems of the device and the high production costs led to the development of new cathode materials, such as lithium cobalt oxide ($LiCoO_2$ - LCO) [11], lithium manganese oxide ($LiMnO_2$ - LMO) [12] and lithium iron phosphate ($LiFePO_4$ – LFP) [13] by John Bannister Goodenough between 1979 and 1997. The first commercial LIB was developed by Sony in 1991, based on the work developed by Akira Yoshino [14]. Whittingham, Goodenough and Yoshino won the Nobel Prize in Chemistry in 2019, because of their significant contributions to the LIB technology field. Nowadays, LIBs are the most worldwide used devices for energy storage purposes due to their high energy density and long cycle life, allowing the production of small and lightweight devices without jeopardizing battery capacity [15].

A common LIB is composed of three basic components (Figure 2.1): two electrodes (cathode and anode) and a separator, usually soaked in an electrolyte solution. The electrodes (that are deposited on aluminum (cathode) and copper (anode) foils) are composed of an active material, a conductive material, and a binder. The separator is placed between the electrodes and is usually a polymeric porous membrane [16].

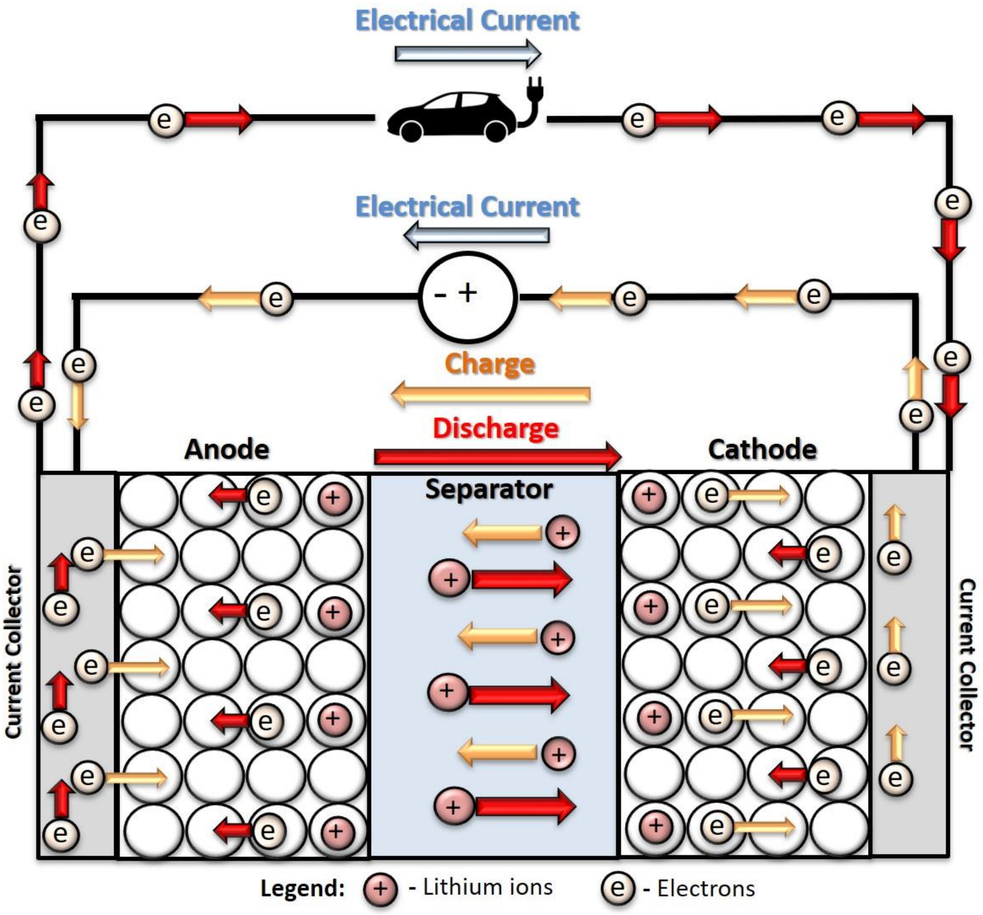

Figure 2.1 – Schematic representation of the composition and charge/discharge process of an archetypal LIB.

The separator plays a key role in the battery, as it works as a physical barrier between the electrodes, avoiding the occurrence of short circuits during the operation. A good separator must show high electronic resistance, but also high ionic conductivity to promote the Li^+ flow [17]. The most widely used materials for separators are polymers, such as poly(ethylene) (PE), poly(propylene) (PP) or poly(vinylidene fluoride) (PVDF). These polymers meet the requirement of high electronic resistance but lack the necessary high ionic conductivity. This is the reason why electrolyte solutions must be present in the system. Other important properties for a separator are high thermal and mechanical resistance, suitable porosity, high wettability in the electrolyte solution, and electrochemical stability [18].

The combination of liquid electrolytes with separators is the source of several critical issues that need to be addressed. The most common used electrolytes are composed of lithium salts, such as lithium hexafluorophosphate ($LiPF_6$), dissolved in organic carbonates, such as ethylene carbonate (EC) and dimethyl carbonate (DMC) [19]. These liquid electrolytes are flammable, increasing the risk of explosion or combustion of the battery. Moreover, they present significant levels of toxicity and are dangerous to the environment. As a consequence, robust battery casing is mandatory to prevent electrolyte leakages. Finally, the application of liquid components in batteries reduces their lifetime, as the electrolytes easily degrade the battery components [20]. The aforementioned shortcomings led to the idea of removing the liquid electrolyte and increasing the ionic conductivity of separator membrane so that the latter component acts simultaneously as separator and electrolyte, a step forward in the SSB approach [21].

SSBs can comprise two types of separators: inorganic electrolytes and SPEs [22]. Inorganic electrolytes are usually composed of ceramic crystalline materials, such as lithium super ionic conductor (LISICON) [23], sodium super ionic conductor (NASICON) [24], perovskites [25] or garnets [26], and possess high ionic conductivity, high electrochemical window, and high thermal stability. However, there are significant issues in the interfacial contact with the electrodes and a higher risk of lithium dendrite growth, as well as difficulties when it comes to production at large scale [27]. SPEs are discussed in detail in the next section.

2.1. Solid polymer electrolytes

SPEs can be defined as "solvent-free salt solutions in a polymer host material that shows sufficient mechanical stability to be considered solid in a macroscopic sense" [28]. These materials are essential in the operation of SSBs.

The main advances in the development of SPEs and SSBs on the last 50 years are summarized in Figure 2.2. The first SSBs were developed in the 1950s being based on silver (Ag) and lead (Pb) [29]. Their first application in LIBs appeared later in 1979 [30]. Materials such as NASICON [31], lithium aluminum titanium phosphate - $Li_{1.3}Al_{0.3}Ti_{1.7}(PO_4)$ (LATP) [32], lithium phosphorus oxynitride (LIPON) [33] or lithium lanthanum titanate (LLTO) [34] were developed in this period. In particular, the development of SPEs started in 1973 with the discovery of the complexation of alkali metal salts, dissolved in poly(ethylene oxide) (PEO), that formed high conductive complexes [35]. A similar approach was taken later, in 1978, using poly(propylene oxide) (PPO) as host polymer matrix [36]. Several polymer matrixes, such as poly(acrylonitrile) (PAN) [37], poly(methyl methacrylate) (PMMA) [38] or PVDF [39], were applied in the following years, particularly for use in lithium metal batteries. The efforts to increase the ionic conductivity of SPEs were extended to the 1980 and 1990 decades, mainly with the introduction of different kinds of nanoparticles and superionic conductors within the polymer matrix [40]. The interest in the functionalization of SPEs has increased in recent years, due to the quick expansion of the electric mobility and the widespread use of LIBs, which raised concerns with respect to security and environmental issues [41].

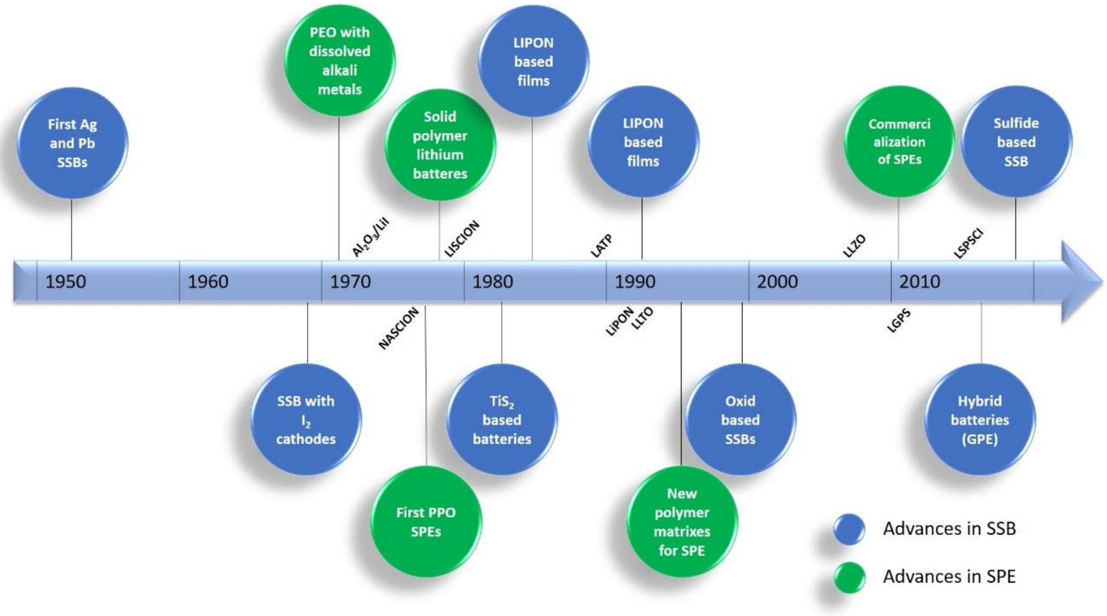

Figure 2.2 – Chronological line of the advances on the development of SSBs. Adapted from [42].

The performance of a SPE in a LIB is affected by different parameters, which must be tuned, in order to produce a functional device. The most critical parameters are those directly related with the ion conduction, in particular ionic conductivity, interfacial compatibility, and lithium-ion transference number. Also, stability parameters, such as thermal or mechanical stability, play an important role in the SPE performance, as they allow the operation in a wider range of conditions. Finally, there are other parameters that are not essential for the operation of the SPE, but are recommendable for environmental, health and safety reasons (Figure 2.3). Specifically, the requirements to be fulfilled by a SPE are high ionic conductivity (above 10^{-5} S cm^{-1}) at room temperature, lithium transference number close to unit, wide electrochemical stability window (up to 5 V), high thermal and mechanical stability (suitable for the normal battery using conditions), compatibility with the electrode materials, non-volatility, low toxicity, and low environmental impacts, in all the battery lifecycle stages. The perfect balance between all these properties is a challenge that must be overcome in the next years [43].

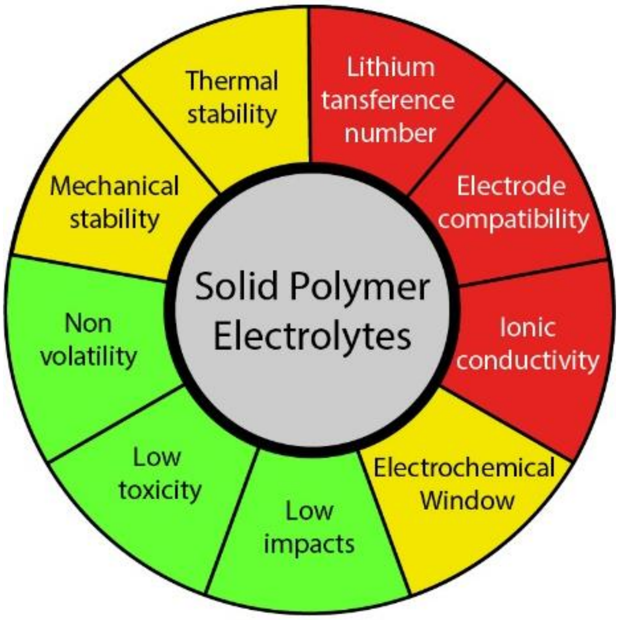

Figure 2.3 – Schematic representation of the main parameters that affect the performance of a SPE: critical (red), important (yellow) and recommended (green).

2.1.1. Main characteristics

SPEs present several advantages over the most commonly used liquid electrolytes. The most important one is safety, mainly due to the low flammability of the solid material when compared to liquid components, as illustrated in Figure 2.4. By avoiding the use of liquid components, the need to apply strong encapsulating materials to the batteries is suppressed, as liquid electrolyte leakage no longer exists [44]. The high mechanical and thermal stability of SPEs allows the battery accommodating more charge/discharge cycles in a wide range of temperatures [45]. The use of polymers is beneficial, as they improve the resistance to the variation of volume in the electrodes [46]. The immobility of the SPE anionic framework allows higher power capabilities, leading to faster charging of the batteries without compromising their structural integrity [47]. Altogether, the use of SPEs instead of common liquid electrolytes is advantageous in terms of safety, stability and durability of LIBs.

The main drawback regarding the application of SPEs is their low room temperature ionic conductivity, which is caused by the poor diffusion of ions in the solid matrix when compared to conventional liquid electrolytes. This issue limits SPE operation to higher temperatures, in which the mobility is increased [48]. Another disadvantage of SPEs relies on the interface between the electrodes and the SPE being often modified due to interfacial reactions between both components, leading to higher ionic resistance in the battery and therefore lower performance. In addition, SPEs are subjected to mechanical stresses during electrochemical cycling, which can affect their structural integrity, due to the development of cracks in their structure [49]. Another issue that derives from the absence of liquid components is that the contact between the SPE and the electrodes is difficult due to the volume changes, increasing the resistance of the battery [50]. Finally, the lithium dendrite growth phenomenon is considered a major concern, particularly at high discharge rates, which can cause loss of battery performance, or even short circuits [51]. Despite the above limitations, it is expected that the advances in research will bring valuable solutions, turning the SPEs in a more effective option to application in LIBs instead of the conventional liquid electrolytes.

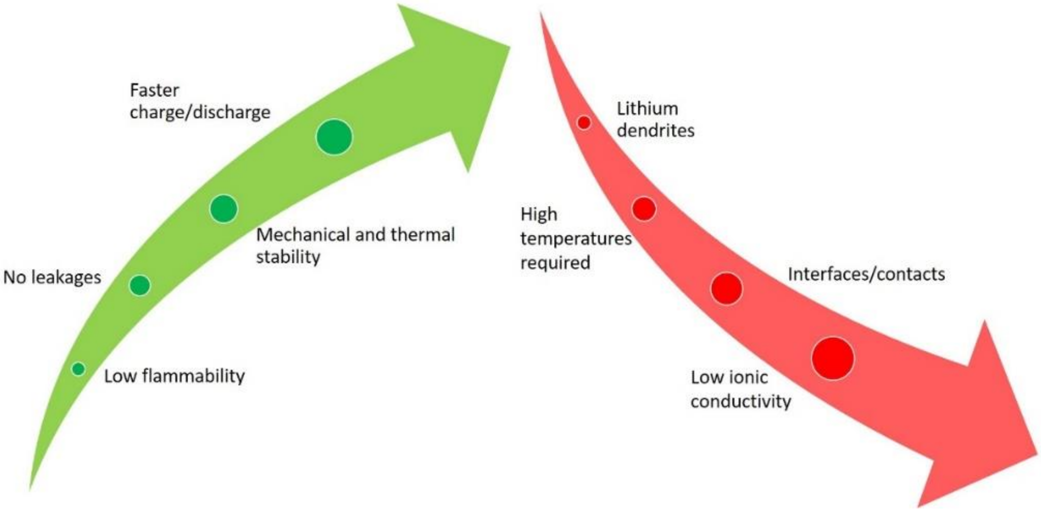

Figure 2.4 – Advantages (green arrow) and disadvantages (red arrow) of SPEs compared with conventional liquid electrolytes for LIB applications.

One of the most critical issues regarding SPEs is the interface between the electrolyte and the electrodes. In commercially available LIBs the presence of a liquid component that allows wetting of the electrodes, and the formation of a passivation layer (usually known as solid electrolyte interphase (SEI)) on the electrodes' surface allows the achievement of a better interface (Figure 2.5). This layer results from the decomposition of the electrolyte during battery operation and prevents further degradation of other battery components [52]. However, the SEI increases the internal resistance of the battery, which limits the charge/discharge process, particularly at high rates. [53, 54].

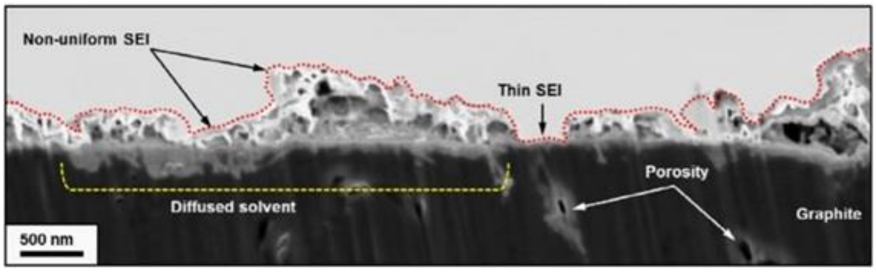

Figure 2.5 – Scanning electron microscopy (SEM) image of the SEI layer in a LIB anode [55].

In the anode/SPE interface, the main problem relies on lithium dendrite growth (Figure 2.6a), particularly when the anode is composed of metallic lithium. The lithium dendrites are rigid tree-like structures that are produced due to the incorrect deposition of lithium ions on the electrode's structure (Figure 2.6b). The dendrites grow throughout the solid electrolyte, particularly when metallic lithium is used as anode, leading to loss of battery performance as the number of available lithium ions decreases. In extreme cases lithium dendrites can pierce the solid electrolyte and cause short circuit in the battery [56]. This phenomenon induces the creation of SPEs with uniform lithium-ion transportation pathways enabling uniform deposition of the charges [57, 58]. Another situation that may occur in the anode is related with the volume changes during the charge/discharge process which leads to contact loss between this electrode and the SPE, increasing the impedance [50].

In the case of the cathode, the interfacial issues are similar to those occurring in the anode, although they are more complex, due to the composition of cathode, which gives rise to various solid-solid interfaces between different particles. To address the latter problem, the formation of stable ion-conducting networks in the cathode is advisable [59].

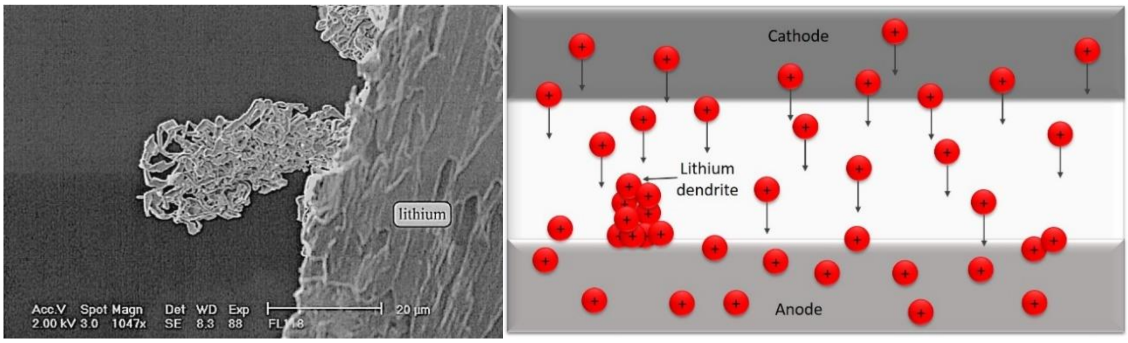

Figure 2.6 – SEM image [60] (a), and schematic representation of the formation process (b) of a lithium dendrite.

2.1.2. Conduction and diffusion mechanisms

The study of the conduction and diffusion mechanisms in a SPE plays a key role in the development of the field, as it allows getting a better insight into the behavior of the charges in the SPE structure and helping to stablish the best strategy to increase the ionic conductivity of the material.

The ionic conductivity is an important property of SPEs, as it represents the ability of the material to allow the ion flux through it, which is the basis of battery operation. However, the ionic conductivity of SPEs is lower comparatively to liquid electrolytes [50]. For a battery to work properly, the minimum room temperature ionic conductivity of the SPE must be higher than 10^{-3} S cm^{-1} [61].

The ionic conductivity (σ) of a SPE can be described by equation 1 [62]:

$$\sigma = F \sum n_i q_i \mu_i \tag{1}$$

where F is the Faraday constant, and n_i, q_i, and μ_i are the number, charge and mobility of the free ions, respectively. According to equation 1, to increase the ionic conductivity of the SPE, one or more of these parameters must be increased.

The ionic conductivity of a material is also strongly dependent on temperature. The Arrhenius model describes this behavior, according to equation (2):

$$\sigma = \sigma_0 \, exp \frac{-Ea}{RT} \tag{2}$$

where σ_0 is a pre-exponential factor, *Ea* is the activation energy, *R* is the universal gas constant, and *T* is the temperature. This model represents how the ionic conductivity of a material increases with increasing temperature, due to the improved mobility of the charges, which is related to the increase in the total energy of the system.

Another alternative to describe the conduction mechanisms in SPE is the Vogel-Tamman-Fulcher (VTF) theory. This model is based on the effect of the ion jump motion and polymer chain relaxation and/or segmental motion in the conductivity, which means that there is nonlinearity in the 1/T curve [63]. This model can be described by equation 3:

$$\sigma = \sigma_0 T^{-\frac{1}{2}} \exp\left(-\frac{B}{T - T_0}\right) \tag{3}$$

where *B* is an action factor, related to the activation energy distribution and T_0 is the reference temperature, usually 10-50 K below the glass transition temperature. At room temperature, the conductivity can be improved with low glass transition temperature polymers, due to the effect of the polymer segmental mobility [64].

The migration of ions in a polymer matrix under the application of an electric field mainly relies on the formation and dissociation of coordination bonds during the motion of polymer chains (Figure 2.7a) [65]. This motion occurs mainly in the amorphous phase of the polymer matrix, meaning that a high crystallinity degree will affect negatively the ionic conductivity of the SPE, due to the higher energy barrier for the movement of the Li^+ between the preferred sites. Typically, the addition of conductive salts contributes to the increase of the glass transition temperature (T_g) of the polymer due to the slowing down of the segmental dynamics [66]. The mechanism of the lithium motion on the polymer matrix can be described by the free volume model. Above T_g, a state of local segmental motion on the polymer chains occur, which increases the free volume near the moving chain segments [67]. This volume allows for the intermolecular coordination of the lithium ions, leading to the possibility of moving between coordination sites, in the presence of an electric field. This interchanging between polymer chains is possible due to the reduced energy barrier [68]. However, Bruce et al. introduced a different conduction mechanism based on the movement of lithium-ions on the spiral-shaped channels found within the ordered structure of the polymer matrix (Figure 2.7b) [69].

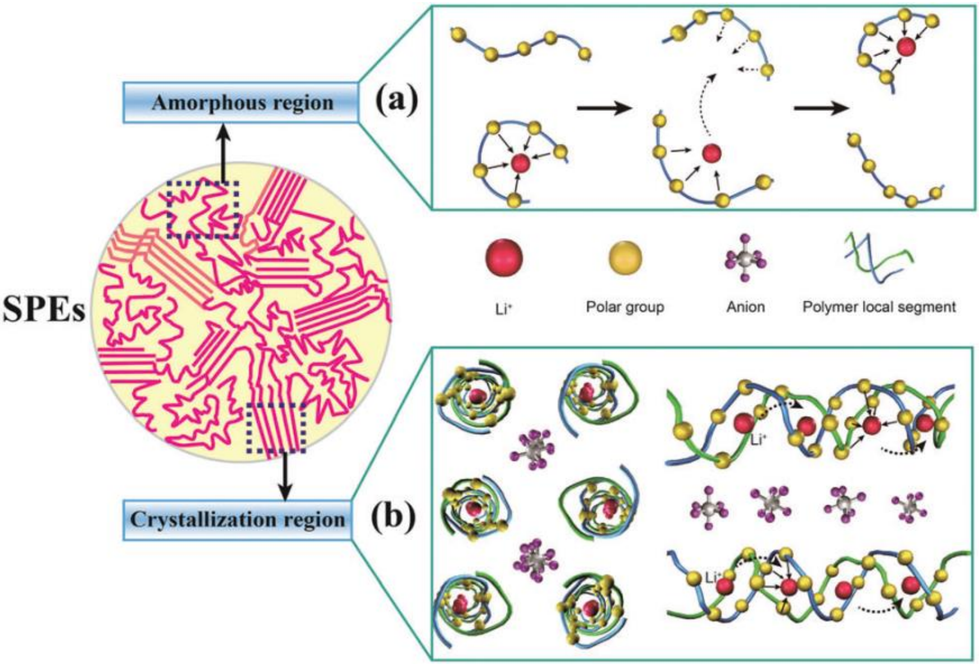

Figure 2.7 – Schematic illustration of conduction mechanisms in amorphous (a) and crystalline (b) SPEs [70].

Several additives allow decreasing the degree of crystallinity of the polymer, leading to an increase on the mobility of the polymer chains and consequently on the mobility of the charges: ceramic fillers [71], metal-organic frameworks (MOFs) [72], ionic liquids (ILs) [73], and ionic salts [74]. The addition of the latter compounds represents the most efficient way to increase the ionic conductivity of a SPE, by also introducing more charges into the system. However, the polymer matrix must be able to dissolve cations by complexing them in its structure. Also, the lattice energy of the salt must be low, and the dielectric constant of the polymer must be high to allow the dissociation of the salt in the polymer host [75]. Finally, for a significant effect on the increase of the ionic conductivity, large amounts of salts are needed, which could also affect other properties of the SPE, namely the mechanical stability, potentially leading to negative effects on the overall performance [76].

2.1.3. Materials for solid polymer electrolytes

A composite solid electrolyte is typically composed of a host polymer matrix that warrants the structural integrity of the electrolyte, and different kinds of fillers. Each filler affects the properties of the electrolyte in different ways, and it is the combination of the polymer matrix with one or more fillers that leads to the electrolyte distinct final characteristics, performance and stability.

As stated above, in a SPE the polymer is the constituent that warrants the structural integrity. Thus, it is important that the selected polymer exhibits suitable mechanical, thermal and electrochemical stability. Traditionally the most widely used polymers belong to the class of thermoplastics, that meet the requirements referred previously [77]. The main limitation of these polymers is their ionic conductivity, which is generally low ($<10^{-5}$ S cm^{-1}) at room temperature, making them a less attractive option for battery applications. The most studied polymer for application in SPEs is PEO, due to its high lithium-ion conductivity, especially at high temperatures, when lithium salts are introduced in a composite form [78]. Other polymers, such as PVDF [79] and its co-polymers [80], (PAN) [81], poly(ethylene carbonate) (PEC) [82] and poly(ethylene glycol) (PEG) [83], have been also studied and tested. Some works have focused on blends, by combining two or more polymers, in order to combine the best properties of the individual ones. Blends of poly(vinyl chloride) (PVC)/PVDF [84], PEO/PMMA [85] and PVDF-hexafluoropropylene (HFP)/poly(aniline) (PANI) [86], are some successful examples of prepared SPEs.

Environmental friendlier approaches have gained increasing attention in recent years, in the search for more sustainable alternatives to conventional polymers. In this field, natural polymers are valid options due to their biodegradability and low environmental impact. Studies with polysaccharides, such as cellulose [87], pectin [88], chitosan [89] and carrageenan [90], have been successfully carried out.

As mentioned above, the incorporation of fillers is essential in the functionalization of a SPE, because these components enhance the properties of the electrolyte, particularly its ionic conductivity and mechanical stability. Fillers can be divided into two categories: active and passive. A*ctive fillers* are able to directly increase the ionic conductivity of the SPE, while *passive fillers* exert their influence on other parameters of the SPE, inducing the increase of the thermal or mechanical stability, or reducing the degree of crystallinity, which indirectly facilitates ion transport [91]. These fillers include ceramics (barium titanate ($BaTiO_3$) [92], alumina (Al_2O_3) [93], silica (SiO_2) [94], titania (TiO_2) [95]), carbonaceous (graphene oxide [96], carbon nanotubes [97]), lithium salts (e.g., lithium tetrafluoroborate ($LiBF_4$) [98], lithium hexafluorophosphate ($LiPF_6$) [99], lithium perchlorate ($LiClO_4$) [100], lithium bis(trifluoromethylsulfonyl)imide (LiTFSI) [101]), ILs (1-ethyl-3-methylimidazolium bis(trifluoromethylsulfonyl)imide ([EMIM][TFSI]) [102], and 1-butyl-3-methylimidazolium chloride ([BMIM][Cl]) [103]) or microporous materials (zeolites [104], nanoclays [105], and MOFs [106]).

In particular, microporous materials are attracting increasing interest for this application, as their properties, such as their tunable micropore structure and their high surface area and capacity to encapsulate other components, show potential to overcome several limitations of the actual SPEs. Nevertheless, they have been scarcely studied up to now.

2.2. Role and contribution of poly(vinylidene fluoride) and its copolymers for solid polymer electrolyte applications

The conventional separator/liquid electrolyte systems used in LIBs nowadays present several issues associated with safety, toxicity, performance and durability of these systems, due to the use of liquid components in their constitution [19, 20]. These limitations brought up the idea of combining the functions of the separator and the electrolyte in one single component with high ionic conductivity and electrical resistance, leading to the research in SSBs [21].

In SSBs the battery liquid components are replaced by the solid electrolyte, which simultaneously has the function of separator and electrolyte combined in the same structure. These electrolytes can be ceramic or polymeric [22]. SPEs are usually constituted by a polymer matrix or a blend of different polymers that warrants the structural integrity, and one or more kinds of fillers, to enhance the properties of the electrolyte [107]. However, SPEs also possess some drawbacks, such as the lack of ionic conductivity, particularly at room temperature, and the lower interfacial compatibility with the electrodes, that limit their application in large scale [48, 50]. Currently, to overcome these limitations, research is focused on an intermediate step between the common separator/electrolyte systems and the SPE, the gel polymer electrolytes (GPE). GPE is a quasi-solid technology that combines the characteristics of SPE and liquid electrolytes, allowing for a better comprehension of the conductivity mechanisms that need to be tuned in order to allow the improvement in the SPE field (Figure2.8) [108]. Although they can overcome the low ionic conductivity and interfacial compatibility issues associated with the SPE, they still maintain some of the limitations of the liquid electrolytes and lack the needed mechanical strength to be fully effective [109].

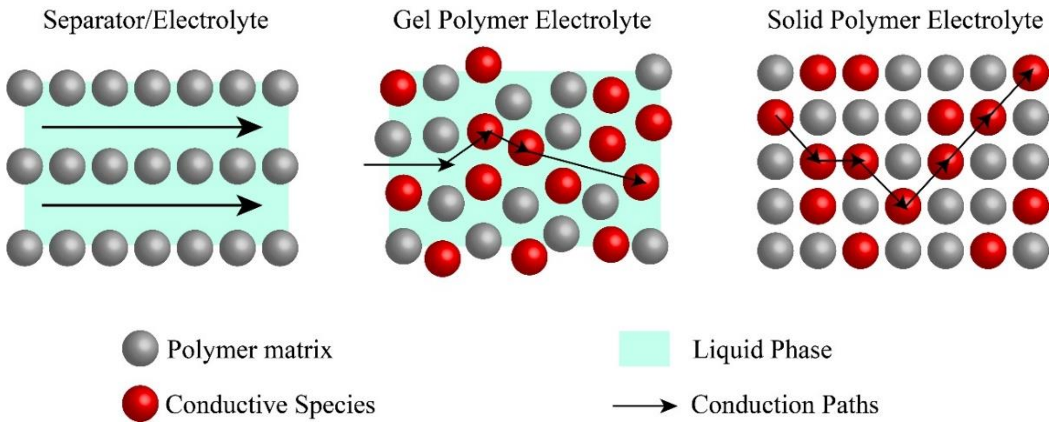

Figure 2.8 – Conduction mechanisms in the different types of electrolyte systems.

As reported in the previous sections, poly(vinylidene fluoride), PVDF, and its copolymers play a key role in the field of SPEs due to its properties, namely high thermal, chemical and mechanical resistance, high dielectric constant and controllable amorphous phase content. Due to its interesting properties, along the years, a growing number of works and reports were carried out to better understand the effects and interactions of PVDF and its copolymers with a great variety of fillers and other polymers. In the following sections, the main advances and the role of the PVDF, since its first application in GPEs to the latest developments in complex composites in SPEs, are summarized.

2.2.1. Poly(vinylidene fluoride) in gel polymer electrolytes

The first reported PVDF based GPE example goes back to 1999, where liquid $LiClO_4$ electrolytes were encapsulated in a poly(vinylidene fluoride-co-hexafluoropropylene) (PVDF-HFP) matrix and the interactions between them were studied [110]. The addition of PE to this system proved to create a thermal shutdown function at about 90°C due to a significant increase in the impedance of the gel resulting from the melting of the PE particles into a film in the gel surface [111]. Polymer blends of PMMA and PVDF were the first reported GPE with PVDF, and the addition of PVDF proved to increase the ionic conductivity through the reduction of the crystallinity [112]. Other relevant advances included the first use of ultraviolet (UV) curing in a PVDF/poly(ethylene glycol) diacrylate (PEGDA) blend [113] and the development of extrusion lamination processes between the battery electrodes [114].

Even after the development of the first SPE, the development of GPEs has continued until nowadays, accompanying the research in the SPE. By combining PVDF-HFP with ILs, it is possible to achieve high room temperature ionic conductivities and excellent cycling performances [115, 116]. The use of ceramic particles, such as LLTO, promoted the suppression of lithium dendrites in the GPE structure [117]. Other ceramic fillers, such as lithium lanthanum zirconium oxide (LLZO), contributed to the increase in the GPE stability, electrochemical window and lithium transference number [118].

2.2.2. PVDF in solid polymer electrolytes

As stated before, SPEs are one of the most promising technologies for the development of SSBs. Much of the work developed in understanding the mechanisms associated with GPEs was very useful in the field SPEs. The tendency is a growing complexity of the SPE structures, as the first ones developed were composed solely of PVDF and a ceramic filler or a lithium salt, and then polymer blends and the combination of several fillers started to be synthesized. Table 2.1 summarizes the main advances in PVDF based SPEs, organized by increasing complexity.

Table 2.1 – Reported developments in PVDF based SPEs.

Polymer	Fillers	Processing Technique	Ionic Conductivity (S cm^{-1})	Battery capacity (mAh g^{-1})	Main goal/ achievement	Ref
Basic SPE (1 polymer; 1 filler)						
PVDF	LiTFSI	Solvent casting	1.1×10^{-4}	-	Study of the solvent effect	[119]
PVDF	LiTFSI; LiFSI	Solvent casting	1×10^{-3} (25°C)	-	Study of the effect of lithium salt	[120]
PVDF	$[C_2mpyr][BF_4]$	Electrospinning	1.2×10^{-6} (25°C)	-	Application of electrospinning in SPE	[121]
PVDF-HFP	LiTFSI	Solvent casting	1.1×10^{-6} (25°C)	51.12 (C/20)	Functional room temperature SPE	[122]
PVDF-HFP	LATP	Solvent casting	6.26×10^{-4} (30°C)	127.8 (C/10)	Use of LATP as ionic conductor	[123]
PVDF-HFP	[Bmim][SCN]	Solvent casting	1.5×10^{-4} (25°C)	148 (C/8)	Application of ionic liquids in a room temperature SPE	[124]
Polymer blends (2 polymers, 1 filler)						
PVDF/MG49	$NH_4CF_3SO_3$	Solvent casting	6.32×10^{-4} (25°C)	-	Use of a natural polymer	[125]
PVDF/PVC	$LiClO_4$	Solvent casting	4.683×10^{-3} (30°C)	-	Study of the influence of Li salt content	[126]
PVDF/PEO	LiTFSI	Solvent casting	2.98×10^{-5} (25°C)	149.6 (C/10)	Optimization of Li salt content	[127]
PVDF/PEO	$LiClO_4$	Solvent casting	2.01×10^{-5} (27°C)	-	Optimization of Li salt content	[128]
PVDF/PEO	$LiClO_4$	Solvent casting	2.8×10^{-5} (25°C)	132.2 (C/5)	Study on the blend mechanical properties	[129]
PVDF/Phtaloyol starch	LiTFSI	Solvent casting	2.04×10^{-4} (25°C)	135.06 (C/20)	Use of biomaterials in SPE	[130]
PVDF/PAA	LiFSI	Solvent casting	9.1×10^{-5} (30°C)	125	Reduction on the interfacial reaction of the SPE upon the introduction of PAA	[131]
PVDF-HFP/PHEMO	LiTFSI	Solvent casting	1.64×10^{-4} (30°C)	-	Use of hyperbranched polymer to increase ionic conductivity	[132]
PVDF-HFP/PVAc	LiTFSI	Solvent casting	1.1×10^{-3} (25°C)	-	Use of PVAc to increase interfacial compatibility	[133]
PVDF-HFP/PEGDA	LiTFSI	Solvent casting	1.04×10^{-3} (27°C)	152 (C/10)	Development of interwined nanosponge SPE	[134]
PVDF-HFP/PEO	LiTFSI	Solvent casting	1.94×10^{-5} (27°C)	133 (C/10)	Study of the optimal PVDF-HFP:PEO ratio	[135]
Ternary-composites (1 polymer, 2 fillers)						

PVDF	$LiClO_4$, HNT	Solvent casting	3.5×10^{-4} (30°C)	71.9 (1C)	Use of HNT to increase ionic conductivity	[136]
PVDF	$LiClO_4$, palygorskite nanowires	Solvent casting	1.2×10^{-4} (25°C)	106.2 (C/5)	Use of palygorskite nanowires to increase the mechanical properties	[137]
PVDF	$LiClO_4$, LLZO	Solvent casting	2.6×10^{-4} (25°C)	-	Study of the effect of the LLZO particle size on the ionic conductivity	[138]
PVDF	LiTFSI, $LiSnZr(PO_4)_3$	Solvent casting	5.76×10^{-5} (27°C)	133 (C/10)	Study of the effect of NASICON-type particles on the SPE	[139]
PVDF	$LiClO_4$, LLTO	Solvent casting	2.37×10^{-3} (25°C)	87.13 (C/10)	Study of the effect of the LLTO particles on the ionic conductivity	[140]
PVDF	$LiClO_4$, LLTO	Solvent casting	5.8×10^{-4} (25°C)	152 (C/5)	Study of the effect of the LLTO nanofibers on foldable batteries	[141]
PVDF	$LiClO_4$, LLTO	Doctor blade	4.7×10^{-4} (25°C)	139 (C/5)	Creation of a layered SPE with different LLTO contents	[142]
PVDF-HFP	$LiClO_4$, ZnO	Solvent casting	1.04×10^{-3} (25°C)	-	Use of ceramic particles to increase ionic conductivity	[143]
PVDF-HFP	CF_3LiO_3S, $BaTiO_3$	Solvent casting	8.89×10^{-6} (27°C)	-	Study of the activation energy and crystallinity upon the addition of $BaTiO_3$ and lithium salt	[144]
PVDF-HFP	LiTFSI, LLZO	Solvent casting	9.5×10^{-4} (25°C)	140 (C/5)	Effect of LLZO nanofiber on ion conduction	[145]
PVDF-HFP	LiTFSI, 3-(1-vinyl-3-imidazolio)-propane sulfonate	Solvent casting	~10^{-5} (25°C)	-	Use of poly(ionic liquids) in SPE	[146]
PVDF-HFP	LiTFSI, LLZTO	Solvent casting	8.80×10^{-5} (25°C)	158.7 (C/10)	Use of LLZTO in SPE	[147]
PVDF-HFP	LiTFSI, LGPS	Solvent casting	1.8×10^{-4} (25°C)	135.1 (C/5)	Use of high conductive LGPS salts	[148]
PVDF-HFP	LiTFSI, LLTO	Solvent casting	5.1×10^{-4} (25°C)	158 (C/10)	Use of electrospun LLTO nanofibers	[149]
PVDF-HFP	LiTFSI, LLZO	Solvent casting	6.5×10^{-3} (20°C)	164 (C/2)	Use of electrospun LLZO nanofibers	[150]
PVDF-HFP	LiFSI, PGCN	Solvent casting	2.3×10^{-4} (30°C)	154.8 (C/10)	Use of high surface area fillers to increase battery performance	[151]

PVDF-HFP	LiTFSI, LATP	Solvent casting	2.3×10^{-4} (25°C)	148 (C/5)	Study of the effect of the LATP content variation	[152]
Complex composites (more than three components)						
PVDF/PEO	LiClO$_4$, silica aerogel	Solvent casting	1.70×10^{-3} (25°C)	-	Study of the effect of the component content variation	[153]
PVDF/PVA	LiTFSI,MMT	Solvent casting	4.31×10^{-3} (25°C)	123 (C/10)	Preparation of an environmentally friendly SPE	[154]
PVDF/PVA	LiCF$_3$SO$_3$, TiO$_2$	Solvent casting	3.7×10^{-3} (30°C)	-	Study on the influence of LiCF$_3$SO$_3$ and TiO$_2$	[155]
PVDF/PVP	LiTFSI, EDTA	Solvent casting	7.19×10^{-4} (30°C)	147.9 (C/10)	Application of EDTA in SPE	[156]
PVDF/PVC	LiTFSI, MMT	Solvent casting	1.67×10^{-4} (25°C)	117.8 (C/10)	Use of organophilic nano montmorillonite to increase ionic conductivity	[84]
PVDF/PAN	LiClO$_4$, LLTO	Solvent casting	1.43×10^{-3} (25°C)	122 (C/10)	Use of LLTO in SPE	[157]
PVDF/PI	LiTFSI, LLZTO	Doctor blade	1.23×10^{-4} (25°C)	152.6 (C/10)	Use of LLZTO in SPE	[158]
PVDF/PEO	LiPF$_6$, LATP	Solvent casting	5.24×10^{-4} (25°C)	136.8 (C/5)	Study of the effect of modifying the SPE structure upon the addition of different components	[159]
PVDF/CA	LiTFSI, MMT	Solvent casting	3.4×10^{-4} (25°C)	112 (C/2)	Use of CA and combining different fillers in a SPE	[160]
PVDF/Soybean protein	LiTFSI, MMT	Solvent casting	2.56×10^{-4} (25°C)	100 (C/2)	Use of natural polymer in SPE	[161]
PVDF-HFP/MEEP	LiBOB, LATP	Coating	2.6×10^{-4} (50°C)	123 (C/10)	Creation of layered electrolytes	[162]
PVDF-HFP/PEO	LiTFSI, LLZTO	Coating	2.29×10^{-4} (30°C)	149.4 (C/10)	Creation of layered electrolytes	[163]
PVDF-HFP	P(MMA-co-VIm(1O2)) (TFSI), [Pyr13][TFSI]	Solvent casting	5.10×10^{-4} (25°C)	102.7 (C/10)	Use of polymeric ionic liquids to achieve fucntional room temperature SPE	[164]
PVDF-HFP/PE	LiTFSI, LLTO	Coating	1.21×10^{-4} (25°C)	135.5 (C/10)	Study of the effect of the LLTO content variation	[165]

The synthesis of a PVDF-HFP/LiTFSI SPE represents one of the first room temperature functional SPEs based on PVDF. This study was accompanied by theoretical simulations that correlated the cycling performance with parameters such as lithium-ion concentration, free ions load and thickness [122]. The effect of the solvent used and the evaporation temperature was studied for a simple PVDF/LiTFSI composite, allowing to conclude that when the solvent is trapped in the polymer structure there is a positive effect on the ionic conductivity. Also, the increase in the LiTFSI content promotes solvent retention [119]. The effect of different salts in the ionic conductivity was carried out for LiTFSI and lithium bis(fluoromethylsulfonyl)imide (LiFSI), concluding that the smaller anion size of LiFSI contributes to an increase in the ionic conductivity [120].

The addition of ceramic particles to increase the ionic conductivity was targeted by some studies, particularly focusing the PVDF-HFP copolymer. Adding LATP to the structure enabled a significant increasing the ionic conductivity and cycling stability maintenance even after 200 cycles [123].

By incorporating ILs into the PVDF-HFP structure, the amorphous polymer phase is promoted, increasing the ionic conduction, which allows for high-capacity room temperature batteries [124]. The use of organic ionic plastic crystals in electrospun PVDF nanofibers promotes polymer crystallization on the electroactive β-phase, simultaneously improving the ionic conductivity due to the changes in the molecular dynamics [121].

Polymer blends are an interesting approach to enhance the properties of a SPE, particularly their thermal and mechanical stability. It also limits the crystallinity of the polymers, improving their ionic conductivity [166]. The use of a graft of natural rubber and PMMA to form MG49, blended with PVDF increases the ionic conductivity of the SPE, and the further addition of the ammonium triflate ($NH_4CF_3SO_3$) salt contributes to the reduction of the crystallinity of the blend [125]. PVDF-HFP can be effectively combined with PVC due to their high compatibility, leading to a stable SPE. Furthermore, the addition of plasticizers contributes to the improvement of the conductivity of the SPE [126]. The application of hyperbranched polymers, as poly(3-{2-[2-(2-hydroxyethoxy)ethoxy]ethoxy}methyl-3'-methoxyloxetane)) (PHEMO) into the PVDF-HFP matrix affords increased ionic conductivity to the SPE due to the increase in the free space, and also to negative groups of PHEMO that can react with the Li ions [132]. On the other hand, poly(vinyl acetate) (PVAc) is well suited to increase the interfacial compatibility of the SPE with lithium metal anodes due to the good adhesive characteristics of PVAc that reduce the interfacial resistance [133]. The study on the optimization of Li salt content in a PEO/PVDF blend showed that the optimal salt content is about 1:5 wt.% regarding salt/polymer ratio, with good cycling performances at high temperatures [127]. Similar studies were carried out for $LiClO_4$ salt, with an optimal ionic conductivity value for 25% wt.% of Li salt [128]. The mechanical properties of a similar blend were studied, leading to the conclusion that the addition of a PVDF support layer can increase the maximum stress of the SPE by 10 times [129]. PVDF-

HFP can also be blended with PEO, with effective results at high temperatures [135]. Phtaloyl starch is a biomaterial that increases the electrochemical stability window and the lithium transference number of the SPE due to the oxygen attraction to Li ions, that promotes the Li ion transfer between the polymer blocks [130]. By creating a intertwined nanosponge SEP based on PVDF-HFP, it is possible to combine it with a PEGDA/LiTFSI solution, without compromising mechanical stability, and adding excellent electrochemical properties, such as ionic conductivity and cycling stability, even at room temperature [134]. The addition of small amounts of PAA to a PVDF matrix contributes to the reduction of the interfacial reaction of PVDF with the electrodes, leading to a better stabilization of the battery system [131].

With advances in research, the idea of using two distinct fillers to meet different requirements of the SPE emerged. PVDF and its copolymers had also a significant relevance in this approach, with several works reported. The simplest methodology is based on the addition of a lithium salt, such as $LiClO_4$, and a ceramic particle, such as ZnO. This combination allows a reduction of the crystallinity of the polymer due to Lewis acid-base interactions with the polymer chains, enhancing the ionic conductivity [143]. A similar behavior is observed for $BaTiO_3$ particles, while lithium triflate ($LiCF_3SO_3$) reduces the activation energy of the SPE [144]. The large amount of amino and hydroxyl groups present in ethylenediaminetetraacetic acid (EDTA) contributes to decrease the PVDF crystallinity, increasing the ionic conductivity of the SPE [156]. LLZO nanofibers increase the transport pathways in the SPE, which enhances the ionic conductivity, allowing for excellent battery performances allied with good mechanical stability [145]. Electrospun LLTO [141, 149] nanofibers were also reported, with strong interactions between the organic and inorganic phases along with the creation of highly conductive pathways and excellent mechanical properties. It was proven that to optimize the ionic conductivity of a LLZO SPE, the best way is to use mixed sized LLZO particles, due to the reduction in the porosity caused by the closely packing of the different sized particles [138]. Similarly, $Li_{6.4}La_3Zr_{1.4}Ta_{0.6}O_{12}$ (LLZTO) can be successfully applied in SPEs, with the further advantage of inhibiting the Li dendrites formation [147]. LLTO has the effect of reducing the binding energy of Li^+ [140]. When different LLTO contents are applied in different SPE layers, it is possible to achieve good interfacial contact, due to the lower LLTO content in the external layers, and enhance the ionic conductivity with high contents in the internal layer [142]. Another interesting material is $Li_{10}GePS_{12}$ (LGPS), which possess high ionic conductivity, leading to SPEs with high Li transference number, and stability up to 300 cycles [148]. NASICON-type ceramic fillers are also a good option for application in SPE due to their high electrochemical stability and the facility to create pathways for the Li^+ transfer [139, 152]. The use of poly(ionic liquids) was also studied, and proved superior to conventional ILs due to their better thermal, mechanical and electrochemical properties [146]. By applying high surface area porous graphitic carbon nitride it is possible to increase the number of organic-inorganic interfaces, leading to an improvement in ionic conductivity and consequently in the battery performance [151].

The tendency in the field of SPE is a continuous increase in the complexity of the structure, with more components able to provide different properties to the SPE. By adding PVDF and silica aerogel to a PEO/$LiClO_4$ composite it was possible to increases the thermal stability and the Li dissociation rate [153]. The use of TiO_2 particles and lithium triflate increases not only the electrochemical properties but also the thermal and mechanical stability of the SPE [155]. Other kinds of ceramic particles as LLTO [157] and LLZTO [158] can also be successfully applied combined with lithium salts. By adding LATP to a PVDF/PEO blend strengthens the interface reactions through the formation of hydrogen bonds between the polymers, which also interacts with the inorganic particles, allowing for higher ionic conductivities and SPE stability (Figure 2.9a) [159]. Polymeric ionic liquids proved to improve the performance of PVDF-HFP SPE, particularly at room temperature, through the increase in the ion mobility and the polymer chain segment motion [164]. A different approach consists in the fabrication of layered structures with different characteristics. A PVDF-HFP/ poly(bis((methoxyethoxy)ethoxy)phosphazene (MEEP) composite can be used to coat a LATP pellet structure, allowing to solve the interfacial compatibility issue between LATP and the Li meal electrode, and resulting in good cycling stability up to 500 cycles at high temperatures [162]. Another reported layered SPE consists of a PVDF-HFP/LLZTO core sandwiched between two PEO/LiTFSI layers, resulting in a SPE with better affinity with the electrodes without compromising the ionic conductivity and battery performance. Also the crosslinking between both polymers significantly reduced the overall crystallinity [163]. LLTO nanorods in a PVDF-HFP matrix were used to coat a PE substrate, resulting in excellent ionic conductivity and cycling performance (Figure 2.9b) [165].

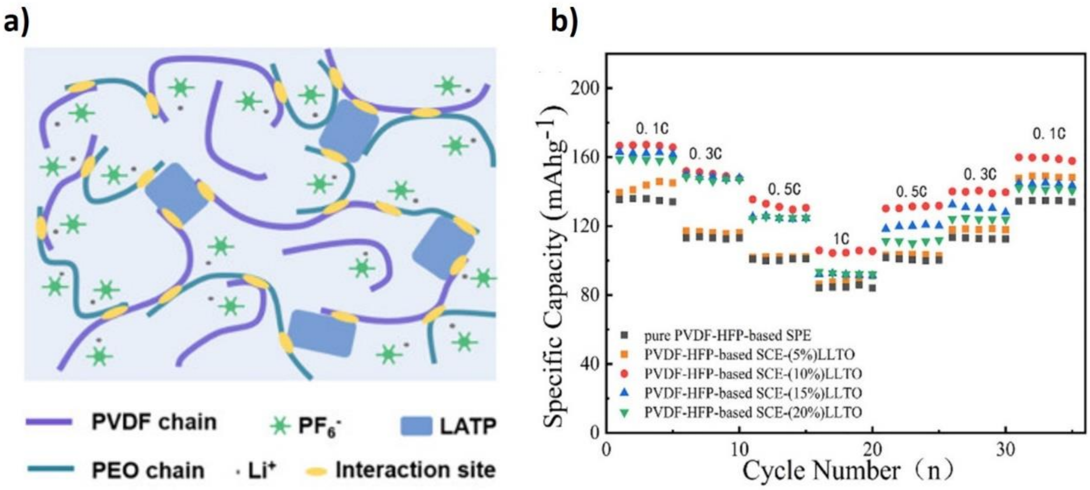

Figure 2.9 - Schematic representation of the interactions between the PVDF/PEO blend and the inorganic LATP and $LiPF_6$ particles [159] (a); rate performance of PVDF-HFP/LLTO based SPE [165] (b).

Addressing environmental concerns also gained significant relevance in recent years, thus it is important to develop SPEs that meet, not only the performance and stability requirements, but also the need for "greener" materials. In this context, a PVDF/PVA blend using LiTFSI and natural montmorillonite (MMT) presented promising results with 123 mAh g^{-1} capacity at C/10 and stability up to 100 cycles [154]. Similar results were reported when the polymer blend is composed by PVDF and PVC [84]. By using natural halloysite nanotubes (HNTs), with their negatively charged surface and high surface area, it is possible to facilitate the Li^+ transfer, increasing the ionic conductivity of the SPE [136]. Palygorskite nanowires increase, not only the electrochemical properties, but also the mechanical stability of the SPE, with an increase on the elastic modulus of around 10 times upon the addition of 5% palygorskite [137]. The combined use of MMT and cellulose acetate (CA) with a PVDF matrix is promising environmentally friendly approach, where the CA contributes to the reduction of the crystallinity, while the MMT improves the compatibility with the polymer. This configuration allows for high ionic conductivity and acceptable cycling performance, even at room temperature [160]. Soybean protein is also a good candidate for this kind of structure, due to the high synergy between the soy and the MMT, leading to the increase in the SPE stability [161].

In summary, PVDF and its copolymers have significant interest in the SPE area, with a growing number of publications along the years. The high compatibility of PVDF with a vast number of other materials, both fillers and other polymers, makes it an interesting option for the development of complex composites that match the desired properties of a functional SPE. This is complemented by the outstanding thermal and mechanical stability of the PVDF, which meets the requirements for SPE technology. Thus, there is plenty of room for improvement in this area, as the only copolymer used in SPEs is PVDF-HFP, and the industry is constantly developing new conformations for this polymer that can present even better characteristics. Another interesting opportunity lies on the development of new production techniques. Particularly, the printing processes can be a major step forward, as they allow, not only the production without material wastes, but also the assembling of a full solid-state battery, with the layer by layer deposition of the different components. Thus, with the right conditions and an extensive study on the mechanisms that drive the conduction and stability, PVDF and its copolymers have the potential to become one of the major options for host materials in SPE applications.

2.3. Application of Ionic Liquids in solid polymer electrolytes

ILs are one of the most promising materials when it comes to improve the performance of SPEs. They contribute directly to the ionic conductivity improvement by increasing the number of charged species in the polymer matrix, and reducing the overall crystallinity of the polymer matrix [164]. The first reports of ILs in SPEs go back to 2010 with the use of the 1-ethyl-3-methylimidazolium tetrafluoroborate [EMIM][BF$_4$] IL in a PVDF-HFP matrix [167]. Since then, the field continuously grew both in battery performance and SPE structural complexity in order to overcome the limitations of SPEs. In table 2.2, the most recent advances in the field of ILs applied to SPEs are reported.

Table 2.2 – Literature reports for the most recent developments in the application of ILs for SPEs.

IL	**Other Filers**	**Polymer**	**Technique**	**Ionic Conductivity (S cm^{-1})**	**Li$^+$ transference number**	**Discharge capacity (mAh g^{-1})**	**Ref**
Basic SPE (1 polymer; 1 filler)							
[BMIM] [SCN]	-	PVDF-HFP	Solvent casting	1.5×10^{-4} (25°C)	-	124 (C/8, 25°C)	[124]
[BMIM]$_2$ [(SCN)$_4$Co]	-	PVDF	Doctor blade	7×10^{-4} (25°C)	-	80 (C/10, 25°C)	[168]
[DEME] [TFSI]	-	PDM-TFSI	Pressing	1.9×10^{-4} (30°C)	0.30	130 (C/10, 25°C)	[169]
Polymer blends (2 polymer, 1 filler)							
POSS-im-TFSI	-	PVDF-HFP, PEO	Solvent casting	3.06×10^{-4} (22°C)	0.32	150.7 (C/10, 25°C)	[170]
Ternary-composites (1 polymer, 2 fillers)							
[DEIM] [TFSI]	LiTFSI	PEO	Solvent casting	6.33×10^{-3} (25°C)	0.47	156 (C/10, 60°C)	[171]
[EMIM] [TFSI]	LiTFSI	PEBA 2533	Solvent casting	3.0×10^{-4} (25°C)	0.40	-	[172]
[EMIM] [TFSI]	LiDFOB	PEO	Solvent casting	1.85×10^{-4} (30°C)	-	155 (C/10, 25°C)	[173]
[PP] [TFSI]	LiTFSI	PEO	Hot pressing	2.06×10^{-4} (25°C)	0.339	120 (C/10, 25°C)	[174]
[PMPYR] [TFSI]	LiTFSI	PDADMA-FSI	Blade coating	8.0×10^{-4} (25°C)	0.44	162 (25°C)	[175]
[PMPYR] [TFSI]	LiTFSI	PAES-co-PEG	Solvent casting	7.2×10^{-4} (25°C)	0.38	139.7 (C/10, 25°C)	[176]
[PMPYR] [TFSI]	LiTFSI	PAES-PEG	Solvent casting	8.9×10^{-4} (25°C)	0.4	138 (C/10, 25°C)	[177]
[PMPYR] [TFSI]	LiTFSI	PEC	Hot pressing	5×10^{-7} (50°C)	0.66	150 (C/20, 80°C)	[178]
[VBIM] [TFSI]	LiTFSI	PTMEG	UV irradiation	3.18×10^{-5} (25°C)	0.54	154.3 (C/10, 25°C)	[179]
[HACC] [TFSI]	LiTFSI	PEO	Solvent casting	1.77×10^{-5} (30°C)	0.34	161.3 (C/5, 60°C)	[180]

P(MMA-co-VBIm-TFSI)	LiTFSI	PVDF-HFP	Solvent casting	1.11×10^{-4} (30°C)	0.36	148 (C/10, 60°C)	[181]
Si-IL	ZIF-90	PEO	Solvent casting	1.17×10^{-4} (30°C)	0.44	148 (C/10, 30°C)	[182]
N_{1222}FSI	LiTFSI	PDADMA-FSI	Solvent casting	2×10^{-4} (25°C)	0.18	151.8 (C/5, 40°C)	[183]
Complex composites (more than three components)							
[BMIM] [DCA]	GO, LiTFSI	PEO	Solvent casting	~10^{-4} (30°C)	0.52	156.2 (C/10, 60°C)	[184]
[EMIM] [TFSI]	ZIF-8, LiTFSI	PEO	Cathode coating	9.02×10^{-4} (20°C)	-	163.6 (C/20, 60°C)	[185]
[EMIM] [TFSI]	UiO-66, LiTFSI	PVDF-HFP	Doctor blade	1.1×10^{-3} (30°C)	0.72	161.3 (C/10, 100°C)	[186]
[EMIM] [TFSI]	C6M, LiTFSI	PVDF-HFP	Solvent casting	1.79×10^{-3} (20°C)	0.67	131.2 (C/10, 25°C)	[187]
[EMIM] [TFSI]	LiTFSI	PEO, glass fiber cloth	3D filling	3.3×10^{-4} (30°C)	0.33	155 (C/5, 60°C)	[188]
[EMIM] [TFSI]	SBA-15, LiTFSI	PEO	Solvent casting	7.5×10^{-6} (25°C)	~	140 (C/10, 60°C)	[189]
[BMIM] [TFSI]	LiTFSI	P[MAPOSS-VIM][TFSI], PVDF-HFP	Solvent casting	4.82×10^{-4} (25°C)	0.27	151.8 (C/10, 25°C)	[190]
[PMPYR] [TFSI]	LiTFSI	PEGMA, CTA	Solvent casting	5.24×10^{-3} (25°C)	0.43	125 (C/20, 25°C)	[191]
[PMPYR] [TFSI]	LLZO, LiTFSI	PEO	Wet coating	3.02×10^{-5} (22°C)	-	153.3 (C/17, 60°C)	[192]
[PMPYR] [TFSI]	LiTFSI	Cellulose, PEG	Hot pressing	1×10^{-5} (20°C)	-	-	[193]
[VEIm] [TFSI]	LATP, LiTFSI	PET	Solvent casting	7.93×10^{-4} (60°C)	0.21	110 (C/10, 25°C)	[194]
[VMIM] [TFSI]	SN, LiTFSI	PI	Thermal polymerization	6.54×10^{-4} (25°C)	0.43	156.5 (C/10, 25°C)	[195]
IL-CN	LiTFSI	PEO, PMHS	Thermal synthesis	3.56×10^{-4} (25°C)	0.29	159.8 (C/10, 25°C)	[196]
P(MMA-co-VIm-TFSI), [PMPYR][TFSI]	LiTFSI	PVDF-HFP	Solvent casting	5.10×10^{-4} (25°C)	0.55	102.7 (C/10, 25°C)	[164]

Imidazolium based ILs are amongst the most explored ILs for battery applications due to their high ionic conductivities and adequate viscosities. [EMIM][TFSI] is one of the most widely used ILs in the context of SPEs, particularly combined with PEO and a lithium salt, which leads to good room temperature ionic conductivities and interesting cycling stability [173]. N-propyl-n-methylpyrrolidinium bis(trifluoromethylsulfonyl)imide ([PMPYR][TFSI]) is another effective option that gained interest in more recent years due to its strong plasticizing effect [178]. N-butyl-N-ethyl-piperidinium bis(trifluoromethylsulfonyl)imide ([PP][TFSI]) is also reported as possessing high ionic conductivity and good electrochemical window [174]. Using ILs with longer cation chains in SPEs seems to improve their ionic conductivity, as proved by the comparison between $[EMIM]^+$ and $[BMIM]^+$-based ILs sharing the same $[SCN]^-$ anion [124]. The use of the magnetic IL $[BMIM]_2[(SCN)_4Co]$ demonstrated to extend the cycle life of a battery when magnetic fields are applied, reducing the aging effect and the SEI growth in the battery [168]. The crosslinking of 1-vinyl-3-butylimidazolium bis(trifluoromethylsulfonyl)imide ([VBIM][TFSI]) with a poly(tetrahydrofuran) (PTMEG) copolymer through UV irradiation led to high battery performance and prolonged cycle life, due to the weak Li^+-O interactions that lead to fast ion transportation (figure 1.11a) [179]. By adding ceramic LLZO particles combined with [PMPYR][TFSI] IL the successful suppression of lithium dendrites growth was achieved, resulting in high performance batteries with good cyclability at different discharge rates [192]. The use of graphene oxide (GO) contributed to anion immobilization in the SPE, reducing the growth of lithium dendrites due to a more uniform assignment of the charges during the cycling process, as schematized in figure 2.10 [184]. The application of ILs as nanofluid plasticizers proved to improve the electrochemical properties of the SPE due to their faster segmental motion, which sets a favorable environment of the Li ions migration. They also tend to improve the interfacial compatibility with the electrodes [171].

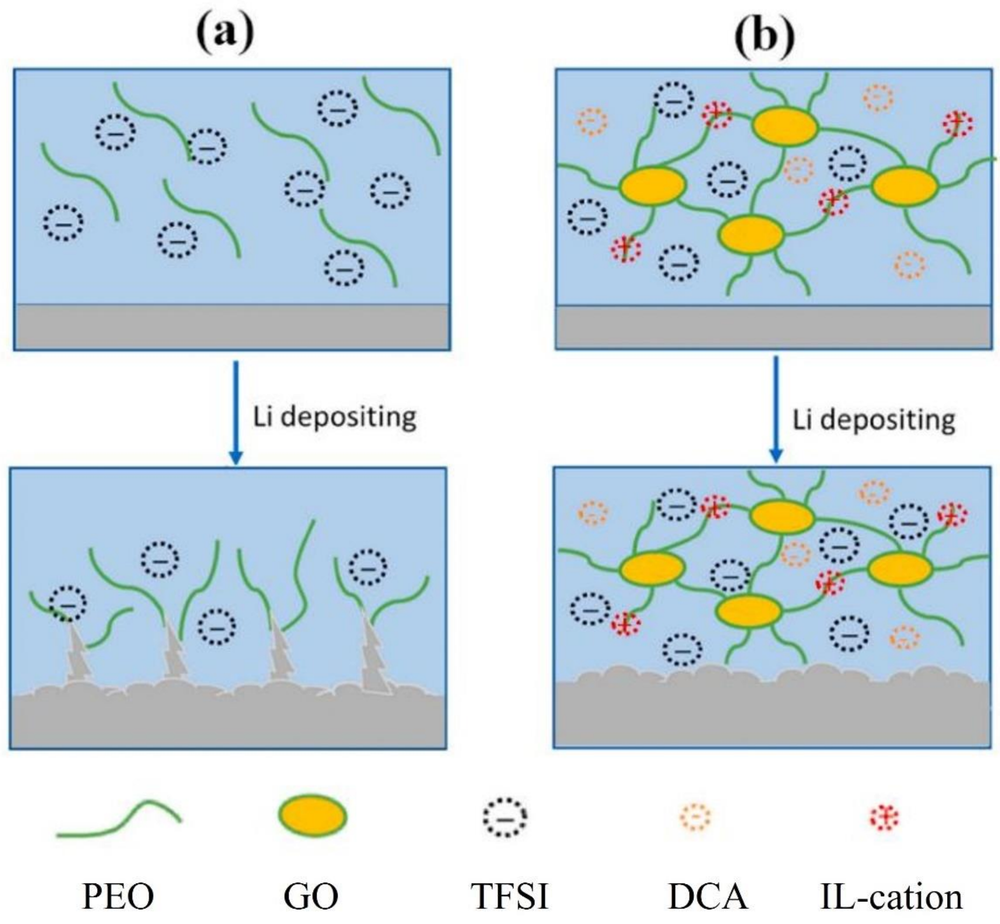

Figure 2.10 – Lithium deposition process in a typical PEO SPE (a), and in a [BMIM][DCA]/GO SPE that limits the lithium dendrites growth (b). Adapted from [184].

By combining two different polymers in a single matrix, it is possible to enhance the SPE properties. As example, the poly(arylene ether sulfone)-co-poly(ethylene glycol) (PAES-co-PEG) matrix combined with [PMPYR][TFSI] showed excellent room temperature results, with high ionic conductivity and good cycling performance [176]. A similar approach was taken with the same materials but with varying functional groups in the polymer matrix, showing that the -CN group exerted the most positive effect on the battery performance [177]. This was also proved by using ILs with -CN groups in a complex matrix of polymethylhydrosiloxane (PMHS) and PEO, which were able to deliver high discharge capacities at room temperature for different active materials [196]. A more environmentally friendly approach was based on the application of cellulose materials blended with a poly(ethylene glycol) methacrylate (PEGMA), which showed promising results, particularly after the application of electrospinning processes [191]. Cellulose can be combined with PEG and mixed with [PMPYR][TFSI] to achieve good room temperature ionic conductivity using solvent free processes [193]. The blend of PVDF-HFP and PEO was studied using a hybrid imidazolium-based IL based on polyhedral oligomeric silsesquioxanes (POSS). The obtained results showed an excellent cycling stability and high discharge capacity, as a result of the good interfacial compatibility between the SPE and the electrodes [170]. The use of elastomeric polymer blocks as a host for different [EMIM]-based ILs showed promising results with ionic conductivity on the order of 10^{-6} (S cm^{-1}) at room temperature and a good Li^{+} transference number [172].

The application of UV polymerized liquid crystals combined with the typical [EMIM][TFSI] IL proved to be an effective strategy in enhancing the room temperature ionic conductivity of the SPE, leading to an excellent cycling stability up to 3500 h and in a wide temperature range [187]. An innovative approach consists in the filling of a glass fiber cloth 3D network with a PEO-LiTFSI-[EMIM][TFSI] solution, improving the thermal and mechanical stability, and also the electrochemical properties when compared with a simple PEO solution [188].

Polymerized ILs (PILs) are an attractive possibility to solve the low ionic conductivity of the current SPEs as they combine the polymer function with the ion conductor function of the IL. The 1-vinyl-3-methylimidazolium bis(trifluoromethylsulfonyl)imide ([VMIM][TFSI]) IL was polymerized using succionitrile (SN) in a thermal process, resulting in excellent room temperature cycling performance when combined with a PI matrix [195]. The use of the poly(diallyldimethylammonium) bis(fluorosulfonyl)imide (PDADMA-FSI) PIL with lithium salts [197], triethylmethylammonium bis(fluorosulfonyl)imide (N_{1222}FSI) [183] and PYR_{13}FSI IL [175] provided a low cost possibility for highly stable SPEs, compatible with most active materials with good obtained performances [175]. A PIL consisting in P(MMA-co-VIm-TFSI) was mixed with PVDF-HFP and [PMPYR][TFSI] resulting in a high Li^{+} transference number and good interfacial compatibility [164]. A more complex P(MMA-co-VBIm-TFSI) PIL was synthesized and combined with PVDF-HFP with good results achieved at high temperatures, and a good capacity retention of 95% after 50 cycles [181]. Dimethylamine-containing PILs with polysubstituted benzene units were synthesized using ion exchange (IE) processes with lithium salts. This approach provided a high charge density structure with high thermal stability and good battery operation at room temperature [169]. The synthesis of an environmentally friendly PIL based on chitosan proved to improve the ion mobility through the interactions between the quaternary ammonium cations and $TFSI^{-}$ anions, which improved the battery operation at high temperatures [180]. 1-Vinyl-3-ethylimidazolium bis(trifluoromethylsulfonyl)imide ([VEIM][TFSI]) was polymerized in a poly(ethylene) (PET) substrate, leading to excellent mechanical properties and good battery performance at high temperatures. The performance was further improved by adding LATP particles, through the increase in the ionic conductivity of the SPE [194]. The room temperature ionic conductivity of the SPEs can be further improved by using imidazolium based PILS containing POSS, as these structures improve both the thermal properties and the ion transportation ability, being also an excellent nanobuilding block for the construction of IL structures [190].

Microporous structures are of growing interest in the field of SPEs. By using mesoporous silica particles to immobilize the [EMIM][TFSI] IL it was possible to develop SPEs with good mechanical properties and a good cycling stability for a prolonged number of cycles due to the inhibition of the lithium dendrites growth [189]. The application of MOFs as UiO-66 combined with [EMIM][TFSI] IL proved to be effective at high temperatures, due to the increase in the amorphous phase content of the SPE and in the dissociation of the lithium salt [186]. The combination of zeolitic structures with different ILs is gaining relevance based on the properties of these materials, such as high porosity and surface area, as well as being a natural occurring material, which reduces their environmental impact in the production phase [198]. Zeolitic imidazolate framework (ZIF)-8 was combined with the [EMIM][TFSI] IL and LiTFSI using a PEO matrix, and the resulted paste was coated onto a NMC cathode, with the ZIF-IL combination leading to a protective effect of the PEO, preventing its oxidation during cycling (figure 2.11b) [185]. ZIF-90 was also successfully applied combined with trimethoxysilane-based ILs, forming a single nanoparticle that was applied in a PEO matrix, with good results for high voltage application [182].

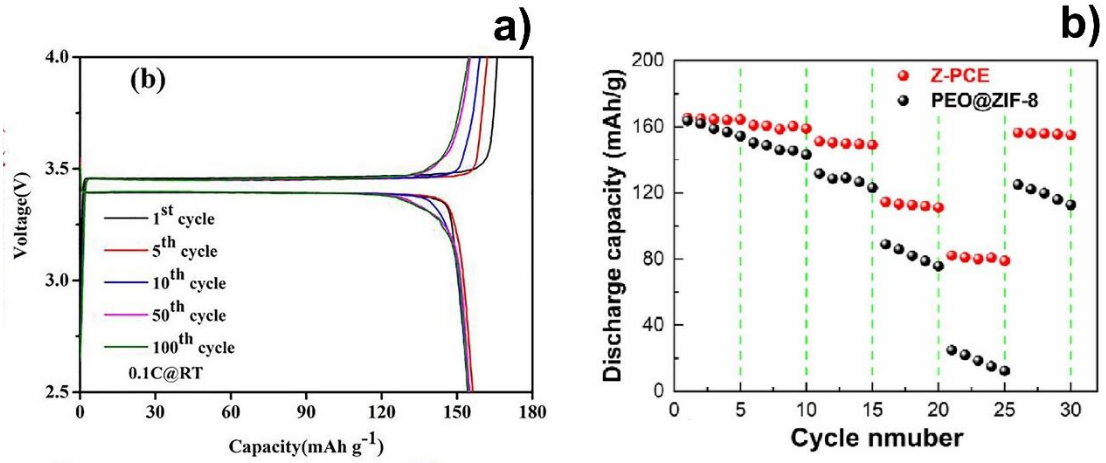

Figure 2.11 – Discharge profile at different cycles of the [VBIM][TFSI]/PTMEG composite [179] (a); rate performance of the ZIF-8/[EMIM][TFSI] SPE at room temperature [185] (b).

2.4. State of art on microporous materials for polymer based composite solid electrolytes

According to the International Union of Pure and Applied Chemistry (IUPAC), porous materials can be classified in three different categories. Microporous materials are characterized by pore sizes smaller than 2 nm; mesoporous materials show pore sizes between 2 and 50 nm; and macroporous materials show pore sizes larger than 50 nm [199].

Microporous materials are particularly appealing for energy storage applications due to their good thermal stability [200] and high surface areas, that offer a high number of sites for interfacial reactions. Further, the adjustable pore sizes and shapes provide the ideal space to encapsulate other components in their structure. Finally these materials are known to possess nanoscale effects, both in their channel structure and in their pore walls, resulting in enhanced mechanical, electrical, and optical properties [201]. There are different kinds of microporous materials, such as aluminosilicates, metal oxides, nanoclays, molecular sieves, zeolites, and MOFs [201]. As previously mentioned, microporous materials have particular interest in the SPE field, as they are able to encapsulate other materials in their structure. In the light of this three-component approach, the microporous material works as a host for the other filler, improving the mechanical and thermal properties of the SPE, while the second filler enhances the ionic conductivity. This approach allows an increase in the quantity of filler that is possible to use without compromising the overall performance of the composite solid electrolytes in terms of mechanical or thermal properties.

2.4.1. Why microporous materials?

Due to their characteristics and properties, composite solid electrolytes aim to replacing the conventional separators and liquid electrolytes employed nowadays in the field of energy storage systems. However, critical issues, such as low ionic conductivity and high interfacial resistance must be addressed in order to make them fully functional and achieve performances similar to the conventional materials. To solve these drawbacks, different approaches have been adopted in recent years, particularly with respect to the used materials and processing techniques [61].

Microporous materials, such as MOFs and zeolites, are interesting candidates for application in composite solid electrolytes owing to their unique properties. Their crystalline structure with controllable parameters, such as pore size and shape, allows building a network of ion pathways with high ionic conductivity. In parallel, these materials can be used to encapsulate/adsorb other materials, such as lithium salts or ILs, to further facilitate the conduction mechanism in the composite solid electrolytes. This three-component approach (one polymer and two complementary fillers) enables the synthesis of more stable and improved solid electrolytes, in which one filler leads to the enhancement of the mechanical or thermal properties, whereas the other promotes the enhancement of ionic conductivity, leading to a reduction of the needed quantity of each one for the electrolyte to perform properly [202].

The main difference between zeolites and MOFs is the nature of their structures. While zeolites are entirely inorganic, MOFs present an inorganic-organic hybrid structure with large pore sizes and volumes. Moreover, zeolites can be found in nature and synthetic structures are mostly mimicked from the natural structures. In contrast, MOFs are exclusively synthetic, allowing the production of a significantly higher number of possible structures, meaning that they are more versatile and adaptable [203]. However, zeolites exhibit higher thermal and chemical stabilities, longer lifetimes, and cheaper production costs, being also an environmentally friendlier option (Figure 2.12) [204].

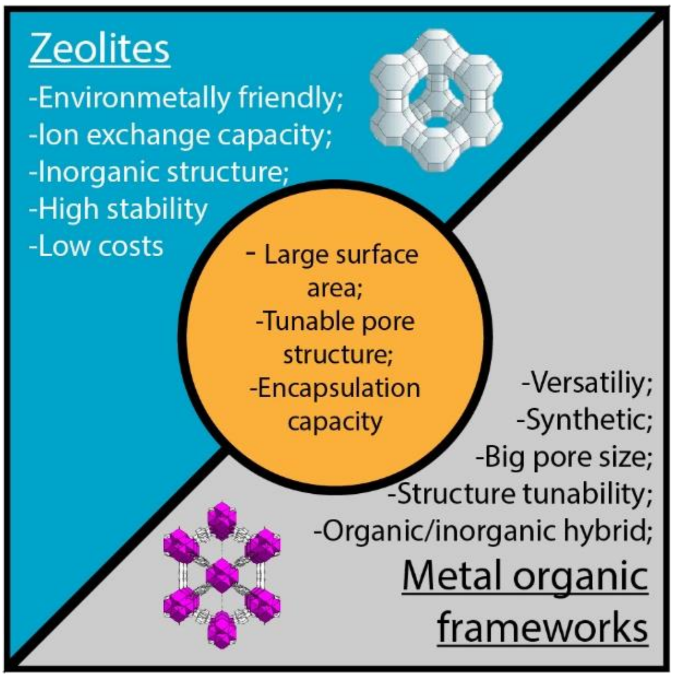

Figure 2.12 – Main characteristics and common properties of zeolites and MOFs.

The most extensively used techniques for the production of composite solid electrolytes are solvent casting and hot pressing. Hot pressing is considered the simplest and cheapest process and has the advantage of being completely solvent-free [205]. However, printing techniques attracted considerable interest in recent years, due to the possibility of tackling the interfacial resistance problems, among others [206]. Printing techniques allow the deposition of the different battery components layer by layer, leading to the manufacturing of hybrid interfaces that are, neither electrode, nor electrolyte, but a mix of both [207].

These interfaces can suppress the issue of high resistance, because the battery is built as a single device, and not by the assembly of different components.

2.4.2. Metal-organic frameworks

MOFs can be defined as crystalline porous solids composed of a three-dimensional (3D) network of metal ions held in place by multidentate organic molecules [208]. The first MOF, inspired in the characteristics of zeolites, was reported in 1995, using 1,3,5-benzenetricarboxylate as building block [209]. This field grew strongly since then, with successive studies and synthesis of new structures. To date almost 70,000 different MOFs have been reported [210].

MOFs present a variety of interesting properties, combining high porosity with large pore size and volume, outstanding surface area (up to the record of 7000 m^2 g^{-1} for the NU-110E MOF [211]), possibility of encapsulating or adsorbing other materials within its structure, and fast electrochemical kinetics. MOFs have been used in a wide range of applications, including gas storage and separation [212, 213], drug delivery [214], catalysis [215], and chemical sensing [216]. The possibility of controlling the pore size, shape and surface physical-chemical characteristics, leads to the synthesis of structures with tailored properties for specific applications, increasing the interest of these materials in the energy area in recent years [217, 218].

The main advantages of the application of MOFs in SPEs are: (1) their 3D and easily tunable pore structures (Figure 2.13) that offer many contact points between the electrolyte and the electrode active material at an atomic level; (2) their adequate electrochemical window; and (3) their good thermal and mechanical properties [219]. Furthermore, the ability to control the surface polarity of the MOFs allows the optimization of their electrochemical properties through the modulation of the interfacial interactions [220].

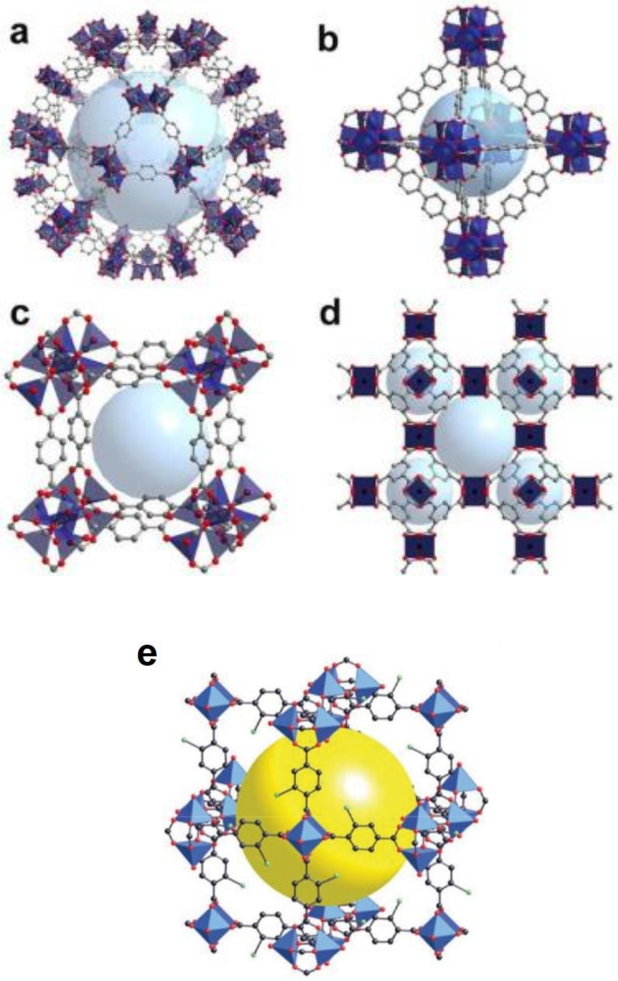

Figure 2.13 – Typical structure of representative MOFs: MIL-101 (a), UIO-67 (b), MOF-5 (c), HKUST-1 (d) [218] and MOF-101 (e) [221, 222].

These characteristics led to a growing interest in the application of MOFs in composite solid electrolytes, due to the possibility of a more efficient transport of the lithium ions through the ordered channels in the MOFs structure [220]. Table 2.3 presents the work developed in recent years regarding the application of different MOFs as fillers in composite solid electrolytes.

Table 2.3 - State of the art of the use of MOFs in the formulation of composite solid electrolytes and corresponding LIB performance.

MOF	**Polymer Matrix**	**Other fillers**	**Technique**	**Ionic conductivity (S cm^{-1})**	**Battery capacity (mAh g^{-1})**	**Ref.**
UiO-66-NH$_2$	PVDF	LiTFSI	Solvent casting	2.07×10^{-4} (25°C)	136 (1C)	[106]
MOF-525(Cu)	-	[EMIM][TFSI]; LiTFSI	Impregnation	3.0×10^{-4}(25°C)	145 (0.1C)	[219]
D-UiO-66-NH$_2$	PEO	LiTFSI	Hot pressing	3.9×10^{-6}(25°C)	63.2 (1C)	[223]
Al(OH)(1,4-NDC)	PEO	LiTFSI	Solvent casting	2.09×10^{-5}(30°C)	80.6 (1C)	[224]
Li-IL@UiO-67	PVDF-HFP	-	Solvent casting	4.3×10^{-4}(25°C)	118.1 (1C)	[225]
Mg-BTC	PEO	LiTFSI	Hot pressing	~10^{-6} (20°C)	110 (1C)	[226]
M-UiO-66-NH$_2$	PEGDA	LiTFSI	UV polymerization	4.31×10^{-5}(30°C)	80 (1C)	[227]
MOF-5	PEO	LiTFSI	Solvent casting	3.16×10^{-5}(25°C)	132 (1C)	[228]
Mg-TPA; Mg-TMA	PEO	LiTFSI	Hot pressing	7.02×10^{-4}	-	[229]
Al-BTC	PEO	LiTFSI	Hot pressing	~10^{-6} (20°C)	45 (1C)	[230]
Al-TPA	PEO	LiTFSI	Hot pressing	1×10^{-4}(60°C)	~50 (1C)	[231]
UiO-66	PEO	-	Solvent casting	1.47×10^{-4}(30°C)	100.1 (1C)	[232]
Li-IL@UiO-66	PEO	LiTFSI	Solvent casting	1.3×10^{-4}(30°C)	151 (0.5C)	[233]
Cu-BDC	PEO	LiTFSI	Hot pressing	~10^{-6} (25°C)	120 (1C)	[234]
Ni$_3$-(BTC)$_2$	PEO	LiTFSI	Hot pressing	1.4×10^{-4}(30°C)	~75 (1C)	[235]
MIL-53(Al)	PEO	LiTFSI	Solvent casting	1.62×10^{-5}(30°C)	127.1 (5C)	[236]
HKUST-1(Cu)	PEO	[EMIM][TFSI]; LiTFSI	Solvent casting	1.20×10^{-4} (30°C)	136.2 (1C)	[237]
M-UiO-66-NH$_2$	PEO	SiO$_2$; LiTFSI	Hot pressing	8.1×10^{-6}(60°C)	64 (1C)	[238]
UiO-66	PEO	LiClO$_4$	Solvent casting	4.8×10^{-5}(25°C)	160 (1C)	[239]

The most extensively used approach in the production of composite solid electrolytes with MOFs is the addition of the MOF to a polymer matrix (e.g., PEO) including a lithium salt (e.g., LiTFSI). Studies with the PEO host matrix have been carried out using different MOFs, with promising results. The addition of aluminum (Al)-MOF nanorods altered the properties of the matrix due to the strong interfacial interactions with the polymer chains, increasing the ionic conductivity and lithium transference number of the SPE when compared with pure PEO, and enlarging in parallel the electrochemical window up to 4.7 V [224]. The use of Zn_4O(1,4-benzenedicarboxylate) (MOF-5) proved to stabilize the resistance in the interfaces of the tested cells and increased the cycling stability of the batteries up to 100 cycles [228]. A comparison between magnesium (Mg)-TPA and Mg-TMA MOFs fillers in a PEO/LiTFSI matrix was performed. The addition of the MOFs promoted a reduction of the degree of crystallinity, further improving the conduction mechanism and increasing the ionic conductivity (Figure 2.14a) [229]. Copper (Cu)-BDC MOFs promoted the thermal stability of the composite solid electrolyte, allowing the battery operation at high temperatures with reduced risks [234]. The characteristics of the Ni$_3$-(BTC)$_2$ MOF proved to enhance the interfacial properties of the SPE, leading to better cycling performances, and to the suppression of lithium dendrites, without compromising the internal resistance of the cell (Figure 2.14b) [235]. The MIL-35(Al) showed exceptional battery performance at high discharge rates, due to its ability to dissolve lithium salts, increasing the ionic conductivity [236].

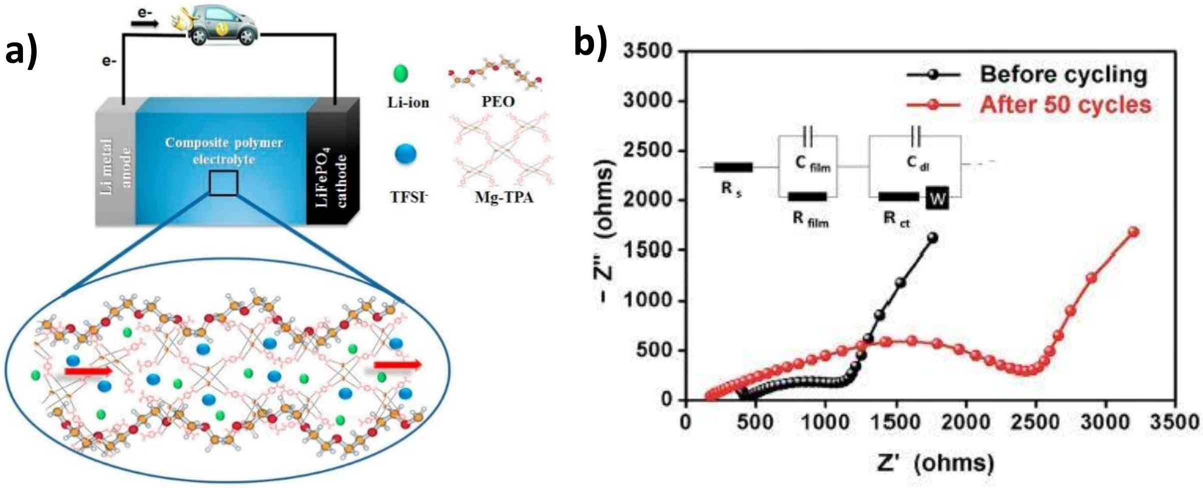

Figure 2.14 – Schematic representation of the lithium-ion migration in the Mg-TPA MOF based composite solid electrolyte (a) [229] and impedance measurements of Ni$_3$-BTC MOF based composite solid electrolytes before and after cycling, with the corresponding equivalent circuit (b) [235].

MOFs as UiO-66 have the ability of encapsulating liquid electrolytes in their nanostructure to form efficient ion conductors. These compounds increase the compatibility between the electrode and the separator, leading to higher performance batteries [232]. Ion exchange techniques have been used in UiO-66-NH$_2$ MOFs to insert lithium salts in their structure, creating a single-ion superionic conductor. Then, the prepared MOFs were applied as fillers in a PVDF matrix by solution casting methods. The membranes presented high ionic conductivity at room temperature and an excellent battery capacity retention of 97% after 500 cycles [106]. UiO-66-NH$_2$ were functionalized with vinyl groups and applied in a UV photopolymerized PEGDA matrix. The ionic conductivity of the prepared electrolyte was enhanced by about 5 times upon addition of the MOF. The latter demonstrated an excellent interfacial contact with the electrodes. The assembled battery showed a good performance, particularly at high temperatures [227]. UiO-66 was also successfully used combined with LiClO$_4$, to form a stable composite solid electrolyte with strong intermolecular interactions, which resulted in a significant increase in the ionic conductivity and excellent battery performance, particularly at high temperatures [239].

MOF-525(Cu) was impregnated with a mixture of [EMIM][TFSI] and LiTFSI to form a solid-like electrolyte with high room temperature ionic conductivity and good compatibility with both $LiFePO_4$ and the Li-metal anode, showing low interfacial resistance. The assembled battery was characterized by a good retention capacity in a wide temperature range (−20 to 150°C) as shown in Figure 2.15 [219]. A similar strategy was applied with the UiO-67 MOF. The prepared MOF was dispersed in a PVDF-HFP matrix, leading to a quasi-solid-state electrolyte, with high ionic conductivity and good cycling stability up to 300 cycles [225]. The encapsulation of [EMIM][TFSI] and lithium salts within the structure of UiO-66 also led to promising results, with ionic conductivities in the order of 10^{-4} S cm^{-1} at 30 °C and excellent discharge capacities at high rates [233]. This method has been also successfully applied with the HKUST-1(Cu) MOF with outstanding room temperature ionic conductivity, due to the formation of a strong ion-conductive network in the polymer matrix [237].

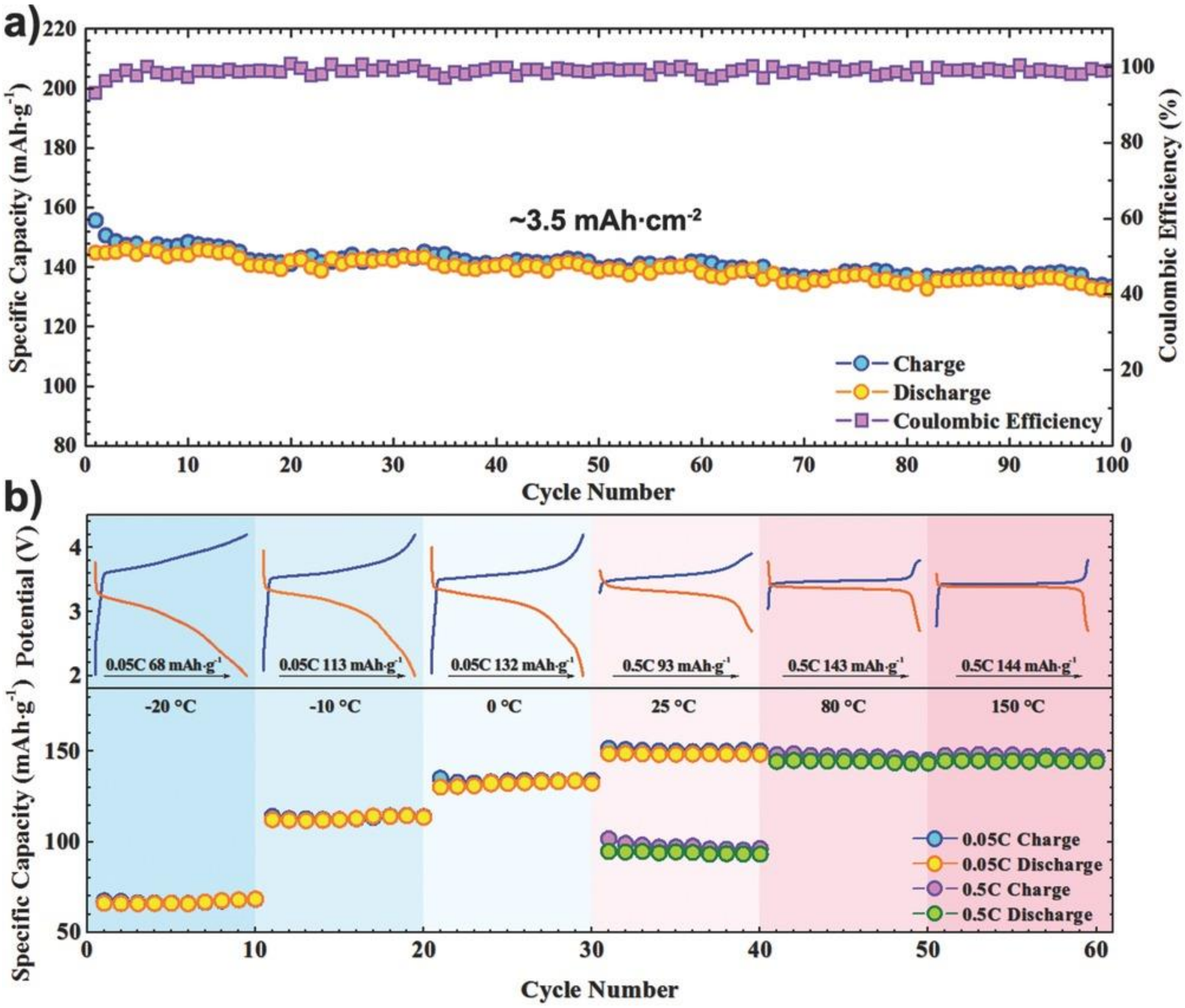

Figure 2.15 - Cycling performance and coulombic efficiency of the Li❙Li-IL@MOF❙LFP SSB with 0.1C charge/discharge rate at room temperature (a); Temperature-dependent cyclability of the Li❙Li-IL@MOF❙LFP SSB with corresponding charge/discharge curves (b) [219].

A cationic MOF was developed from UIO-66 and used as filler in an anion-immobilized polymer electrolyte for lithium dendrite-free batteries. The polymer electrolyte was synthesized by hot pressing. The addition of the cationic MOF increased the ionic conductivity of the polymer matrix and inhibited the formation of lithium dendrites [223]. The addition of SiO_2 to the UIO-66 structure promoted a more uniform diffusion of the lithium through the composite solid electrolyte, and a better interface between the composite solid electrolyte and the electrodes [238]. Hot pressing was also successfully applied in the synthesis of PEO SPEs using Mg-BTC (Figure 2.16) [226] and Al-BTC MOFs [230], leading to an increase of the ionic conductivity by two orders of magnitude even at low temperatures. Hot pressed PEO/Al-TPA was applied in both lithium-metal and lithium-sulfur batteries, presenting stable performances up to 100 cycles in both studies [231].

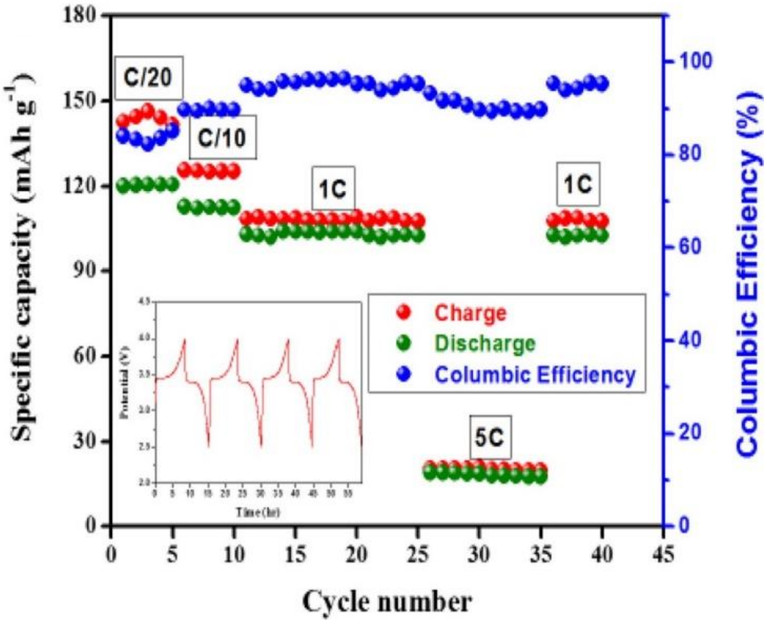

Figure 2.16 – Rate performance of a Li/Mg-BTC/$LiFePO_4$ hot pressed cell at 70°C and corresponding cycling profile [226].

2.4.3. Zeolites

Zeolites are micro or mesoporous structures composed of aluminosilicate minerals linked by oxygen atoms, resulting in a 3D network with pores of molecular size [240]. Generally, zeolites have the following chemical formula [241]:

$$M_xD_y(Al_{x+2y}\,Si_{n-(x+2y)}O_{2n})\;m.H_2O$$

where M is a monovalent cation, such as K^+ or Na^+, and D is a divalent cation, such as Mg^{2+}, Ca^{2+}, Sr^{2+} or Ba^{2+}.

The first reported zeolite, stilbite, was discovered by the Swedish mineralogist Cronstedt in 1756 [242]. The characteristic properties of zeolites were described in a couple of works at the end of the XVIII century. The first synthetic zeolites were developed in 1948 by Richard M. Barrer [243, 244]. The field has grown through the years until now, with more than 250 different identified structures.

Zeolites can occur naturally and can be synthesized in laboratory. According to the Zeolite Association Structure Commission, there are 252 different zeolite frameworks reported nowadays, with 47 known to occur in nature. The natural zeolites are divided into 7 families (Analcime, Chabazite, Gismondine, Harmotome, Heulandite, Natrolite and Stilbite) depending on their structure (Figure 2.17) [245]. They are mainly applied as catalysts and sorbents [246]. The most important properties of zeolites are their well-defined pore structure that allows for the selective encapsulation of other materials, their large surface area, which offers more sites for the occurrence of interfacial reactions, their cation exchange capacity that allows the introduction of specific species of interest in the zeolite's structure, and their high thermal stability which allows their operation at high temperatures[241].

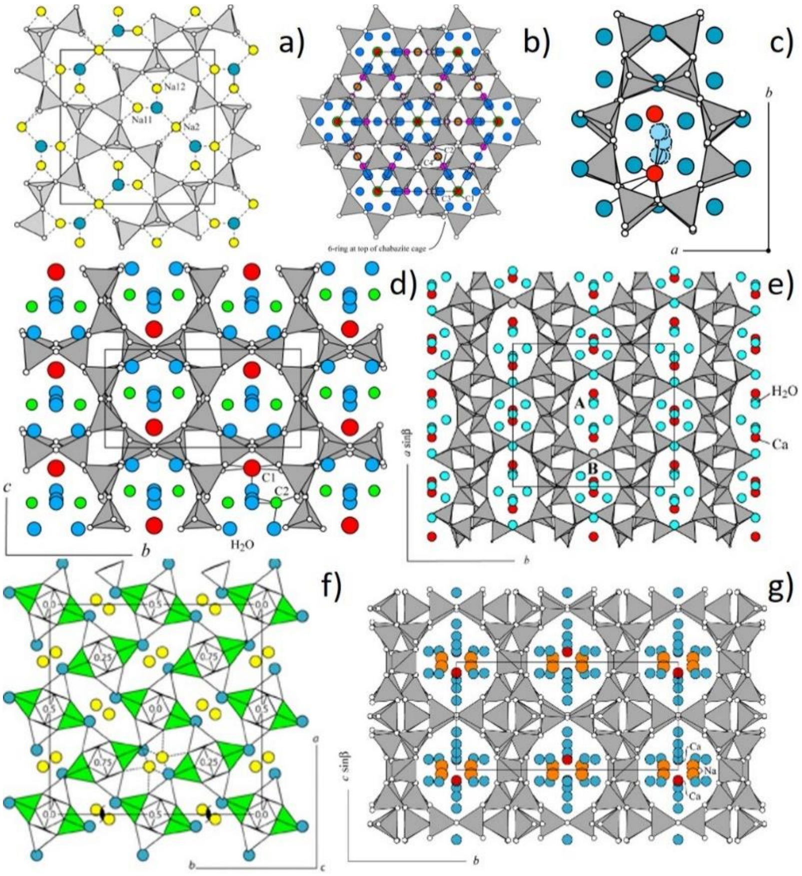

Figure 2.17 - Typical structure of the natural zeolites Analcime (a), Chabazite (b), Gismondine (c), Harmotome (d), Heulandite (e), Natrolite (f) and Stilbite (g). Source: International Zeolite Association.

Some interesting applications of zeolites are the production of dyes for microfluidics [247], biomass conversion processes [248], carbon dioxide (CO_2) capture and conversion [249, 250], air pollution remediation [251, 252], and water purification [253]. Zeolites are commonly used in energy applications, such as thermal energy storage [254] and fuel cell technology, both in the fuel production and in the cell operation fields [255, 256].

In the field of the LIBs, zeolites are employed in the anodes, to prevent the volume changes during the charge and discharge processes, and to increase the specific energy of the batteries [257, 258]. Zeolites are also used in the development of nanocomposite separators, with the goal of increasing the wettability and electrolyte uptake of the membranes, as well as to improve their stability at high temperatures [259, 260]. Zeolites, such as 13X [259], ZSM-5 [260, 261] and 4A [262], have been used with this purpose, due to their interstitial cavities that increased the overall porosity of the separator. Ion exchange techniques were applied in zeolite H [156], and MFI [263] to improve the conduction characteristics of the separator. However, the use of zeolites in SPEs has not been object of an extensive study so far. The only reported work in this field included the use of a modified high silica SSZ-13 zeolite and LiTFSI fillers in an PEO matrix. The synthesized SPE presented an outstanding ionic conductivity of 5.34×10^{-2} Scm^{-1} at 70°C, and high battery performance using both $LiFePO_4$ and $LiNiCoAlO_2$ cathodes, with good capacity retention after 80 cycles [264]. Despite the fact that wettability and electrolyte uptake are not useful properties in the performance of a composite solid electrolyte due to the absence of liquid components, the thermal stability is important to improve the operation of solid-state batteries that usually work at high temperatures. Also, the IE properties and the interstitial cavities can represent advantages both for the introduction of other materials in the zeolite structure and for the development of high ionic conductivity channels in the composite solid electrolyte.

2.5. References

1. Singh, R.P., A. Singh, and V. Srivastava, *Environmental issues surrounding human overpopulation*. 2016: IGI Global.
2. *Transforming our world : the 2030 Agenda for Sustainable Development*. 2015, UN General Assembly.
3. Scrosati, B., J. Hassoun, and Y.-K. Sun, *Lithium-ion batteries. A look into the future.* Energy & Environmental Science, 2011(4): p. 3287–3295
4. Scrosati, B. and J. Garche, *Lithium batteries: Status, prospects and future.* Journal of Power Sources, 2010(195): p. 2419–2430.
5. Väyrynen, A. and J. Salminen, *Lithium ion battery production.* Journal of Chemical Thermodynamics, 2012: p. 80-85.
6. Volta, A., *XVII. On the electricity excited by the mere contact of conducting substances of different kinds. In a letter from Mr. Alexander Volta, F. R. S. Professor of Natural Philosophy in the University of Pavia, to the Rt. Hon. Sir Joseph Banks, Bart. K.B. P. R. S.* Philosophical Transactions of the Royal Society of London, 1800. **90**: p. 403-431.
7. Zhang, H., et al., *From Solid-Solution Electrodes and the Rocking-Chair Concept to Today's Batteries.* Angewandte Chemie International Edition, 2020. **59**(2): p. 534-538.
8. van Gool, W. and N.A.T.O.S.A. Division, *Fast Ion Transport in Solids: Solid State Batteries and Devices. Proceedings of the NATO Sponsored Advanced Study Institute on Fast Ion Transport in Solids, Solid State Batteries and Devices, Belgirate, Italy, 5-15 September 1972*. 1973: North Holland Publishing Company.
9. Whittingham, M.S., *Electrical Energy Storage and Intercalation Chemistry.* Science, 1976. **192**(4244): p. 1126.
10. Winn, D.A., J.M. Shemilt, and B.C.H. Steele, *Titanium disulphide: A solid solution electrode for sodium and lithium.* Materials Research Bulletin, 1976. **11**(5): p. 559-566.

11. Mizushima, K., et al., *LixCoO2 (0<x<-1): A new cathode material for batteries of high energy density.* Materials Research Bulletin, 1980. **15**(6): p. 783-789.
12. Thackeray, M.M., et al., *Lithium insertion into manganese spinels.* Materials Research Bulletin, 1983. **18**(4): p. 461-472.
13. Padhi, A., K.S. Nanjundaswamy, and J. Goodenough, *Phospho-Olivines as Positive-Electrode Materials for Rechargeable Lithium Batteries.* Journal of The Electrochemical Society, 1997. **144**: p. 1188-1194.
14. Nishi, Y., *The development of lithium ion secondary batteries.* The Chemical Record, 2001. **1**(5): p. 406-413.
15. Abraham, K.M., *Prospects and Limits of Energy Storage in Batteries.* The Journal of Physical Chemistry Letters, 2015. **6**(5): p. 830-844.
16. Miranda, D., et al., *Theoretical simulation of the optimal relation between active material, binder and conductive additive for lithium-ion battery cathodes.* Energy, 2019. **172**: p. 68-78.
17. Costa, C.M., M.M. Silva, and S. Lanceros-Méndez, *Battery separators based on vinylidene fluoride (VDF) polymers and copolymers for lithium ion battery applications.* RSC Advances, 2013. **3**(29): p. 11404-11417.
18. Barbosa, J.C., et al., *Recent Advances in Poly(vinylidene fluoride) and Its Copolymers for Lithium-Ion Battery Separators.* Membranes (Basel), 2018. **8**(3).
19. Li, Q., et al., *Progress in electrolytes for rechargeable Li-based batteries and beyond.* Green Energy & Environment, 2016. **1**(1): p. 18-42.
20. Yamada, Y., et al., *Advances and issues in developing salt-concentrated battery electrolytes.* Nature Energy, 2019. **4**(4): p. 269-280.
21. Lisbona, D. and T. Snee, *A review of hazards associated with primary lithium and lithium-ion batteries.* Process Safety and Environmental Protection, 2011. **89**(6): p. 434-442.
22. Costa, C.M., et al., *Recent advances on separator membranes for lithium-ion battery applications: From porous membranes to solid electrolytes.* Energy Storage Materials, 2019. **22**: p. 346-375.
23. Okumura, T., et al., *LISICON-Based Amorphous Oxide for Bulk-Type All-Solid-State Lithium-Ion Battery.* ACS Applied Energy Materials, 2020. **3**(4): p. 3220-3229.
24. DeWees, R. and H. Wang, *Synthesis and Properties of NaSICON-type LATP and LAGP Solid Electrolytes.* ChemSusChem, 2019. **12**(16): p. 3713-3725.
25. Li, Y., et al., *A Perovskite Electrolyte That Is Stable in Moist Air for Lithium-Ion Batteries.* Angewandte Chemie International Edition, 2018. **57**(28): p. 8587-8591.
26. Liu, Q., et al., *Challenges and perspectives of garnet solid electrolytes for all solid-state lithium batteries.* Journal of Power Sources, 2018. **389**: p. 120-134.
27. Zhao, Q., et al., *Designing solid-state electrolytes for safe, energy-dense batteries.* Nature Reviews Materials, 2020. **5**(3): p. 229-252.
28. Mindemark, J., et al., *Beyond PEO—Alternative host materials for Li+-conducting solidpolymer electrolytes.* Progress in Polymer Science, 2018. **81**: p. 114-143.
29. Sator, A., *Pile Reversible Dont Lelectrolyte Est Un Cristal Depose En Lame Mince Par Evaporation.* COMPTES RENDUS HEBDOMADAIRES DES SEANCES DE L ACADEMIE DES SCIENCES, 1952. **234**(23): p. 2283-2285.
30. Armand, M.B., J.M. Chabagno, and M.J. Duclot, *Poly-ethers as solid electrolytes*, in *Fast ion transport in solids:electrodes and electrolytes.*, P.V. P, J.N. Mundy, and G.K. Shenoy, Editors. 1979, Elsevier: Amsterdam, Netherlands. p. 131-136.
31. Goodenough, J.B., H.-P. Hong, and J. Kafalas, *Fast Na+-ion transport in skeleton structures.* Materials Research Bulletin, 1976. **11**(2): p. 203-220.

32. Aono, H., et al., *Ionic conductivity of the lithium titanium phosphate (Li/sub 1+ x/M/sub x/Ti/sub 2-x/(PO/sub 4/)/sub 3/, M= Al, Sc, Y, and La) systems.* Journal of the Electrochemical Society, 1989. **136**(2): p. 590.
33. Bates, J., et al., *Electrical properties of amorphous lithium electrolyte thin films.* Solid state ionics, 1992. **53**: p. 647-654.
34. Inaguma, Y., et al., *High ionic conductivity in lithium lanthanum titanate.* Solid State Communications, 1993. **86**(10): p. 689-693.
35. Fenton, D.E., J.M. Parker, and P.V. Wright, *Complexes of alkali metal ions with poly(ethylene oxide).* Polymer, 1973. **14**(11): p. 589.
36. Armand, M., *Polymer solid electrolytes - an overview.* Solid State Ionics, 1983. **9-10**: p. 745-754.
37. Wang, Z., et al., *Investigation of the position of Li+ ions in a polyacrylonitrile-based electrolyte by Raman and infrared spectroscopy.* Electrochimica Acta, 1996. **41**(9): p. 1443-1446.
38. Appetecchi, G.B., F. Croce, and B. Scrosati, *Kinetics and stability of the lithium electrode in poly(methylmethacrylate)-based gel electrolytes.* Electrochimica Acta, 1995. **40**(8): p. 991-997.
39. Choe, H.S., et al., *Preparation and characterization of poly(vinyl sulfone)- and poly(vinylidene fluoride)-based electrolytes.* Electrochimica Acta, 1995. **40**(13): p. 2289-2293.
40. Yoshino, A., *The Birth of the Lithium-Ion Battery.* Angewandte Chemie International Edition, 2012. **51**(24): p. 5798-5800.
41. Scrosati, B. and J. Garche, *Lithium batteries: Status, prospects and future.* Journal of Power Sources, 2010. **195**(9): p. 2419-2430.
42. Chen, R., et al., *Approaching Practically Accessible Solid-State Batteries: Stability Issues Related to Solid Electrolytes and Interfaces.* Chemical Reviews, 2019.
43. Wu, F., et al., *Polymer electrolytes and interfaces toward solid-state batteries: Recent advances and prospects.* Energy Storage Materials, 2020. **33**: p. 26-54.
44. Zhang, Q., et al., *Recent advances in solid polymer electrolytes for lithium batteries.* Nano Research, 2017.
45. Li, J., et al., *Solid Electrolyte: the Key for High-Voltage Lithium Batteries.* Advanced Energy Materials, 2015. **5**(4): p. 1401408.
46. Stephan, A. and K.-S. Nahm, *Review on composite polymer electrolytes for lithium batteries. Polymer.* Polymer, 2006. **47**: p. 5952-5964.
47. Kato, Y., et al., *High-power all-solid-state batteries using sulfide superionic conductors.* Nature Energy, 2016. **1**(4): p. 16030.
48. Song, J.Y., Y. Wang, and C. Wan, *Review of gel-type polymer electrolytes for lithium-ion batteries.* Journal of Power Sources, 1999. **77**: p. 183–197.
49. Koerver, R., et al., *Chemo-mechanical expansion of lithium electrode materials – on the route to mechanically optimized all-solid-state batteries.* Energy & Environmental Science, 2018. **11**(8): p. 2142-2158.
50. Xu, L., et al., *Interfaces in Solid-State Lithium Batteries.* Joule, 2018. **2**(10): p. 1991-2015.
51. Barai, P., K. Higa, and V. Srinivasan, *Lithium dendrite growth mechanisms in polymer electrolytes and prevention strategies.* Physical Chemistry Chemical Physics, 2017. **19**(31): p. 20493-20505.
52. Wang, A., et al., *Review on modeling of the anode solid electrolyte interphase (SEI) for lithium-ion batteries.* npj Computational Materials, 2018. **4**(1): p. 15.
53. Lv, H., X. Huang, and Y. Liu, *Analysis on pulse charging–discharging strategies for improving capacity retention rates of lithium-ion batteries.* Ionics, 2020. **26**(4): p. 1749-1770.

54. Hartmann, P., et al., *Degradation of NASICON-Type Materials in Contact with Lithium Metal: Formation of Mixed Conducting Interphases (MCI) on Solid Electrolytes.* The Journal of Physical Chemistry C, 2013. **117**(41): p. 21064-21074.
55. Bhattacharya, S., A.R. Riahi, and A. Alpas, *Thermal Cycling Induced Capacity Enhancement of Graphite Anodes in Lithium-ion Cells.* Carbon, 2013. **67**.
56. Bhattacharyya, R., et al., *In situ NMR observation of the formation of metallic lithium microstructures in lithium batteries.* Nat Mater, 2010. **9**(6): p. 504-10.
57. Lin, D., Y. Liu, and Y. Cui, *Reviving the lithium metal anode for high-energy batteries.* Nature Nanotechnology, 2017. **12**(3): p. 194-206.
58. Zhao, C.-Z., et al., *An anion-immobilized composite electrolyte for dendrite-free lithium metal anodes.* Proceedings of the National Academy of Sciences, 2017. **114**(42): p. 11069.
59. Li, J., et al., *Lithium-Ion Batteries: Solid Electrolyte: the Key for High-Voltage Lithium Batteries (Adv. Energy Mater. 4/2015).* Advanced Energy Materials, 2015. **5**(4).
60. Orsini, F., et al., *In situ Scanning Electron Microscopy (SEM) observation of interfaces within plastic lithium batteries.* Journal of Power Sources, 1998. **76**: p. 19-29.
61. Li, S., et al., *Progress and Perspective of Ceramic/Polymer Composite Solid Electrolytes for Lithium Batteries.* Advanced Science, 2020. **7**(5): p. 1903088.
62. Wang, W.M., *Study on All Solid-State Composite Polymer Electrolyte.* Advanced Materials Research, 2012. **571**: p. 13-16.
63. Agrawal, R.C. and G.P. Pandey, *Solid polymer electrolytes: materials designing and all-solid-state battery applications: an overview.* Journal of Physics D: Applied Physics, 2008. **41**(22): p. 223001.
64. Yao, P., et al., *Review on Polymer-Based Composite Electrolytes for Lithium Batteries.* Frontiers in Chemistry, 2019. **7**(522).
65. Xue, Z., D. He, and X. Xie, *Poly(ethylene oxide)-based electrolytes for lithium-ion batteries.* Journal of Materials Chemistry A, 2015. **3**(38): p. 19218-19253.
66. Zou, Z., et al., *Mobile Ions in Composite Solids.* Chemical Reviews, 2020. **120**(9): p. 4169-4221.
67. Famprikis, T., et al., *Fundamentals of inorganic solid-state electrolytes for batteries.* Nature Materials, 2019. **18**(12): p. 1278-1291.
68. Bresser, D., et al., *Decoupling segmental relaxation and ionic conductivity for lithium-ion polymer electrolytes.* Molecular Systems Design & Engineering, 2019. **4**(4): p. 779-792.
69. Gadjourova, Z., et al., *Ionic conductivity in crystalline polymer electrolytes.* Nature, 2001. **412**(6846): p. 520-3.
70. Chen, R., et al., *The pursuit of solid-state electrolytes for lithium batteries: from comprehensive insight to emerging horizons.* Materials Horizons, 2016. **3**(6): p. 487-516.
71. Zhang, Y., et al., *Effects of the shapes of BaTiO3 nanofillers on PEO-based electrolytes for all-solid-state lithium-ion batteries.* Ionics, 2018. **25**.
72. Chen, S., et al., *Progress and future prospects of high-voltage and high-safety electrolytes in advanced lithium batteries: from liquid to solid electrolytes.* Journal of Materials Chemistry A, 2018. **6**(25): p. 11631-11663.
73. Osada, I., et al., *Ionic-Liquid-Based Polymer Electrolytes for Battery Applications.* Angewandte Chemie International Edition, 2016. **55**(2): p. 500-513.
74. Tominaga, Y., Y. Kinno, and K. Kimura, *An end-capped poly(ethylene carbonate)-based concentrated electrolyte for stable cyclability of lithium battery.* Electrochimica Acta, 2019. **302**: p. 286-290.
75. Long, L., et al., *Polymer electrolytes for lithium polymer batteries.* Journal of Materials Chemistry A, 2016. **4**(26): p. 10038-10069.

76. Manuela Silva, M., et al., *Novel solid polymer electrolytes based on poly(trimethylene carbonate) and lithium hexafluoroantimonate.* Solid State Sciences, 2006. **8**(11): p. 1318-1321.
77. Deimede, V. and C. Elmasides, *Separators for Lithium-Ion Batteries: A Review on the Production Processes and Recent Developments.* Energy Technology, 2015. **3**(5): p. 453-468.
78. Wright, P.V., *Electrical conductivity in ionic complexes of poly (ethylene oxide).* British polymer journal, 1975. **7**(5): p. 319-327.
79. Lun, P., et al., *Enhanced ionic conductivity in halloysite nanotube-poly(vinylidene fluoride) electrolytes for solid-state lithium-ion batteries.* RSC Advances, 2018. **8**: p. 34232-34240.
80. Shang, D., et al., *A novel polyhedral oligomeric silsesquioxane based ionic liquids (POSS-ILs) polymer electrolytes for lithium ion batteries.* Solid State Ionics, 2018. **319**: p. 247-255.
81. Zhang, X., et al., *Effects of Li6.75La3Zr1.75Ta0.25O12 on chemical and electrochemical properties of polyacrylonitrile-based solid electrolytes.* Solid State Ionics, 2018. **327**: p. 32-38.
82. Kimura, K. and Y. Tominaga, *Understanding Electrochemical Stability and Lithium Ion-Dominant Transport in Concentrated Poly(ethylene carbonate) Electrolyte.* ChemElectroChem, 2018. **5**(24): p. 4008-4014.
83. Guzmán-González, G., et al., *Electrochemical Characterization of Single Lithium-Ion Conducting Polymer Electrolytes Based on sp3 Boron and Poly(ethylene glycol) Bridges.* ACS Applied Materials & Interfaces, 2018. **10**(36): p. 30247-30256.
84. Xie, M., et al., *Preparation and performance evaluation of organophilic nano-montmorillonite conducting polymer electrolyte for all-solid-state lithium ion batteries.* Journal of Materials Science: Materials in Electronics, 2019. **30**(3): p. 2030-2036.
85. Lim, Y., H.-A. Jung, and H. Hwang, *Fabrication of PEO-PMMA-LiClO4-Based Solid Polymer Electrolytes Containing Silica Aerogel Particles for All-Solid-State Lithium Batteries.* Energies, 2018. **11**: p. 2559.
86. Ahmad, A.L., U.R. Farooqui, and N.A. Hamid, *Porous (PVDF-HFP/PANI/GO) ternary hybrid polymer electrolyte membranes for lithium-ion batteries.* RSC Advances, 2018. **8**(45): p. 25725-25733.
87. Sohaimy, M. and M.I.N. Mohamad Isa, *Conductivity and Dielectric Analysis of Cellulose Based Solid Polymer Electrolytes Doped with Ammonium Carbonate (NH4CO3).* Applied Mechanics and Materials, 2015. **719-720**: p. 67-72.
88. Perumal, P., et al., *Plasticizer incorporated, novel eco-friendly bio-polymer based solid bio-membrane for electrochemical clean energy applications.* Polymer Degradation and Stability, 2018. **159**.
89. Side, S., D. Pratiwi, and F. Hadianita, *Synthesis of chitosan-LiOH polymer electrolyte membrane with addition of sodium tripolyphosphate*. 2018. 020285.
90. Chitra, R., et al., *Synthesis and characterization of iota-carrageenan solid biopolymer electrolytes for electrochemical applications.* Ionics, 2019. **25**(5): p. 2147-2157.
91. Boaretto, N., et al., *Review—Polymer Electrolytes for Rechargeable Batteries: From Nanocomposite to Nanohybrid.* Journal of The Electrochemical Society, 2020. **167**(7): p. 070524.
92. Zhang, Y., et al., *The effects of the size and content of BaTiO3 nanoparticles on solid polymer electrolytes for all-solid-state lithium-ion batteries.* Journal of Solid State Electrochemistry, 2019. **23**.

93. Li, D., et al., *Enhancement of electrochemical performance of lithium-ion battery by single-ion conducting polymer addition in ceramic-coated separator.* Journal of Materials Science, 2018. **53**(15): p. 11038-11049.
94. Choudhury, S., et al., *Soft Colloidal Glasses as Solid-State Electrolytes.* Chemistry of Materials, 2018. **30**(17): p. 5996-6004.
95. Li, X., et al., *Preparation and performance of poly(ethylene oxide)-based composite solid electrolyte for all solid-state lithium batteries.* Journal of Applied Polymer Science, 2019. **136**: p. 47498.
96. Ahmad, A.L., U.R. Farooqui, and N.A. Hamid, *Synthesis and characterization of porous poly(vinylidene fluoride-co-hexafluoro propylene) (PVDF-co-HFP)/poly(aniline) (PANI)/graphene oxide (GO) ternary hybrid polymer electrolyte membrane.* Electrochimica Acta, 2018. **283**: p. 842-849.
97. Nunes-Pereira, J., et al., *Li-ion battery separator membranes based on poly(vinylidene fluoride-trifluoroethylene)/carbon nanotube composites.* Solid State Ionics, 2013. **249-250**: p. 63-71.
98. Whba, R., et al., *Influence of Binary Lithium Salts on 49% Poly(Methyl Methacrylate) grafted Natural Rubber Based Solid Polymer Electrolytes.* Arabian Journal of Chemistry, 2018.
99. Arya, A. and A.L. Sharma, *Structural, microstructural and electrochemical properties of dispersed-type polymer nanocomposite films.* Journal of Physics D: Applied Physics, 2018. **51**(4): p. 045504.
100. Zeng, H., et al., *Enhanced cycling performance for all-solid-state lithium ion battery with LiFePO4 composite cathode encapsulated by poly (ethylene glycol) (PEG) based polymer electrolyte.* Solid State Ionics, 2018. **320**: p. 92-99.
101. Wei, Z., et al., *Superior lithium ion conduction of polymer electrolyte with comb-like structure via solvent-free copolymerization for bipolar all-solid-state lithium battery.* Journal of Materials Chemistry A, 2018. **6**(27): p. 13438-13447.
102. Yang, G., et al., *Ion Pair Integrated Organic-Inorganic Hybrid Electrolyte Network for Solid-State Lithium Ion Batteries.* Energy Technology, 2018. **6**(12): p. 2319-2325.
103. Wang, A., et al., *Polyimide-Based Self-Standing Polymer Electrolyte Membrane for Lithium-Ion Batteries.* Energy Technology, 2018. **6**(2): p. 326-332.
104. Di Noto, V., et al., *Zeolitic inorganic–organic polymer electrolytes: synthesis, characterization and ionic conductivity of a material based on oligo(ethylene glycol) 600, (CH3)2SnCl2 and K4Fe(CN)6.* Electrochimica Acta, 2001. **46**(10): p. 1587-1594.
105. Lin, Y., et al., *Natural halloysite nano-clay electrolyte for advanced all-solid-state lithium-sulfur batteries.* Nano Energy, 2017. **31**: p. 478-485.
106. Zhu, F., et al., *High-Performance Metal–Organic Framework-Based Single Ion Conducting Solid-State Electrolytes for Low-Temperature Lithium Metal Batteries.* ACS Applied Materials & Interfaces, 2019. **11**(46): p. 43206-43213.
107. Ngai, K.S., et al., *A review of polymer electrolytes: fundamental, approaches and applications.* Ionics, 2016. **22**(8): p. 1259-1279.
108. Song, J.Y., Y.Y. Wang, and C.C. Wan, *Review of gel-type polymer electrolytes for lithium-ion batteries.* Journal of Power Sources, 1999. **77**(2): p. 183-197.
109. Feng, J., et al., *PEO based polymer-ceramic hybrid solid electrolytes: a review.* Nano Convergence, 2021. **8**(1).
110. Mustarelli, P., et al., *Cation dynamics in PVdF-based polymer electrolytes.* Solid State Ionics, 1999. **122**(1): p. 285-289.

111. Liu, X., H. Kusawake, and S. Kuwajima, *Preparation of a PVdF-HFP/polyethylene composite gel electrolyte with shutdown function for lithium-ion secondary battery.* Journal of Power Sources, 2001. **97-98**: p. 661-663.
112. Rajendran, S., O. Mahendran, and R. Kannan, *Characterisation of [(1−x)PMMA−xPVdF] polymer blend electrolyte with Li+ ion.* Fuel, 2002. **81**(8): p. 1077-1081.
113. Song, M.-K., et al., *Characterization of UV-cured gel polymer electrolytes for rechargeable lithium batteries.* Journal of Power Sources, 2002. **110**(1): p. 209-215.
114. Ward, I.M., et al., *Separator-free rechargeable lithium ion cells produced by the extrusion lamination of polymer gel electrolytes.* Journal of Power Sources, 2006. **162**(2): p. 818-822.
115. Tong, Y., et al., *Design of amphiphilic poly(vinylidene fluoride-co-hexafluoropropylene)-based gel electrolytes for high-performance lithium-ion batteries.* Ionics, 2016. **22**(8): p. 1311-1318.
116. Ravi, M., et al., *Hybrid gel polymer electrolyte based on 1-methyl-1-Propylpyrrolidinium Bis(Trifluoromethanesulfonyl) imide for flexible and shape-variant lithium secondary batteries.* Journal of Membrane Science, 2021. **621**: p. 119018.
117. Le, H.T.T., et al., *Composite Gel Polymer Electrolyte Based on Poly(vinylidene fluoride-hexafluoropropylene) (PVDF-HFP) with Modified Aluminum-Doped Lithium Lanthanum Titanate (A-LLTO) for High-Performance Lithium Rechargeable Batteries.* ACS Applied Materials & Interfaces, 2016. **8**(32): p. 20710-20719.
118. Liang, Y.F., et al., *A superior composite gel polymer electrolyte of Li7La3Zr2O12-poly(vinylidene fluoride-hexafluoropropylene) (PVDF-HFP) for rechargeable solid-state lithium ion batteries.* Materials Research Bulletin, 2018. **102**: p. 412-417.
119. Zhou, C., et al., *Understanding the Role of Solvents on the Morphological Structure and Li-Ion Conductivity of Poly(vinylidene fluoride)-Based Polymer Electrolytes.* Journal of The Electrochemical Society, 2020. **167**(7): p. 070552.
120. Jeong, M.U., et al., *The effect of lithium salt type on ionic conductivity of poly(vinylidene difluoride)-based solid polymer electrolytes.* Molecular Crystals and Liquid Crystals, 2020. **705**(1): p. 93-98.
121. Wang, X., et al., *Enhancement of ion dynamics in organic ionic plastic crystal/PVDF composite electrolytes prepared by co-electrospinning.* Journal of Materials Chemistry A, 2016. **4**(25): p. 9873-9880.
122. Gonçalves, R., et al., *Solid polymer electrolytes based on lithium bis(trifluoromethanesulfonyl)imide/poly(vinylidene fluoride -co-hexafluoropropylene) for safer rechargeable lithium-ion batteries.* Sustainable Materials and Technologies, 2019. **21**: p. e00104.
123. Liang, X., et al., *Preparation and performance study of a PVDF–LATP ceramic composite polymer electrolyte membrane for solid-state batteries.* RSC Advances, 2018. **8**(71): p. 40498-40504.
124. Serra, J.P., et al., *Ionic liquid based Fluoropolymer solid electrolytes for Lithium-ion batteries.* Sustainable Materials and Technologies, 2020. **25**: p. e00176.
125. Ataollahi, N., et al., *Preparation and characterization of PVDF-MG49-NH4CF3SO3 based solid polymer electrolyte.* e-Polymers, 2014. **14**(2): p. 115-120.
126. Rajendran, S. and P. Sivakumar, *An investigation of PVdF/PVC-based blend electrolytes with EC/PC as plasticizers in lithium battery applications.* Physica B: Condensed Matter, 2008. **403**(4): p. 509-516.
127. Li, J., et al., *Optimisation of conductivity of PEO/PVDF-based solid polymer electrolytes in all-solid-state Li-ion batteries.* Materials Technology, 2020: p. 1-8.

128. Sengwa, R.J. and P. Dhatarwal, *Predominantly chain segmental relaxation dependent ionic conductivity of multiphase semicrystalline PVDF/PEO/LiClO4 solid polymer electrolytes.* Electrochimica Acta, 2020. **338**: p. 135890.

129. Wang, H., et al., *Mechanical property-reinforced PEO/PVDF/LiClO4/SN blend all solid polymer electrolyte for lithium ion batteries.* Journal of Electroanalytical Chemistry, 2020. **869**: p. 114156.

130. Xie, M., et al., *Mastering high ion conducting of room-temperature all-solid-state lithium-ion batteries via safe phthaloyl starch-poly(vinylidene fluoride)–based polymer electrolyte.* Ionics, 2020. **26**(3): p. 1109-1117.

131. Xue, C., et al., *Organic–Organic Composite Electrolyte Enables Ultralong Cycle Life in Solid-State Lithium Metal Batteries.* ACS Applied Materials & Interfaces, 2020. **12**(22): p. 24837-24844.

132. Wu, F., et al., *Preparation and characterization of solid polymer electrolytes based on PHEMO and PVDF-HFP.* Solid State Ionics, 2009. **180**(9): p. 677-680.

133. Sasikumar, M., et al., *The effects of PVAc on surface morphological and electrochemical performance of P(VdF-HFP)-based blend solid polymer electrolytes for lithium ion-battery applications.* Ionics, 2019. **25**(5): p. 2171-2181.

134. Oh, S., et al., *Intertwined Nanosponge Solid-State Polymer Electrolyte for Rollable and Foldable Lithium-Ion Batteries.* ACS Applied Materials & Interfaces, 2020. **12**(10): p. 11657-11668.

135. Li, J., et al., *Boosting the performance of poly(ethylene oxide)-based solid polymer electrolytes by blending with poly(vinylidene fluoride-co-hexafluoropropylene) for solid-state lithium-ion batteries.* International Journal of Energy Research, 2020. **44**(9): p. 7831-7840.

136. Lun, P., et al., *Enhanced ionic conductivity in halloysite nanotube-poly(vinylidene fluoride) electrolytes for solid-state lithium-ion batteries.* RSC Advances, 2018. **8**(60): p. 34232-34240.

137. Yao, P., et al., *PVDF/Palygorskite Nanowire Composite Electrolyte for 4 V Rechargeable Lithium Batteries with High Energy Density.* Nano Letters, 2018. **18**(10): p. 6113-6120.

138. Sun, Y., et al., *Improving Ionic Conductivity with Bimodal-Sized Li7La3Zr2O12 Fillers for Composite Polymer Electrolytes.* ACS Applied Materials & Interfaces, 2019. **11**(13): p. 12467-12475.

139. Pareek, T., et al., *Effect of NASICON-type LiSnZr(PO4)3 ceramic filler on the ionic conductivity and electrochemical behavior of PVDF based composite electrolyte.* Journal of Alloys and Compounds, 2020. **824**: p. 153991.

140. Sivaraj, P., et al., *Performance Enhancement of PVDF/LiClO4 Based Nanocomposite Solid Polymer Electrolytes via Incorporation of Li0.5La0.5TiO3 Nano Filler for All-Solid-State Batteries.* Macromolecular Research, 2020. **28**(8): p. 739-750.

141. Li, B., et al., *Biomimetic PVDF/LLTO composite polymer electrolyte enables excellent interface contact and enhanced ionic conductivity.* Applied Surface Science, 2021. **541**: p. 148434.

142. Li, B., et al., *Ultrathin, flexible, and sandwiched structure composite polymer electrolyte membrane for solid-state lithium batteries.* Journal of Membrane Science, 2021. **618**: p. 118734.

143. Padmaraj, O., M. Venkateswarlu, and N. Satyanarayana, *Effect of ZnO filler concentration on the conductivity, structure and morphology of PVdF-HFP nanocomposite solid polymer electrolyte for lithium battery application.* Ionics, 2013. **19**(12): p. 1835-1842.

144. Kumar, A., et al., *Impacts of ceramic filler and the crystallite size of polymer matrix on the ionic transport properties of lithium triflate/poly (vinylidene fluoride-co-hexafluoropropene) based polymer electrolytes.* Electrochimica Acta, 2016. **215**: p. 1-11.
145. Li, Y., et al., *Li7La3Zr2O12 ceramic nanofiber-incorporated composite polymer electrolytes for lithium metal batteries.* Journal of Materials Chemistry A, 2019. **7**(7): p. 3391-3398.
146. Yu, Y., et al., *Zwitterion-containing electrolytes with semi–crystalline PVDF-Co-HFP as a matrix for safer lithium-ion batteries.* Journal of Molecular Liquids, 2019. **282**: p. 340-346.
147. Lu, J., et al., *Hybridizing poly(vinylidene fluoride-co-hexafluoropropylene) with Li6.5La3Zr1.5Ta0.5O12 as a lithium-ion electrolyte for solid state lithium metal batteries.* Chemical Engineering Journal, 2019. **367**: p. 230-238.
148. Cong, L., et al., *Unlocking the Poly(vinylidene fluoride-co-hexafluoropropylene)/Li10GeP2S12 composite solid-state Electrolytes for Dendrite-Free Li metal batteries assisting with perfluoropolyethers as bifunctional adjuvant.* Journal of Power Sources, 2020. **446**: p. 227365.
149. Yang, H., et al., *Chemical interaction and enhanced interfacial ion transport in a ceramic nanofiber–polymer composite electrolyte for all-solid-state lithium metal batteries.* Journal of Materials Chemistry A, 2020. **8**(15): p. 7261-7272.
150. Zhang, W., et al., *Li7La3Zr2O12 Ceramic Nanofiber-Incorporated Solid Polymer Electrolytes for Flexible Lithium Batteries.* ACS Applied Energy Materials, 2020. **3**(6): p. 5238-5246.
151. Sun, Y., et al., *Composite Solid Electrolyte for Solid-State Lithium Batteries Workable at Room Temperature.* ACS Applied Energy Materials, 2020. **3**(12): p. 12127-12133.
152. Li, Y. and H. Wang, *Composite Solid Electrolytes with NASICON-Type LATP and PVdF–HFP for Solid-State Lithium Batteries.* Industrial & Engineering Chemistry Research, 2021. **60**(3): p. 1494-1500.
153. Yoon, M.Y., S.K. Hong, and H.J. Hwang, *Fabrication of Li-polymer/silica aerogel nanocomposite electrolyte for an all-solid-state lithium battery.* Ceramics International, 2013. **39**(8): p. 9659-9663.
154. Ma, Y., et al., *Effect of montmorillonite on the ionic conductivity and electrochemical properties of a composite solid polymer electrolyte based on polyvinylidenedifluoride/polyvinyl alcohol matrix for lithium ion batteries.* Electrochimica Acta, 2016. **187**: p. 535-542.
155. Hema, M., P. Tamilselvi, and G. Hirankumar, *Influences of LiCF 3 SO 3 and TiO 2 nanofiller on ionic conductivity and mechanical properties of PVA:PVdF blend polymer electrolyte.* Ionics, 2017. **23**(10): p. 2707-2714.
156. Wang, F., et al., *Influence of additives in a PVDF-based solid polymer electrolyte on conductivity and Li-ion battery performance.* Sustainable Energy & Fuels, 2018. **2**(2): p. 492-498.
157. Sivaraj, P., et al., *Free-standing, high Li-ion conducting hybrid PAN/PVdF/LiClO4/Li0.5La0.5TiO3 nanocomposite solid polymer electrolytes for all-solid-state batteries.* Journal of Solid State Electrochemistry, 2021. **25**(3): p. 905-917.
158. Hu, J., et al., *Porous film host-derived 3D composite polymer electrolyte for high-voltage solid state lithium batteries.* Energy Storage Materials, 2020. **26**: p. 283-289.
159. Yi, S., et al., *Fast ion conductor modified double-polymer (PVDF and PEO) matrix electrolyte for solid lithium-ion batteries.* Solid State Ionics, 2020. **355**: p. 115419.
160. Li, L., Y. Shan, and X. Yang, *New insights for constructing solid polymer electrolytes with ideal lithium-ion transfer channels by using inorganic filler.* Materials Today Communications, 2021. **26**: p. 101910.

161. Zhou, D., et al., *Synergistic effect of soy protein isolate and montmorillonite on interface stability between polymer electrolyte and electrode of all-solid lithium-ion battery.* Ionics, 2021. **27**(1): p. 137-143.
162. Yu, S., et al., *Insights into a layered hybrid solid electrolyte and its application in long lifespan high-voltage all-solid-state lithium batteries.* Journal of Materials Chemistry A, 2019. **7**(8): p. 3882-3894.
163. Xie, Z., et al., *A sandwich-type composite polymer electrolyte for all-solid-state lithium metal batteries with high areal capacity and cycling stability.* Journal of Membrane Science, 2020. **596**: p. 117739.
164. Sha, Y., et al., *A new strategy for enhancing the room temperature conductivity of solid-state electrolyte by using a polymeric ionic liquid.* Ionics, 2020. **26**(10): p. 4803-4812.
165. Li, J., et al., *Approaching high performance PVDF-HFP based solid composite electrolytes with LLTO nanorods for solid-state lithium-ion batteries.* International Journal of Energy Research, 2021. **n/a**(n/a).
166. Ulaganathan, M. and S. Rajendran, *Effect of different salts on PVAc/PVdF-co-HFP based polymer blend electrolytes.* Journal of Applied Polymer Science, 2010. **118**(2): p. 646-651.
167. Li, Z.H., et al., *Effect of zwitterionic salt on the electrochemical properties of a solid polymer electrolyte with high temperature stability for lithium ion batteries.* Electrochimica Acta, 2010. **56**(2): p. 804-809.
168. Serra, J.P., et al., *Lithium-Ion Battery Solid Electrolytes Based on Poly(vinylidene Fluoride)–Metal Thiocyanate Ionic Liquid Blends.* ACS Applied Polymer Materials, 2022. **4**(8): p. 5909-5919.
169. Guo, C., et al., *Polymerized Ionic Networks Solid Electrolyte with High Ionic Conductivity for Lithium Batteries.* Industrial & Engineering Chemistry Research, 2021. **60**(12): p. 4630-4638.
170. Fu, J., et al., *Multiclaw-shaped octasilsesquioxanes functionalized ionic liquids toward organic-inorganic composite electrolytes for lithium-ion batteries.* Chemical Engineering Journal, 2021. **405**: p. 126942.
171. Deb, D., P. Bose, and S. Bhattacharya, *Ionanofluid plasticized electrolyte with improved electrical and electrochemical properties for high-performance lithium polymer battery.* International Journal of Energy Research, 2020. **44**(13): p. 10506-10522.
172. da Silva Filho, S.B., et al., *Free-standing solid polymer electrolytes based on elastomeric material and ionic liquids for safer lithium-ion battery applications.* Solid State Ionics, 2022. **379**: p. 115901.
173. Polu, A.R. and H.-W. Rhee, *Ionic liquid doped PEO-based solid polymer electrolytes for lithium-ion polymer batteries.* International Journal of Hydrogen Energy, 2017. **42**(10): p. 7212-7219.
174. Yongxin, A., et al., *Improved properties of polymer electrolyte by ionic liquid PP1.3TFSI for secondary lithium ion battery.* Journal of Solid State Electrochemistry, 2012. **16**(1): p. 383-389.
175. Fu, C., et al., *A Polymerized-Ionic-Liquid-Based Polymer Electrolyte with High Oxidative Stability for 4 and 5 V Class Solid-State Lithium Metal Batteries.* Advanced Energy Materials, 2022. **12**(27): p. 2200412.
176. Kim, S., A. Le Mong, and D. Kim, *Accelerated ion conduction by co-grafting of poly(ethylene glycol) and nitrile-terminated ionic liquid on poly(arylene ether sulfone) for solid electrolyte membranes for lithium ion battery.* Journal of Power Sources, 2022. **529**: p. 231255.

177. Tian, Z. and D. Kim, *Solid electrolyte membranes prepared from poly(arylene ether sulfone)-g-poly(ethylene glycol) with various functional end groups for lithium-ion battery.* Journal of Membrane Science, 2021. **621**: p. 119023.
178. Kimura, K., et al., *Electrochemical properties of a poly(ethylene carbonate)-LiTFSI electrolyte containing a pyrrolidinium-based ionic liquid.* Ionics, 2015. **21**(3): p. 895-900.
179. Dong, L., et al., *Cross-linked ionic copolymer solid electrolytes with loose Coordination-assisted lithium transport for lithium batteries.* Chemical Engineering Journal, 2021. **423**: p. 130209.
180. Tan, J., et al., *Polycation ionic liquid tailored PEO-based solid polymer electrolytes for high temperature lithium metal batteries.* Energy Storage Materials, 2020. **33**: p. 173-180.
181. Ruan, Z., et al., *Incorporation of Poly(Ionic Liquid) with PVDF-HFP-Based Polymer Electrolyte for All-Solid-State Lithium-Ion Batteries.* Polymers, 2022. **14**(10).
182. Lei, Z., et al., *Composite polymer electrolytes with uniform distribution of ionic liquid-grafted ZIF-90 nanofillers for high-performance solid-state Li batteries.* Chemical Engineering Journal, 2021. **412**: p. 128733.
183. Yang, K., et al., *Ionic plastic crystal-polymeric ionic liquid solid-state electrolytes with high ionic conductivity for lithium ion batteries.* Materials Letters, 2019. **236**: p. 554-557.
184. Hu, Z., X. Zhang, and S. Chen, *A graphene oxide and ionic liquid assisted anion-immobilized polymer electrolyte with high ionic conductivity for dendrite-free lithium metal batteries.* Journal of Power Sources, 2020. **477**: p. 228754.
185. Shen, J., Z. Lei, and C. Wang, *An ion conducting ZIF-8 coating protected PEO based polymer electrolyte for high voltage lithium metal batteries.* Chemical Engineering Journal, 2022. **447**: p. 137503.
186. Yao, M., et al., *High-Voltage and Wide-Temperature Lithium Metal Batteries Enabled by Ultrathin MOF-Derived Solid Polymer Electrolytes with Modulated Ion Transport.* ACS Applied Materials & Interfaces, 2021. **13**(39): p. 47163-47173.
187. Yao, M., et al., *Ultralong cycling and wide temperature range of lithium metal batteries enabled by solid polymer electrolytes interpenetrated with a poly(liquid crystal) network.* Journal of Materials Chemistry A, 2021. **9**(10): p. 6232-6241.
188. Zhang, Z., et al., *3D glass fiber cloth reinforced polymer electrolyte for solid-state lithium metal batteries.* Journal of Membrane Science, 2021. **621**: p. 118940.
189. Shen, X., et al., *Enhancing Li+ transport kinetics of PEO-based polymer electrolyte with mesoporous silica-derived fillers for lithium-ion batteries.* Solid State Ionics, 2020. **354**: p. 115412.
190. Lu, Q., et al., *Polymeric polyhedral oligomeric silsesquioxane ionic liquids based solid polymer electrolytes for lithium ion batteries.* Journal of Power Sources, 2019. **414**: p. 31-40.
191. Kale, S.B., et al., *Cellulose-Derived Flame-Retardant Solid Polymer Electrolyte for Lithium-Ion Batteries.* ACS Sustainable Chemistry & Engineering, 2021. **9**(4): p. 1559-1567.
192. Nguyen, Q.H., et al., *Li(7)La(3)Zr(2)O(12) Garnet Solid Polymer Electrolyte for Highly Stable All-Solid-State Batteries.* Front Chem, 2020. **8**: p. 619832.
193. Nematdoust, S., et al., *Partially Oxidized Cellulose grafted with Polyethylene Glycol mono-Methyl Ether (m-PEG) as Electrolyte Material for Lithium Polymer Battery.* Carbohydrate Polymers, 2020. **240**: p. 116339.
194. Ma, F., et al., *Solid Polymer Electrolyte Based on Polymerized Ionic Liquid for High Performance All-Solid-State Lithium-Ion Batteries.* ACS Sustainable Chemistry & Engineering, 2019. **7**(5): p. 4675-4683.

195. Liu, K., et al., *In situ polymerized succinonitrile-based solid polymer electrolytes for lithium ion batteries.* Solid State Ionics, 2020. **345**: p. 115159.
196. Zhan, X., et al., *Advanced Polymer Electrolyte with Enhanced Electrochemical Performance for Lithium-Ion Batteries: Effect of Nitrile-Functionalized Ionic Liquid.* ACS Applied Energy Materials, 2019. **2**(3): p. 1685-1694.
197. Wang, X., et al., *Poly(Ionic Liquid)s-in-Salt Electrolytes with Co-coordination-Assisted Lithium-Ion Transport for Safe Batteries.* Joule, 2019. **3**(11): p. 2687-2702.
198. Barbosa, J.C., et al., *Metal–organic frameworks and zeolite materials as active fillers for lithium-ion battery solid polymer electrolytes.* Materials Advances, 2021. **2**(12): p. 3790-3805.
199. Rouquerol, J., et al., *Recommendations for the characterization of porous solids (Technical Report).* Pure and Applied Chemistry, 1994. **66**(8): p. 1739-1758.
200. Akhtar, F., et al., *Structuring adsorbents and catalysts by processing of porous powders.* Journal of the European Ceramic Society, 2014. **34**: p. 1643–1666.
201. Li, W., J. Liu, and D. Zhao, *Mesoporous materials for energy conversion and storage devices.* Nature Reviews Materials, 2016. **1**(6): p. 16023.
202. Barbosa, J.C., et al., *Toward Sustainable Solid Polymer Electrolytes for Lithium-Ion Batteries.* ACS Omega, 2022. **7**(17): p. 14457-14464.
203. Martínez T, L.M., et al., *Synthesis and Identification Methods for Zeolites and MOFs*, in *Zeolites and Metal-Organic Frameworks*, V. Blay, L.F. Bobadilla, and A.C. García, Editors. 2018, Amsterdam University Press. p. 25-52.
204. Valtchev, V. and S. Mintova, *Zeolites and MOFs? Dare to Know Them!*, in *Zeolites and Metal-Organic Frameworks*, V. Blay, L.F. Bobadilla, and A.C. García, Editors. 2018, Amsterdam University Press. p. 13-24.
205. Agrawal, R. and G.P. Pandey, *Solid polymer electrolytes: Materials designing and all-solid-state battery applications: An overview.* Journal of Physics D: Applied Physics, 2008. **41**: p. 223001.
206. Sousa, R.E., C.M. Costa, and S. Lanceros-Méndez, *Advances and Future Challenges in Printed Batteries.* ChemSusChem, 2015. **8**(21): p. 3539-3555.
207. Zeng, L., et al., *Recent progresses of 3D printing technologies for structural energy storage devices.* Materials Today Nano, 2020. **12**: p. 100094.
208. James, S.L., *Metal-organic frameworks.* Chemical Society Reviews, 2003. **32**(5): p. 276-288.
209. Yaghi, O.M., G. Li, and H. Li, *Selective binding and removal of guests in a microporous metal–organic framework.* Nature, 1995. **378**(6558): p. 703-706.
210. Moghadam, P.Z., et al., *Development of a Cambridge Structural Database Subset: A Collection of Metal–Organic Frameworks for Past, Present, and Future.* Chemistry of Materials, 2017. **29**(7): p. 2618-2625.
211. Farha, O.K., et al., *Metal–Organic Framework Materials with Ultrahigh Surface Areas: Is the Sky the Limit?* Journal of the American Chemical Society, 2012. **134**(36): p. 15016-15021.
212. Tian, T., et al., *A sol–gel monolithic metal–organic framework with enhanced methane uptake.* Nature Materials, 2018. **17**(2): p. 174-179.
213. Bobbitt, N.S., et al., *Metal–organic frameworks for the removal of toxic industrial chemicals and chemical warfare agents.* Chemical Society Reviews, 2017. **46**(11): p. 3357-3385.
214. Teplensky, M.H., et al., *Temperature Treatment of Highly Porous Zirconium-Containing Metal–Organic Frameworks Extends Drug Delivery Release.* Journal of the American Chemical Society, 2017. **139**(22): p. 7522-7532.

215. Rogge, S.M.J., et al., *Metal–organic and covalent organic frameworks as single-site catalysts.* Chemical Society Reviews, 2017. **46**(11): p. 3134-3184.
216. Hu, Z., B.J. Deibert, and J. Li, *Luminescent metal–organic frameworks for chemical sensing and explosive detection.* Chemical Society Reviews, 2014. **43**(16): p. 5815-5840.
217. Qiu, T., et al., *Metal–Organic Framework-Based Materials for Energy Conversion and Storage.* ACS Energy Letters, 2020. **5**(2): p. 520-532.
218. Li, X., et al., *Metal–organic frameworks as a platform for clean energy applications.* EnergyChem, 2020. **2**(2): p. 100027.
219. Wang, Z., et al., *A Metal–Organic-Framework-Based Electrolyte with Nanowetted Interfaces for High-Energy-Density Solid-State Lithium Battery.* Advanced Materials, 2018. **30**(2): p. 1704436.
220. Zhao, R., et al., *Metal–organic frameworks for solid-state electrolytes.* Energy & Environmental Science, 2020. **13**(8): p. 2386-2403.
221. Kim, J., H. Cho, and W.-s. Ahn, *Synthesis and Adsorption/Catalytic Properties of the Metal Organic Framework CuBTC.* Catalysis Surveys from Asia, 2012. **16**.
222. Frem, R.C.G., et al., *MOFs (METAL-ORGANIC FRAMEWORKS): UMA FASCINANTE CLASSE DE MATERIAIS INORGÂNICOS POROSOS.* Química Nova, 2018. **41**: p. 1178-1191.
223. Huo, H., et al., *Anion-immobilized polymer electrolyte achieved by cationic metal-organic framework filler for dendrite-free solid-state batteries.* Energy Storage Materials, 2019. **18**: p. 59-67.
224. Zhang, Z., et al., *Metal Organic Framework Nanorod Doped Solid Polymer Electrolyte with Decreased Crystallinity for High-Performance All-Solid-State Lithium Batteries.* ChemElectroChem, 2020. **7**(5): p. 1125-1134.
225. Liu, L. and C. Sun, *Flexible Quasi-Solid-State Composite Electrolyte Membrane Derived from a Metal-Organic Framework for Lithium-Metal Batteries.* ChemElectroChem, 2020. **7**(3): p. 707-715.
226. Angulakshmi, N., et al., *Composite Polymer Electrolytes Encompassing Metal Organic Frame Works: A New Strategy for All-Solid-State Lithium Batteries.* The Journal of Physical Chemistry C, 2014. **118**(42): p. 24240-24247.
227. Wang, Z., et al., *Covalently linked metal–organic framework (MOF)-polymer all-solid-state electrolyte membranes for room temperature high performance lithium batteries.* Journal of Materials Chemistry A, 2018. **6**(35): p. 17227-17234.
228. Yuan, C., et al., *Enhanced electrochemical performance of poly(ethylene oxide) based composite polymer electrolyte by incorporation of nano-sized metal-organic framework.* Journal of Power Sources, 2013. **240**: p. 653-658.
229. Mathew, D.E., et al., *Influence of MOF ligands on the electrochemical and interfacial properties of PEO-based electrolytes for all-solid- state lithium batteries.* Electrochimica Acta, 2019. **319**: p. 189-200.
230. Gerbaldi, C., et al., *Innovative high performing metal organic framework (MOF)-laden nanocomposite polymer electrolytes for all-solid-state lithium batteries.* Journal of Materials Chemistry A, 2014. **2**(26): p. 9948-9954.
231. Suriyakumar, S., et al., *Metal organic framework laden poly(ethylene oxide) based composite electrolytes for all-solid-state Li-S and Li-metal polymer batteries.* Electrochimica Acta, 2018. **285**: p. 355-364.
232. Zhang, Z., et al., *MOF-derived ionic conductor enhancing polymer electrolytes with superior electrochemical performances for all solid lithium metal batteries.* Journal of Membrane Science, 2020. **598**: p. 117800.

233. Wu, J.-F. and X. Guo, *MOF-derived nanoporous multifunctional fillers enhancing the performances of polymer electrolytes for solid-state lithium batteries.* Journal of Materials Chemistry A, 2019. **7**(6): p. 2653-2659.
234. Kumar, R., et al., *Metal organic framework-laden composite polymer electrolytes for efficient and durable all-solid-state-lithium batteries.* RSC Advances, 2014. **4**: p. 26171.
235. Suriyakumar, S., et al., *Charge–discharge studies of all-solid-state Li/LiFePO4 cells with PEO-based composite electrolytes encompassing metal organic frameworks.* RSC Advances, 2016. **6**(99): p. 97180-97186.
236. Zhu, K., Y. Liu, and J. Liu, *A fast charging/discharging all-solid-state lithium ion battery based on PEO-MIL-53(Al)-LiTFSI thin film electrolyte.* RSC Advances, 2014. **4**(80): p. 42278-42284.
237. Wang, Z., et al., *Enhancing Ion Transport: Function of Ionic Liquid Decorated MOFs in Polymer Electrolytes for All-Solid-State Lithium Batteries.* ACS Applied Energy Materials, 2020. **3**(5): p. 4265-4274.
238. Angulakshmi, N., et al., *Microporous Metal–Organic Framework (MOF)-Based Composite Polymer Electrolyte (CPE) Mitigating Lithium Dendrite Formation in All-Solid-State-Lithium Batteries.* ACS Omega, 2020. **5**(14): p. 7885-7894.
239. Yang, J., et al., *Effect of intermolecular interactions on the performance of UiO-66-laden solid composite polymer electrolytes.* Journal of Alloys and Compounds, 2020. **845**: p. 155179.
240. Corma, A., *State of the art and future challenges of zeolites as catalysts.* Journal of Catalysis, 2003. **216**(1): p. 298-312.
241. Ozaydin, S., G. Kocer, and A. Hepbasli, *Natural Zeolites in Energy Applications.* Energy Sources, Part A: Recovery, Utilization, and Environmental Effects, 2006. **28**(15): p. 1425-1431.
242. Flanigen, E.M., R.W. Broach, and S.T. Wilson, *Zeolites in Industrial Separation and Catalysis*, ed. Wiley. 2010.
243. Barrer, R.M., *435. Syntheses and reactions of mordenite.* Journal of the Chemical Society (Resumed), 1948(0): p. 2158-2163.
244. Barrer, R.M., *33. Synthesis of a zeolitic mineral with chabazite-like sorptive properties.* Journal of the Chemical Society (Resumed), 1948(0): p. 127-132.
245. *Chapter 2 Basics of Zeolites*. 2020.
246. Roth, W.J., et al., *Two-Dimensional Zeolites: Current Status and Perspectives.* Chemical Reviews, 2014. **114**(9): p. 4807-4837.
247. Bertão, A.R., et al., *Modification of microfluidic paper-based devices with dye nanomaterials obtained by encapsulation of compounds in Y and ZSM5 zeolites.* Sensors and Actuators B: Chemical, 2018. **261**: p. 66-74.
248. Ennaert, T., et al., *Potential and challenges of zeolite chemistry in the catalytic conversion of biomass.* Chemical Society Reviews, 2016. **45**(3): p. 584-611.
249. Pera-Titus, M., *Porous Inorganic Membranes for CO2 Capture: Present and Prospects.* Chemical Reviews, 2014. **114**(2): p. 1413-1492.
250. Wei, J., et al., *Directly converting CO2 into a gasoline fuel.* Nature Communications, 2017. **8**(1): p. 15174.
251. Zhang, R., et al., *Selective Transformation of Various Nitrogen-Containing Exhaust Gases toward N2 over Zeolite Catalysts.* Chemical Reviews, 2016. **116**(6): p. 3658-3721.
252. Meng, Y., et al., *One-Step Hydrothermal Synthesis of Manganese-Containing MFI-Type Zeolite, Mn–ZSM-5, Characterization, and Catalytic Oxidation of Hydrocarbons.* Journal of the American Chemical Society, 2013. **135**(23): p. 8594-8605.

253. Swenson, P., et al., *Water desalination and de-oiling with natural zeolite membranes — Potential application for purification of SAGD process water.* Desalination, 2012. **286**: p. 442-446.
254. Yu, N., R.Z. Wang, and L.W. Wang, *Sorption thermal storage for solar energy.* Progress in Energy and Combustion Science, 2013. **39**(5): p. 489-514.
255. Sun, Q., et al., *Subnanometric Hybrid Pd-M(OH)2, M = Ni, Co, Clusters in Zeolites as Highly Efficient Nanocatalysts for Hydrogen Generation.* Chem, 2017. **3**(3): p. 477-493.
256. Kaur, B., R. Srivastava, and B. Satpati, *Highly Efficient CeO2 Decorated Nano-ZSM-5 Catalyst for Electrochemical Oxidation of Methanol.* ACS Catalysis, 2016. **6**(4): p. 2654-2663.
257. Kim, N., et al., *Zeolite-Templated Mesoporous Silicon Particles for Advanced Lithium-Ion Battery Anodes.* ACS Nano, 2018. **12**(4): p. 3853-3864.
258. Park, H., et al., *Electrochemical characteristics and energy densities of lithium-ion batteries using mesoporous silicon and graphite as anodes.* Electrochimica Acta, 2020. **357**: p. 136870.
259. Badini Pourazar, M., et al., *Preparation and characterization of poly(vinylidene fluoride)-13X zeolite mixed matrix membranes for lithium ion batteries' separator with enhanced performance.* Journal of Applied Polymer Science, 2020. **137**(44): p. 49367.
260. Li, Y., et al., *Design of A High Performance Zeolite/Polyimide Composite Separator for Lithium-Ion Batteries.* Polymers, 2020. **12**(4).
261. Zhang, J., et al., *Polymers/zeolite nanocomposite membranes with enhanced thermal and electrochemical performances for lithium-ion batteries.* Journal of Membrane Science, 2018. **564**: p. 753-761.
262. Shekarian, E., et al., *Preparation of 4A zeolite coated polypropylene membrane for lithium-ion batteries separator.* Journal of Applied Polymer Science, 2019. **136**(32): p. 47841.
263. Dong, X., et al., *Zeolite coated polypropylene separators with tunable surface properties for lithium-ion batteries.* Microporous and Mesoporous Materials, 2016. **226**: p. 406-414.
264. Kim, J.H., et al., *Enhancement of ionic conductivity of a composite polymer electrolyte via surface functionalization of SSZ-13 zeolite for all-solid-state Li-ion batteries.* Journal of Materials Chemistry A, 2021.

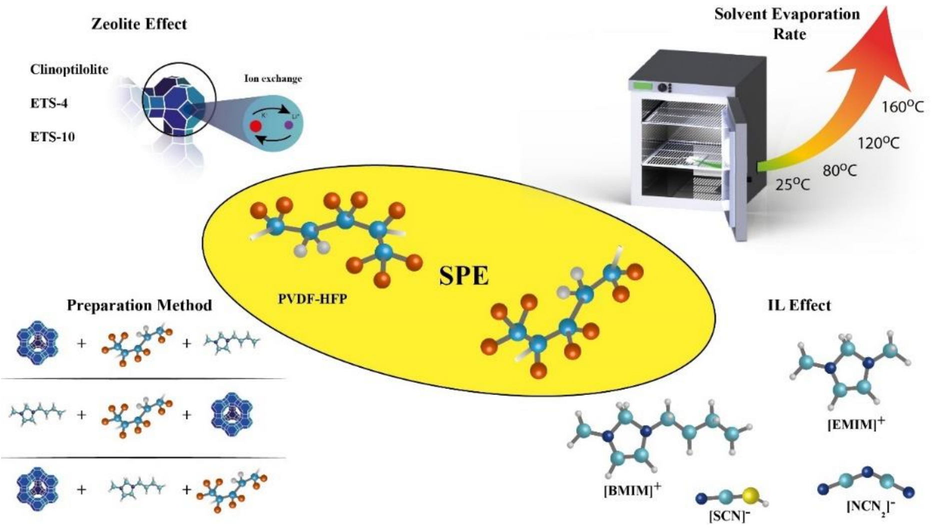

3. Experimental: Materials and Methods

The materials, experimental conditions and procedures used for the samples' preparation and the characterization techniques applied to determine their properties are described in detail in this section. Also, the methods for the assessment of the battery cycling performance are explained.

In order to achieve the proposed objectives, several samples were produced and studied in detail in each section. The specific materials and conditions applied in the different works are summarized in table 3.1.

Table 3.1 – Materials and experimental conditions studied in the different experimental works.

Chapter	Polymer	Active filler	Passive filler	Solvent evaporation temperature	Preparation method
3.1	PVDF-HFP	[BMIM][SCN]	ETS-4	120°C	Zeolite-IL-Polymer
			ETS-10		
			CPT		
3.2		[EMIM][SCN]			
		[BMIM][SCN]			
		[EMIM][N(CN)$_2$]			
		[BMIM][N(CN)$_2$]			
3.3		[BMIM][SCN]		25°C	
				80°C	
				120°C	
				160°C	
3.4				120°C	Zeolite-Polymer-IL
3.5		[PMPYR][TFSI]		160°C	IL-Polymer-zeolite
		LiTFSI			
	P(VDF-TrFE-CFE)	[BMIM][SCN]			

3.1. Sample preparation

3.1.1. Materials

The polymers PVDF-HFP, (Kynarflex PVDF-HFP 2801–00107) and Poly(vinylidene fluoride-trifluoroethylene-chlorofluoroethylene) (P(VDF-TrFE-CFE) were supplied by Arkema.

Natural clinoptilolite (CPT) was purchased from Newstone International LLC, Japan. The other zeolites, ETS-4 and ETS-10 were synthesized according to previously described procedures [1]. ETS-4 is a highly disordered microporous titanosilicate whose framework is built up of 8-ring channels extended along the b-axis and filled with water molecules and other 12-ring channels whose blockage along the c-axis creates smaller 7-ring elliptical pores occupied only by Na^+ cations. ETS-10 is also a disordered titanosilicate composed of a three-dimensional (3D) porous system of large 12-ring channels filled with water molecules and charge-balancing Na^+ and K^+ cations. The porous system of the aluminosilicate zeolite clinoptilolite is two-dimensional (2D). Along the c-axis, there are 10-and 8-ring channels, while along the a-axis there are 8-ring channels filled with water molecules and charge-compensation cations [2]. Among the three zeolites, ETS-4 has the highest theoretical cation exchange capacity of 6.3 meq g^{-1} [3], followed by ETS-10 (4.5 meq g^{-1}) [3] and CPT (2.2 meq g^{-1}) [4]. Thus, ETS-4 is the material with the largest number of mobile cations in the porous framework. Furthermore, in ETS-4 there are channels that are occupied only by charge compensation cations with relatively long Na-O bond distances (2.41-2.81 Å) [5] which decrease the possibility for nonbonding interactions between cations and water molecules in the pore system. Furthermore, the only exchangeable cation of ETS-4 is Na^+, while ETS-10 and CPT contain large K^+ ions that may influence the intercationic reactions and the resulting cation conductivity. Considering these characteristics, ETS-4 is logically the zeolite-like material with the highest cationic conductivity.

The ILs 1-butyl-3-methylimidazolium thiocyanate ([BMIM][SCN]), 1-ethyl-3-methylimidazolium thiocyanate ([EMIM][SCN]), 1-ethyl-3-methylimidazolium dicyanamide ([EMIM][$N(CN)_2$]), 1-butyl-3-methylimidazolium dicyanamide ([BMIM][$N(CN)_2$]) and 1-butyl-3-methylpyrrolidinium bis(trifluoromethylsulfonyl) imide ([PMPYR][TFSI]) were obtained from Iolitec. Lithium salt LiTFSI was obtained from Solvay. N,N-dimethylformamide (99%) (DMF) and N-methyl-2-pyrrolidone (99%), (NMP) were purchased from Merck. LFP and Super P conductive carbon black were obtained from Phostech Lithium and Timcal Graphite & Carbon, respectively.

3.1.2. Sample production

For the zeolite preparation (section 3.1) an IE process was carried out. This process was based on an aqueous solution of 1M LiOH. This solution was added to the powder sample at a rate of 50 mL of the solution for each 0.5 g of the zeolite, which was then placed in an oven (PSelecta) at 90 °C for 72 h. More LiOH solution was gradually added upon evaporation of the previous one. After this process, the solutions were filtered and the resulting powders were washed with distilled water. Then, the samples were prepared by doctor blade technique. A polymer/zeolite ratio of 84:16 and a polymer/IL ratio of 60:40 were used. These ratios are proved to be the most suitable to obtain the best possible film properties without compromising their structural integrity [6]. The basic sample for all the works consisted in a mixture of [BMIM][SCN] IL with CPT zeolite in a PVDF-HFP matrix, added in the order zeolite-IL-polymer, and evaporated at 120°C. First, the zeolites (CPT, ETS-4 and ETS-10, with and without IE in the section 3.1) were mixed with the ILs ([EMIM][SCN], [BMIM][SCN], [EMIM][$N(CN)_2$] and [EMIM][$N(CN)_2$] in the section 3.2). Then, DMF solvent was added and the solution was placed in an ultrasonic bath for 3 h. After that, PVDF-HFP was added and dissolved under magnetic stirring for about an hour. The solution was then cast onto a glass substrate and a doctor blade was used to uniformize the thickness to about 50 µm. The glass was then put in an oven for 30 min at 120°C to evaporate the solvent. In section 3.3, the evaporation temperature was varied to room temperature, 80°C (60 min), 120°C (30 min) and 160°C (20 min). For section 3.4 the addition order of the materials was changed from zeolite-IL-polymer to zeolite-polymer-IL and IL-polymer-zeolite.

3.2. Characterization techniques

3.2.1. Sample characterization

High resolution transmission electron microscopy (HRTEM) measurements were performed using a FEI TEM Tecnai G2 instrument with an accelerating voltage of 200 kV.

The morphology of the samples was evaluated by SEM, in a Carl Zeiss EVO 40, EDX Oxford Instruments equipment, with an accelerating voltage of 10 kV. The samples were previously coated with a gold layer using a Polaron, model SC502.

The morphology and roughness of the samples were analyzed by Atomic Force Microscopy (AFM) using a Nano-Observer CSI using of 20 µm × 20 µm. The average roughness values (R_a) values represent the arithmetic average in different areas of the sample.

X-ray photoelectron spectroscopy (XPS) spectra of the zeolites powder after IE were obtained using a Theta Probe AR-XPS system.

X-ray diffraction was determined in a Panalytical X'pert CuKα diffractometer 2θ range= 5-70°. Step size = 0.015° and exposure time of 10 s/step. The crystallinity degree of the samples was calculated using a two-phase model, assuming that the samples have both amorphous and crystalline regions [7] and the DIFFRAC.EVA (Bruker, AXS) software package by computing and comparing the global and the reduced area of each diffractograms using equation 4:

$$\%Amorphous = \frac{Global\ area - Reduced\ area}{Global\ area} \times 100; \tag{4}$$

%Crystallinity = 100 - %Amorphous

Inductively coupled plasma atomic emission spectroscopy (ICP-AES) was used to determine the amount of Li element in the zeolite structures after IE. This analysis was carried out in a Prodigy7, Teledyne LeemansLab, USA, after a HCl treatment.

Fourier transform infrared (FTIR) spectroscopy in the attenuated total reflection (ATR) mode was used to complement the morphological analysis. A Jasco FT/IR-6100 equipment was used and a wavelength range between 4000 to 600 cm^{-1} after 64 scans at a resolution of 4 cm^{-1} was applied to the samples. The polymer β-phase ($F(\beta)$) content in each sample was calculated using equation 5 [8]:

$$F(\beta) = \frac{A_\beta}{\left(\frac{k_\beta}{k_\alpha}\right)(A_\alpha + A_\beta)} \tag{5}$$

where A_α and A_β are the absorbances at 760 and 840 cm^{-1}, corresponding to the α and the β phases, respectively, and K_α and K_β are the absorption coefficients for the these bands (6.1×10^4 and 7.7×10^4 cm^2 mol^{-1}, respectively) [8].

The Thermal properties were evaluated using differential scanning calorimetry (DSC) in a Perkin-Elmer DSC 6000 apparatus, in a temperature range from 20 to 200 °C at 10 °C min^{-1} under nitrogen atmosphere. Thermogravimetric analysis (TGA) was made under a nitrogen atmosphere, in a NETZSCH STA 449F3 thermobalance with a crucible comprising about 10 mg of the sample, in the temperature range from 20 to 800 °C at 5 °C min^{-1}.

The mechanical properties were evaluated in a Linkam Scientific Instruments TST 360 apparatus with controlled temperature and tensile stress testing stage, at a strain rate of 15 μm s^{-1} in samples with dimensions of 30 mm x 10 mm x 50 mm.

3.2.2. Electrochemical properties and battery characterization

The ionic conductivity of the samples was determined using the complex plane impedance technique. An Autolab PGSTAT-12 (Eco Chemie) equipment was used in the temperature range from 25 to 80 °C. The samples were pretreated at 60 °C in a Buchi TO51 tube oven with a type K thermocouple, between two gold electrodes (Goodfellow, >99.95%) of 10 mm diameter. The ionic conductivity (σ_i) was calculated using equation 6:

$$\sigma_i = \frac{d}{R_b \times A} \tag{6}$$

where R_b is the bulk resistance of the sample, d is its thickness and A is the area.

The temperature (T) dependence of the ionic conductivity of the samples follows the Arrhenius equation (7) in the measured range:

$$\sigma = \sigma_0 e^{(-E_a/RT)} \tag{7}$$

where E_a is the apparent activation energy, R is the gas constant (8.314 J mol^{-1} K^{-1}) and σ_0 is a pre-exponential factor.

Cyclic voltammetry (CV) was carried out in a Autolab PGSTAT-12 (Eco Chemie) equipment, in a voltage range between 0 and 4.5 V, at a rate of 0.01 V s^{-1}. The cell was assembled under argon atmosphere using a two electrodes configuration, with a gold microelectrode as working electrode.

Li-ion transference number (tLi$^+$) was measured in symmetrical lithium cells and then calculated by the equation proposed by Bruce and Evans (equation 8) [9]:

$$t_{Li+} = \frac{I^s[\Delta V - I^0 R^0]}{I^0[\Delta V - I^s R^s]} \tag{8}$$

Where I^0 and I^s are initial and steady currents. The initial (R^0) and final (R^s) resistances of the interfacial layers of the Li electrode/electrolyte were recorded in the impedance spectra before and after the direct current (DC) polarization, respectively.

The battery testing was made using a series of half cells, which were assembled in a glovebox under argon atmosphere (H_2O, O_2 <1 ppm). The studied samples were applied as SPE, with two electrodes consisting in lithium metal as anode and LFP as cathode. The production of the cathodes is explained in [10], with an active material: conductive material: polymer binder weight ratio of 80:10:10. The active mass loading of the cathodes was about 1.650 mg. The cathodes and SPEs were dried overnight in a Buchi TO51 tube oven at 60 °C under vacuum before being put in the glovebox.

The battery performance was evaluated in a Landt CT2001A Instrument with 30 cycles at C/10 rate (C=170 mAh g^{-1}) and with 10 cycles at five different rates (C/15, C/8, C/5, C/2 and C). Impedance spectroscopy was also used to evaluate the electrical properties of the batteries, using an Autolab PGSTAT12 instrument in the frequency range from 10 mHz to 500 kHz and with a signal amplitude of 10 mV.

3.3. References

1. Kostov-Kytin, V., et al., *Hydrothermal synthesis of microporous titanosilicates.* Microporous and Mesoporous Materials, 2007. **105**(3): p. 232-238.
2. Armbruster, T., *Dehydration mechanism of clinoptilolite and heulandite: Single-crystal X-ray study of Na-poor, Ca-, K-, Mg-rich clinoptilolite at 100 K.* American Mineralogist, 1993. **78**(3-4): p. 260-264.
3. Oleksiienko, O., C. Wolkersdorfer, and M. Sillanpää, *Titanosilicates in cation adsorption and cation exchange – A review.* Chemical Engineering Journal, 2017. **317**: p. 570-585.
4. Ganrot, Z., *Use of zeolites for improved nutrient recovery from decentralized domestic wastewater.* Handbook of Natural Zeolites, 2012: p. 410-435.
5. Cruciani, G., et al., *Rietveld refinement of the zorite structure of ETS-4 molecular sieves.* Microporous and Mesoporous Materials, 1998. **21**(1): p. 143-153.
6. Barbosa, J.C., et al., *High-Performance Room Temperature Lithium-Ion Battery Solid Polymer Electrolytes Based on Poly(vinylidene fluoride-co-hexafluoropropylene) Combining Ionic Liquid and Zeolite.* ACS Applied Materials & Interfaces, 2021. **13**(41): p. 48889-48900.
7. Segerman, E. and P.G. Stern, *Two-phase Model for Structure of Polymers.* Nature, 1966. **210**(5042): p. 1258-1259.
8. Martins, P., A.C. Lopes, and S. Lanceros-Mendez, *Electroactive phases of poly(vinylidene fluoride): Determination, processing and applications.* Progress in Polymer Science, 2014. **39**(4): p. 683-706.
9. Bruce, P.G., J. Evans, and C.A. Vincent, *Conductivity and transference number measurements on polymer electrolytes.* Solid State Ionics, 1988. **28-30**: p. 918-922.
10. Gonçalves, R., et al., *Optimized Printed Cathode Electrodes for High Performance Batteries.* Energy Technology, 2021. **9**(1): p. 2000805.

4. Results and discussion

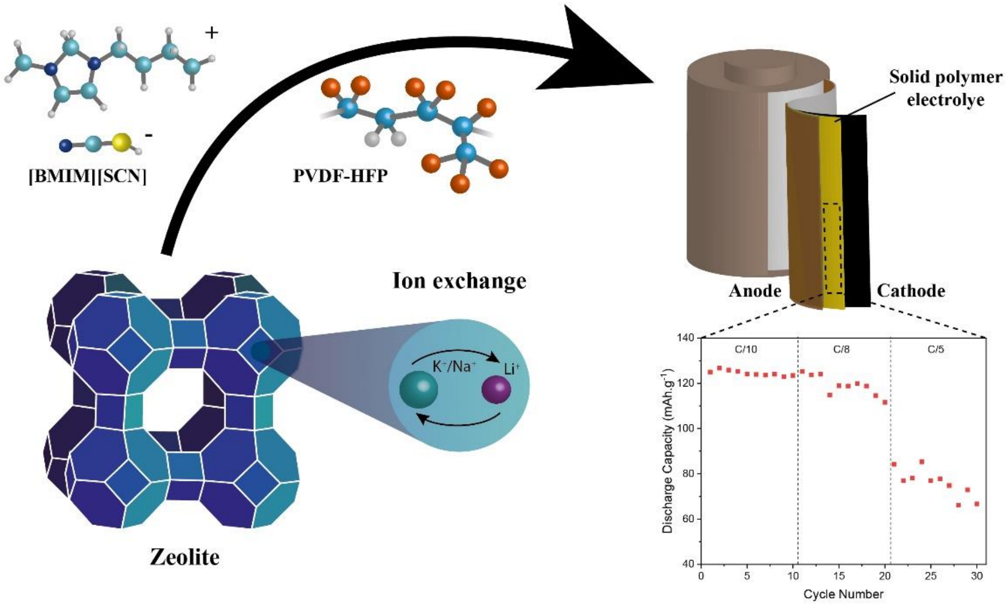

4.1. Three-component solid polymer electrolytes based on li-ion exchanged microporous silicates and an ionic liquid for solid-state batteries

The addition of different zeolites (CPT, ETS-4 and ETS-10) to a SPE was studied in detail, with focus on the effect of the ion exchange in the performance and stability of the assembled batteries. It is proven that the presence of zeolites stabilizes the SPE, allowing for a higher battery stability, an effect that is further improved upon the ion exchange process.

Based on “Three-Component Solid Polymer Electrolytes Based on Li-Ion Exchanged Microporous Silicates and an Ionic Liquid for Solid-State Batteries”; João C. Barbosa et. al, Advanced Engineering Materials, 2022, 2200849.

The first focus of this work was the selection of the most suitable passive filler for the three component SPE system, being based on different zeolite structures, natural zeolite CPT and the synthetic microporous titanosilicates ETS-4 and ETS-10. Furthermore, the effect of the IE process to increase the Li^+ amount in the samples was also studied. Ion exchange using zeolites and related porous solids is widely applied for water softening, radionuclide separations, and wastewater treatments [1]. Its effectiveness depends on several factors, such as the possible exchange sites, the zeolite framework flexibility and hysteresis, and the zeolite stability. However, the cation exchange capacity of zeolite structures has never been studied in terms of applications in battery-based energy storage. This process allows to increase the selectivity and affinity of the zeolite into the desired application. Thus, the IE capability was a key factor in the zeolite choice in the framework of this work [2].

For this work, the following samples were prepared: of CPT, CPT IE, ETS-4, ETS-4 IE, ETS-10, ETS-10 IE. Each sample was named after the used zeolite. PVDF-HFP and [BMIM][SCN] were used as polymer matrix and active filler, respectively. The addition order of the components was zeolite-IL-polymer. The samples were processed by doctor blade technique and the solvent was evaporated at 120°C for 30 min. The zeolite structure was analyzed by TEM and XPS, the morphology of the samples was characterized by SEM, the structure by XRD and FTIR, the thermal properties by DSC and TGA and the mechanical properties by stress-strain tests. The electrochemical properties were assessed by impedance spectroscopy and cyclic voltammetry. Finally, batteries were evaluated in half cells. The experimental details can be found in section 3.

4.1.1. Ion exchange and morphological analysis

To assess the effect of the IE process on the zeolite structure, HRTEM images and XPS analyses were performed and the results are shown as supplementary information in Figures 6.1 and 6.2 (Annex I), respectively. Figure 6.1 shows that particles of the zeolites present a polyhedron shape, which is independent of the IE process. Oriented crystals are observed within the particles, demonstrating the presence of crystallinity, as identified also by the lattice fringes. In addition, the presence of lithium in the zeolites powder was examined by XPS. Figure 6.2 shows the XPS spectra of Li 1s from zeolites powder after the IE process, showing the presence of lithium ions in the zeolite structure, which is absent in the non-exchanged zeolites.

The ICP analysis allowed quantifying the amount of lithium trapped within the zeolite structure upon the IE process. Table 4.1 lead us to conclude that the titanosilicates ETS-4 and ETS-10 present the highest concentration of Li, which is in line with the reported literature [3]. Further, the obtained values are slightly different among the different samples due to their different structure and porous framework, leading to different electrostatic interactions between the negatively charged framework and the mobile charge-balance cations in the pores, which affect the ionic conductivity value.

Table 4.1 - Li concentration for the different porous silicates after the IE process.

Zeolites	Li concentration (±1 ppm)
CPT	22.6
ETS-4	26.0
ETS-10	28.0

The representative surface and cross-section SEM images (Figure 4.1) of the developed tricomposite (polymer, IL and zeolite) SPEs shows a compact structure for all samples, independently of zeolite type and IE.

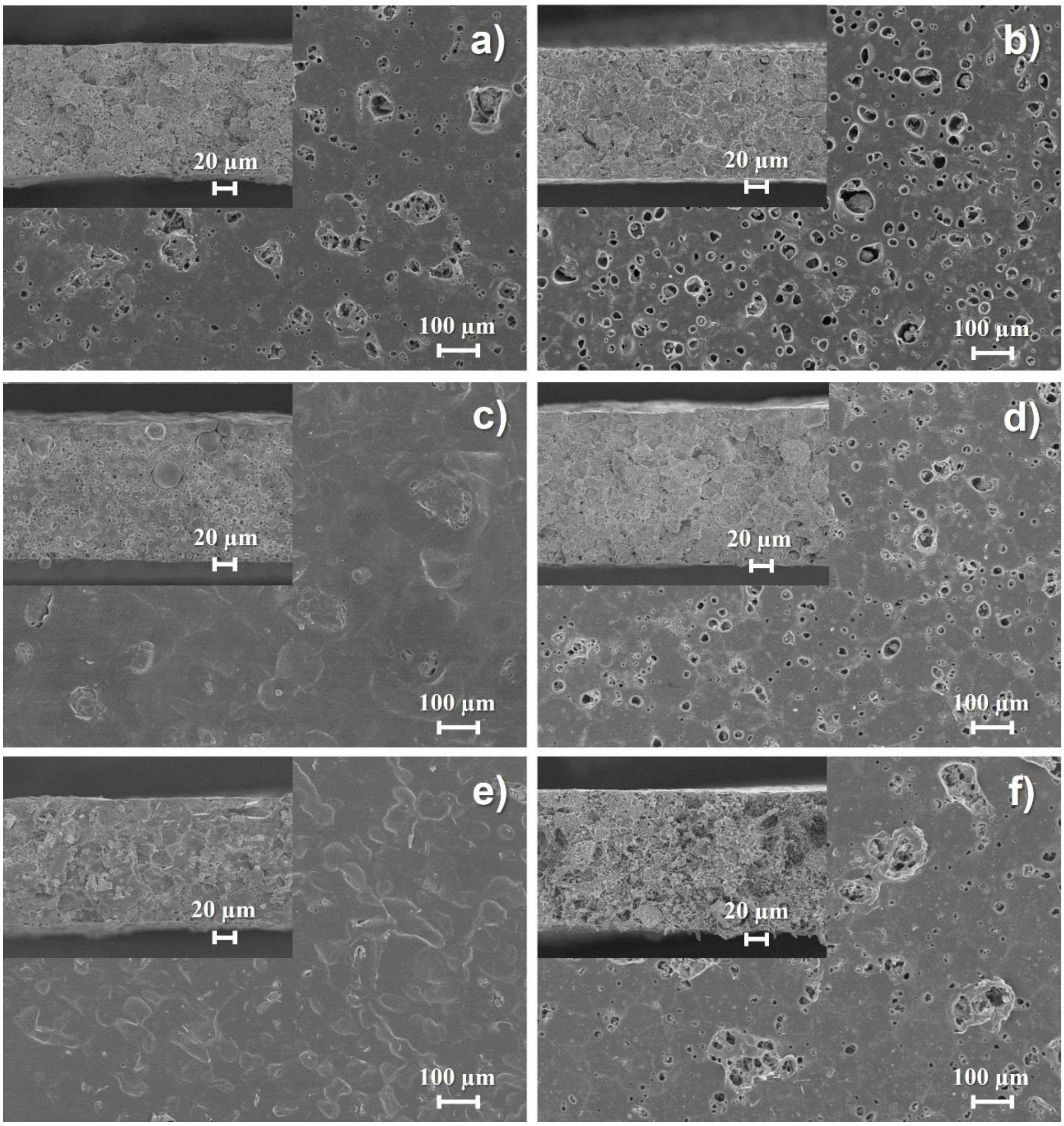

Figure 4.1 - Surface and cross-section SEM images of CPT (a), CPT IE (b), ETS-4 (c), ETS-4 IE (d), ETS-10 (e); ETS-10 IE (f).

The surface SEM images of the composites with zeolites without IE (Figures 4.1a), c) and e), reveal a homogeneous distribution of the fillers along the samples and the good compatibility of the zeolite filler within the host polymer, as demonstrated by the proper wetting of the filler by the polymer. The typical spherulite structure of pristine PVDF-HFP is not observed [4] due to the hindered crystallization in the presence of the fillers. However, the applied IE significantly increases the number of voids in the surface of the samples regardless of the zeolite type (Figures 4.1b), d) and f)). This fact is attributed to the interaction between the lithium-ion in the zeolite structure, the IL and the solvent, leading to phase separation processes in the surface of the crystallizing polymer during solvent evaporation and polymer crystallization process [5]. These voids have been shown to positively contribute to battery performance, as stated in previous works [6]. The homogeneous nature of the composites along the cross section proves the good compatibility between the three components (polymer, ionic liquid and zeolites), and the absence of spherulites is attributed to the hindered crystallization due to the high loading content [7].

Figures 4.2a and 3.2b show the XRD patterns of PVDF-HFP and the corresponding composites doped with the microporous silicates CPT, ETS-10, and ETS-4, without and with IE, respectively. Neat PVDF-HFP is characterized by peaks at $2\theta = 17.9$, 18.6, 20.1 and 26.9°, which correspond to (100) (020), (110) and (021) crystalline planes of α-PVDF, respectively [8]. Regardless of the zeolite type and IE, these peaks disappear in the composite samples and a new peak at 20.26° is observed that corresponds to the (110) (200) crystalline plane of β-PVDF [8]. The β-phase nucleation is due to electrostatic interactions (ion-dipole) between the ILs anions and cations and the PVDF chain dipoles [9]. The quantification of the β-phase is performed using FTIR spectra (Figure 4.2c).

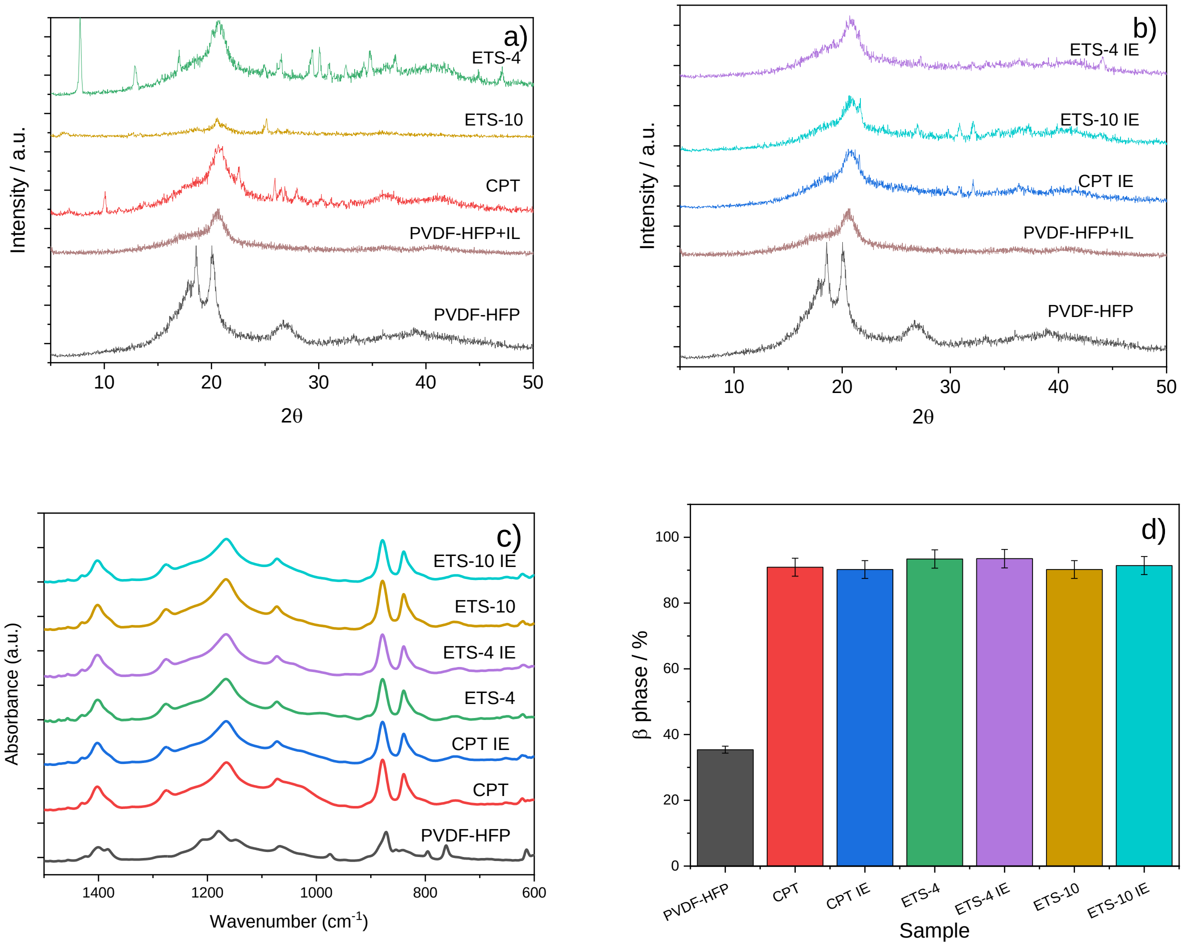

Figure 4.2 - PVDF-HFP and corresponding composites with IL and the different microporous silicates without IE (a) and with the Li-exchanged microporous silicates (b) ATR/FTIR spectra of the prepared samples (c), and respective β-phase content derived from the FTIR analysis (d).

Furthermore, other crystalline peaks are observed for the different composites associated with diffraction peaks of the porous fillers.

The degree of crystallinity was calculated for the different samples: ETS-10/ PVDF-HFP (48%) > PVDF-HFP+IL (37%) > PVDF-HFP (35%) > ETS-4/ PVDF-HFP (33 %) > CPT/ PVDF-HFP (31%), showing that different inorganic fillers have a different effect on the ratio between the crystalline and amorphous fractions in the composite, as they are determined by the specific surface interactions occurring with the different fillers [10]. Compared to PVDF-HFP, fillers such as ETS-4 and CPT lead to reduced crystallinity, whereas ETS-10 leads to higher crystallinity. Regarding the [BMIM][SCN] composite, there is no significant effect on the polymer crystallinity degree when compared to the neat PVDF-HFP. This behavior is due to the reduction of the nucleation effect caused by the high IL content (40%).

Figure 4.2b reproduces the XRD patterns of PVDF-HFP and the corresponding composites with Li-exchanged microporous silicates CPT IE, ETS-10 IE, and ETS-4 IE, respectively. In this case, the crystallinity of the composites is ordered as follows: PVDF-HFP+IL (37%) > PVDF-HFP (35%) > ETS-4 IE/ PVDF-HFP (28%) > ETS-10 IE/ PVDF-HFP (27%) > CPT IE/ PVDF-HFP (24 %). This trend shows the general tendency to lower crystallinity when compared with the Li-free composites. This difference may be due to the overall lower number of XRD peaks that belong to the inorganic filler. Another distinctive difference is in the order of crystallinity between the as-synthesized and Li-exchanged based samples in ETS-10-based composites, where the as-synthesized filler contributes to higher while the Li-exchanged leads to lower than PVDF-HFP crystallinity. This difference suggests that the alkaline cation in the porous system of the filler also influences the crystallization process of the polymer, due to the interaction with the highly polar polymer chains.

The influence of the inclusion of the IL and the different microporous silicates, without and with IE, on the samples' structure at the molecular level was determined through the analysis of the FTIR/ATR spectra (Figure 4.2c). The characteristic absorption bands of PVDF-HFP at 976, 795, 763, and 678 cm^{-1} are present independently of the sample and are attributed to the stretching of the CF_2 and CH_2 groups of the polymer chains [8]. There is a significant amount of β-phase present in the composite samples, as shown by the high intensity peak around 840 cm^{-1}. This β-phase content was quantified using equation 5 and is presented in Figure 4.2d. All samples except neat PVDF-HFP present β-phase contents above 85%, which is due to the inclusion of the [BMIM][SCN] in the structure, that changes the conformation of the PVDF-HFP chains to an all-trans (TTT) planar zigzag conformation, characteristic of the β-phase, due to the strong ion-dipole interactions [9]. This behavior is observed for PVDF-HFP+IL (β-phase = 89%) [6]. Thus, the crystallization of the polymer in the specific polar phase is fully determined by the presence of the IL and independent of the zeolite type and ion-exchange process.

4.1.2. Thermal and mechanical analysis

Thermal behaviour

DSC allowed for the evaluation of the thermal stability and phase transitions of the prepared samples. The obtained thermograms (Figure 4.3a) for the composite samples show a decrease in the endothermic peak attributed to polymer melting at about 145 °C compared to the neat PVDF-HFP sample. This peak presents also a shift to lower temperatures (125 °C) for the composite samples, an indication of the destabilization of the crystalline phase due to the ion-dipole electrostatic interaction between the [BMIM][SCN] IL and the polar polymer chains [11]. This thermal behavior is independent of the zeolite type and IE. The degree of crystallinity deduced from the DSC curves is in agreement with that observed in the XRD patterns (Figure 4.2a and 3.2b).

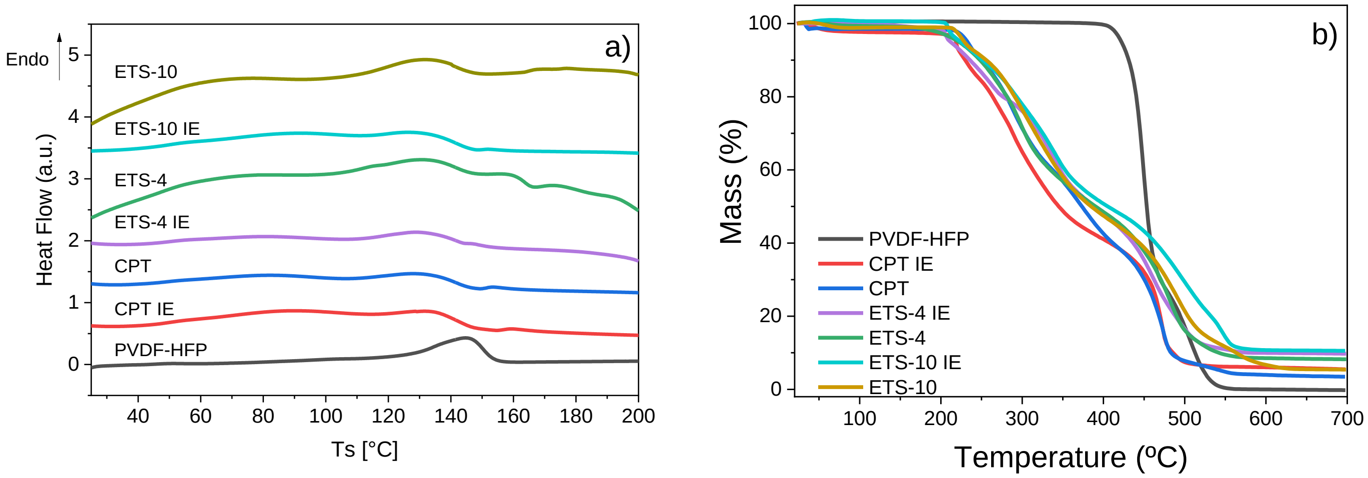

Figure 4.3 - DSC (a) and TGA (b) thermograms of the different samples.

Regarding the TGA analysis, the weight loss of the samples with increasing temperature was evaluated (Figure 4.3b). The composite samples present several weight loss steps associated with the degradation of the different components, in contrast with the pristine PVDF-HFP one, that shows a single step at around 475 °C, corresponding to the polymer degradation associated with chain stripping where scission carbon- fluorine (C-F) and carbon-hydrogen (C-H) bonds occur [12]. For the composite samples, the different weight loss steps are identified ascribed to the evaporation of water in the zeolite (80-100°C), which is a typical behavior for this kind of structures [13], the degradation of the IL (265 °C) and the different microporous solids, with ETS-10 IE being the most stable (500 °C), followed by ETS-4 IE (480°C) and CPT IE (450°C), in line with the literature [14-16]. There is a slight reduction of the degradation temperature of the samples containing zeolites subjected to the IE process, possibly due to the destabilization of the zeolite structure upon IE. It is shown that the samples show thermal stability up to above 100 °C, except for the water loss content (less than 3%) [17].

Mechanical properties

Figure 4.4 shows representative stress-strain curves for the different samples. It is observed that the addition of fillers reduces the mechanical stability of the samples when compared with neat PVDF-HFP, which presents the typical thermoplastic behavior with well-defined elastic and plastic regions [18].

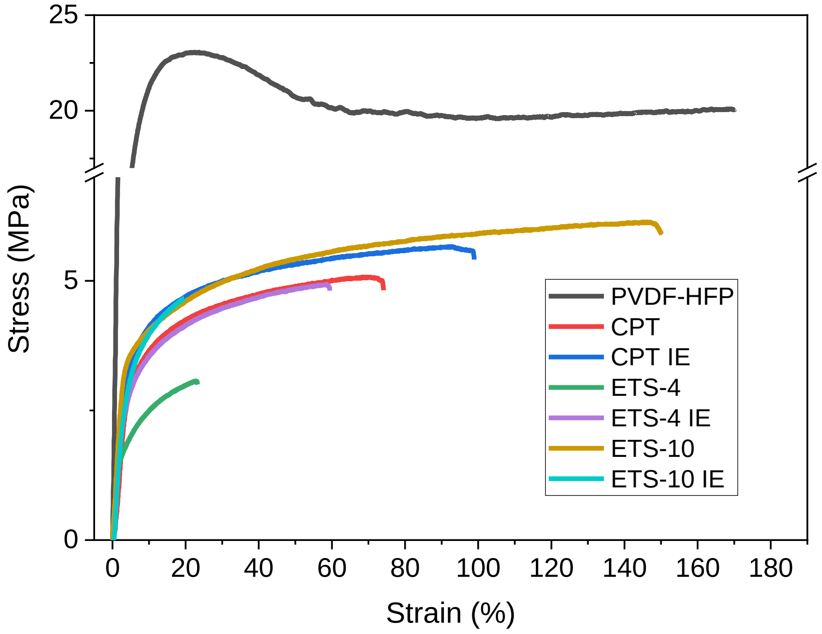

Figure 4.4 - Stress-strain mechanical response of the prepared samples.

The most relevant parameters associated with the mechanical response of the samples (Young modulus and yield stress) are presented in Table 4.2. The Young modulus was calculated by the tangent method at 3% of maximum elongation in the elastic region and is similar for all composite samples. Young modulus and yield stress values are higher than those reported for simple polymer + IL samples [19], proving the role of the zeolites as a mechanical reinforcement of the polymer matrix by restricting the polymer chain motion in a similar way for the different zeolite types [20]. Both mechanical parameters are reduced when compared to the pristine PVDF-HFP sample, due to the plasticizing effect of the [BMIM][SCN] IL [9]. This effect is dominated by the [BMIM][SCN] IL content but also modulated by the presence of the zeolite structures. It is also to notice that the IE improves the mechanical properties of the samples in the case of CPT and ETS-4. On the contrary, these properties are reduced after the IE of the ETS-10.

Table 4.2 - Values of Young modulus and yield stress for the prepared samples, calculated from the stress-strain curves.

Sample	Young Modulus ± 5% (MPa)	Yield Stress ± 5% (MPa)
PVDF-HFP	261	18
CPT	80	2.2
CPT IE	92	2.8
ETS-4	91	1.1
ETS-4 IE	98	1.9
ETS-10	95	3.3
ETS-10 IE	95	2.1

For the composite samples, despite their lower mechanical properties, they are still suitable for application in LIB SPEs [17].

4.1.3. Electrochemical analysis

The ionic conductivity is an important parameter to determine the suitability of a SPE for LIB applications and was evaluated for the different samples by electrochemical impedance spectroscopy (EIS). The obtained Nyquist plots (Figure 4.5a and 4.5b) present three characteristic regions: a semicircle in the high frequency range, corresponding to the charge transfer process, a transition region indicating the diffusion of counter-ions inside the electrode; and a straight line at lower frequencies, related to the ion diffusion process [21]. The latter is the main process occurring in the prepared samples due to the presence of mobile charge carrier species [22]. The Arrhenius plot that represents the ionic conductivity of the samples, calculated through equation 6, as a function of temperature is shown in Figures 4.5c and 4.5d. The typical decrease in the resistance upon increasing temperature, attributed both to the increase of free charges due to the dissociation of the [BMIM][SCN] and the increased mobility of the polymer chains, also supports the ion conduction process [23]. Thus, the presence of the IL mainly determines the ionic conductivity of the SPE, through the high number of charge carriers and it was observed in [19].

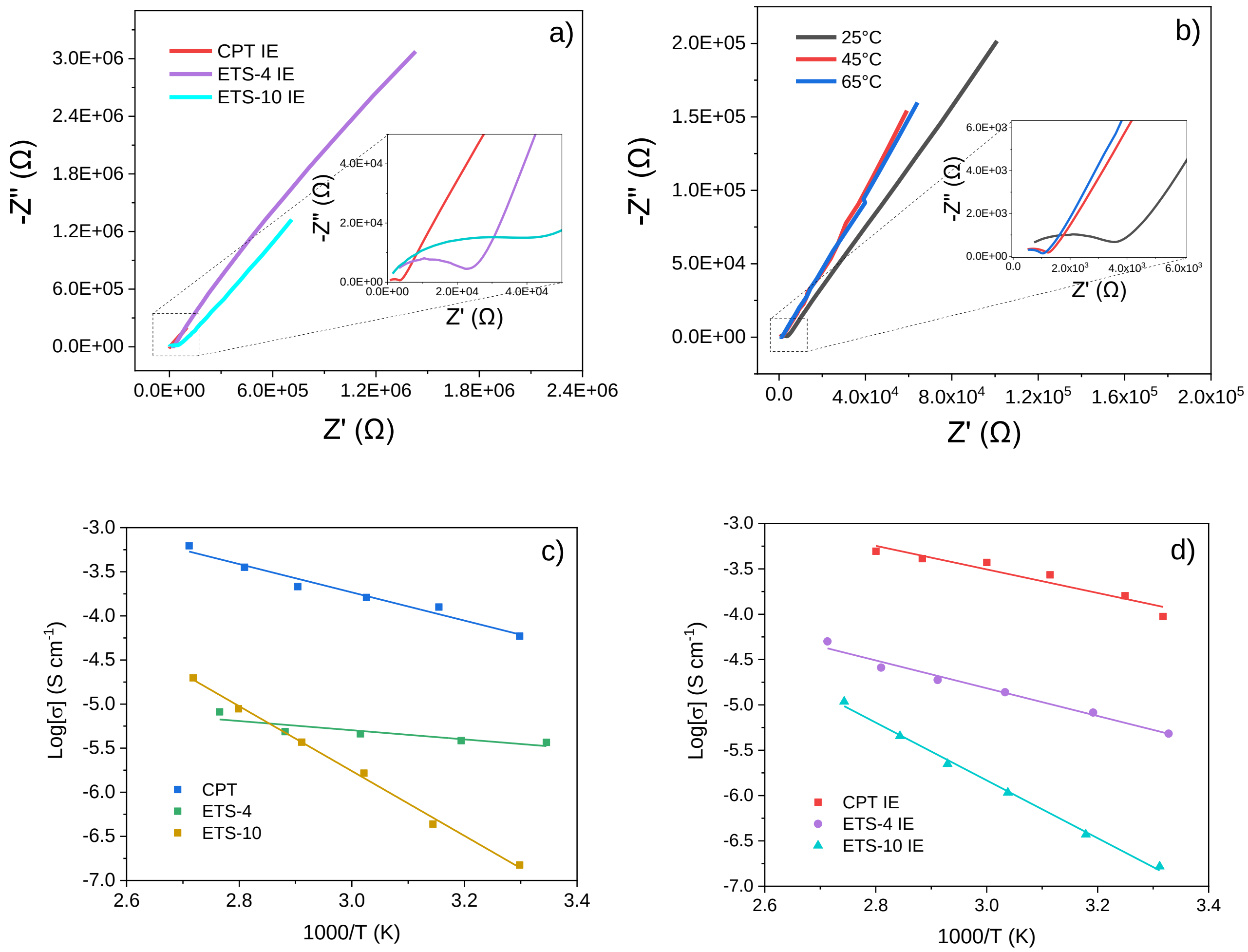

Figure 4.5 - Nyquist plot of the prepared samples with IE at 25 °C (a) and Nyquist plots of the CPT IE sample at 25 °C, 45 °C and 65 °C (b); ionic conductivity of the samples without (c) and with (d) IE as a function of temperature.

Nevertheless, the addition of zeolites causes a reduction in the ionic conductivity as a result of their interactions with the [BMIM][SCN] IL [6]. With respect to the effect of the different zeolites, the highest ionic conductivity is found for samples with CPT, followed by ETS-4 and ETS-10, which can be explained by the higher crystallinity of the ETS-10 films, as well as by the different pore system, pore size and amount of water molecules in the zeolites [24].

The structures of the microporous titanosilicates ETS-4 ($Na_9Si_{12}Ti_5O_{38}(OH)\cdot 12H_2O$) [25], ETS-10 [$(Na,K)_2Si_5TiO_{13}$] [26] and of clinoptilolite ([$Na_2,K_2,Ca)_3Al_6Si_30O_{72}\cdot 24H_2O$)] [27] led to different modulation effects of the ionic [BMIM][SCN] conductivity after their IE (Figure 4.5d). Considering that the electrostatic interaction between negatively charged framework and mobile charge-balancing cations in the pores determines the ionic conductivity in zeolites [28], the ion conductivity of the samples is increased upon IE, as demonstrated in Table 4.3.

Table 4.3 - Ionic conductivity of the samples at room temperature and 60 °C.

Sample	**Ionic Conductivity (S cm^{-1})**		**Activation Energy (kJ mol^{-1})**
	25°C	**60°C**	
CPT	5.9×10^{-5}	1.6×10^{-4}	13.3
CPT IE	9.4×10^{-5}	3.7×10^{-4}	10.8
ETS-4	3.7×10^{-6}	4.5×10^{-6}	4.3
ETS-4 IE	4.8×10^{-6}	1.4×10^{-5}	12.5
ETS-10	1.5×10^{-7}	1.6×10^{-6}	30.5
ETS-10 IE	1.7×10^{-7}	2.2×10^{-6}	26.5

Table 4.3 shows the activation energy values of the samples determined from equation 7, which are all below 23 kJ mol$^{-1.}$ The values depend on the specific zeolite and decrease in the samples with zeolites with IE. Regarding the lithium transference number, it is around 0.22 for all samples, which is within the typical range for this type of electrolytes [29].

The electrochemical stability of the samples was determined between 0 and 4.5 V at 0.01 V s^{-1} and room temperature (Figure 6.3, Annex I). Regardless of the different zeolites and IE present in the samples, no anodic and cathodic peak are observed where these samples demonstrate excellent electrochemical stability for the referred window, which is appropriate for the applied active material.
The obtained electrochemical results prove the suitability of these samples for application in LIBs.

4.1.4. Battery Performance

The samples assembled in half-cells were those with IE zeolites due to their overall improved ionic conductivity when compared with the simple zeolite samples. For comparison purposes, CPT samples without IE were also assembled in batteries. The batteries were tested for their cycle life and rate performance, as well as impedance spectroscopy before and after cycling. The obtained results are presented in figure 4.6. Figure 4.6a shows the life cycle for the composite samples with IE and for the sample with CPT at C/10 and room temperature after 50 cycles.

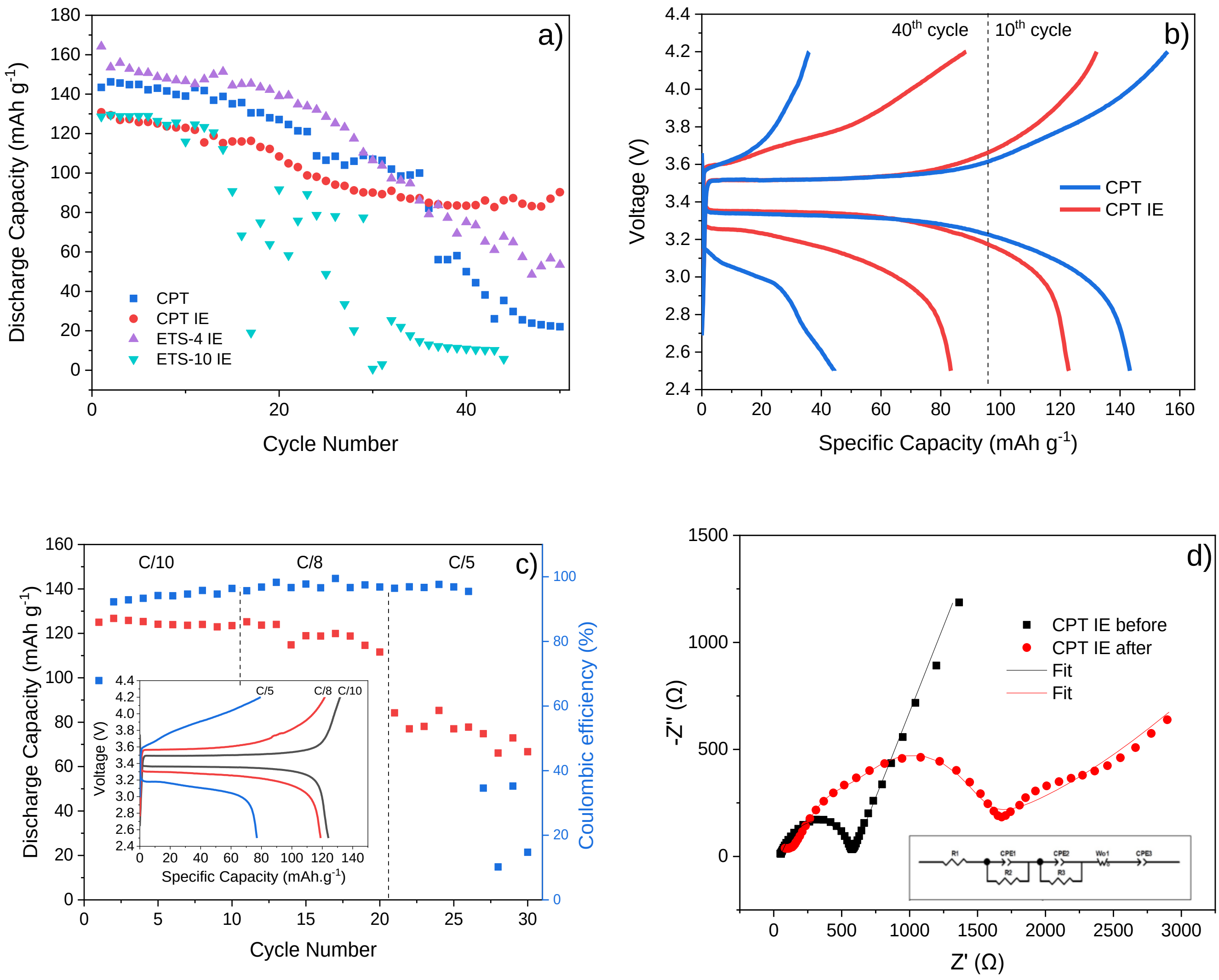

Figure 4.6 - Cycling stability of the different SPEs at C/10 (a); comparison between the charge/discharge profiles at the 10th and 40th cycles for the CPT and CPT IE samples (b); cycling performance of the CPT IE sample at different discharge rates at room temperature and respective charge/discharge profiles at the 5th cycle of each rate (c); impedance spectroscopy of the CPT IE sample before and after cycling (Inset: fitting of the equivalent circuit) (d).

Analysis of Figure 4.6a allows inferring that despite the higher initial discharge capacity of the ETS-4 IE sample due to the high cationic conductivity of this zeolite, this sample does not present proper cycling stability, with almost 50% of capacity loss after 30 cycles. On the other hand, the CPT IE sample is the most stable one, with an initial discharge capacity of about 130 mAh g^{-1} at C/10, and a capacity retention of 70% after 50 cycles, with a more stable behavior than the CPT sample. This sample has a higher initial discharge capacity (about 140 mAh g^{-1}), but the destabilization of the structure after a prolonged number of cycles leads to a significantly higher loss of capacity when compared with the CPT IE sample after 40 cycles (45 and 85 mAh g^{-1} for CPT and CPT IE, respectively), meaning that the IE has a positive effect on the stabilization of the SPE structure. It is also observed that IE improves the discharge capacity value taking into account the ionic conductivity value. Furthermore, the zeolite type affects battery performance due to its morphology and degree of crystallinity.

The charge-discharge profiles of these batteries present the typical voltage plateau between 3.3 and 3.5 V, corresponding to the insertion and extraction of lithium ions in the structure of the LFP cathode [30] (Figure 4.6b). The CPT IE SPE also shows a good rate performance, particularly at C/10 and C/8 rates, independently of the cycle number, with almost no loss of capacity, as denoted in Figure 4.6c. Further, it shows a high coulombic efficiency, up to 95%, except for the first cycles, in which the system is not fully activated and the interfaces are not properly formed [31]. In addition, this sample shows a discharge capacity value of ~80 mAh g^{-1} at C/5 rate and room temperature. The charge/discharge profile shown in the inset of Figure 4.6c highlights the loss of capacity associated with the increasing discharge rate, as a result of the cathode polarization [32].

The impedance spectroscopy analysis allows to better understand the battery performance through the conduction mechanisms associated to the charge and discharge processes. Figure 4.6d shows the Nyquist plot for the CPT IE battery before and after cycling, with the semicircle representing the overall resistance at high frequencies, the line in the low frequency region associated with the Li^+ conduction process, and the capacitance element describing the differential intercalation of the LFP active material. This behavior is characterized by the equivalent circuit composed by the overall resistance (R_T) that is the sum of the ohmic resistances (R_1), the contact film resistance (R_2) and resistance contributions from the charge-transfer reaction resistance (R_3) (inset of figure 4.6d).

A significant increase in the overall resistance is observed after cycling (from 600 to 1700 Ω), which is explained by the formation of the solid electrolyte interface layer during cycling [33].

The obtained results allow to conclude that the IE in zeolite structures has a positive effect in the battery performance and stability. This performance demonstrated that this technology is promising for application in LIBs as shown in Table 4.4 for related three component SPEs.

Table 4.4 - Comparison between the obtained results in this work and those obtained in the literature.

Polymer	**Fillers**	**Conductivity (S cm^{-1})**	**Battery capacity of LFP batteries (mAh g^{-1})/C-rate**	**Ref.**
PVDF-HFP	IL@UiO-67	4.3×10^{-4} (25°C)	118 (1C); 25°C	[34]
PVDF-HFP	LiTFSI, LLZTO	8.80×10^{-5} (25°C)	158.7 (C/10); 25°C	[35]
PVDF	$LiClO_4$, LLTO	5.8×10^{-4} (25°C)	152 (C/5); 25°C	[36]
PEO	SSZ-13, LiTFSI	5.34×10^{-2} (70°C)	154 (C/10); 60°C	[37]
PVDF-HFP	CPT IE, [BMIM] [SCN]	5.9×10^{-5} (25°C)	130 (C/10); 25°C	This work

The ionic conductivity value obtained in this work is better than those reported in the literature at room temperature and the cycling performance observed at C/5-rate is excellent. Most of the literature reports on battery results at high temperatures, which has limitations to practical applications. This work shows the benefit of the two filler approach, which allows for a better cycling stability of the SPE structure upon the addition of the microporous silicate, when compared with similar samples without this filler [19], and an increase in the ionic conductivity provided by the IL. Thus, this means that combining two complementary fillers is critical to achieve high stability and high performance LIBs [38]. This new approach including ion-exchanged of zeolite structures has proven to be excellent for the next generation of SPEs for high-performance solid-state LIBs, as the increase of lithium ions in the structure of the SPE allows for a better conduction mechanism in the battery, which increases its performance, the zeolites also improving SPE mechanical and thermal stability with respect to the SPE prepared just in IL.

4.1.5. Conclusion

Three composite SPEs were prepared by doctor blade technique, using different microporous silicates (clinoptilolite, ETS-4 and ETS-10) and IL ([BMIM][SCN]) as fillers. The prepared samples were characterized at the morphological, thermal, mechanical, and electrochemical levels. In addition, the influence of the ion-exchanged porous structures on the SPE properties was evaluated. The composite samples show a homogeneous and compact nature, with voids just in the surface of the samples. The IE of the microporous silicates tends to reduce the crystallinity of the samples (from 48% to 27% in the ETS-10 sample, and from 31% to 24% in the CPT sample). There are no significant changes on the thermal and mechanical properties, with suitable values for application in LIBs (up to 98MPa for Young modulus, regardless of the porous solid and IE process). The ionic conductivity is improved with the IE process (from 5.9×10^{-5} to 9.4×10^{-4} S cm^{-1} at room temperature for the CPT sample) in the samples through the increase in the number of lithium ions in the structure. Consequently, the batteries containing ion-exchanged zeolite or microporous titanosilicates show better performance results compared to those containing the same porous materials without IE. In particular, the CPT IE sample presents the best performance and stability behavior, with an initial discharge capacity of 130 mAh g^{-1} at C/10 rate, and a capacity retention of 70% after 50 cycles. This work demonstrates the relevance of combining two complementary fillers in order to improve their individual properties. In this particular case, the microporous silicates have a modulation effect on the composite properties, stabilizing the SPE structure and improving the overall cycling stability when compared with samples without zeolites. The application of IE process increases the number of Li^+ charges, improving the overall battery performance. These results show the potential of the IE process in the next generation of solid-state LIBs.

4.1.6. References

1. Townsend, R.P. and E.N. Coker, *Chapter 11 Ion exchange in zeolites*, in *Studies in Surface Science and Catalysis*, H. van Bekkum, et al., Editors. 2001, Elsevier. p. 467-524.
2. Sherry, H.S., *The Ion-Exchange Properties of Zeolites. I. Univalent Ion Exchange in Synthetic Faujasite.* The Journal of Physical Chemistry, 1966. **70**(4): p. 1158-1168.
3. Oleksiienko, O., C. Wolkersdorfer, and M. Sillanpää, *Titanosilicates in cation adsorption and cation exchange – A review.* Chemical Engineering Journal, 2017. **317**: p. 570-585.
4. Ma, W., H. Yuan, and X. Wang, *The Effect of Chain Structures on the Crystallization Behavior and Membrane Formation of Poly(Vinylidene Fluoride) Copolymers.* Membranes, 2014. **4**(2): p. 243-256.
5. Sousa, R.E., et al., *Microstructural variations of poly(vinylidene fluoride co-hexafluoropropylene) and their influence on the thermal, dielectric and piezoelectric properties.* Polymer Testing, 2014. **40**: p. 245-255.
6. Barbosa, J.C., et al., *High-Performance Room Temperature Lithium-Ion Battery Solid Polymer Electrolytes Based on Poly(vinylidene fluoride-co-hexafluoropropylene) Combining Ionic Liquid and Zeolite.* ACS Applied Materials & Interfaces, 2021. **13**(41): p. 48889-48900.
7. Lopes, A.C., et al., *Influence of zeolite structure and chemistry on the electrical response and crystallization phase of poly(vinylidene fluoride).* Journal of Materials Science, 2013. **48**(5): p. 2199-2206.
8. Martins, P., A.C. Lopes, and S. Lanceros-Mendez, *Electroactive phases of poly(vinylidene fluoride): Determination, processing and applications.* Progress in Polymer Science, 2014. **39**(4): p. 683-706.
9. Correia, D.M., et al., *Ionic Liquid Cation Size-Dependent Electromechanical Response of Ionic Liquid/Poly(vinylidene fluoride)-Based Soft Actuators.* The Journal of Physical Chemistry C, 2019. **123**(20): p. 12744-12752.
10. Jing, M., et al., *Enhancing crystallization and mechanical properties of poly(lactic acid)/milled glass fiber composites via self-assembled nanoscale interfacial structures.* Composites Part A: Applied Science and Manufacturing, 2019. **117**: p. 219-229.
11. Meira, R.M., et al., *Ionic-Liquid-Based Electroactive Polymer Composites for Muscle Tissue Engineering.* ACS Applied Polymer Materials, 2019. **1**(10): p. 2649-2658.
12. Polat, K., *Energy harvesting from a thin polymeric film based on PVDF-HFP and PMMA blend.* Applied Physics A, 2020. **126**(7): p. 497.

13. Stanciakova, K., et al., *Understanding Water–Zeolite Interactions: On the Accuracy of Density Functionals.* The Journal of Physical Chemistry C, 2021. **125**(37): p. 20261-20274.
14. Pavel, C.C., et al., *Study of the thermal dehydration of metal-exchange ETS-10 titanosilicate*, in *Studies in Surface Science and Catalysis*, J. Čejka, N. Žilková, and P. Nachtigall, Editors. 2005, Elsevier. p. 805-812.
15. Marathe, R.P., et al., *Effect of Ion Exchange and Dehydration Temperature on the Adsorption and Diffusion of Gases in ETS-4.* Industrial & Engineering Chemistry Research, 2004. **43**(17): p. 5281-5290.
16. Mansouri, N., et al., *Porosity, characterization and structural properties of natural zeolite - Clinoptilolite - As a sorbent.* Environment Protection Engineering, 2013. **39**: p. 139.
17. Barbosa, J.C., et al., *Recent Advances in Poly(vinylidene fluoride) and Its Copolymers for Lithium-Ion Battery Separators.* Membranes, 2018. **8**(3).
18. Costa, C.M., et al., *Microscopic origin of the high-strain mechanical response of poled and non-poled poly(vinylidene fluoride) in the β-phase.* Journal of Non-Crystalline Solids, 2008. **354**(32): p. 3871-3876.
19. Serra, J.P., et al., *Ionic liquid based Fluoropolymer solid electrolytes for Lithium-ion batteries.* Sustainable Materials and Technologies, 2020. **25**: p. e00176.
20. Metın, D., et al., *The effect of interfacial interactions on the mechanical properties of polypropylene/natural zeolite composites.* Composites Part A: Applied Science and Manufacturing, 2004. **35**(1): p. 23-32.
21. Chang, B.-Y. and S.-M. Park, *Electrochemical Impedance Spectroscopy.* Annual Review of Analytical Chemistry, 2010. **3**(1): p. 207-229.
22. Park, M., et al., *A review of conduction phenomena in Li-ion batteries.* Journal of Power Sources, 2010. **195**(24): p. 7904-7929.
23. Ribeiro, C., et al., *Electroactive poly(vinylidene fluoride)-based structures for advanced applications.* Nature Protocols, 2018. **13**(4): p. 681-704.
24. Shi, H., J. Zhang, and J. Li, *The effect of guest cations on proton conduction of LTA zeolite.* RSC Advances, 2021. **11**(10): p. 5393-5398.
25. Cruciani, G., et al., *Rietveld refinement of the zorite structure of ETS-4 molecular sieves.* Microporous and Mesoporous Materials, 1998. **21**(1): p. 143-153.
26. Anderson, M., et al., *Structure of the microporous titanosilicate ETS-10.* Nature, 1994. **367**(6461): p. 347-351.
27. *Clinoptilolite*, in *Encyclopedia Britannica*. 2018.
28. Kelemen, G. and G. Schön, *Ionic conductivity in dehydrated zeolites.* Journal of Materials Science, 1992. **27**(22): p. 6036-6040.
29. Pożyczka, K., et al., *IONIC CONDUCTIVITY AND LITHIUM TRANSFERENCE NUMBER OF POLY(ETHYLENE OXIDE):LiTFSI SYSTEM.* Electrochimica Acta, 2017. **227**: p. 127-135.
30. Gören, A., et al., *Influence of Solvent Evaporation Rate in the Preparation of Carbon-Coated Lithium Iron Phosphate Cathode Films on Battery Performance.* Energy Technology, 2016. **4**(5): p. 573-582.
31. Xiao, Y., et al., *Understanding interface stability in solid-state batteries.* Nature Reviews Materials, 2020. **5**(2): p. 105-126.
32. Ram, P., et al., *Improved performance of rare earth doped LiMn2O4 cathodes for lithium-ion battery applications.* New Journal of Chemistry, 2016. **40**(7): p. 6244-6252.
33. Guo, J., et al., *Cyclability study of silicon–carbon composite anodes for lithium-ion batteries using electrochemical impedance spectroscopy.* Electrochimica Acta, 2011. **56**(11): p. 3981-3987.

34. Liu, L. and C. Sun, *Flexible Quasi-Solid-State Composite Electrolyte Membrane Derived from a Metal-Organic Framework for Lithium-Metal Batteries.* ChemElectroChem, 2020. **7**(3): p. 707-715.
35. Yu, Y., et al., *Zwitterion-containing electrolytes with semi–crystalline PVDF-Co-HFP as a matrix for safer lithium-ion batteries.* Journal of Molecular Liquids, 2019. **282**: p. 340-346.
36. Abdelkareem, M.A., et al., *Environmental aspects of fuel cells: A review.* Science of The Total Environment, 2021. **752**: p. 141803.
37. Jamal, H., et al., *Enhancement of the ionic conductivity of a composite polymer electrolyte via surface functionalization of SSZ-13 zeolite for all-solid-state Li-metal batteries.* Journal of Materials Chemistry A, 2021. **9**(7): p. 4126-4137.
38. Barbosa, J.C., et al., *Metal–organic frameworks and zeolite materials as active fillers for lithium-ion battery solid polymer electrolytes.* Materials Advances, 2021. **2**(12): p. 3790-3805.

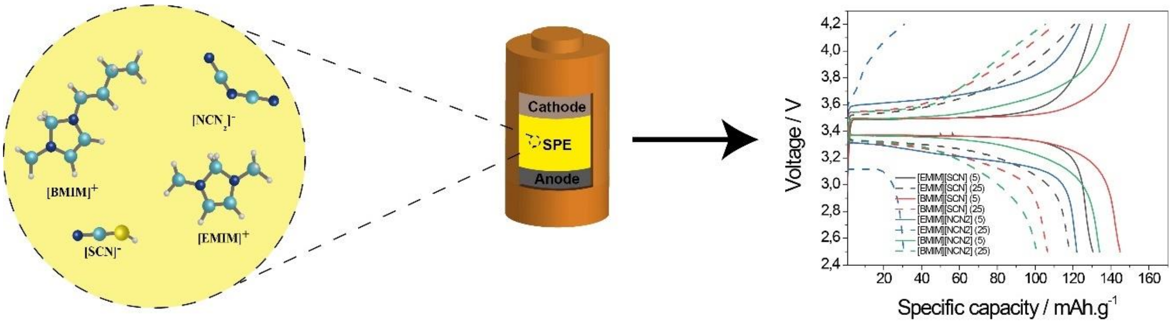

4.2. Influence of ionic liquid characteristics in the performance of ternary solid polymer electrolytes with poly(vinylidene fluoride-co-hexafluoropropylene) and zeolite.

Several ILs were evaluated ([EMIM][SCN], [BMIM][SCN], [EMIM][$N(CN)_2$] and [BMIM][$N(CN)_2$]) in order to assess the effect of the cation chain length and anion type in the SPE performance. It was concluded that longer cation chains improve the battery capacity but decrease the cycling stability. Similarly, smaller cations contribute to improved battery cycling stability.

Based on "Influence of ionic liquid characteristics on the performance of ternary solid polymer electrolytes with poly(vinylidene fluoride-co-hexafluoropropylene) and zeolite"; João C. Barbosa et. al, published on Journal of Power Sources, 2023. 572: p. 233095

The active filler plays a critical role in the operation of SPEs as it is the main contributor to the ion conductivity during the LIB cycling process. Thus, the choice of an adequate active filler, that combines the good conduction properties with high compatibility with both the polymer matrix and the active filler, has a significant importance in the SPE development. In this work, the effect of different ILs in the SPE properties was studied with the purpose to find the most suitable candidate to the proposed system. In this regard, four highly conductive ILs combining two different anions ([SCN] and [N(CN)$_2$]) with different chain length cations ([EMIM] and [BMIM]) were chosen and studied. The main properties of the used ILs are presented in table 4.5.

Table 4.5 – Main properties of the ILs (provided by the supplier).

IL	Viscosity (cp)	σ_i (mS cm^{-1}) at room temperature	Molecular Weight (g.mol^{-1})	Density (g cm^{-3})
[EMIM][SCN]	24.7	17.8	169.25	1.12
[BMIM][SCN]	35.9	8.98	197.3	1.07
[EMIM][N N(CN)$_2$]	14.6	17.7	177.21	1.1
[BMIM][N N(CN)$_2$]	33.4	9.54	205.26	1.06

For this work, the following samples were prepared: PVDF-HFP/CPT/[EMIM][SCN], PVDF-HFP/CPT/[BMIM][SCN], PVDF-HFP/CPT/[EMIM][N(CN)$_2$] and PVDF-HFP/CPT/[BMIM][N(CN)$_2$]. PVDF-HFP and CPT were used as polymer matrix and passive filler, respectively. The addition order of the components was zeolite-IL-polymer. The samples were processed by doctor blade technique and the solvent was evaporated at 120°C for 30 min. The morphology of the samples was characterized by SEM and AFM, the structure by XRD and FTIR, the thermal properties by DSC and TGA and the mechanical properties by stress-strain tests. The electrochemical properties were assessed by impedance spectroscopy and cyclic voltammetry. Finally, batteries were evaluated in half cells. The experimental details can be found in section 3.

4.2.1. Morphological, structural and chemical properties

The SEM images show a homogeneous filler distribution in the host polymer matrix, indicating good compatibility between both these components. A clear influence of the different ILs in the samples' microstructure is observed (Figure 4.7). The cation size affected the surface porosity of the samples. While the ILs including the smaller cation (EMIM$^+$) yielded less porous composite films (Figures 4.7a and 4.7c), the ILs incorporating the larger cation (BMIM$^+$) produced more voids in the samples' surface (Figures 4.7b and 4.7d). These voids are typical for this kind of composites, as reported previously [1].

They were attributed to the reduced surface interaction between the CPT zeolite and the PVDF-HFP-IL solution [1]. The absence of spherulites is correlated with the high loading of fillers in the samples, which hinders the polymer crystallization process [2]. As SEM analysis of a PVDF-HFP sample doped solely with CPT demonstrated good compatibility and adequate dispersion of CPT within the PVDF-HFP matrix [1], proving the suitability of this filler to SPE development. The cross-section images of the samples reveal a more compact film for the PVDF-HFP/CPT/[BMIM][SCN] composite (inset in Figure 4.7b). The other samples present a less compact film structure as a consequence of the different ion-dipole interactions between the IL fillers and the polymer matrix. The more compact morphology and the presence of voids on the surface of the samples containing [BMIM]$^+$ cation can be related to the high viscosity of these ILs, as well as its higher size, compared with those with [EMIM]$^+$ (Table 4.5), since the solution viscosity is known to influence the porosity of the sample through the solvent evaporation process [3].

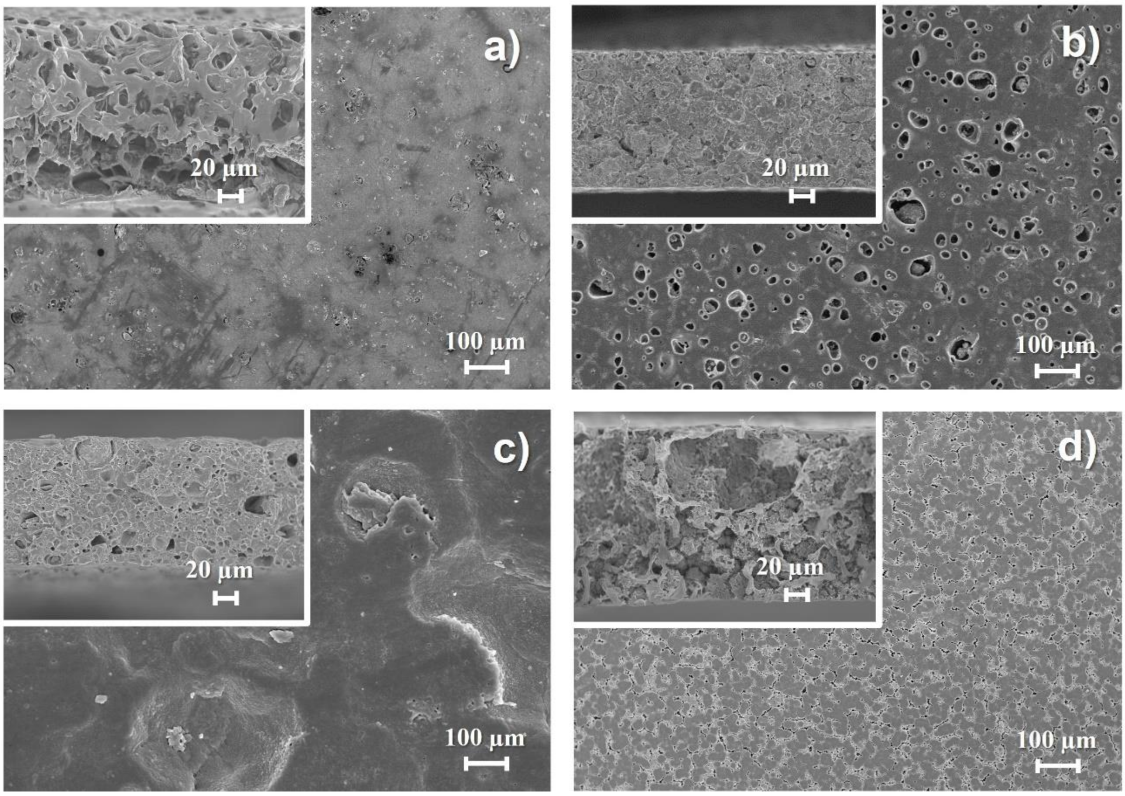

Figure 4.7 – Surface and cross-section (inset) SEM images of the PVDF-HFP/CPT/X composite samples: X=[EMIM][SCN] (a), X= [BMIM][SCN] (b), X=[EMIM][$N(CN)_2$] (c) and X= [BMIM][$N(CN)_2$] (d).

Complementary to SEM images, the AFM analysis enables a better understanding of the samples' surface characteristics, which are critical for a better interfacial compatibility between the SPE and the electrodes. As noted above for the SEM images (Figure 4.7), the AFM data also demonstrate that the IL type affects the surface morphology (Figure 4.8). All the samples exhibit a relatively smooth surface with roughness values of 11.34, 52.89, 34.79 and 18.49 nm for the PVDF-HFP/CPT/X samples with X=[EMIM][SCN], [BMIM][SCN], [EMIM][N(CN)$_2$] and [BMIM][N(CN)$_2$], respectively. The increase in roughness can have a positive effect on the SPE, as it allows for a larger surface area and more possible contact points with the electrodes, increasing the interfacial compatibility between them [4].

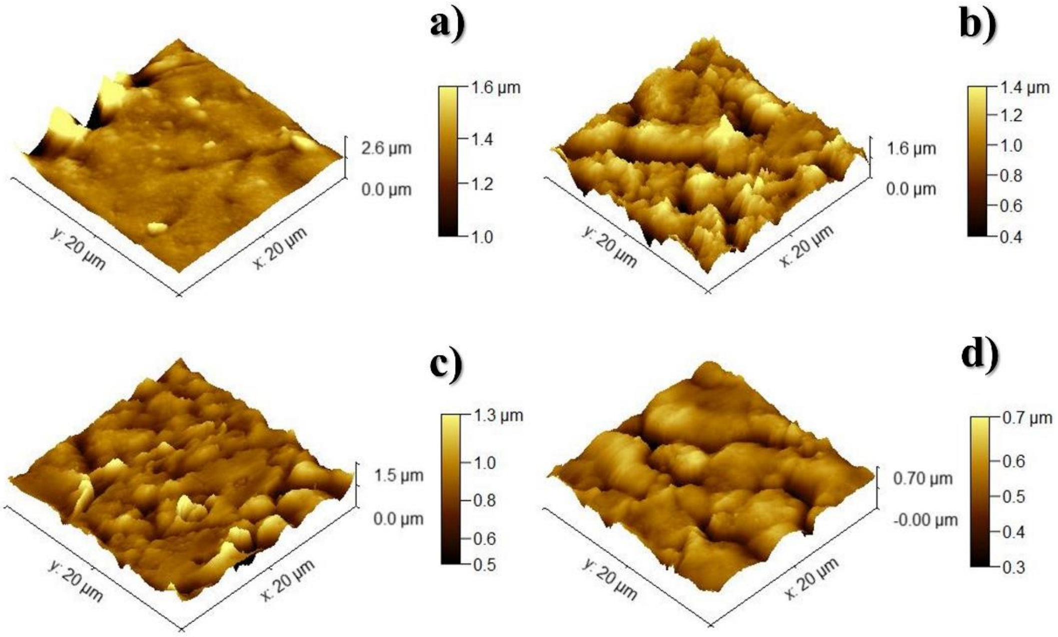

Figure 4.8 – AFM images for the PVDF-HFP/CPT/X composite samples: X=[EMIM][SCN] (a), X= [BMIM][SCN] (b), X= [EMIM][N(CN)$_2$] (c) and X= [BMIM][N(CN)$_2$] (d).

Figure 4.9a shows the XRD patterns of the PVDF-HFP/CPT/X samples together with a composite sample devoid of IL, i.e., PVDF-HFP/CPT. All diffractograms contain sharp peaks characteristic of the zeolite and broad reflections typical of the polymer.

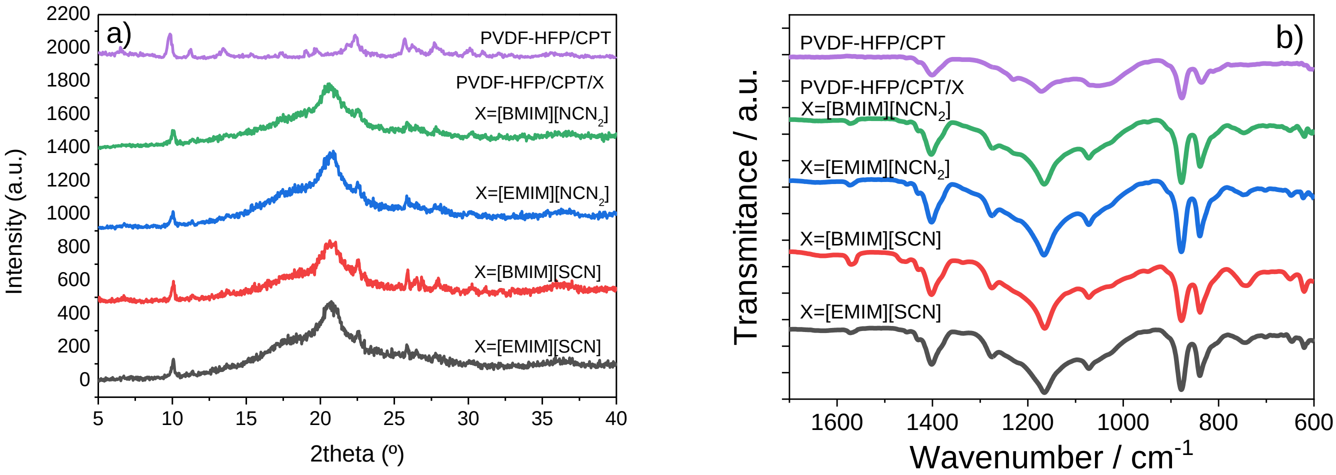

Figure 4.9 – XRD patterns (a) and ATR/FTIR spectra (b) of the PVDF-HFP/CPT/X composite samples compared with the PVDF-HFP/CPT sample.

Due to the high IL content (40 wt.%) in the PVDF-HFP/CPT/X samples, the crystalline peaks of PVDF-HFP expected at 2θ = 17.9, 18.6, 20.1 and 26.9°, are not observed [5]. Furthermore, the zeolite peak at 10° indicates that the structure of the inorganic filler remained stable after the preparation of the composite. However, there are distinct differences between the crystallinity of the four PVDF-HFP/CPT/X composites. Considering that the polymer/zeolite and polymer/IL weight ratios are similar for all samples (cf. experimental section) the difference in the degree of crystallinity calculated with equation 4 ([EMIM][SCN] (26.5%) < [BMIM][N(CN)2] (29.3 %) < [EMIM][N(CN)2] (30.7%) < [BMIM][SCN] (33.2%)) should originate from the specific interactions zeolite-polymer-IL. In this ternary system, the higher crystallinity is favored by specific combinations of cationic and anionic parts of the ionic liquid. Thus, composites containing [BMIM]$^+$ and [SCN]$^-$ or [EMIM]$^+$ and [N(CN)2]$^-$ tend to show higher crystallinity than those composed of [BMIM]$^+$ and [N(CN)2]$^-$ or [EMIM]$^+$ and [SCN]$^-$, respectively. The interaction between the ILs and the zeolite has a significant effect in the crystallinity of the polymer matrix. Further, free ILs in the SPE structure lead to more significant nucleation effects, resulting in a higher polymer crystallization [6]. The interaction between the IL and the zeolite, tends to reduce this nucleation effect of the polymer chains, as the nucleation is inhibited in both zeolite and IL due to their combined overall larger size of the zeolite+IL system and reduced interactions with the polymer chains [1]. This means that the lower crystallinity samples ([EMIM][SCN] and [BMIM][NCN2]) are those corresponding to the one with the higher affinity between the IL and the zeolite.

ILs are known to have a significant influence on polymer conformation at a molecular level due to the strong ionic interaction with the polar chains of PVDF and co-polymers [7]. Thus, in order to assess this effect in the present samples, ATR/FTIR analysis was carried out, and the results are reproduced in Figure 4.9b. The absorption bands corresponding to the stretching vibrations of the CF_2 and CH_2 groups of the polymer chains [5] are observed at 976, 795, 763, and 678 cm^{-1} for all samples. The typical band corresponding to the Al-O bonds in the CPT zeolite is also discerned at 1087 cm^{-1} [8]. There are no presence of the characteristic band of the DMF (1670 cm^{-1} corresponding to C=O stretching vibration bond), which indicates the complete evaporation of the solvent during the production of the samples [9]. The characteristic β phase band at 840 cm^{-1} is indicative of a high content of this polymer conformation in the samples. This result was confirmed through the application of equation 5 to obtain the electroactive phase content. The results, presented in Table 4.6, show that the β phase content is well above 80% for all samples due to the low solvent evaporation temperature, which in the present case was the main factor affecting polymer crystallization in the polar phase (also proved comparing with the PVDF-HFP/CPT sample) [10]. This is also corroborated by a slight increase of the polar phase content for the ILs including cations with longer chains ($[BMIM]^+$ > $[EMIM]^+$), suggesting stronger ion-dipole interactions with the increase in the cation chain size [7].

4.2.2. Thermal and mechanical analysis

The DSC thermograms reproduced in Figure 4.10a reveal that all the composite samples present a single endothermic peak that corresponds to the polymer melting.

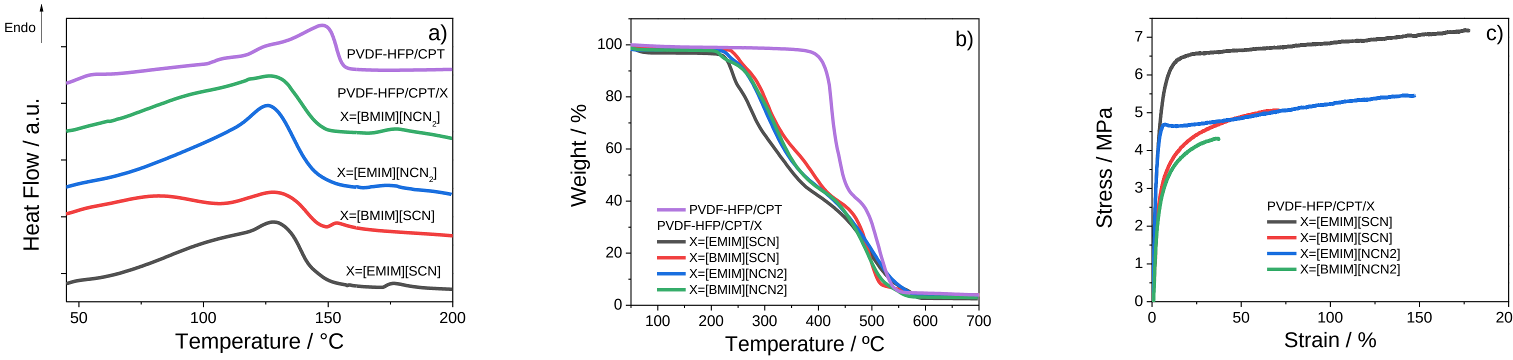

Figure 4.10 – DSC thermograms (a), TGA curves (b) and stress-strain curves (c) of the PVDF-HFP/CPT/X composites.

In all the cases the value is below the 145 °C reported for pristine PVDF-HFP [1]. This downshift is associated with the addition of the IL, which caused the partial breakdown of the crystalline polymer phase through the strong ion-dipole electrostatic interactions established between the IL and the polar polymer matrix [11]. Regarding the degree of crystallinity deduced from DSC data, these values follow the same trend observed in the XRD patterns where the degree of crystallinity depends on the anion and cation present in the ILs, differing only at the crystallinity degree absolute value. The derived values are driven by the presence of CPT and IL in the samples, which affect the nucleation and growth kinetics of the polymer during processing, as reported in [1].

Table 4.6 – β-phase content, crystallinity degree (calculated from DSC), Young modulus and yield stress for the different PVDF-HFP/CPT/X composites.

Sample	β-phase ± 3 (%)	Crystallinity degree ± 2 (%)	Young Modulus ± 5 (MPa)	Yield Stress ± 5 (MPa)
[EMIM][SCN]	87.5	13	140	3.8
[BMIM][SCN]	82.6	23	87	2.3
[EMIM][N(CN)$_2$]	90.3	16	131	3.7
[BMIM][N(CN)$_2$]	86.9	12	80	2.2
PVDF-HFP [1]	89.0	23	638	20.1

The TGA thermograms of the sample (Figure 4.10b) are characterized by the degradation steps corresponding to PVDF-HFP, CPT, and the IL (between 250 and 280°C depending on the IL) (Figure 4.10b). The onset of CPT degradation (450°C) [12] occurs at lower temperatures for the ternary composite samples (thus containing IL) than for the binary composite PVDF-HFP/CPT for which the CPT degradation was reported at 475°C) [13]. There is a clear influence of the IL addition on the polymer thermal stability of the samples. In fact, the presence of the different ILs led to a significantly decrease of the degradation temperature of the polymer (between 280 and 320 °C). This effect is attributed to the scission of carbon-fluorine (C-F) and carbon-hydrogen (C-H) bonds [13], resulting from the degradation of the ILs, thus proving the strong interaction between the guest fillers and the host polymer matrix. Moreover, these data support that IL cations with longer chains lead to a slight increase in the thermal stability for a fixed anion.

Regarding mechanical properties, stress-strain curves of the different samples are shown in Figure 4.10c. The presence of the different ILs and CPT significantly altered the typical thermoplastic behavior of PVDF-HFP [1]. The calculated Young modulus and yield stress of the composite samples were calculated and are given in Table 4.6. Close analysis of the different Young modulus values allows concluding that it increases for ILs with smaller cation chains (EMIM), indicating the stronger plasticizing effect exerted by cations comprising longer chains [7]. Complementary, a slight reduction in the Young modulus seems to occur for the [N(CN)$_2$]$^-$ anion when compared to the [SCN]$^-$ one, for a fixed cation. The yield strength values accompany this tendency, suggesting that the size of the ILs allows tuning the mechanical behavior to the samples.

4.2.3. Electrochemical analysis

The ionic conductivity is an important parameter for the evaluation of the potential of a SPE for battery applications [14]. In this regard, the room temperature Nyquist plots of the prepared samples are presented in Figure 4.11. These Nyquist plots are characterized by three well defined regions: a semicircle located in the high-frequency range which corresponds to the charge transfer process, a transition controlled by the diffusion of counter-ions in the electrode, and a straight line at lower frequencies representing the diffusion process [15]. In the present case the most important conduction mechanism corresponds to the diffusion process due to the high number of charge carriers provided by the ILs, meaning that the semicircle is barely visible in the Nyquist plots. These regions are temperature-dependent, with the diffusion process becoming more relevant with increasing temperature when compared with the charge transfer process [16], resulting in lower resistance due to higher polymer chain mobility. The use of CPT within the ternary composite leads to an increase of the overall resistance due to its interactions with the ILs [1]. The presence of the different ILs as high mobility charge carriers makes ion diffusion the main mechanism for ion conduction in these systems [17]. The use of different ILs shows that longer chain cations lead to lower overall resistance in the composite samples as proven by the smaller semicircles in the [BMIM][SCN]- and [BMIM][N(CN)$_2$]-containing samples.

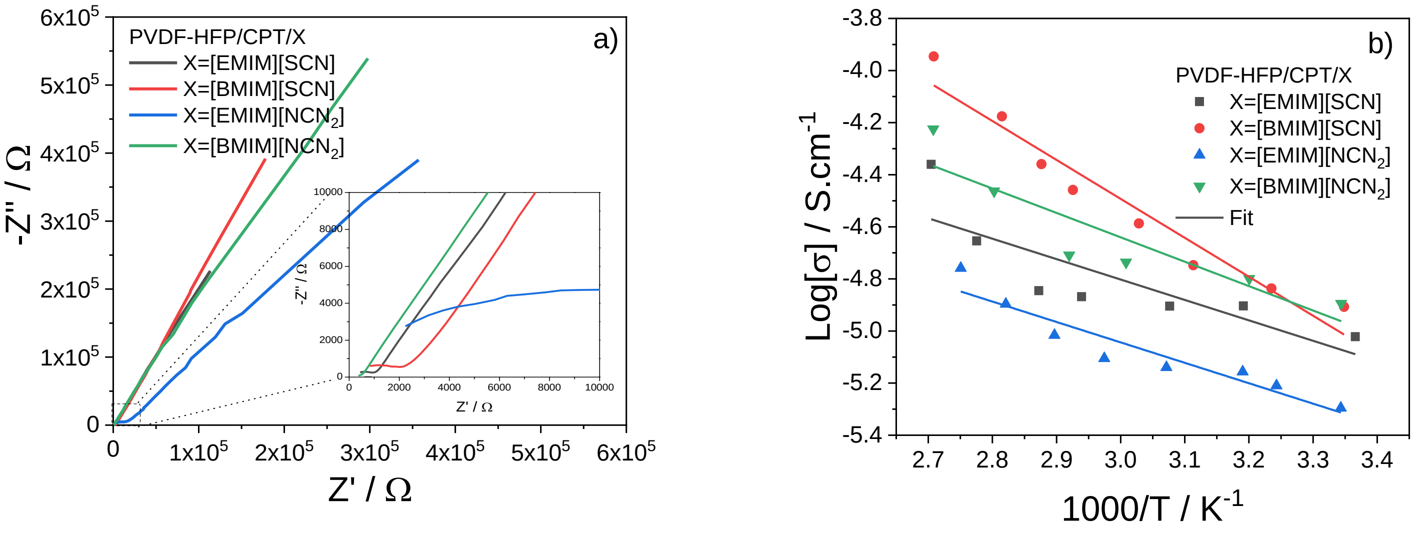

Figure 4.11 – Nyquist plots at room temperature (a) and Arrhenius plots (b) for the PVDF-HFP/CPT/X composites (R^2= 0.7012; 0.9440; 0.8997; 0.8246 for the [EMIM][SCN], [BMIM][SCN], [EMIM][NCN$_2$] and [BMIM][NCN$_2$] fittings, respectively).

The ionic conductivity of the samples was determined using the Nyquist plots at different temperatures, and the resulting Arrhenius plots are reproduced in Figure 4.11b. The obtained values for ionic conductivity at room temperature and 60 °C, as well as the activation energy values obtained from the slope of the Arrhenius plot, are gathered in Table 4.7. The expected improvement in the ionic conductivity resulting from the increase in the polymer chain mobility with increasing temperature is clearly verified. Above 60°C, this improvement is more significant because of the influence of the a-relaxation of the polymer, related to relaxation within the crystalline component [18], as well as to the increase in the number of mobile charges of the IL that are trapped in the zeolite structure at lower temperatures [1]. Also, the use of different ILs leads to different ion conduction behaviors due to the distinct types of charge carriers, their size, as well as the nature of their interactions with the host polymer and the CPT zeolite. These interactions determine whether the ionic conductivity will suffer a more significant increase with rising temperature or not. The change on the ionic conductivity behavior with increasing temperature is more significant for the [EMIM][SCN] and the [BMIM][NCN_2] samples, which are the ones with stronger affinity with the zeolite, accordingly to the crystallinity analysis. Also, as expected, the use of different ILs leads to different ion conduction behaviors due to the distinct types of charge carriers present, their size, as well as the nature of their interactions with the host polymer and the CPT zeolite. The samples with the $[SCN]^-$ anion tend to present higher ionic conductivity than those incorporating the $[N(CN)_2]^-$ anion, an effect that is also related to the degree of crystallinity However, the degree of crystallinity is not the only factor influencing the ion conduction behavior, as other parameters also have significant impact, such as viscosity and ionic conductivity of the IL itself, size of the ion chains and also the IL/zeolite interaction (Table 4.5) [7].

Table 4.7 – Ionic conductivity at 25°C and 60°C, activation energy and lithium transference number for the PVDF-HFP/CPT/X composites.

Sample	Ionic conductivity (S cm^{-1})		Activation energy (kJ mol^{-1})	Lithium transference number (t_{Li^+})
	25°C	60°C		
[EMIM][SCN]	9,5×10^{-6}	1.4×10^{-5}	6.5	0.61
[BMIM][SCN]	1.2×10^{-5}	3.5×10^{-5}	11.1	0.64
[EMIM][$N(CN)_2$]	5.1×10^{-6}	7.8×10^{-6}	6.5	0.56
[BMIM][$N(CN)_2$]	1.3×10^{-5}	2.0×10^{-5}	7.8	0.57

Regarding the activation energy, it may be inferred from Table 3.7 that the cation with longer chain led to higher activation energy values, as more energy should be provided to the system for the ion conduction to occur.

In addition, Table 4.7 shows that regardless of the IL type used in the SPE, the value of the lithium transference number is above 0.5, demonstrating the significant mobility of Li^+ ions in the SPE [19].

Furthermore, there is a correlation between the ionic conductivity value and the lithium transference number, which depends more on the anion than on the cation. The sample with the highest lithium transference number ([BMIM][SCN]) corresponds to the one with the lower affinity between the IL and zeolite, as shown in the conductivity analysis, also corresponding to the most performing battery. Regarding the electrochemical stability, there was no significant redox peaks in the operation range of the assembled batteries (2.5-4.5 V), demonstrating an adequate electrochemical window for the battery applications.

4.2.4. Battery performance

The prepared samples were tested as SPEs in LIBs, and their performance was evaluated by charge-discharge tests. These tests were carried out at the levels of cycling stability and rate performance of the batteries at room temperature. The results obtained are presented in Figure 4.12.

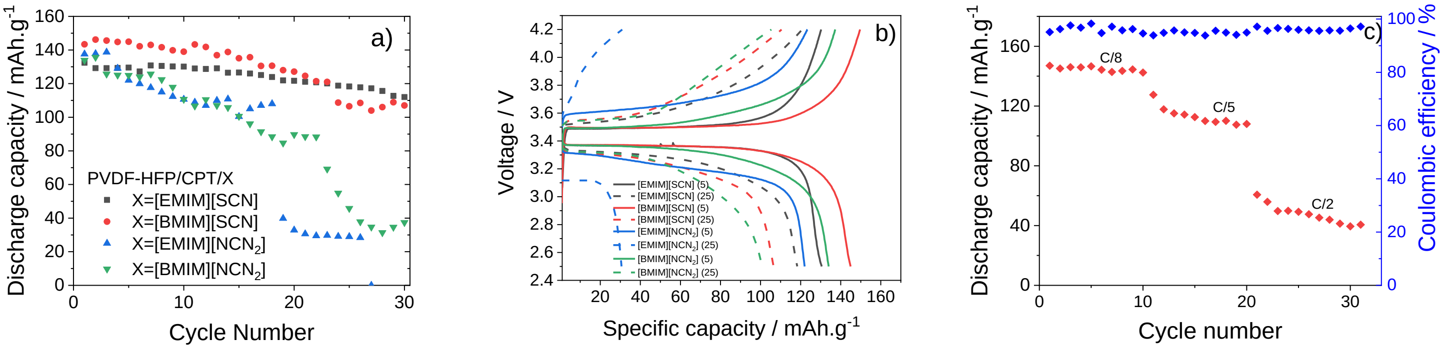

Figure 4.12– Room temperature cycling performance of the prepared PVDF-HFP/CPT/X composite SPEs at C/10 rate (a); charge/discharge profiles of the 5th and 25th cycles; (b) room temperature cycling performance of the PVDF-HFP/CPT/[BMIM][SCN] sample at different discharge rates (c).

Figure 4.12a) shows the cycling stability of the prepared LIBs for 30 cycles at C/10 rate. Despite similar initial discharge capacity for all samples (between 135 and 145 mAh g^{-1}), the SPE with the anion $[SCN]^-$ is significantly more suitable for SPE applications as, independently of the cation size, the assembled batteries are able to maintain their capacity after 30 cycles with losses lower than 30%, and can even hold a good performance after 50 cycles. This behavior contrasts with those of the samples with the $[N(CN)_2]^-$ anion, that present a significant drop in their capacity after 15 cycles due to the destabilization of the SPE structure, caused by the higher anion size compared with the $[SCN]^-$. For the samples with the $[SCN]^-$ anion, it is observed a correlation between the cation size and the performance and stability. Larger cation sizes lead to a higher initial discharge capacity, however, this capacity is reduced along cycling due to the destabilization of the structure caused by this difference. On the other hand, the smaller $[EMIM]^+$ cation presents a smaller initial capacity, which is maintained for a prolonged number of cycles as it causes a smaller disruption of the SPE structure. This is confirmed by the analysis of the charge-discharge profiles in Figure 4.12b, in which the typical voltage plateau corresponding to the insertion and extraction of Li^+ ions in the structure of the LFP cathode between 3.3 and 3.5 V is observed [20]. For the sample with higher performance, the samples including the IL [BMIM][SCN], a rate performance test was carried out at different discharge rates, as shown in Figure 4.12c. The assembled batteries presented acceptable rate performances at the different discharge rates, particularly up to C/8, and also a good capacity recovery at the end of the test at C/15, as well as high coulombic efficiency above 90%. This does not apply on the first cycles, due to the need to activate the system and the interface modifications [21].

In order to relate battery performance to the electrode/SPE interface, EIS analysis was carried out before cycling to assess the roles of the anion and cation present in IL. The Nyquist plots shown in Figure 4.12d contain a semicircle in the high and medium frequency region, associated with the overall resistance, and a straight line in the low frequency region, related to the Li^+ diffusion process [1]. The analysis of the batteries' impedance spectra before and after cycling (Figure 4.13) shows that the batteries with the SPE comprising the $[N(CN)_2]^-$ anion present higher initial resistance, which is an indicator of the lower battery performance. Moreover, it may be inferred that the longer chain cation led to higher resistance, as proven by the bigger semicircles obtained in the Nyquist plots of these samples at high frequencies. However, after cycling the opposite is verified, as the longer cation chains present the lower resistance.

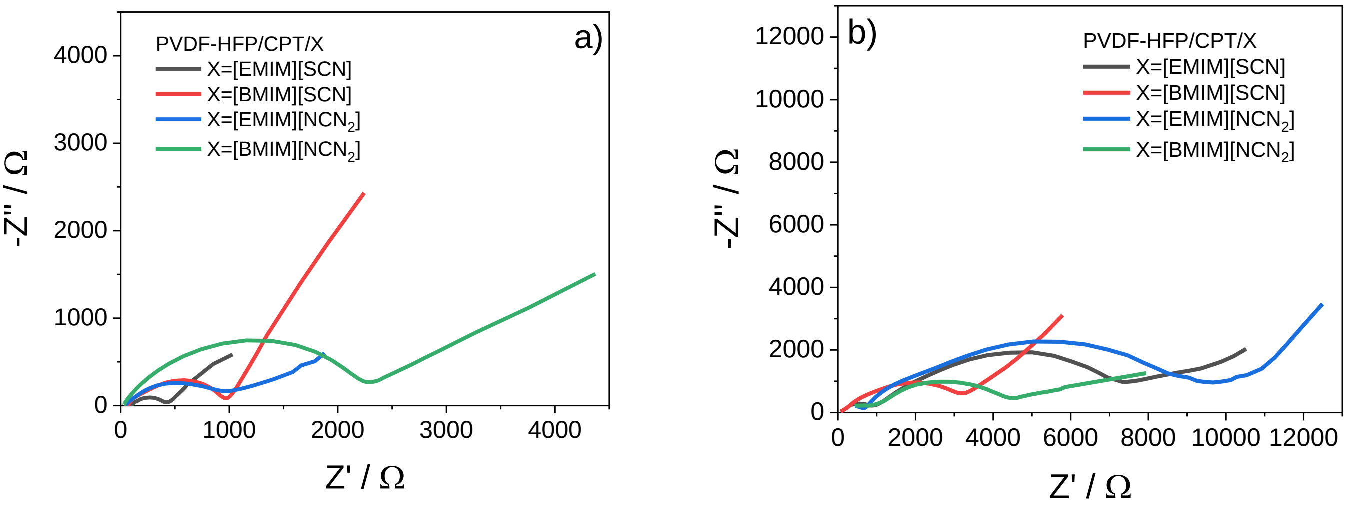

Figure 4.13 - Impedance spectroscopy of the batteries before (a) and after cycling (b).

The results herein obtained are in line with those reported in the literature for other related composites, as shown in Table 4.8, proving the suitability of the use of ILs in SPEs as active fillers to improve ionic conductivity, with the contribution of the CPT zeolite as a stabilization of the SPE over cycling [22].

These findings allow concluding that the IL type plays an important role in the cycling behavior and that the ternary composite approach is a valuable strategy to obtain good battery performance at room temperature, which is also an advantage for application at large scales in commonly used devices.

Table 4.8 – Main results reported in the literature compared with those obtained in this work.

Host polymer	**Fillers**	**Conductivity (S cm^{-1})**	**Battery capacity of LFP batteries (mAh g^{-1})/C-rate**	**Ref.**
PVDF-HFP	IL@UiO-67	4.3×10^{-4} (25°C)	118 (1C); 25°C	[23]
PVDF-HFP	LiTFSI, LLZTO	8.80×10^{-5} (25°C)	158.7 (C/10); 25°C	[24]
PVDF	LLTO	5.3×10^{-4} (25°C)	121 (C); 25°C	[25]
PEO	SSZ-13, LiTFSI	5.34×10^{-2} (70°C)	154 (C/10); 60°C	[26]
PEO	ZYNa, LiTFSI	1.66×10^{-2} (60°C)	152 (C/5); 60°C	[27]
PVDF-HFP	CPT, [BMIM][SCN]	1.2×10^{-5} (30°C)	143 (C/10); 25°C	This work

4.2.5. Conclusions

SPEs based on a three-component approach (ternary composites) were developed by doctor blade using ILs with two sorts of anions and cations (1-ethyl-3-methylimidazolium thiocyanate, [EMIM][SCN], 1-butyl-3-methylimidazolium thiocyanate, [BMIM][SCN], 1-ethyl-3-methylimidazolium dicyanamide, [EMIM][NCN$_2$] and 1-butyl-3-methylimidazolium dicyanamide, [BMIM][NCN$_2$]) and a zeolite (clinoptilolite, CPT) as fillers. The influence of the IL type on the SPE properties was evaluated and samples were characterized at different levels, in terms of morphological, structural, thermal, mechanical, electrical and battery performance. The morphological study showed that there is good compatibility between the fillers and the host polymer matrix. In addition, it was demonstrated that different ILs in the samples influence the compactness and roughness of the samples, the smaller cation (EMIM$^+$) giving rise to more compact films. Also, the specific interaction zeolite-polymer-IL affected the degree of crystallinity that depends on the anion and cation presents in the IL. In contrast, the melting and degradation temperatures were not significantly affected by the IL type. Regarding the mechanical behavior, the Young's modulus values increase for ILs with shorter chain cation (EMIM)$^+$, indicating a stronger plasticizing effect by the long chain cation. In general, there is a tendency to a slight reduction of the thermal and mechanical stability upon the addition of the different ILs when compared to the use of just CPT as a filler. At room temperature, the highest ionic conductivity was measured for the SPE with the IL [BMIM][NCN$_2$] (1.3×10^{-5} S.cm^{-1}). This value depends on the anion and cation present in IL, as well as on the degree of crystallinity. The battery performance at room temperature was affected by the anion and cation present in the IL and an excellent cycling behavior of 135 mAh.g^{-1} after 30 cycles with losses lower than 30% were observed for the SPE prepared with the IL [BMIM][SCN]. It was concluded that there is a balance between the number of mobile charges and their effect on the SPE stability due to their size. Also, it was demonstrated that the SPE main characteristics and the corresponding battery performance can be tuned by the judicious selection of anion and cation of the IL in ternary composites based on a polymer matrix with embedded ILs as active conductive fillers and a zeolite to stabilize cycling performance. Thus, this works proves the suitability of ternary composite SPE for the next generation of room temperature solid-state batteries and also states the importance of the choice of the right IL for the desired application, as its characteristics may significantly influence the SPE properties and consequently its performance.

4.2.6. References

1. Barbosa, J.C., et al., *High-Performance Room Temperature Lithium-Ion Battery Solid Polymer Electrolytes Based on Poly(vinylidene fluoride-co-hexafluoropropylene) Combining Ionic Liquid and Zeolite.* ACS Applied Materials & Interfaces, 2021. **13**(41): p. 48889-48900.
2. Lopes, A.C., et al., *Influence of zeolite structure and chemistry on the electrical response and crystallization phase of poly(vinylidene fluoride).* Journal of Materials Science, 2013. **48**(5): p. 2199-2206.
3. Chen, Z., et al., *Study on structure and vacuum membrane distillation performance of PVDF membranes: II. Influence of molecular weight.* Chemical Engineering Journal, 2015. **276**: p. 174-184.
4. Song, W., et al., *Effect of the surface roughness on interfacial properties of carbon fibers reinforced epoxy resin composites.* Applied Surface Science, 2011. **257**(9): p. 4069-4074.
5. Martins, P., A.C. Lopes, and S. Lanceros-Mendez, *Electroactive phases of poly(vinylidene fluoride): Determination, processing and applications.* Progress in Polymer Science, 2014. **39**(4): p. 683-706.
6. Correia, D.M., et al., *Influence of Cation and Anion Type on the Formation of the Electroactive β-Phase and Thermal and Dynamic Mechanical Properties of Poly(vinylidene fluoride)/Ionic Liquids Blends.* The Journal of Physical Chemistry C, 2019. **123**(45): p. 27917-27926.
7. Correia, D.M., et al., *Ionic Liquid Cation Size-Dependent Electromechanical Response of Ionic Liquid/Poly(vinylidene fluoride)-Based Soft Actuators.* The Journal of Physical Chemistry C, 2019. **123**(20): p. 12744-12752.
8. Ruíz-Baltazar, A., et al., *Preparation and Characterization of Natural Zeolite Modified with Iron Nanoparticles.* Journal of Nanomaterials, 2015. **2015**: p. 364763.
9. Ren, Y.-K., et al., *Controllable intermediates by molecular self-assembly for optimizing the fabrication of large-grain perovskite films via one-step spin-coating.* Journal of Alloys and Compounds, 2017. **705**: p. 205-210.

10. Sousa, R.E., et al., *Microstructural variations of poly(vinylidene fluoride co-hexafluoropropylene) and their influence on the thermal, dielectric and piezoelectric properties.* Polymer Testing, 2014. **40**: p. 245-255.
11. Meira, R.M., et al., *Ionic-Liquid-Based Electroactive Polymer Composites for Muscle Tissue Engineering.* ACS Applied Polymer Materials, 2019. **1**(10): p. 2649-2658.
12. Mansouri, N., et al., *Porosity, characterization and structural properties of natural zeolite - Clinoptilolite - As a sorbent.* Environment Protection Engineering, 2013. **39**: p. 139.
13. Polat, K., *Energy harvesting from a thin polymeric film based on PVDF-HFP and PMMA blend.* Applied Physics A, 2020. **126**(7): p. 497.
14. Yao, P., et al., *Review on Polymer-Based Composite Electrolytes for Lithium Batteries.* Frontiers in Chemistry, 2019. **7**(522).
15. Chang, B.-Y. and S.-M. Park, *Electrochemical Impedance Spectroscopy.* Annual Review of Analytical Chemistry, 2010. **3**(1): p. 207-229.
16. Ribeiro, C., et al., *Electroactive poly(vinylidene fluoride)-based structures for advanced applications.* Nature Protocols, 2018. **13**(4): p. 681-704.
17. Park, M., et al., *A review of conduction phenomena in Li-ion batteries.* Journal of Power Sources, 2010. **195**(24): p. 7904-7929.
18. Correia, D.M., et al., *Ionic and conformational mobility in poly(vinylidene fluoride)/ionic liquid blends: Dielectric and electrical conductivity behavior.* Polymer, 2018. **143**: p. 164-172.
19. Zhao, Y., et al., *Solid Polymer Electrolytes with High Conductivity and Transference Number of Li Ions for Li-Based Rechargeable Batteries.* Advanced Science, 2021. **8**(7): p. 2003675.
20. Gören, A., et al., *Influence of Solvent Evaporation Rate in the Preparation of Carbon-Coated Lithium Iron Phosphate Cathode Films on Battery Performance.* Energy Technology, 2016. **4**(5): p. 573-582.
21. Xiao, Y., et al., *Understanding interface stability in solid-state batteries.* Nature Reviews Materials, 2020. **5**(2): p. 105-126.
22. Barbosa, J.C., et al., *Three-Component Solid Polymer Electrolytes Based on Li-Ion Exchanged Microporous Silicates and an Ionic Liquid for Solid-State Batteries.* Advanced Engineering Materials, 2022. **n/a**(n/a): p. 2200849.
23. Liu, L. and C. Sun, *Flexible Quasi-Solid-State Composite Electrolyte Membrane Derived from a Metal-Organic Framework for Lithium-Metal Batteries.* ChemElectroChem, 2020. **7**(3): p. 707-715.
24. Yu, Y., et al., *Zwitterion-containing electrolytes with semi–crystalline PVDF-Co-HFP as a matrix for safer lithium-ion batteries.* Journal of Molecular Liquids, 2019. **282**: p. 340-346.
25. Li, B., et al., *Li0.35La0.55TiO3 Nanofibers Enhanced Poly(vinylidene fluoride)-Based Composite Polymer Electrolytes for All-Solid-State Batteries.* ACS Applied Materials & Interfaces, 2019. **11**(45): p. 42206-42213.
26. Jamal, H., et al., *Enhancement of the ionic conductivity of a composite polymer electrolyte via surface functionalization of SSZ-13 zeolite for all-solid-state Li-metal batteries.* Journal of Materials Chemistry A, 2021. **9**(7): p. 4126-4137.
27. Jamal, H., et al., *Enhanced compatibility of a polymer-based electrolyte with Li-metal for stable and dendrite-free all-solid-state Li-metal batteries.* Journal of Materials Chemistry A, 2021. **9**(48): p. 27304-27319.

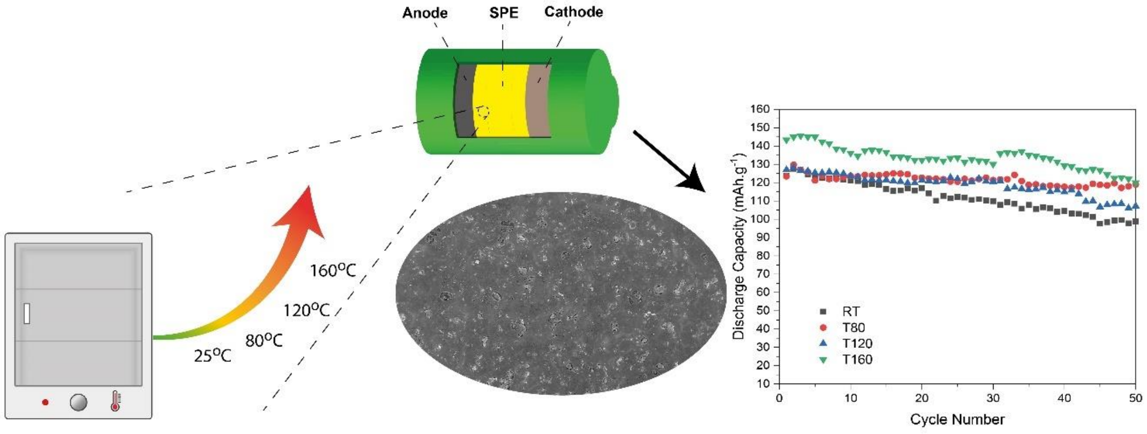

4.3. Influence of evaporation solvent temperature in the performance of ternary solid polymer electrolytes with poly(vinylidene fluoride-co-hexafluoropropylene) combining ionic liquid and zeolite

After the selection of the best materials, the effect of processing conditions was also evaluated. Four samples were produced at different temperatures (room temperature, 80°C, 120°C and 160°C) in order to optimize solvent evaporation temperature conditions. The samples were named after the solvent evaporation temperature used It was concluded that solvent evaporation at higher temperature improve battery performance due to the changes in the SPE morphology that lead to increased ionic conductivity and lithium transference number.

Based on "Influence of solvent evaporation temperature on the performance of ternary solid polymer electrolytes based on poly(vinylidene fluoride-co-hexafluoropropylene) combining an ionic liquid and a zeolite"; João C. Barbosa et. al, published on Applied Energy Materials, 2023. 6 (10): p. 5239-5248.

The most adequate selection of the materials is not the only important parameter in the development of SPEs. The experimental preparation conditions also play an important role during the development of a SPE. An important parameter that has not yet been studied in SPE is the solvent evaporation temperature, since in a polymer/solvent solution, it affects the solvent evaporation rate and consequently the morphology, physical-chemical, thermal and electrical properties of the produced SPE [1]. Thus, the goal of this work was to study the effect on evaporation temperature varying the temperature from room temperature to 160 °C (RT, 80°C, 120°C and 160°C) for a ternary SPE based on PVDF-HFP, CPT and [BMIM][SCN] composite, in order to evaluate its influence on SPE stability, ionic conductivity, electrochemical windows, lithium transference number and battery performance. Also, the morphology, polymer phase, thermal and mechanical properties were evaluated for ternary SPEs.

For this work, the following samples were prepared: RT, T80, T120 and T160. Each sample was named after the solvent evaporation temperature. PVDF-HFP, [BMIM][SCN] and CPT were used as polymer matrix and passive filler, respectively. The addition order of the components was zeolite-IL-polymer. The samples were processed by doctor blade technique and the solvent was evaporated at different temperatures: 160°C for 15 min, 120°C for 30 min, 80°C for 15 min and RT overnight. The morphology of the samples was characterized by SEM, the structure by XRD and FTIR, the thermal properties by DSC and TGA and the mechanical properties by stress-strain tests. The electrochemical properties were assessed by impedance spectroscopy and cyclic voltammetry. Finally, batteries were evaluated in half cells. The experimental details can be found in section 3.

4.3.1. Morphology and structural properties

The morphology of the ternary SPEs prepared at different temperatures from RT to 160 °C is presented in the representative surface and cross-section SEM images of Figure 4.14. The surface SEM images of the samples demonstrate a good and homogeneous distribution of the fillers throughout the polymer matrix without the presence of large agglomerates, indicating a good compatibility between the different components.

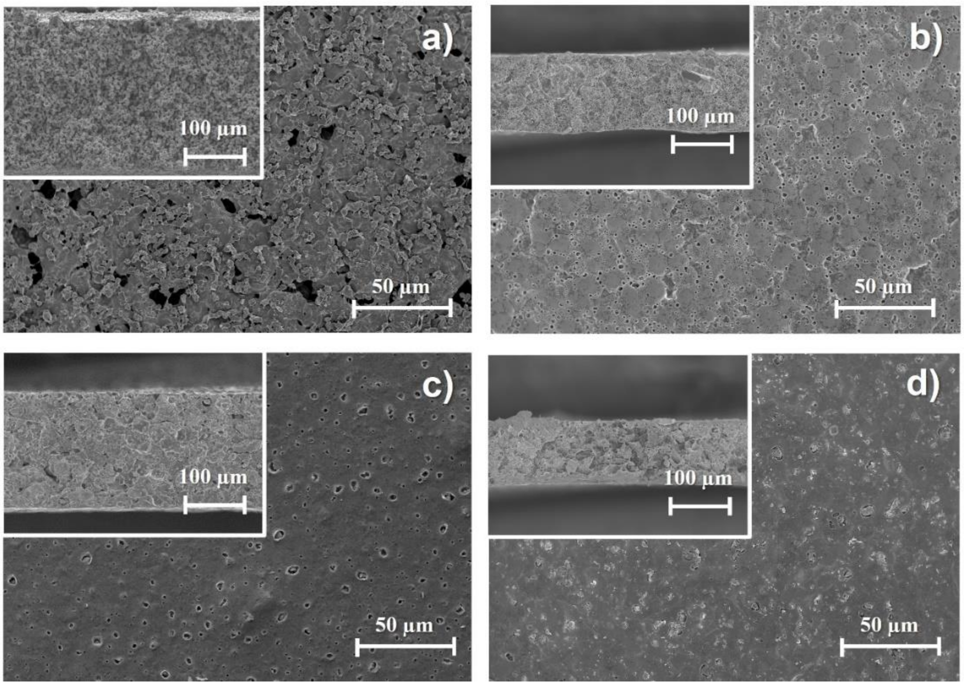

Figure 4.14 – Surface and cross section SEM images of the ternary SPE PVDF-HFP/CPT/[BMIM][SCN] samples prepared at RT (a), 80°C (b), 120°C (c), and 160°C (d).

The analysis of the SEM images shows that the processing temperature influences the morphology of the samples. The sample prepared at RT shows a porous texture due to a phase separation process [1] and to the low evaporation temperature used, which reduces the solvent evaporation rate as well as the polymer chains mobility, limiting their capacity to occupy the free space left by the solvent [2]. With increasing temperature and solvent evaporation rate, the phase separation process is reduced and finally it is inhibited [1] and the mobility of the polymer chains is increased, reducing the free space left by the solvent, which leads to a significant reduction in the samples' porosity. This is particularly evident in the cross-section images in the insets of Figure 4.14. The remaining voids present at higher temperatures (120 and 160 °C) originate just from the presence of the CPT zeolite in the structure [3]. PVDF-HFP spherulites are not evidenced in any sample due to the high amount of filler in the samples that limits the crystallization of the polymer [4].

Figure 4 shows the XRD patterns (Figure 4.15a) and ATR/FTIR spectra (Figure 4.15) of the ternary SPE samples prepared at different temperatures. The characteristic crystalline peak of the zeolite observed at 10° [5] (Figure 4.15a), confirms the presence of this filler. The intensity of this peak is independent of the solvent evaporation temperature. The peak at 20.26°, that corresponds to the polar β phase of PVDF-HFP, corresponds to the (110) (200) crystalline planes [6]. The degree of crystallinity of the samples, determined through equation 1, is presented in Table 4.9. The samples with the lowest degrees of crystallinity are those prepared at RT and 160 °C due to the polymer crystallization governed by the phase separation dynamics [1] in the former case and to the rapid solvent evaporation process at higher temperatures, that leads to ill-crystallized regions [1], in the latter case.

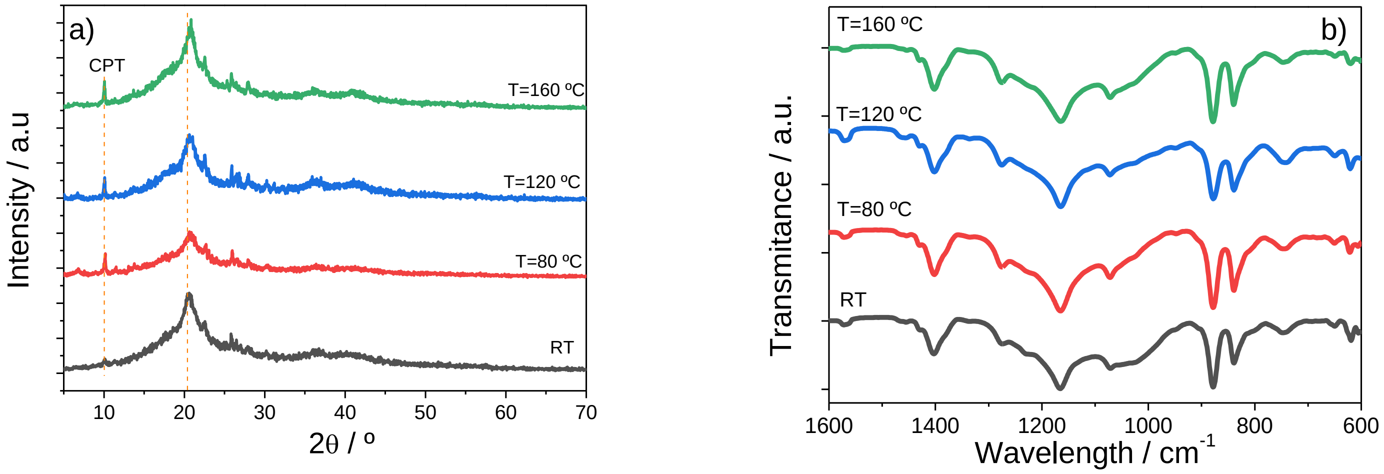

Figure 4.15 – XRD patterns (a) and ATR/FTIR spectra (b) of the ternary SPE PVDF-HFP/CPT/[BMIM][SCN] samples.

The effect of the processing temperature on the SPE chemical structure and polymer conformation was assessed by ATR/FTIR analysis (Figure 4.15b). The typical bands corresponding to the stretching vibrations of CH_2 and CF_2 of the PVF-HFP matrix are present in all the samples at 976, 795, 763 and 678 cm^{-1} [6]. The characteristic asymmetric stretching band of the Al-O bonds, attributed to the CPT zeolite, is also observed at 1087 cm^{-1} [7]. The high amount of [Bmim][SCN] IL in the samples leads to a dominant polymer chain conformation corresponding to the planar zig-zag, which indicates a polar β-phase content above 80%, as demonstrated by the high intensity of the 840 cm^{-1} band. The β-phase content calculated for all samples is presented in Table 4.9. The different solvent evaporation temperatures used for sample preparation have not a significant influence on the polymer conformation in the present case, as the main driver for the crystallization of the β-phase is the ion-dipole interactions between the IL and the polymer chains [8].

4.3.2. Thermal and mechanical analysis

The influence of the presence of CPT zeolite and IL in the thermal and mechanical properties of the ternary SPEs samples prepared at different temperatures were evaluated by DSC and TGA and the results are presented in Figures 4.16a and 4.16b, respectively.

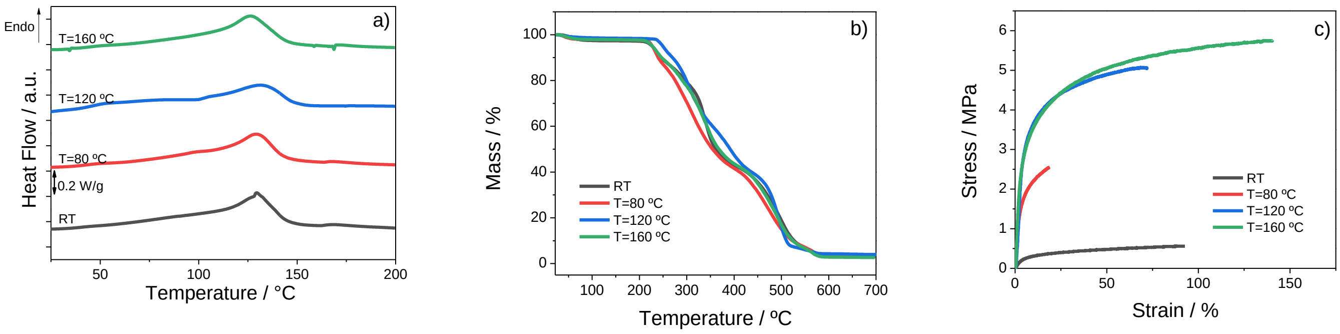

Figure 4.16 – DSC thermograms (a), TGA curves (b) and stress-strain characteristic (c) curves of the ternary SPE PVDF-HFP/CPT/[BMIM][SCN] samples.

DSC analysis allowed getting insight into the thermal behavior of the samples. The presence of the IL in the polymer matrix led to a destabilization of the SPE crystalline structure, resulting in a lower melting temperature than that reported for pristine PVDF-HFP (145 °C) [3]. This destabilization is attributed to the electrostatic ion-dipole interactions between the polymer matrix and the IL [9]. The resulting melting temperature is around 125°C, regardless of the sample's production temperature, as shown in Figure 4.16a). The enthalpy area, related to the degree of crystallinity, is represented in table 4.9, revealing a slight decrease with increasing processing temperature, in particular for higher processing temperature (160 °C), being in agreement with the results obtained from the XRD data (Figure 4.15a), suggesting a positive effect for battery performance, since the ion conduction process occurs mainly through the amorphous part of the polymer [10].

Table 4.9 - Enthalpy, Degree of crystallinity, β-phase content, Young modulus and yield stress for the ternary composites prepared at different temperatures.

Sample processing temperature /ºC	**Enthalpy/ J g^{-1} and Degree of crystallinity / % ± 2 %**	**β-phase / % ± 2 %**	**Young Modulus / MPa ± 2 MPa**	**Yield Stress / MPa ± 0.1 MPa**
RT	24.1 / 26.9	84	7	0.2
80	20.3 / 33.1	86	45	1.5
120	20.2 / 33.2	90	83	2.4
160	17.7 / 29.7	89	95	2.7

The thermal degradation behavior of the samples has been evaluated by TGA (Figure 4 .16b). Distinct degradation steps associated with the different components of the samples are evident. The CPT degradation step occurs around 475°C [11], thus overlapping with the PVDF-HFP degradation step at nearly the same temperature [11]. The [BMIM][SCN] degradation occurs at lower temperatures

(265°C). However, in the prepared samples this process is shifted to higher temperatures due to the interaction between the IL and the CPT zeolite, as reported previously [3]. These findings lead to conclude that the processing temperature does not have a significant influence in the thermal degradation of the samples, as all of them present similar behaviors and degradation temperatures and steps.

Figure 4.15c reproduces the stress-strain characteristic curves of the prepared samples, providing information about their mechanical properties, which were evaluated by the parameters presented in Table 4.9. All the samples are characterized by the typical stress-strain behavior of a thermoplastic polymer composed of the elastic and plastic regimes separated by the yielding region.

The observed mechanical reinforcement effect of the CPT upon inclusion in a polymer matrix reported in previous works [3, 12] is attributed to the restriction of the polymer chain motion due to the presence of the zeolite, as demonstrated by the high Young modulus values obtained when compared with those of the pristine polymer (373 MPa) [13]. The exception is the sample prepared at RT sample, which presents a low Young modulus because of its porous structure [14]. We may thus infer that the effect of the IL, which typically leads to a plasticizing effect in the matrix [8], leading to a decrease of the Young modulus, is overcome by the presence of the zeolite. Regarding the different processing temperatures, it seems that higher temperatures lead to more rigid samples with a more compact microstructure, as proved by the increasing Young modulus and the elongation at break.

4.3.3. Ionic Conductivity, electrochemical window and lithium transference number

To assess the samples' suitability when applications as SPE for LIBs are envisaged, electrochemical tests were carried out. Electrochemical impedance spectroscopy was used to evaluate the ionic conductivity of the samples. The obtained Nyquist plots are presented in Figure 4.17a.

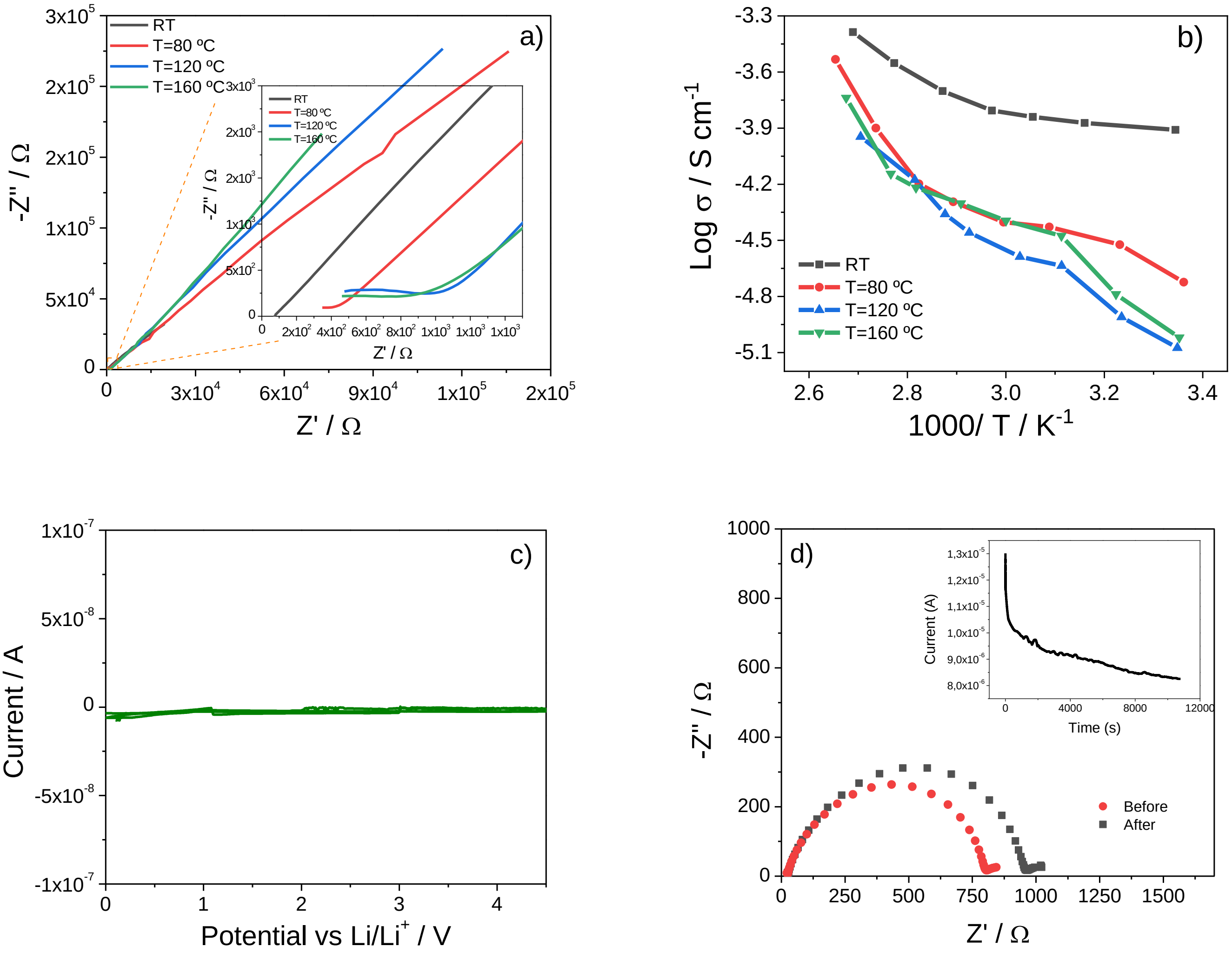

Figure 4.17 – Nyquist plots of the ternary SPE PVDF-HFP/CPT/[BMIM][SCN] samples (a). Inset: amplification of the Nyquist plot at high frequencies. Arrhenius plots for the SPE PVDF-HFP/CPT/[BMIM][SCN] samples (b). Cycle voltammogram (c) and lithium-transference number for the sample obtained at 160 °C (d). Inset: current vs a time.

The Nyquist plots are typically characterized by three characteristic regions which are a high frequency semicircle corresponding to the charge transfer process, a transition zone indicating the diffusion of counter-ions inside the electrode and a line at lower frequencies associated with ion diffusion [15]. The latter is the main process in the prepared samples as the presence of the IL significantly increases the number of mobile charge carriers [16]. Furthermore, Figure 4.17a) shows that the presence of the semi-circle depends on the evaporation temperature, which could be attributed to the more compact structures obtained at higher temperatures [1]. By analyzing the Nyquist plots at different temperatures, it is possible to determine the characteristics of the ionic conductivity through the Arrhenius equation (Figure 4.17b). The obtained plots show the typical increase in the ionic conductivity with increasing temperature attributed both to the increase of free charges resulting from the IL dissociation, as well as to the increase in the mobility of the mobile ionic species and the polymer chains, together with the segmental relaxation of the polymer chains [17]. In particular, it is observed a change in the slope of the ionic conductivity around 60 °C associated to the a-relaxation of the polymer [18]. The samples processed at RT are characterized by a less compact structure due to the phase separation process [1], which leads to the highest ionic conductivity among the prepared samples, (up to 1.2×10^{-4} S cm^{-1} at RT). Furthermore, the higher ionic conductivity value of this sample is due to the low degree of crystallinity, as the ionic conductivity also depends on factors such as microstructure, crystallinity and the related mechanical characteristics. The other samples show similar temperature behaviors, the main difference being in the value of the electrical conductivity, as shown in Table 4.10. Also, the activation energy value for all samples is low, with values below 14 kJ mol^{-1}, demonstrating the low thermal energy required for the ion hopping process.

Figure 4.17c shows the cycle voltammogram for the PVDF-HFP/CPT/[BMIM][SCN] sample obtained at 160 °C, as representative of the rest of the samples, for which the behavior is similar. The cyclic voltammogram was obtained between 0 V to +4.5 V at 0.1 V s^{-1} and good electrochemical stability was observed, with no anodic and cathodic peaks at current values below 10^{-9} A, being suitable for battery applications. In addition, the sample preparation temperature did not affect the electrochemical stability of the samples.

Regarding the lithium transference number, Figure 4.17d shows the corresponding curves for its calculation for the PVDF-HFP/CPT/[BMIM][SCN] sample prepared at 160 °C. The values of the lithium transference number for the different samples are given in Table 4.10. These data reveal that this parameter is affected by the sample processing temperature, leading to larger values for the samples obtained at higher temperatures due to microstructural features, which improve the ion diffusion through the amorphous phase of the sample [10] as well as though the ions solvation by the entangled polymer chains [19]. This value is due to the fact that the interaction of the CPT particles with the PVDF-HFP polymer chains favor a more compact microstructure, and to the presence of the IL, which allows to improve the ionic conductivity, leading to a highest value of the lithium transference number of 0.66 for the SPE evaporated at 160 °C. The sample evaporated at RT possesses a distinct behavior due to its porous structure, leading to a transference number of about 0.51. Also, it seems to exist a correlation between the lithium transference number and the thermal activation energy of the samples, as they vary in a similar way.

.

Table 4.10 – Electrochemical parameters of the prepared samples: ionic conductivity at different temperatures, activation energy and lithium transference number.

Sample	**σ_i/ S cm^{-1}**		**Activation energy/kJ mol^{-1}**	**Li$^+$ transference number**
	25°C	**60°C**		
RT	1.2×10^{-4}	1.6×10^{-4}	11.9	0.51
T=80 °C	1.9×10^{-5}	3.2×10^{-5}	9.9	0.35
T=120 °C	8.5×10^{-6}	3.5×10^{-5}	12.8	0.64
T=160 °C	9.5×10^{-6}	3.7×10^{-5}	14.0	0.66

The analysis of the overall electrochemical results allows to conclude that the prepared samples are suitable for application in LIBs, due to the combination of high RT ionic conductivity and Li$^+$ transference number, as well as excellent electrochemical stability.

4.3.4. Battery performance

The prepared SPEs were assembled in LIBs, and their performance was evaluated through galvanostatic charge-discharge tests at room temperature and at C/10 rate. Both cycle life and rate performance tests were carried out at room temperature, to assess their suitability for solid-state battery applications. The results are presented in Figure 4.18.

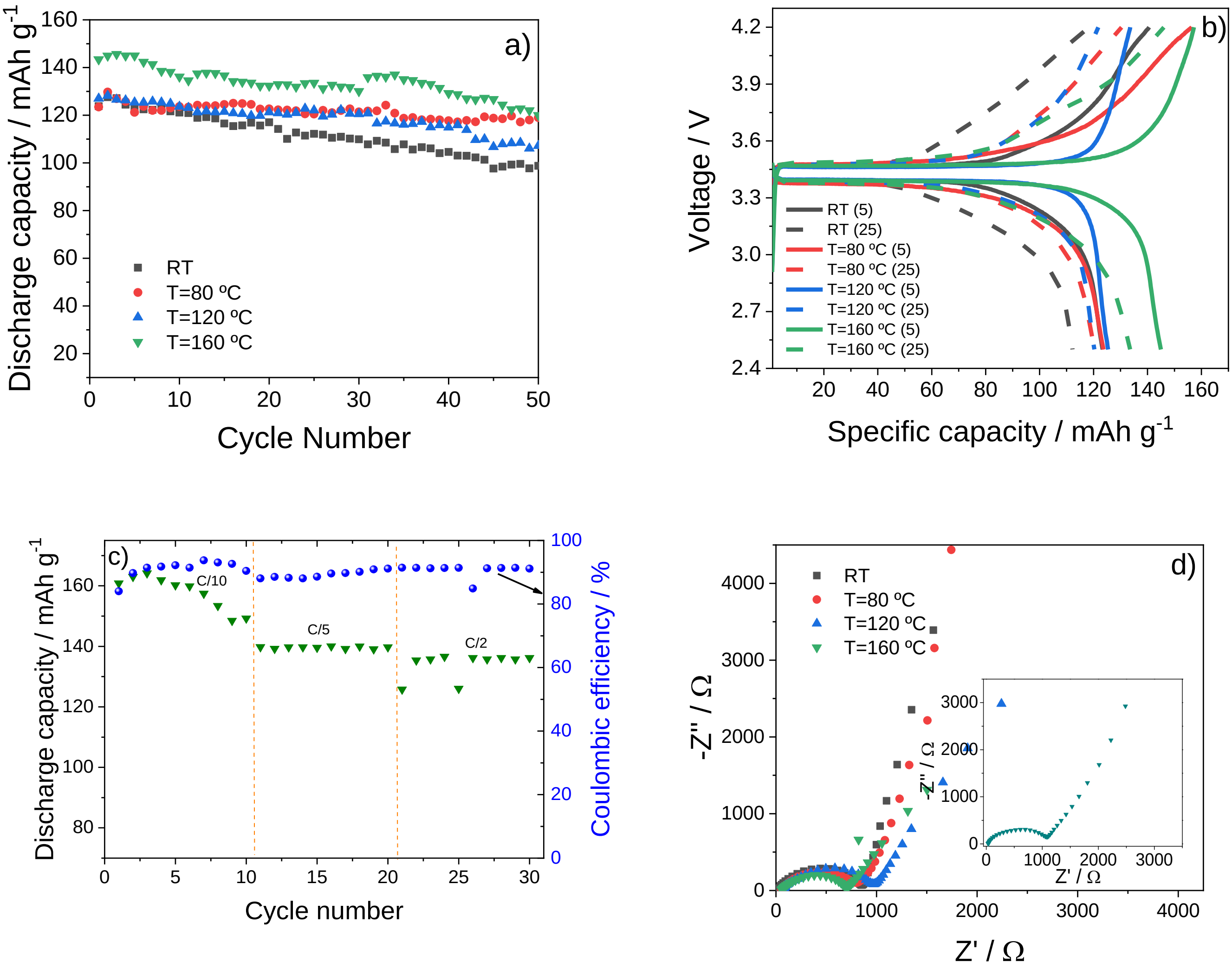

Figure 4.18 – Cycling stability of the prepared samples at C/10 rate (a); charge/discharge profiles of the different samples at the 5th and 25th cycles at C/10 rate (b); rate performance of the SPE PVDF-HFP/CPT/[BMIM][SCN] sample prepared at 160 °C (c) and Nyquist plot of the assembled batteries before cycling (d) (insert: Nyquist plot after cycling for the sample prepared at 160 °C).

The cycle stability tests (Figure 4.18a) show a high stability in all the prepared samples, with the best discharge capacity value found for the SPE PVDF-HFP/CPT/[BMIM][SCN] prepared at 160°C (145 mAh g^{-1}), and a capacity retention of 84% after 50 cycles. This behavior is attributed to the combination of the lower crystallinity of the sample and the high Li^{+} transference number, when compared to the other samples, such as the sample obtained at RT that exhibits a high ionic conductivity value. Some instability on the first cycles is attributed to the necessity to fully activate the system before the device is operational [20]. This instability is also proven by the lower coulombic efficiency value at the first cycles, which then stabilizes to about 80 to 100% efficiency. Despite the lower initial discharge capacity of the SPE sample obtained at 80 °C (123 mAh g^{-1}), its stability is significantly higher, being able to preserve 94% of its initial capacity after 50 cycles. This is proven by the charge-discharge profiles presented in Figure 4.18b, which show a small decay in the discharge capacity of the sample evaporated at 80 °C, despite the lower coulombic efficiency when compared to other samples. The charge-discharge profiles also show the typical voltage plateau of the LFP active material between 3.3 and 4.5 V, representing the mechanism of insertion and extraction of the Li ions in the electrode's structure [21]. Considering that the best cycle life test is observed for SPE PVDF-HFP/CPT/[BMIM][SCN] obtained at 160 °C due to its high lithium transference number, Figure 4.18c shows the rate performance for this sample, presenting 10 cycles for each rate. The discharge capacity values for this sample were 149, 140 and 136 mAh g^{-1} at C/10, C/5 and C/2 rates, respectively, the discharge capacity value decreasing with increasing C-rate due to the ohmic polarization effect [22]. Except for C/10-rate, the discharge capacity value is very stable for all cycle numbers as the sample shows high lithium transference number.

Impedance spectroscopy tests were carried out on the batteries, with the Nyquist plot of the samples before cycling being shown in Figure 4.18d. The three regions described above are present in these plots, with a bigger relevance of the semicircle at high frequencies, which is an indicator of the internal resistance of the battery components. Before cycling, a difference in overall resistance is observed between the different samples due to the variations in microstructure and surface compatibilization with the electrodes (Table 4.11). Also, there is an increase in the overall resistance of the batteries after cycling, which is ascribed to the formation of the solid electrolyte interphase (Table 4.11), the values, below 3694 Ω, being low due to the good compatibilization between the prepared samples and the electrode material [23]. It is evidenced that the SPE solvent evaporation temperature influences this resistance, showing values ranging from 1067 Ω to 3694 Ω, which decrease with increasing solvent evaporation temperature, both before and after cycling. This fact is also related to the better battery performance of the SPE sample prepared at 160 °C. It is to notice that, after cycling, the SPE samples prepared at 80°C and 120 °C show the higher increase in resistance, which is attributed to a decrease of the compatibility with the Li metal electrode, due to the higher degree of crystallinity.

Table 4.11 – Internal resistance of the assembled batteries before and after cycling.

Sample	Resistance before (Ω)	Resistance after (Ω)
RT	877	1221
80	788	2547
120	866	3694
160	704	1067

The obtained results prove the suitability of this three-composite system when compared to SPEs reported in the literature, as shown in table 4.12.

Table 4.12 – Literature results for related SPEs.

Polymer	Components Doping Agents ou Dopants	Ionic Conductivity (S cm^{-1})	Li$^+$ transference number	Battery capacity of LFP batteries (mAh g^{-1})/C-rate	Ref.
PVDF-HFP	IL@UiO-67	4.3×10^{-4} (25°C)	0.45	118 (1C); 25°C	[24]
PVDF-HFP	LiTFSI, LLZTO	8.80×10^{-5} (25°C)	0.27	158.7 (C/10); 25°C	[25]
PVDF	$LiClO_4$, LLTO	5.8×10^{-4} (25°C)	0.80	152 (C/5); 25°C	[26]
PEO	SSZ-13, LiTFSI	5.34×10^{-2} (70°C)	0.85	154 (C/10); 60°C	[27]
PEO	ZYNa Zeolite, LiTFSI	1.66×10^{-2} (60°C)	0.84	152 (C/5); 60°C	[28]
PVDF-HFP	CPT, [BMIM][SCN]	1.2×10^{-5} (30°C)	0.66	132 (C/2) 25°C	This work

The obtained values are in line with those reported in the literature, which hints the suitability of this approach for future developments in the solid-state battery field. The assembled batteries showed suitable ionic conductivity, a high Li$^+$ transference number, and an excellent cycling stability with high discharge capacity values even at room temperature. Furthermore, the influence of the preparation method, namely the processing temperature is also stated, with a positive effect for higher sample preparation temperatures. This work highlights the importance of the solvent evaporation temperature as an important parameter on the preparation of SPEs. In particular, it is observed a correlation between degree of crystallinity, lithium transference number and consequently battery performance, which proves the relevance of this parameter for further application at an industrial scale.

4.3.5. Conclusions

Ternary solid polymer electrolytes, SPEs, based on poly(vinylidene fluoride-co-hexafluoropropylene) (PVDF-HFP) as a polymer host, and clinoptilolite (CPT) zeolite and the ionic liquid (IL) (1-butyl-3-methylimidazolium thiocyanate ([BMIM][SCN])) as fillers, were produced by doctor blade technique, with varying solvent evaporation temperature, from RT to 160 °C. The effect of solvent evaporation temperature on the SPE morphology, thermal, mechanical and electrical properties was analyzed. The microstructure of the SPEs is affected by the solvent evaporation temperature. Processing at RT leads to a porous morphology, whereas the samples prepared at higher temperatures are characterized by a compact morphology. Regardless of the processing temperature, excellent compatibility is observed between the zeolite, the IL and the polymer matrix. The processing temperature slightly affected the degree of crystallinity of the samples, the melting and thermal degradation temperatures being practically independent of the processing conditions. At RT, the highest ionic conductivity was obtained for the sample obtained at RT (1.2×10^{-4} S cm^{-1}), whereas the highest value of the lithium transference number (0.66) was obtained for the sample prepared at 160 °C. The charge-discharge behavior at RT for the sample processed at 160 °C shows excellent battery performance with 149 and 136 mAh g^{-1} at C/10 and C/2 rates, respectively, which is attributed to the combination of two synergetic effects: ionic conductivity and lithium transference number. This work demonstrates that the processing temperature of the SPEs affects the battery performance due to its influence on sample morphology and physical-chemical properties, being a relevant parameter to consider in order to enhance the performance of RT solid-state batteries.

4.3.6. References

1. Sousa, R.E., et al., *Microstructural variations of poly(vinylidene fluoride co-hexafluoropropylene) and their influence on the thermal, dielectric and piezoelectric properties.* Polymer Testing, 2014. **40**: p. 245-255.
2. Magalhães, R., et al., *The Role of Solvent Evaporation in the Microstructure of Electroactive β-Poly(Vinylidene Fluoride) Membranes Obtained by Isothermal Crystallization.* Soft Materials, 2010. **9**(1): p. 1-14.
3. Barbosa, J.C., et al., *High-Performance Room Temperature Lithium-Ion Battery Solid Polymer Electrolytes Based on Poly(vinylidene fluoride-co-hexafluoropropylene) Combining Ionic Liquid and Zeolite.* ACS Applied Materials & Interfaces, 2021. **13**(41): p. 48889-48900.
4. Lopes, A.C., et al., *Influence of zeolite structure and chemistry on the electrical response and crystallization phase of poly(vinylidene fluoride).* Journal of Materials Science, 2013. **48**(5): p. 2199-2206.
5. Vollprecht, D., et al., *Ammonium Sorption from Landfill Leachates Using Natural and Modified Zeolites: Pre-Tests for a Novel Application of the Ion Exchanger Loop Stripping Process.* Minerals, 2019. **9**(8): p. 471.
6. Martins, P., A.C. Lopes, and S. Lanceros-Mendez, *Electroactive phases of poly(vinylidene fluoride): Determination, processing and applications.* Progress in Polymer Science, 2014. **39**(4): p. 683-706.
7. Ruíz-Baltazar, A., et al., *Preparation and Characterization of Natural Zeolite Modified with Iron Nanoparticles.* Journal of Nanomaterials, 2015. **2015**: p. 364763.
8. Correia, D.M., et al., *Ionic Liquid Cation Size-Dependent Electromechanical Response of Ionic Liquid/Poly(vinylidene fluoride)-Based Soft Actuators.* The Journal of Physical Chemistry C, 2019. **123**(20): p. 12744-12752.
9. Meira, R.M., et al., *Ionic-Liquid-Based Electroactive Polymer Composites for Muscle Tissue Engineering.* ACS Applied Polymer Materials, 2019. **1**(10): p. 2649-2658.

10. Patla, S.K., et al., *Investigation of ionic conduction in PEO–PVDF based blend polymer electrolytes.* Journal of Applied Physics, 2018. **123**(12): p. 125102.
11. Polat, K., *Energy harvesting from a thin polymeric film based on PVDF-HFP and PMMA blend.* Applied Physics A, 2020. **126**(7): p. 497.
12. Barbosa, J.C., et al., *Three-Component Solid Polymer Electrolytes Based on Li-Ion Exchanged Microporous Silicates and an Ionic Liquid for Solid-State Batteries.* Advanced Engineering Materials, 2022. **n/a**(n/a): p. 2200849.
13. Metın, D., et al., *The effect of interfacial interactions on the mechanical properties of polypropylene/natural zeolite composites.* Composites Part A: Applied Science and Manufacturing, 2004. **35**(1): p. 23-32.
14. Li, Z.H., et al., *Effects of the porous structure on conductivity of nanocomposite polymer electrolyte for lithium ion batteries.* Journal of Membrane Science, 2008. **322**(2): p. 416-422.
15. Chang, B.-Y. and S.-M. Park, *Electrochemical Impedance Spectroscopy.* Annual Review of Analytical Chemistry, 2010. **3**(1): p. 207-229.
16. Park, M., et al., *A review of conduction phenomena in Li-ion batteries.* Journal of Power Sources, 2010. **195**(24): p. 7904-7929.
17. Ribeiro, C., et al., *Electroactive poly(vinylidene fluoride)-based structures for advanced applications.* Nature Protocols, 2018. **13**(4): p. 681-704.
18. Correia, D.M., et al., *Ionic and conformational mobility in poly(vinylidene fluoride)/ionic liquid blends: Dielectric and electrical conductivity behavior.* Polymer, 2018. **143**: p. 164-172.
19. Diederichsen, K.M., E.J. McShane, and B.D. McCloskey, *Promising Routes to a High Li+ Transference Number Electrolyte for Lithium Ion Batteries.* ACS Energy Letters, 2017. **2**(11): p. 2563-2575.
20. Xiao, Y., et al., *Understanding interface stability in solid-state batteries.* Nature Reviews Materials, 2020. **5**(2): p. 105-126.
21. Gören, A., et al., *Influence of Solvent Evaporation Rate in the Preparation of Carbon-Coated Lithium Iron Phosphate Cathode Films on Battery Performance.* Energy Technology, 2016. **4**(5): p. 573-582.
22. Barbosa, J.C., et al., *Sustainable Lithium-Ion Battery Separators Based on Poly(3-Hydroxybutyrate-Co-Hydroxyvalerate) Pristine and Composite Electrospun Membranes.* Energy Technology, 2022. **10**(2): p. 2100761.
23. Safari, M., et al., *Multimodal Physics-Based Aging Model for Life Prediction of Li-Ion Batteries.* Journal of The Electrochemical Society, 2009. **156**(3): p. A145.
24. Liu, L. and C. Sun, *Flexible Quasi-Solid-State Composite Electrolyte Membrane Derived from a Metal-Organic Framework for Lithium-Metal Batteries.* ChemElectroChem, 2020. **7**(3): p. 707-715.
25. Yu, Y., et al., *Zwitterion-containing electrolytes with semi–crystalline PVDF-Co-HFP as a matrix for safer lithium-ion batteries.* Journal of Molecular Liquids, 2019. **282**: p. 340-346.
26. Sivaraj, P., et al., *Performance Enhancement of PVDF/LiClO4 Based Nanocomposite Solid Polymer Electrolytes via Incorporation of Li0.5La0.5TiO3 Nano Filler for All-Solid-State Batteries.* Macromolecular Research, 2020. **28**(8): p. 739-750.
27. Jamal, H., et al., *Enhancement of the ionic conductivity of a composite polymer electrolyte via surface functionalization of SSZ-13 zeolite for all-solid-state Li-metal batteries.* Journal of Materials Chemistry A, 2021. **9**(7): p. 4126-4137.
28. Jamal, H., et al., *Enhanced compatibility of a polymer-based electrolyte with Li-metal for stable and dendrite-free all-solid-state Li-metal batteries.* Journal of Materials Chemistry A, 2021. **9**(48): p. 27304-27319.

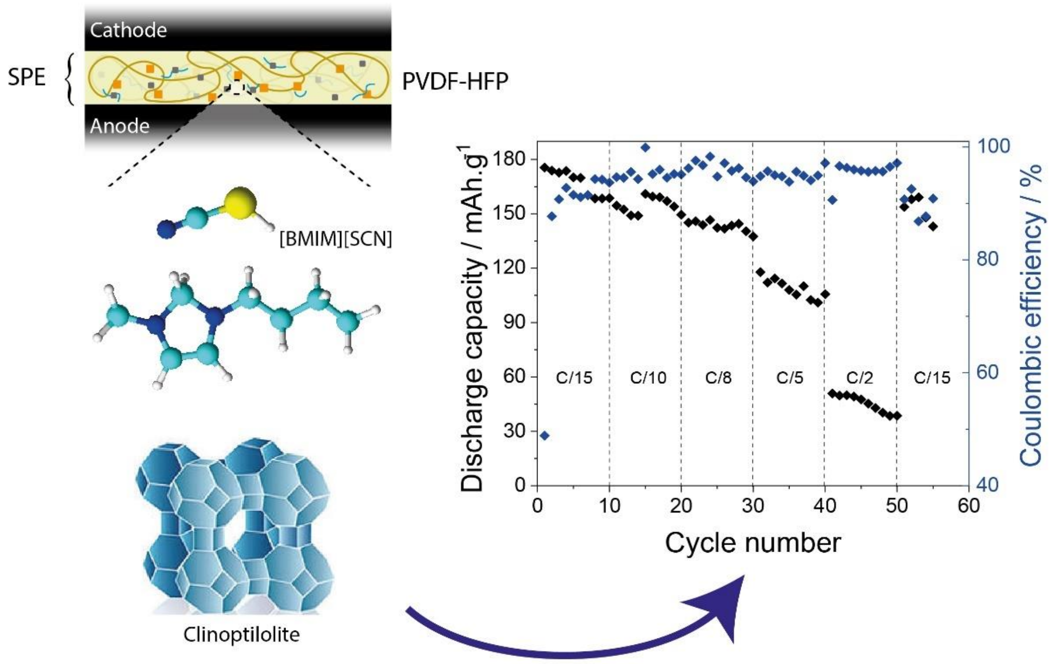

4.4. High Performance Room Temperature Lithium-Ion Battery Solid Polymer Electrolytes Based on Poly(vinylidene Fluoride-co-Hexafluoropropylene) Combining Ionic Liquid and Zeolite

The selection of the preparation method can have a significant influence on the battery performance. Samples were prepared with different component addition orders, which led to distinct interactions between the SPE components, and consequently to different battery cycling behaviors, with the IL-polymer-zeolite addition order being the most favorable for battery applications.

Based on "High Performance Room Temperature Lithium-Ion Battery Solid Polymer Electrolytes Based on Poly(vinylidene Fluoride-co-Hexafluoropropylene) Combining Ionic Liquid and Zeolite"; João C. Barbosa et. al, ACS Applied Materials & Interfaces, 2021. 13(41): p. 48889-48900.

Along the temperatures, the preparation method is also an important parameter that is not intensively studied in the literature. The component addition order can have a significant influence on the performance of the SPEs, due to the different interactions that are established between the components. In this work, this effect was studied, by adding the components at different orders, as shown in figure 4.19.

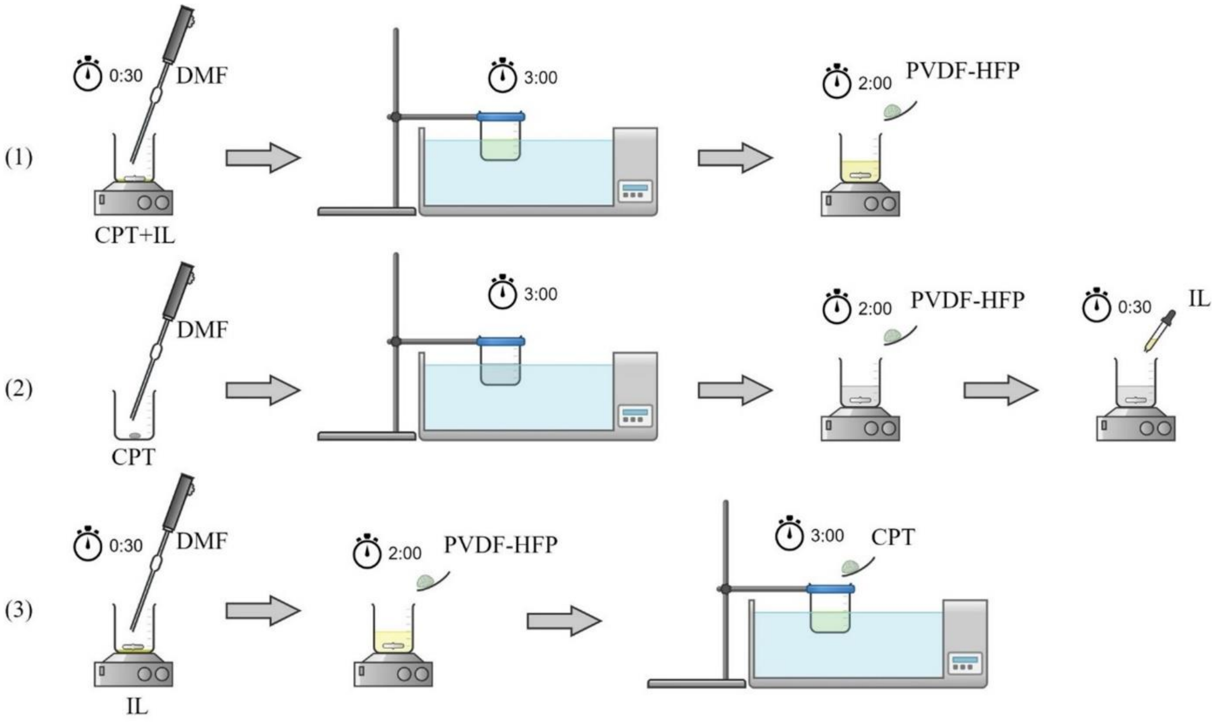

Figure 4.19 – Preparation methods used for the SPE samples.

For this work, four samples were prepared, each one named after the addition order as follows: CPT+IL+PVDF-HFP, IL+PVDF-HFP+CPT and CPT+PVDF-HFP+IL. PVDF-HFP, [BMIM][SCN] and CPT were used as polymer matrix and passive filler, respectively. The samples were processed by doctor blade technique and the solvent was evaporated at 120°C for 30 min. The morphology of the samples was characterized by SEM, the structure by XRD and FTIR, the thermal properties by DSC and TGA and the mechanical properties by stress-strain tests. The electrochemical properties were assessed by impedance spectroscopy and cyclic voltammetry. Finally, batteries were evaluated in half cells. The experimental details can be found in section 3.

4.4.1. Morphology and EDX analysis

The CPE filler is characterized by a flake-like crystal morphology, as shown in Figure 6.4 (Annex II). Representative SEM images of the prepared films are shown in Figure 4.20. All samples exhibit a compact non-porous texture, independently of processing conditions and sample composition. This behavior is also observed in the cross-section image (Figure 6.5 – Annex II).

Analysis of the SEM images allows concluding that the order of addition of the components affects the spherulite-like structure typical of PVDF-HFP and related polymers [1]. The formation of spherulites is evidenced both in all cases, but the sample with IL shows larger spherulites (Figure 4.20b) than the pristine co-polymer (Figure 4.20a) and the rest of the samples (Figures 4.20c-f). These results confirm that the IL employed formed strong ion-dipole interactions with the polar polymer chains, working as a nucleation agent for PVDF-HFP during the crystallization process, as already suggested elsewhere [2].

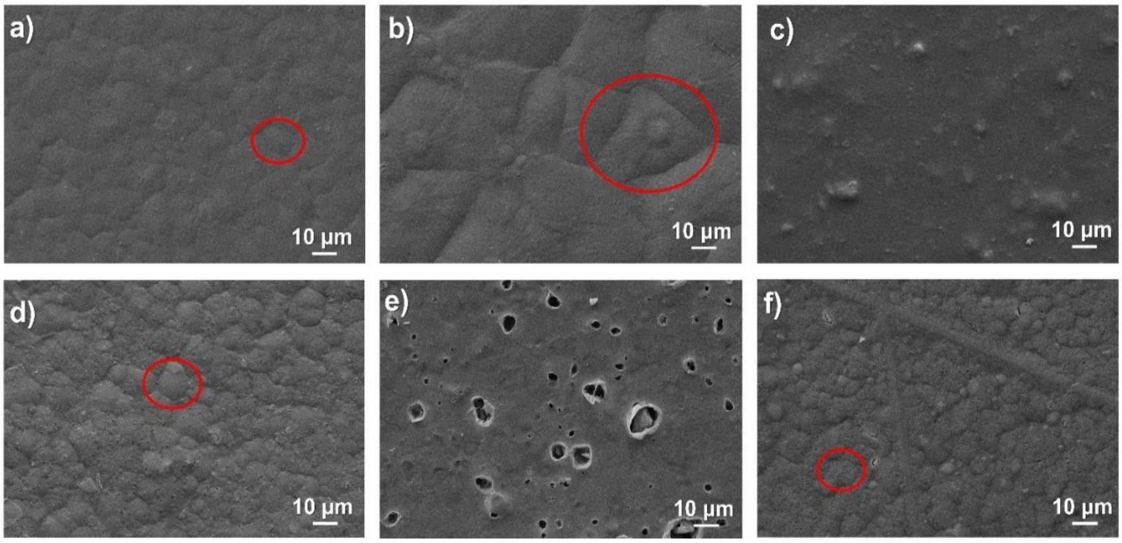

Figure 4.20 - SEM images of pristine PVDF-HFP (a), PVDF-HFP+IL (b), PVDF-HFP+CPT (c), CPT+IL+PVDF-HFP (d), IL+PVDF-HFP+CPT (e) and CPT+PVDF-HFP+IL (f) with identification of representative spherulites.

The absence of heterogeneous crystallization regions and the suitable distribution of the CPT filler within the host polymer (cf. the good distribution of small particle aggregates in Figure 4.20c) demonstrate the good compatibility between CPT and PVDF-HFP [3]. The presence of CPT inhibited the formation of large spherulites, in particular when compared with the samples with the inclusion of IL, causing a general reduction in the spherulite size when compared with the samples lacking CPT. This effect is attributed to the high silicon (Si) content in the CPT zeolites and to the strong surface interactions occurring between the high surface area filler and the polar polymer chains, which have been reported to promote the reduction of the spherulites' size while increasing their number [4]. The high Si content in CPT was in fact proven by EDX analysis (Figures 4.21b and 4.21d) (about 3% Si per sample).

In the case of Figure 4.20e, representing the sample in which CPT was added last, the size of the spherulites is also strongly reduced, suggesting that the subsequent addition of CPT led to the weakening of the IL-PVDF ion-dipole interactions during the stirring process, and also in parallel to a deficient mixing of the CPT particles (reduced surface interaction between the filler and the PVDF-HFP-IL solution). This is demonstrated by the existence of voids in the surface of the films, associated to CPT particles sifted to the surface and later removed due to deficient attachment for the polymer matrix. [5]. The SEM images clearly demonstrate that the different processing methods modified the main filler-polymer interactions in the solution and, therefore, to variations in the filler dispersion, crystallization process and the final film morphology. Moreover, these morphologies (different sizes and numbers of spherulites) will affect the degree of crystallinity, mechanical properties and ionic conductivity of the samples, which in turn will affect battery performance [2, 6].

Figure 4.21 shows the EDX mapping images of the nitrogen and silicon elements for the prepared samples. The presence of nitrogen and sulfur due to the IL, and silicon, oxygen, aluminum and sodium due to the CPT, allows evaluating the distribution of these two components within the PVDF-HFP matrix and therefore the filler distribution within the polymer matrix.

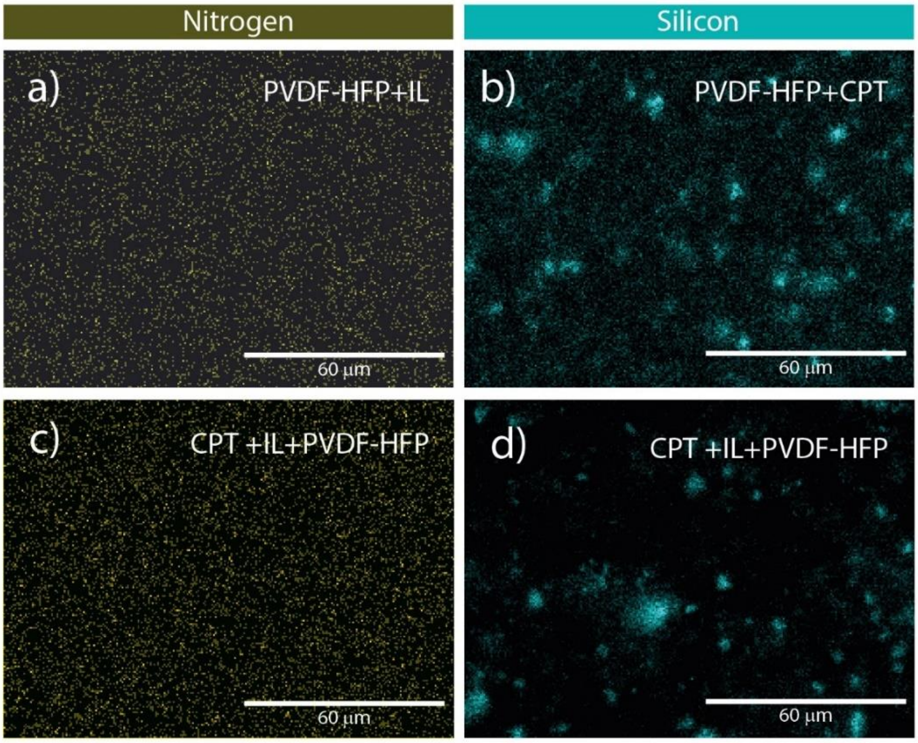

Figure 4.21 - EDX mapping images of nitrogen for PVDF-HFP+IL (a) and CPT+IL+PVDF-HFP (c) and silicon for PVDF-HFP+CPT (b) and CPT+IL+PVDF-HFP (d).

The equivalent distribution of the nitrogen and silicon elements into the prepared samples demonstrate that both IL and CPT are homogeneously distributed along the sample, regardless of the different preparation methods adopted. In particular, the characteristic elements of the IL are identified homogeneously on the surface of the samples, indicating a possible migration of part of the IL from the bulk to the surface of the sample [6]. In the CPT case, some small aggregates along the surface of the sample are detected through the presence of its characteristic elements. The addition of the IL influenced the size and distribution of the CPT aggregates, as suggested in Figures 4.21b and 4.21d. This behavior is common to all preparation methods. Furthermore, Figure 6.5 (Annex II) shows the EDX mapping of other elements present in IL and CPT fillers, demonstrating an excellent distribution within the polymer matrix.

4.4.2. Polymer phase content, thermal and mechanical properties

The influence of the incorporation of the different components into the polymer matrix at a molecular level was evaluated by ATR/FTIR (Figure 4.22a). The main absorption bands of PVDF-HFP, attributed to the stretching vibrations of the CF_2 and CH_2 groups of the polymer chains, are present at 976, 795, 763 and 678 cm^{-1} [7] in all samples, independently of the filler inclusion or processing method. The high intensity of the absorption band at 840 cm^{-1} indicates a high β phase content in the samples, which was quantified by means of equation 5. The β phase content is around 88% for all samples, regardless of the preparation method and components present (Table 4.13) due to the low temperature solvent evaporation [8]. In all the materials the polar β phase of PVDF-HFP is thus solely governed by the polymer content in the solutions and by solvent evaporation temperature. Therefore, this indicates that it is not influenced in the present case by the filler-polymer chain interactions [8].

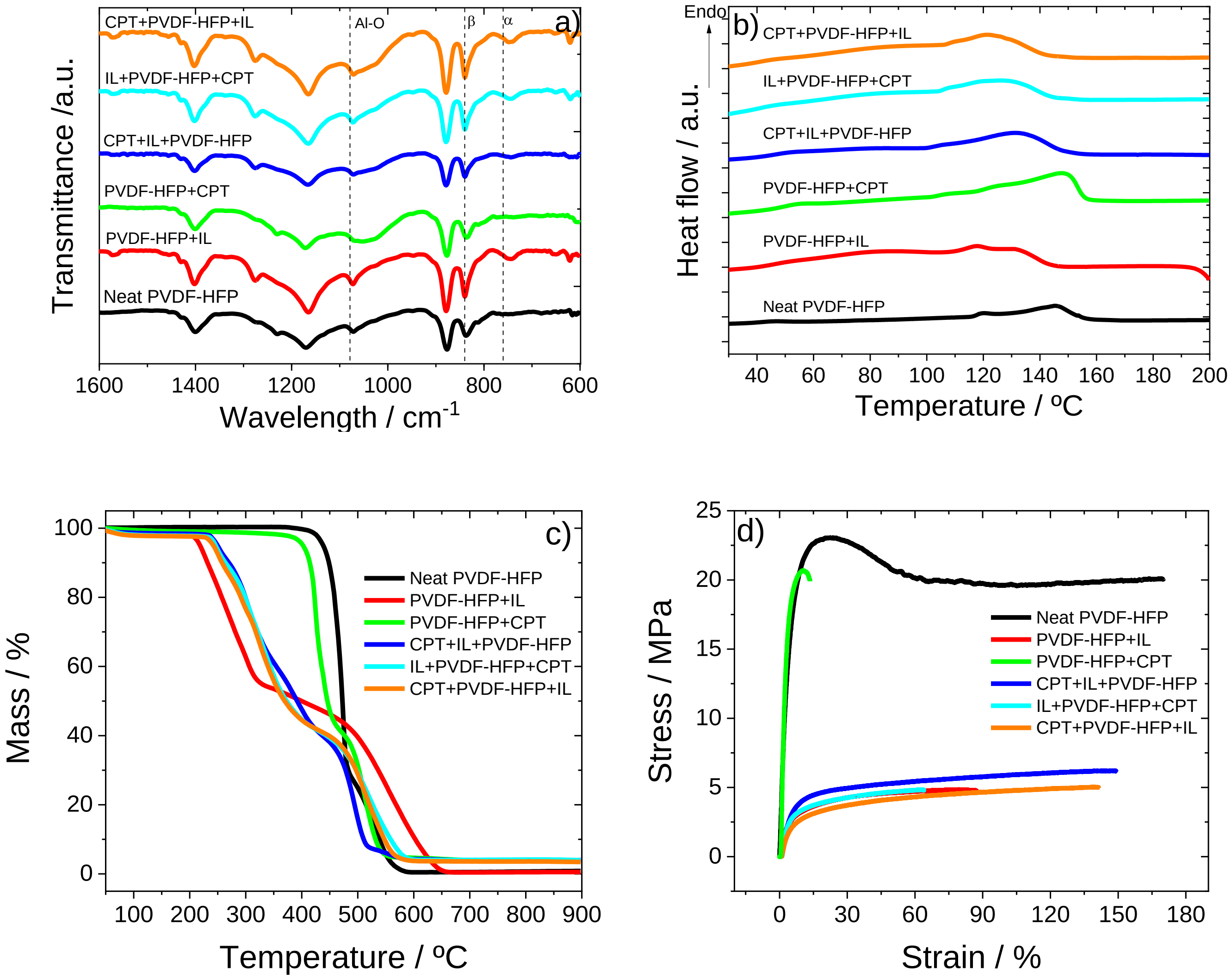

Figure 4.22 - Physical-chemical characterization of the samples: ATR/FTIR spectra (a), DSC curves (b) TGA curves (c) and stress-strain mechanical response (d).

Regarding CPT, the main band observed in the FTIR spectra is located at 1087 cm^{-1}, corresponding to the Al-O bonds [9]. This band is more intense in the PVDF-HFP+CPT, CPT+PVDF-HFP+IL and CPT+IL+PVDF-HFP samples than IL+PVDF-HFP+CPT, indicating the different interactions between the IL, the CPT and the PVDF-HFP, as previously. The lower intensity of this band in the IL+PVDF-HFP+CPT sample indicates a weakening of this bond originated by the interactions between CPT and the other two components.

Table 4.13 - β phase content, degree of crystallinity and main mechanical characteristic of the prepared samples.

Sample	**β phase ± 3 (%)**	**Δχ ± 2 (%)**	**Young Modulus ± 5% (MPa)**	**Yield Stress ± 5% (MPa)**	**Yield Strain ± 5 (%)**
Neat PVDF-HFP	87	13	373	22	14
PVDF-HFP+IL	89	14	51	3.2	8.2
PVDF-HFP+CPT	89	23	638	20.1	4.8
CPT+IL+PVDF-HFP	90	23	88	4.2	6.9
IL+PVDF-HFP+CPT	87	17	78	3.0	6.0
CPT+PVDF-HFP+IL	88	15	64	2.2	7.6

The DSC allowed evaluating the influence of CPT and IL addition on the thermal stability of the PVDF-HFP matrix (Figure 4.22b). A single endothermic peak above 120°C, mainly related to the melting of the polymer, is produced by all the samples, the behavior of which depended on the type of filler added to the PVDF-HFP matrix. Thus, the addition of CPT to the PVDF-HFP matrix resulted in an increase of the melting temperature of the composite up to 150°C, when compared to that of neat PVDF-HFP sample at 145°C. This effect is related to the zeolite filler affecting the nucleation and growth kinetics of the PVDF-HFP polymer during crystallization, as demonstrated by the increase of both melting temperature and degree of crystallinity (Table 4.13) [10]. Upon addition of IL, the melting temperature decreased due to the destabilization of the crystalline phase caused by the ion-dipole electrostatic interactions between the polymer matrix and the IL [11]. These interactions are also present in the composites with both components, revealing an increase of degree of crystallinity of the samples with CPT in comparison with the neat polymer. This effect is stronger when both dopants are added first, probably because of the IL imprisonment in the zeolite structure, leaving a smaller amount of free IL to interact with the polymer chains [12].

Figure 4.22c shows the TGA curves of all samples which exhibit the decomposition steps that correspond to the degradation of IL, CPT and polymer. The PVDF-HFP sample presents the typical one-step degradation curve of a polymer at around 475°C, in agreement with the literature [13]. The order of addition of the different fillers leads to different interactions between the different components (as discussed in the previous sections) that are reflected in the differences observed in the thermal degradation of the samples. For the PVDF-HFP+IL sample, while the first degradation step corresponds to the degradation of the IL, at around 265°C, the PVDF-HFP stability increases due to the electrostatic interactions with the IL. In the PVDF-HFP+CPT sample, the first step corresponds to the CPT degradation at around 450°C. This means that a higher thermal stability of the samples upon the addition of CPT into the PVDF-HFP, resulted with respect to the composite containing IL. The TGA curves of the composites with the three components show three degradation steps corresponding to the degradation processes of the IL, zeolites and polymer at 265, 375 and 500°C, respectively. Upon addition of CPT, the IL degradation temperature increased to around 300°C, due to the electrostatic interaction between the two components that prevent the immediate degradation of the IL [14].

The order of addition of the components affected the thermal stability of the composite electrolyte. The composite sample with the largest thermal stability is IL+PVDF-HFP+CPT due to the different zeolite interactions with the IL. These interactions are stronger for the CPT+IL+PVDF-HFP sample where the two components are added first. This fact is shown in the TGA curve with an increase and decrease in the degradation temperature of the first and second steps, respectively. For the other two samples, a slight shift to higher temperatures is observed in the PVDF-HFP degradation step, due to the bonding between the IL and the polymer.

Figure 4.22d shows the stress-strain curves for the samples studied. The pristine PVDF-HFP polymer shows the typical thermoplastic behavior of PVDF-based polymers with an elastic and a plastic regions separated by yielding [15]. The mechanical parameters for all samples are shows in Table 4.13 in which the Young modulus values were determined at 3% of maximum elongation in the elastic region by the tangent method. These data reveal that CPT acts as a mechanical reinforcement for the polymer matrix, leading to better mechanical properties. Its Young modulus, the largest of all the samples (Table 4.13), is attributed the increase in the rigidity of the polymer that results from the presence of the CPT particles, which restrict the polymer chain motion [16]. In contrast, the IL acts as a plasticizer, leading to poorer mechanical properties [2], as shown by the higher yield strain values displayed by IL-containing samples when compared to that of the PVDF-HFP+CPT sample. This effect is explained by the reduction of the overlapped polymer chains [17]. This fact is also observed for the composite samples comprising both components, showing that once the IL is present, its influence on the mechanical properties is much more important than that exerted by the zeolite filler. This fact is manifested by the reduction of the Yield stress values for all the samples incorporating IL, with respect to PVDF-HFP+CPT. The order in which the components are added affects the mechanical characteristics of the samples, namely the CPT+IL+PVDF-HFP, in which the interaction between the IL and the CPT increases the stiffness of the sample, improving the mechanical properties, even with respect to the PVDF-HFP+IL sample. This behavior is also related to the higher degree of crystallinity of the sample.

The above analysis of the physical-chemical properties allowed us concluding that the prepared three-component electrolytes are suitable for application in batteries, both at thermal and mechanical stability levels.

4.4.3. Electrochemical properties

The determination of the ionic conductivity of the electrolyte samples is of prime importance to evaluate their suitability for battery application [18]. Thus, the room temperature Nyquist plots of the prepared electrolyte samples comprising two components (CPT and IL) and that incorporating solely the IL are shown in Figure 4.23. Neat PVDF-HFP and PVDF-HFP+CPT show ionic conductivities of the order of 10^{-11} S cm^{-1}, a value that hinders these samples to be applied as SPE in the context of energy storage. The Nyquist plots are characterized by a semicircle located in the high-frequency range (inset in Figure 4.23a) that corresponds to the charge transfer process (bulk material properties), a transition controlled by the diffusion of counter-ions inside the electrode, and a straight line at lower frequencies related to the diffusion process [19]. Regardless of the composite sample, the linear region associated with the diffusion of ions indicates that this is the main mechanism of ion conduction due to the charge carrier species (i.e., the IL ions) and their mobility [20].

In addition, different values in the resistive part (ionic resistance calculated in the Z' axis) are observed for the three-component electrolytes prepared by the different method (Figure 4.23a). This finding is associated with the interactions that occur between IL, CPT and the PVDF-HFP matrix.

The Nyquist plot of the representative IL+ PVDF-HFP+CPT electrolyte at different temperatures. Figure 4.23b) demonstrates that the overall resistance of this material decreases with increasing temperature as a consequence of the increase in the polymer chain mobility, and the IL dissociation, which leads to an increase of the number of free ions [21].

The ionic conductivity of the samples was obtained from the Nyquist plots using equation 6 and is represented in Table 4.14 at 30 and 60°C.

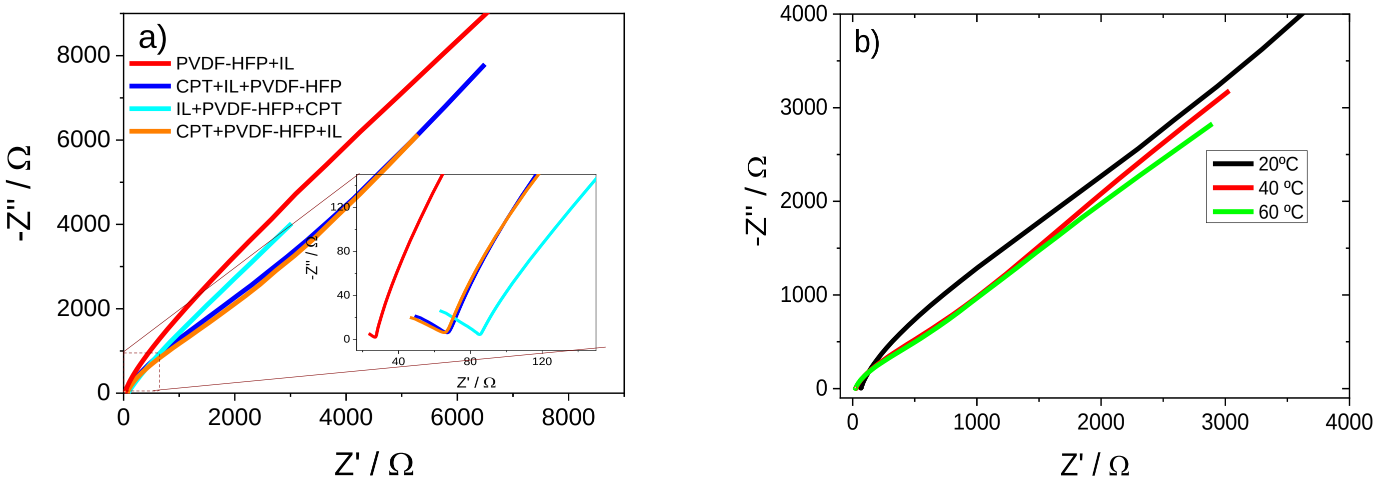

Figure 4.23 - Room temperature Nyquist plots for the prepared electrolytes (a) and Nyquist plot of the IL+PVDF-HFP+CPT electrolyte at different temperatures between 20 and 60°C (b).

The Arrhenius plots obtained from the ionic conductivity as a function of temperature for the set of electrolyte samples are shown in Figure 4.24. The room temperature ionic conductivity for the three-component electrolyte samples varies between 1.1×10^{-4} and 1.9×10^{-4} S cm^{-1}, which is lower than for the two-component PVDF-HFP+IL electrolyte (3.3×10^{-4} S cm^{-1}). The main reason for this result is the fact that in the latter sample the IL cations and anions are located in the spaces between the lamellae or between spherulites, as demonstrated in previous works [6], resulting in higher ionic conductivity value. For the samples with three components, the interaction between the IL and CPT, demonstrated by the ATR/FTIR and TGA data (Figures 4.22a and 4.22c), leaves less free IL on the surface of the samples, which reduces its effect on the ionic conductivity, as shown in Figure 4.24a.

There is a clear influence of the preparation method on the ionic conductivity, associated with the strength of the electrostatic interactions between the IL and CPT. There is a significant enhancement of the ionic conductivity of CPT+IL+PVDF-HFP with increasing temperatures, indicating a significant increase in the mobility and number of free charge carriers in the system, that can be attributed to the weakening of the IL-CP interactions with increasing temperature. On the other hand, the IL+PVDF-HFP+CPT sample shows stronger electrostatic interaction between polymer and IL and lower with the CP, that is added latter during the preparation of the samples, which results in a lower IL-CP interaction and lower dependence of the ionic conductivity with increasing temperature.

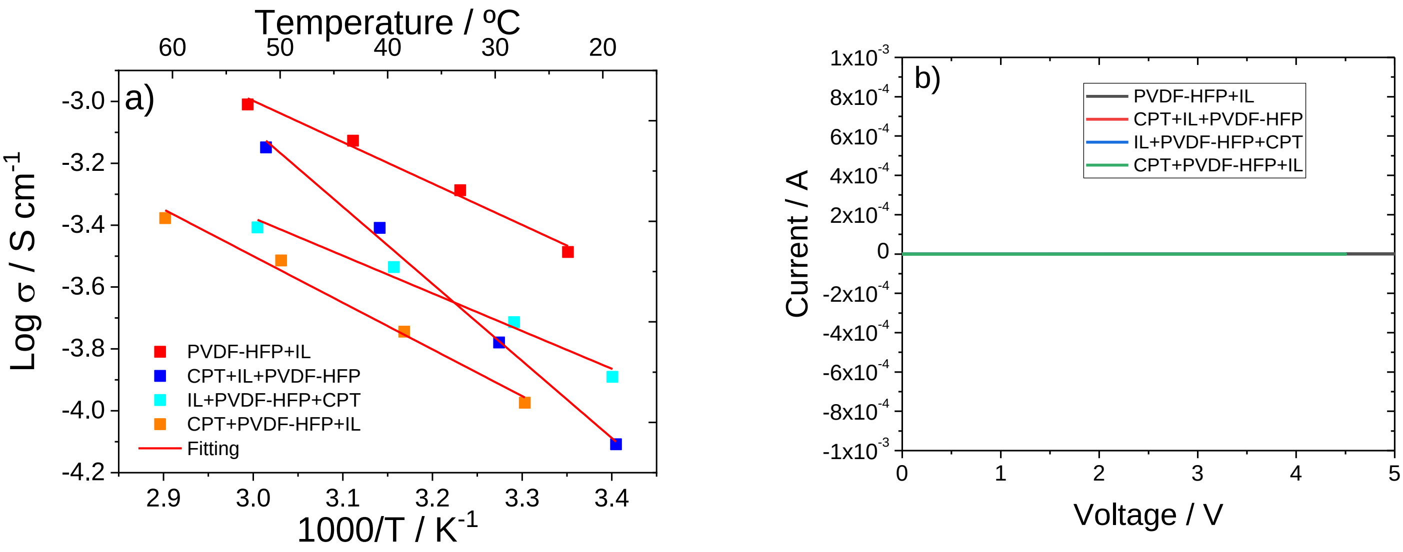

Figure 4.24 - Ionic conductivity as a function of temperature (a) and cycle voltammetry (b) for the prepared electrolytes.

Equation 7 allowed to obtain the activation energy of the samples, the values being presented in Table 4.14. It is demonstrated that the values of the activation energy are similar for all samples, except for CPT+IL+PVDF-HFP, resulting from the stronger interaction between both components, as pointed out by the TGA and ATR/FTIR results.

Table 4.14 – Ionic conductivity (σ_i) at 30 and 60 °C and activation energy of the electrolytes.

Sample	**Ionic conductivity ($S\ cm^{-1}$)**		**E_a ($kJ\ mol^{-1}$)**
	25°C	**60°C**	
PVDF-HFP+IL	3.3×10^{-4}	9.8×10^{-4}	11.1
CPT+IL+PVDF-HFP	1.7×10^{-4}	7.1×10^{-4}	20.7
IL+ PVDF-HFP+CPT	1.1×10^{-4}	3.1×10^{-4}	10.1
CPT+ PVDF-HFP+IL	1.9×10^{-4}	3.9×10^{-4}	12.5

The ionic conductivity values obtained for these samples are in the range of suitability for being used in LIBs [22]. Electrochemical stability of the prepared films was determined at 25°C and 0.01 V s^{-1} (figure 4.24b). The polymer electrolyte films showed good electrochemical stability, independently of the preparation method and the scan rate, without any anodic and cathodic peak. Electrochemical potential range determined for these samples demonstrate that these solid polymer electrolytes show the required specifications to be used in lithium-ion batteries. In addition, the compatibility of the prepared films with metallic lithium was evaluated in symmetric lithium cells, being shown an excellent compatibility for all samples as represented in Figure 6.6 (Annex II) for IL + PVDF-HFP + CPT, as representative sample.

4.4.4. Battery performance

On the basis of the good ionic conductivity values obtained for the different electrolyte samples, half-cell cathode batteries were assembled to test their performance and cycling stability as SPE. The obtained results at room temperature are presented in Figure 4.25. Figure 4.25a shows the comparison of the discharge capacity value at C/15-rate between the different samples, together with their coulombic efficiency of ~95%, which demonstrates the excellent reversibility of the process for all samples. Initially all samples had a high discharge capacity value around 150 mAh g^{-1}. After 10th cycle the PVDF-HFP+IL sample was not stable, resulting in a decrease of discharge capacity. This behavior is attributed to the IL charges movement from the inside to the surface of the polymer matrix during cycling [6]. Regardless of the preparation method, the addition of the zeolite improved the stabilization of the battery performance. It is also clear that the preparation method affects battery performance, as observed in the 50 cycle experiments, and the best cycling behavior was observed for IL+PVDF-HFP+CPT and CPT+PVDF-HFP+IL, where the activation energy is lower and the ion mobility is higher resulting from weaker interactions between the components. The IL+PVDF-HFP+CPT sample shows a capacity retention about 76% after 50 cycles against 8% for the PVDF-HFP+IL sample.

Figure 4.25b shows the charge/discharge profiles between 2.5 and 4.2 V vs. Li^+/Li of the different electrolyte samples at the 5 and 25th cycles at C/15-rate. Independently of the sample, the typical profile of the LFP active material ascribed to the Fe^{2+}/Fe^{3+} redox couple reaction resulted, corresponding to the extraction and insertion of lithium ions in the structure [23]. Figure 4.25b allows concluding that the IL+PVDF-HFP+CPT electrolyte is the most stable over cycling. Figure 4.25c shows the rate performance of IL+PVDF-HFP+CPT sample at various C-rates (C/15 to C/2) over 10 cycles for each rate. It is to notice for the C-15 rate, that the discharge capacity initially increases as a function of the cycle number due to the formation of the SEI [24]. An excellent battery performance was observed at different C-rates, with discharge capacity values close to the theoretical value of LFP active material (170 mAh g^{-1}) at C/15-rate, and being able to deliver about 45 mAh g^{-1} even at the C/2 rate where the discharge capacity value decreases with increasing the C-rate due to the ohmic drop effect. For each C-rate, the discharge capacity is stable along the 10 cycles [25]. The coulombic efficiency of the cell is about 95% for most of the cycles, despite being reduced on the first ones due to the time it takes to fully activate the system and create the interface [26]. Figure 4.25d shows the charge/discharge profile of the 5th cycle at different rates for the IL+PVDF-HFP+CPT sample, showing the typical voltage plateau for the LFP cathode between 3.3 and 3.6 V, as well as the loss of capacity associated with the increase of the cathode's polarization, resulting from the higher applied discharge rates [23].

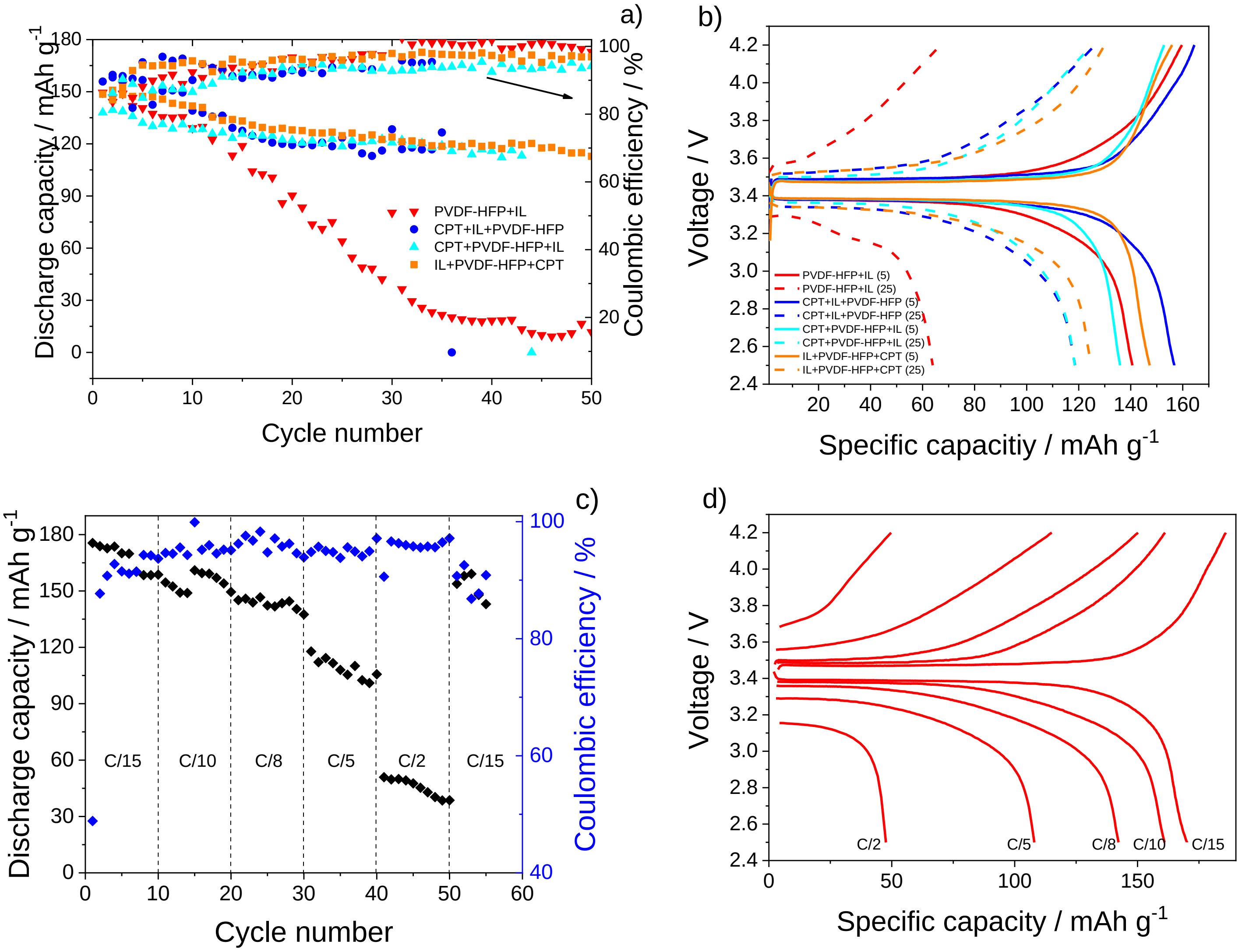

Figure 4.25 - Comparison of the cycling stability of the electrolytes at C/15, together with the corresponding coulombic efficiency (a); charge/discharge profiles at the 5th and 25th cycles for the different samples (b); rate performance for IL+PVDF-HFP+CPT sample at room temperature (c); charge/discharge profile for IL+PVDF-HFP+CPT at the 5th cycle for different rates (d).

Figure 4.26 shows the schematic representation of the proposed ion transport mechanism in the three-component electrolyte in comparison with that in the PVDF-HFP+IL sample.

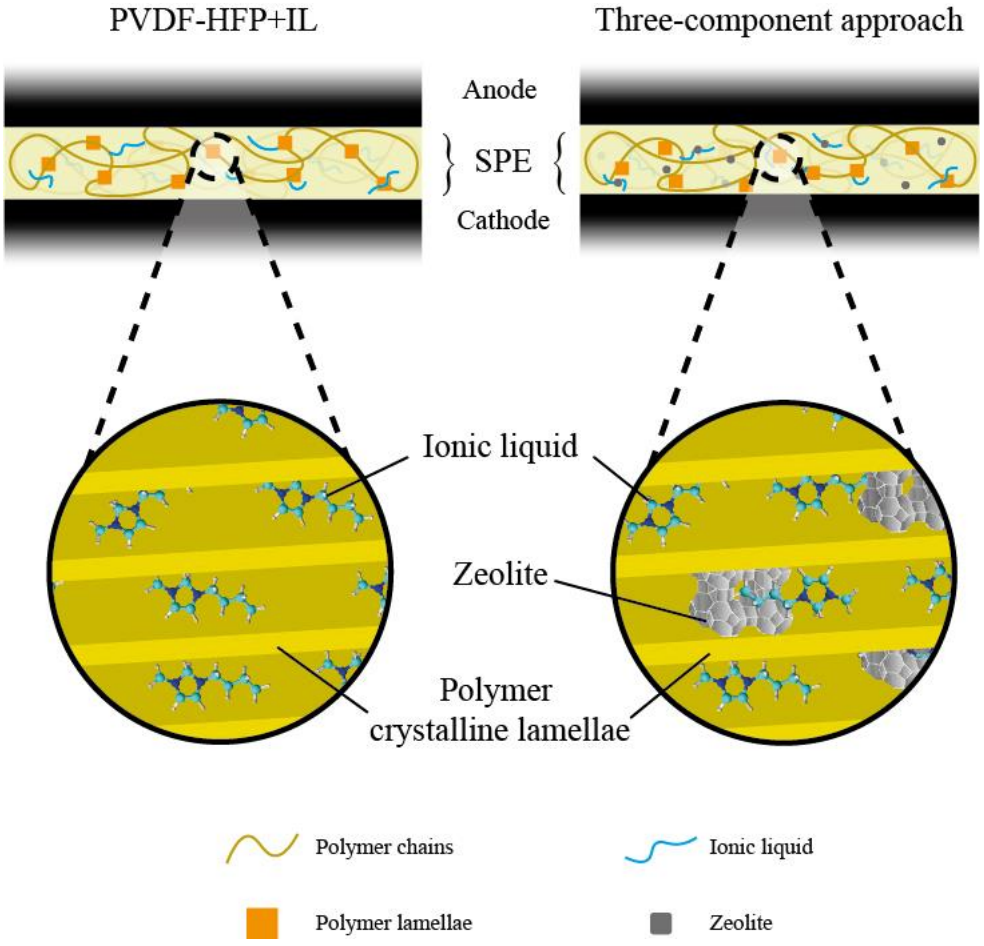

Figure 4.26 - Schematic representation of the lithium-ion transport mechanism in the PVDF-HFP+IL and PVDF-HFP with IL and CPT.

The addition of the zeolite and its interaction with the other components increases the overall stability of the system and affects the amount of the free charges and their mobility in the composite. This mechanism is supported by the new bands observed in the ATR/FTIR (Figure 4.22a) spectra for the samples with CPT and the increase in the thermal stability in the TGA curves (Figure 4.22c). This results in an improvement of the electrochemical properties, enhancing the cycling performance of the assembled batteries.

To better understand the battery performance of the samples, impedance spectroscopy analysis was performed before and after cycling. Figure 4.27 shows the Nyquist plots of all the electrolyte samples that are characterized by a semicircle that described the overall resistance in the high and medium frequency region, a straight line in the low frequency region that is associated with the Li^+ diffusion process, and capacitance element that describes the differential intercalation of the active material. This behavior is characterized by the equivalent circuit shown in the insert of Figure 4.27a. The overall resistance (R_T) is the sum of the ohmic resistances (R_1), that represents the contact film resistance (R_2) and resistance contributions from the charge-transfer reaction resistance (R_3). The resistances before cycling (Figure 4.27a) were evaluated from the equivalent circuit and the obtained values for R_2 are 232, 379, 452, and 447 Ω, and for R_T are 480, 800, 945 and 950 Ω for PVDF-HFP+IL, CPT+IL+PVDF-HFP, IL+PVDF-HFP+CPT and CPT+PVDF-HFP+IL, respectively. It is observed that before cycling the IL has the major role in the conduction, as the sample without CPT is the one with the lowest resistance, and that the preparation method affects the electrical resistance of the film based on variations in the aforementioned interactions between the different SPE components and, in particular, between IL and CP.

Regardless of the sample, the overall resistance after cycling increased due to the formation of SEI layer during cycling as shown in Figure 4.27b [27].

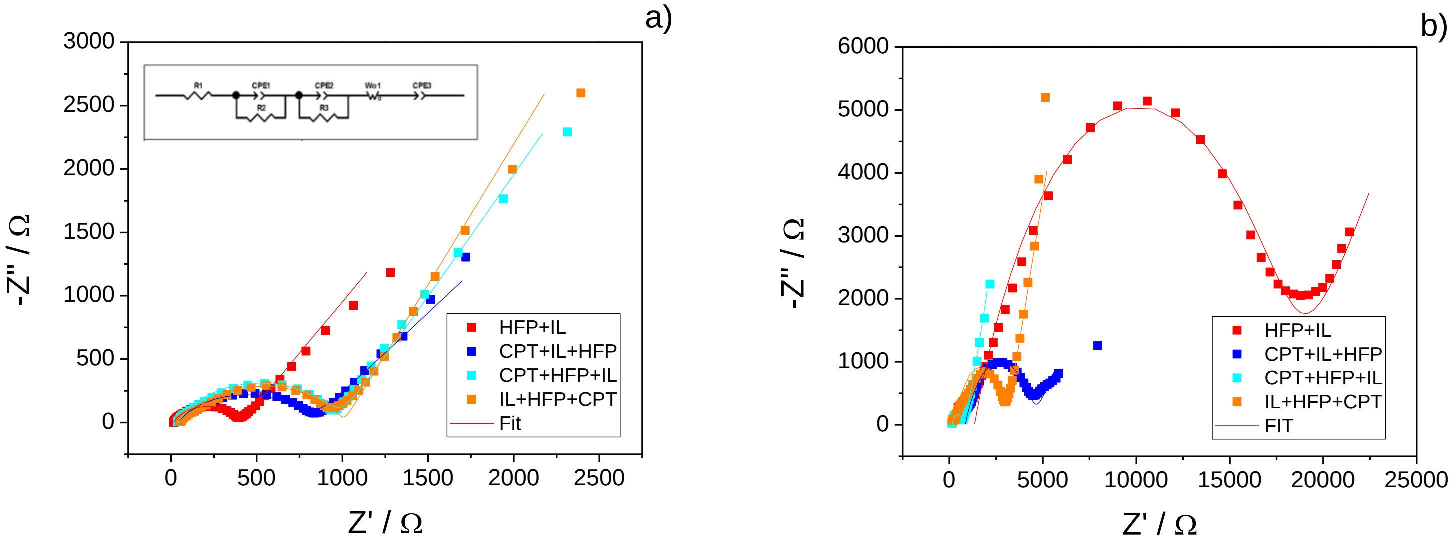

Figure 4.27 - Nyquist plot of the assembled batteries before (a) and after (b) cycling with the corresponding fit with the equivalent circuit shown as inset in (a).

However, after cycling, both the R_2 (927 Ω) and R_T (18810 Ω) of PVDF-HFP+IL increased significantly, due to the migration of the IL to the surface of the SPE during cycling. On the other hand, the samples with CPT showed a smaller increase in R_T (710, 2996 and 4526 Ω for CPT+IL+PVDF-HFP, IL+PVDF-HFP+CPT and CPT+PVDF-HFP+IL, respectively) because of the stabilization effect of the CPT that kept the IL in the SPE structure, consequently improving the cycling behavior. The R_2 is reduced when compared with before cycling batteries (116, 214 and 725 Ω for CPT+IL+PVDF-HFP, IL+PVDF-HFP+CPT and CPT+PVDF-HFP+IL, respectively) due to the SEI stabilization during the cycling process.

As a summary, Table 4.15 shows the comparison of the results obtained for the electrolytes developed in this work with literature data. The obtained results for ionic conductivity value and cycling behavior are in line or even better than those reported in the literature, particularly due to the fact that the battery performance reported here regards room temperature, which clearly represents a step forward in the solid-state technology. Particularly this work presents a cycling performance similar to the reported literature with zeolite materials in its structure, despite the higher temperatures used in the previous work. Furthermore, when compared to conventional battery technology, the main advantages of the presented SPE technology are the higher thermal and mechanical stability of the battery, due to the removal of the liquid electrolyte, which allows to increase safety and reduce environmental impact.

Table 4.15 – Comparison of the behavior of the proposed electrolytes with the best data from the literature, including two and three-component approaches.

Polymer	Fillers	Technique processing	Ionic Conductivity (S cm^{-1})	Battery capacity of LFP batteries (mAh g^{-1})	Ref
PVDF	LiTFSI, $LiSnZr(PO_4)_3$	Solvent casting	5.76×10^{-5} (27°C)	133 (C/10); 25°C	[28]
PVDF	$LiClO_4$, LLTO		5.8×10^{-4} (25°C)	152 (C/5); 25°C	[29]
PVDF-HFP	LiTFSI, LLZTO		8.80×10^{-5} (25°C)	158.7 (C/10); 25°C	[30]
PVDF-HFP	IL@UiO-67		4.3×10^{-4} (25°C)	118 (1C); 25°C	[31]
PVDF	UiO-66, LiTFSI		2.07×10^{-4} (25°C)	136 (1C); 25°C	[32]
PEO	SSZ-13, LiTFSI		5.34×10^{-2} (70°C)	154 (C/10); 60°C	[33]
PVDF-HFP	CPT, [BMIM] [SCN]		1.1×10^{-4} (30°C)	160.3 (C/15); 25°C	This work

Thus, this work reports on a novel combination between a zeolite structure and an IL, resulting in a fully functional high-performance room temperature electrolyte, with high conductivity and high mechanical/thermal stability. In the developed electrolyte system, the zeolite works as a thermal and mechanical stabilizer, through the interactions established with the polymer, whereas the IL induces the increase of the ionic conductivity and improvement of battery performance. The importance of the preparation method in the SPE properties and battery performance is also highlighted, showing that the different interactions that are formed upon different order of addition of the components play a key role in the characteristics of the final materials. This is an important result that must be kept in mind in related SPE development processes.

Thus, the combination and application of zeolites and ILs for the development of SPEs has the potential to be effectively applied in the future generation of room temperature solid-state batteries, leading to excellent performance and stability, as well as taking advantage of more sustainable materials such as natural CPT.

4.4.5. Conclusion

PVDF-HFP films were prepared and applied as SPEs for LIBs, in a three-component approach, using CPT and ILs as doping agents. CPT was used as a stabilizer for the mechanical and thermal properties while the IL allowed to improve the ion conductivity of the SPE. Different preparation methods were used, and their influence on the SPE properties was analyzed. We showed that the order of addition of the components has a significant influence on the film structure and polymer crystallization. The ATR/FTIR analyses shows differences in the intensity of the absorption band characteristic of the CPT indicating that the preparation method influences the strength of the electrostatic interactions that occurs between the IL and CPT. Further, the CPT have a stabilizing effect in the SPE, as proven by the thermal and mechanical properties. The variation of the ionic conductivity over temperature was also affected by the preparation method, with the measured values (up to 1.9×10^{-4} S·cm^{-1} at 30°C) being suitable for application in batteries. The different SPEs assembled into the batteries demonstrated an enhancement in the battery stability during 50 cycles, when compared with the SPEs devoid of CPT, with an excellent discharge capacity value of 160.3 mAh g^{-1} at C/15-rate and room temperature for the IL+PVDF-HFP+CPT sample. The assembled batteries also show a good behavior in fast charging, being able to deliver 45 mAh g^{-1} at C/2-rate. The promising results reported in this work represent an interesting option for future generation of safer, more durable and environmentally friendlier solid-state batteries, by overcoming the present limitations at room temperature operation.

4.4.6. References

1. Ma, W., H. Yuan, and X. Wang, *The Effect of Chain Structures on the Crystallization Behavior and Membrane Formation of Poly(Vinylidene Fluoride) Copolymers.* Membranes, 2014. **4**(2): p. 243-256.
2. Serra, J.P., et al., *Ionic liquid based Fluoropolymer solid electrolytes for Lithium-ion batteries.* Sustainable Materials and Technologies, 2020. **25**: p. e00176.
3. Dzinun, H., M.H.D. Othman, and A.F. Ismail, *Photocatalytic performance of TiO2/Clinoptilolite: Comparison study in suspension and hybrid photocatalytic membrane reactor.* Chemosphere, 2019. **228**: p. 241-248.
4. Lopes, A.C., et al., *Influence of zeolite structure and chemistry on the electrical response and crystallization phase of poly(vinylidene fluoride).* Journal of Materials Science, 2013. **48**(5): p. 2199-2206.
5. Kajtár, D.A., et al., *Interfacial interactions and reinforcement in thermoplastics/zeolite composites.* Composites Part B: Engineering, 2017. **114**: p. 386-394.
6. Correia, D.M., et al., *Effect of Ionic Liquid Content on the Crystallization Kinetics and Morphology of Semicrystalline Poly(vinylidene Fluoride)/Ionic Liquid Blends.* Crystal Growth & Design, 2020. **20**(8): p. 4967-4979.

7. Martins, P., A.C. Lopes, and S. Lanceros-Mendez, *Electroactive phases of poly(vinylidene fluoride): Determination, processing and applications.* Progress in Polymer Science, 2014. **39**(4): p. 683-706.
8. Sousa, R.E., et al., *Microstructural variations of poly(vinylidene fluoride co-hexafluoropropylene) and their influence on the thermal, dielectric and piezoelectric properties.* Polymer Testing, 2014. **40**: p. 245-255.
9. Ruíz-Baltazar, A., et al., *Preparation and Characterization of Natural Zeolite Modified with Iron Nanoparticles.* Journal of Nanomaterials, 2015. **2015**: p. 364763.
10. Nunes-Pereira, J., et al., *Microporous membranes of NaY zeolite/poly(vinylidene fluoride–trifluoroethylene) for Li-ion battery separators.* Journal of Electroanalytical Chemistry, 2013. **689**: p. 223-232.
11. Meira, R.M., et al., *Ionic-Liquid-Based Electroactive Polymer Composites for Muscle Tissue Engineering.* ACS Applied Polymer Materials, 2019. **1**(10): p. 2649-2658.
12. Ntais, S., et al., *Ionic Liquid/Zeolite Composites: Synthesis and Characterization Using Vibrational Spectroscopy Techniques.* ECS Transactions, 2019. **33**(7): p. 41-47.
13. Polat, K., *Energy harvesting from a thin polymeric film based on PVDF-HFP and PMMA blend.* Applied Physics A, 2020. **126**(7): p. 497.
14. Saxena, P., B. Velaga, and N.R. Peela, *Ionic Liquid-Encapsulated Zeolite Catalysts for the Conversion of Glucose to 5-Hydroxymethylfurfural.* ChemistrySelect, 2017. **2**(32): p. 10379-10386.
15. Costa, C.M., et al., *Microscopic origin of the high-strain mechanical response of poled and non-poled poly(vinylidene fluoride) in the β-phase.* Journal of Non-Crystalline Solids, 2008. **354**(32): p. 3871-3876.
16. Metın, D., et al., *The effect of interfacial interactions on the mechanical properties of polypropylene/natural zeolite composites.* Composites Part A: Applied Science and Manufacturing, 2004. **35**(1): p. 23-32.
17. Jansen, J.C., et al., *High Ionic Liquid Content Polymeric Gel Membranes: Preparation and Performance.* Macromolecules, 2011. **44**(1): p. 39-45.
18. Yao, P., et al., *Review on Polymer-Based Composite Electrolytes for Lithium Batteries.* Frontiers in Chemistry, 2019. **7**(522).
19. Chang, B.-Y. and S.-M. Park, *Electrochemical Impedance Spectroscopy.* Annual Review of Analytical Chemistry, 2010. **3**(1): p. 207-229.
20. Park, M., et al., *A review of conduction phenomena in Li-ion batteries.* Journal of Power Sources, 2010. **195**(24): p. 7904-7929.
21. Ribeiro, C., et al., *Electroactive poly(vinylidene fluoride)-based structures for advanced applications.* Nature Protocols, 2018. **13**(4): p. 681-704.
22. Hassoun, J., et al., *A lithium ion battery using nanostructured Sn–C anode, LiFePO4 cathode and polyethylene oxide-based electrolyte.* Solid State Ionics, 2011. **202**(1): p. 36-39.
23. Gören, A., et al., *Influence of Solvent Evaporation Rate in the Preparation of Carbon-Coated Lithium Iron Phosphate Cathode Films on Battery Performance.* Energy Technology, 2016. **4**(5): p. 573-582.
24. Peled, E., D. Golodnitsky, and G. Ardel, *Advanced Model for Solid Electrolyte Interphase Electrodes in Liquid and Polymer Electrolytes.* Journal of The Electrochemical Society, 1997. **144**(8): p. L208-L210.
25. Ram, P., et al., *Improved performance of rare earth doped LiMn2O4 cathodes for lithium-ion battery applications.* New Journal of Chemistry, 2016. **40**(7): p. 6244-6252.
26. Xiao, Y., et al., *Understanding interface stability in solid-state batteries.* Nature Reviews Materials, 2020. **5**(2): p. 105-126.

27. Guo, J., et al., *Cyclability study of silicon–carbon composite anodes for lithium-ion batteries using electrochemical impedance spectroscopy.* Electrochimica Acta, 2011. **56**(11): p. 3981-3987.
28. Pareek, T., et al., *Effect of NASICON-type LiSnZr(PO4)3 ceramic filler on the ionic conductivity and electrochemical behavior of PVDF based composite electrolyte.* Journal of Alloys and Compounds, 2020. **824**: p. 153991.
29. Li, B., et al., *Biomimetic PVDF/LLTO composite polymer electrolyte enables excellent interface contact and enhanced ionic conductivity.* Applied Surface Science, 2021. **541**: p. 148434.
30. Lu, J., et al., *Hybridizing poly(vinylidene fluoride-co-hexafluoropropylene) with Li6.5La3Zr1.5Ta0.5O12 as a lithium-ion electrolyte for solid state lithium metal batteries.* Chemical Engineering Journal, 2019. **367**: p. 230-238.
31. Liu, K., et al., *In situ polymerized succinonitrile-based solid polymer electrolytes for lithium ion batteries.* Solid State Ionics, 2020. **345**: p. 115159.
32. Zhu, F., et al., *High-Performance Metal–Organic Framework-Based Single Ion Conducting Solid-State Electrolytes for Low-Temperature Lithium Metal Batteries.* ACS Applied Materials & Interfaces, 2019. **11**(46): p. 43206-43213.
33. Kim, J.H., et al., *Enhancement of ionic conductivity of a composite polymer electrolyte via surface functionalization of SSZ-13 zeolite for all-solid-state Li-ion batteries.* Journal of Materials Chemistry A, 2021.

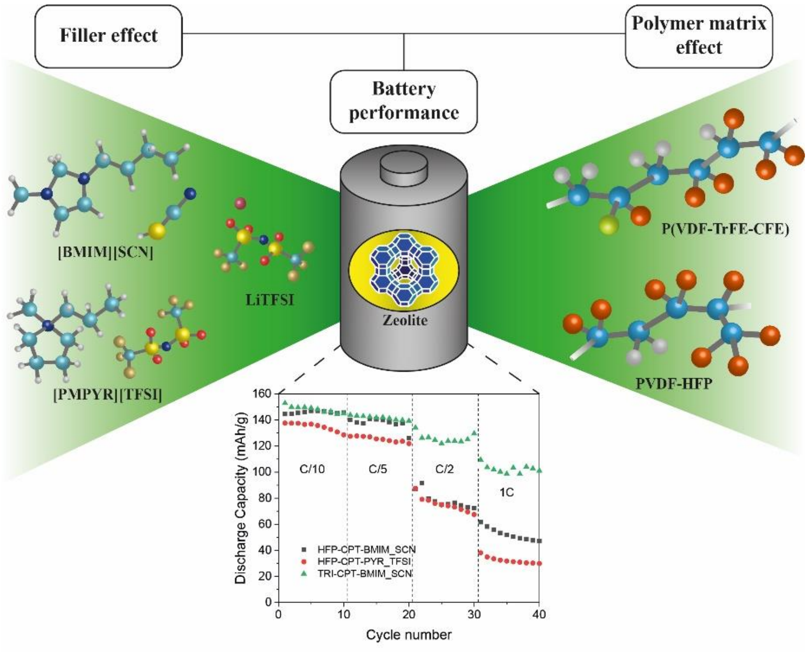

4.5. High performance ternary solid polymer electrolytes based on poly(vinylidene fluoride) copolymers with zeolite, lithium salt and ionic liquids for solid state lithium-ion battery applications

After the study of the optimization of the different parameters SPE materials and processing parameters, the best materials and experimental conditions were combined to achieve the best battery performance in this particular system. Also, other materials reported in the literature for high battery performance were applied. The effect of a high dielectric constant polymer was also studied, leading to an excellent battery performance, with high discharge capacities at high discharge rates.

Based on "High performance ternary solid polymer electrolytes based on poly(vinylidene fluoride) copolymers with zeolite, lithium salt and ionic liquids for solid state lithium-ion battery applications"; João C. Barbosa et. al, published in Applied Materials and Interfaces

The previously presented works allowed for the determination of a condition set for an optimized SPE. Thus, those conditions were applied in a single optimized SPE, consisting on ion exchanged CPT, [BMIM][SCN] IL and PVDF-HFP polymer, with an addition order of IL-polymer-zeolite, and a solvent evaporation temperature of 160°C. This SPE was accompanied with the production of other samples with the same conditions, but using some of the most successfully applied materials reported in the literature. It is the case of a lithium salt (LiTFSI) [1, 2] and the [PMPYR][TFSI] IL [3] (Figure 4.28). Also, a different approach was taken by replacing the widely used PVDF-HFP with the P(VDF-TrFE-CFE) terpolymer, which was never applied in LIBs before, and presents some interesting properties, such as outstanding mechanical stability and high dielectric constant (ε' = 40) [4].

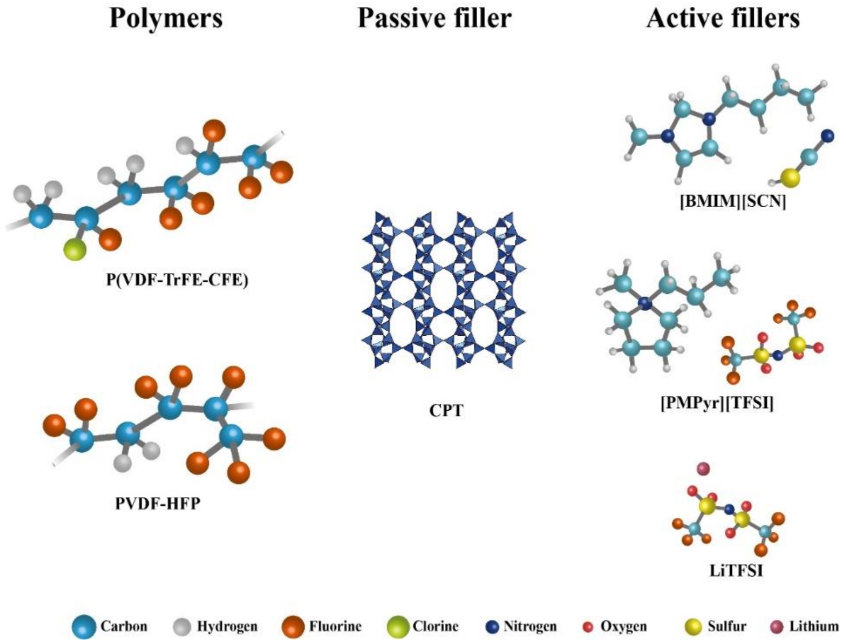

Figure 4.28 – Schematic representation of the materials used in the SPE preparation.

The samples were named after the materials used in their processing as follows: PVDF-HFP-CPT-[BMIM][SCN], PVDF-HFP-CPT-[PMPyr][TFSI], PVDF-HFP-CPT-LiTFSI and TER-CPT-[BMIM][SCN]. The component addition order was IL-polymer-zeolite. The samples were processed by doctor blade technique and the solvent was evaporated at 160°C for 15 min. The morphology of the samples was characterized by SEM, the structure by XRD and FTIR, the thermal properties by DSC and TGA and the mechanical properties by stress-strain tests. The electrochemical properties were assessed by impedance spectroscopy and cyclic voltammetry. Finally, batteries were evaluated in half cells. The experimental details can be found in section 3.

4.5.1. Morphological analysis

The morphology of the samples was evaluated using SEM (figure 4.29). The surface images of the samples show a good homogeneity and distribution of the fillers indicating a suitable compatibility between all the components.

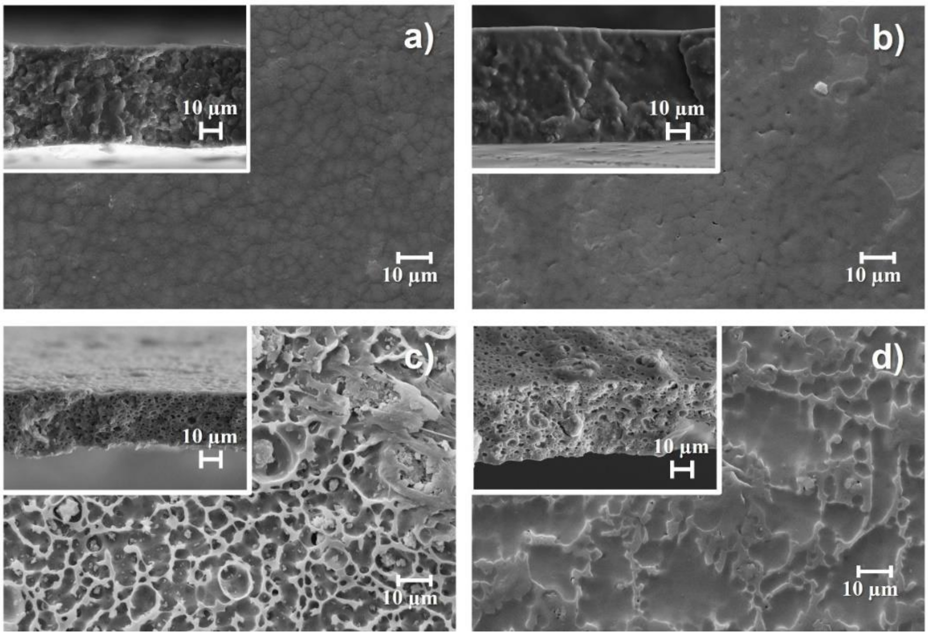

Figure 4.29 – SEM surface and cross section images of the PVDF-HFP-CPT-[BMIM][SCN] (a), PVDF-HFP-CPT-[PMPyr][TFSI] (b), PVDF-HFP-CPT-LiTFSI (c) and TER-CPT-[BMIM][SCN] (d) samples.

These findings lead us to conclude that the presence of the fillers leads to the inhibition of the spherulite growth, resulting in a large number of small spherulites throughout the samples [34]. This is particularly visible in the case of the PVDF-HFP/IL samples (figures 4.29a and 4.29b), as the ILs act as a nucleation agent for crystallization in the PVDF-HFP matrix [23]. On the other hand, upon addition of the LiTFSI salt (figure 4.29c), a homogeneous porous structure was formed due to a phase separation process during polymer crystallization, ascribed to the interaction of the Li+ salt with the solvent [35]. A similar behavior is also visible for the P(VDF-TrFE-CFE) matrix, in contrast with the PVDF-HFP one for the same filler (CPT and [BMIM][SCN]), which presents a large microporous network along the cross-section (figure 4.29d) due to a phase separation process ascribed to the different nature of the polymer matrix and its interaction with the solvent [36].

Figure 4.30a) shows the XRD patterns for the SPE samples, demonstrating a similar trend in all cases. In fact, the typical peaks of PVDF-HFP and P(VDF-TrFE-CFE) polymers at $2\theta = 17.9$, 18.6, 20.1 and 26.9° are not observed, due to the high filler loading in the samples [31]. The degree of crystallinity of the samples was calculated from these XRD patterns, and the results are provided in table 4.16. The crystallinity of the samples is independent of the IL and polymer matrix used, due to the high IL content that hinders polymer crystallization [37]. In the PVDF-HFP-CPT-LITFSI sample, the crystallinity was further reduced due to the complexation of the salts by the polymer matrix [38].

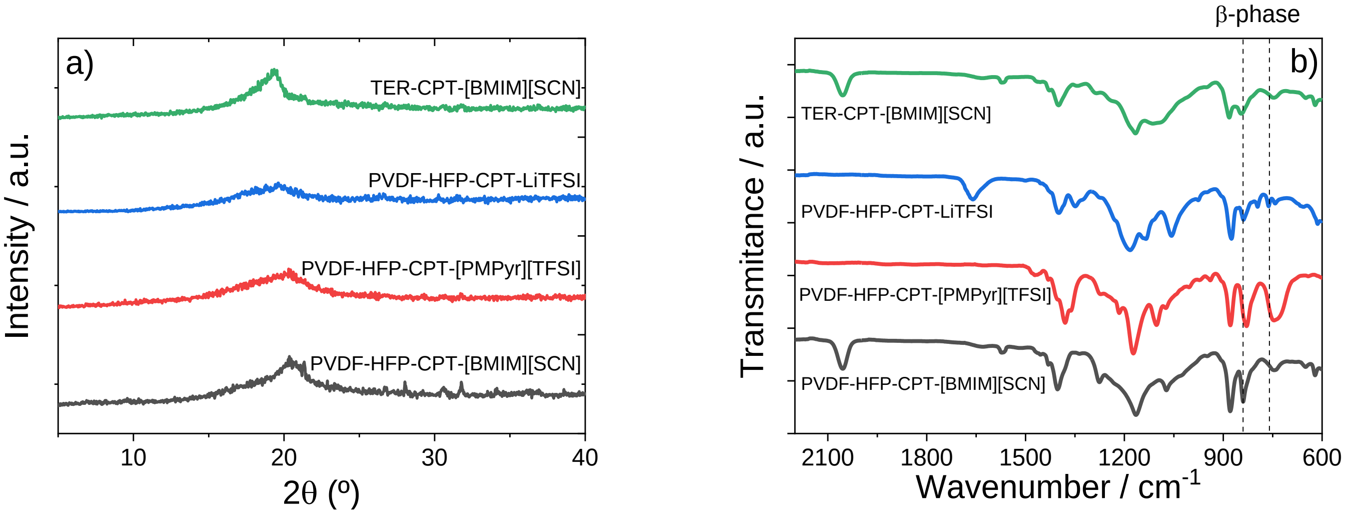

Figure 4.30 – XRD patterns (a) and ATR/FTIR spectra (b) of the prepared samples.

The influence of the fillers on the polymer chain conformation was analyzed using ATR/FTIR spectroscopy (figure 4.30b). The stretching vibration of the CF_2 and CH_2 groups of the polymer chains are observed at 976, 795, 763, and 678 cm^{-1}, regardless of the sample [31]. The 840 and 760 cm^{-1} bands, which are characteristic of the polar β phase conformation of PVDF, show high intensity in the spectra, pointing out the high content of this phase in the samples. This is confirmed by the β-phase content determination based on equation 5 (Table 4.16). The high β-phase content is attributed to the role of the ILs as nucleation agents, which lead to strong ion-dipole interactions which promote the crystallization of the polymers in the all-trans planar zigzag conformation [37]. The low β-phase content value calculated for the PVDF-HFP-CPT-[PMPyr][TFSI] sample may be attributed to the overlapping of the characteristic α phase bands with those of the [PMPyr][TFSI] IL, which affect the phase calculation.

Table 4.16 – Calculated values for β-phase content and crystallinity degree of the samples

Sample	β-phase (%)	Crystallinity degree (%)
PVDF-HFP-CPT-[BMIM][SCN]	87.4	26.3
PVDF-HFP-CPT-[PMPyr][TFSI]	46.2	26.3
PVDF-HFP-CPT-LiTFSI	74.6	21.7
TER-CPT-[BMIM][SCN]	81.2	26.1

4.5.2. Thermal and mechanical properties

DSC analysis was used to evaluate the thermal behavior of the samples (figure 4.31a). The polymer melting peak expected at about 145 °C is present in all samples [15], with a slight shift to lower temperatures due to the breakdown of the crystalline polar phase of the polymer, resulting from its electrostatic interactions with the IL [39]. The exception is the PVDF-HFP-CPT-LiTFSI sample, in which the endothermic peak is shifted to higher temperatures due to the overlapping of the polymer melting peak with a LiTFSI solid-solid transition at 152°C [40].

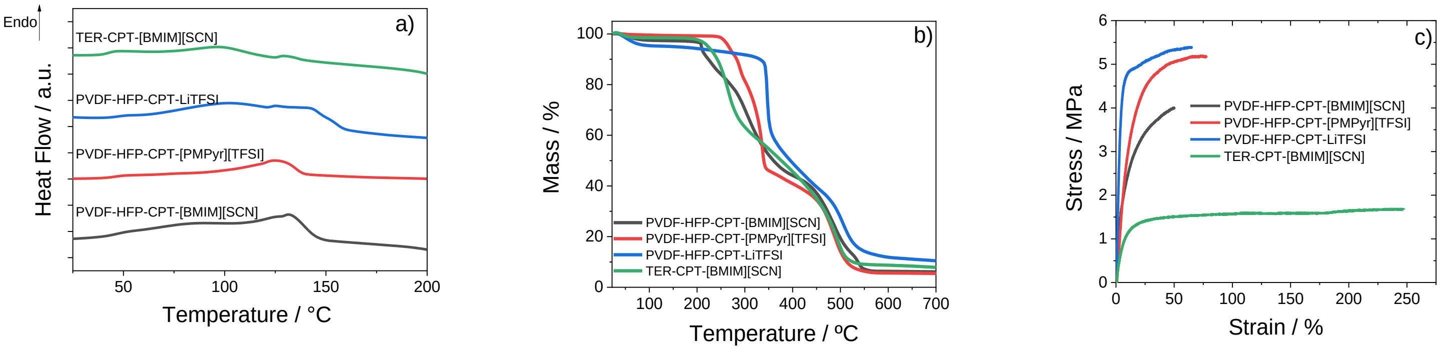

Figure 4.31 – DSC (a), TGA (b) and stress-strain (c) curves of the prepared samples.

Regarding the samples' thermal degradation, TGA data (figure 4.31b) show that all samples present distinct degradation steps corresponding to the different components. The PVDF-HFP and P(VDF-TrFE-CFE) degradation steps attributed to the scission of carbon–hydrogen (C–H) bonds is overlapped with the degradation step of the CPT at about 475°C [41]. The degradation step of the ILs are around 265 and 320°C for [BMIM][SCN] and [PMPyr][TFSI], respectively. These values are slightly higher to those found in the literature due to the CPT interaction with the ILs previously reported [15], which delays their thermal degradation. The TGA curve of the PVDF-HFP-CPT-LiTFSI sample presents an extra mass loss below 100°C associated with water evaporation from the salt structure, and the degradation step of the LiTFSI at around 350°C, which is in line with the reported values [42].

The stress-strain mechanical curves of these samples are shown in Figure 4.31c, showing the mechanical characteristic behavior of a thermoplastic polymer [43]. In this curve, the elastic and plastic region separated by the yield region are affected by the presence of the fillers. The mechanical tests show the typical mechanical reinforcement effect of the CPT due to the restriction of the polymer chain motion, as proven by the Young modulus values presented in Table 4.17 [44]. The Young modulus values were determined by the tangent method, at 3% of maximum elongation in the elastic region, and they are lower than those obtained for the pristine PVDF-HFP polymer [15]. The Young modulus of the PVDF-HFP-CPT-

LiTFSI sample is the highest among the prepared samples, and is ascribed to the strongest interaction of the salt with the high dielectric polymer, leading to a more rigid response [45]. Regarding the polymer matrix, the use of the P(VDF-TrFE-CFE) proves to significantly increase the mechanical stability of the samples, which are able to stretch more than 250% of their initial length without breaking, as previously observed [6].

Table 4.17 – Young modulus and yield strength values of the samples obtained from the stress-strain tests.

Sample	Young modulus (MPa)	Yield Strength (MPa)
PVDF-HFP-CPT-[BMIM][SCN]	59	1.54
PVDF-HFP-CPT-[PMPyr][TFSI]	39	1.05
PVDF-HFP-CPT-LiTFSI	92	3.37
TER-CPT-[BMIM][SCN]	12	0.59

4.5.3. Electrochemical properties

Electrochemical characterization is an effective way to evaluate the suitability of a SPE to be applied in LIBs [46]. The ionic conductivity was determined using electrochemical impedance spectroscopy at different temperatures. The room temperature Nyquist plots of the samples are presented in Figure 4.32a. Usually, the Nyquist plots present three well defined regions: a semicircle at the high-frequency range, corresponding to the charge transfer process, a transition corresponding to the diffusion of counter-ions in the electrode, and a straight line at lower frequencies representing the diffusion process [47].

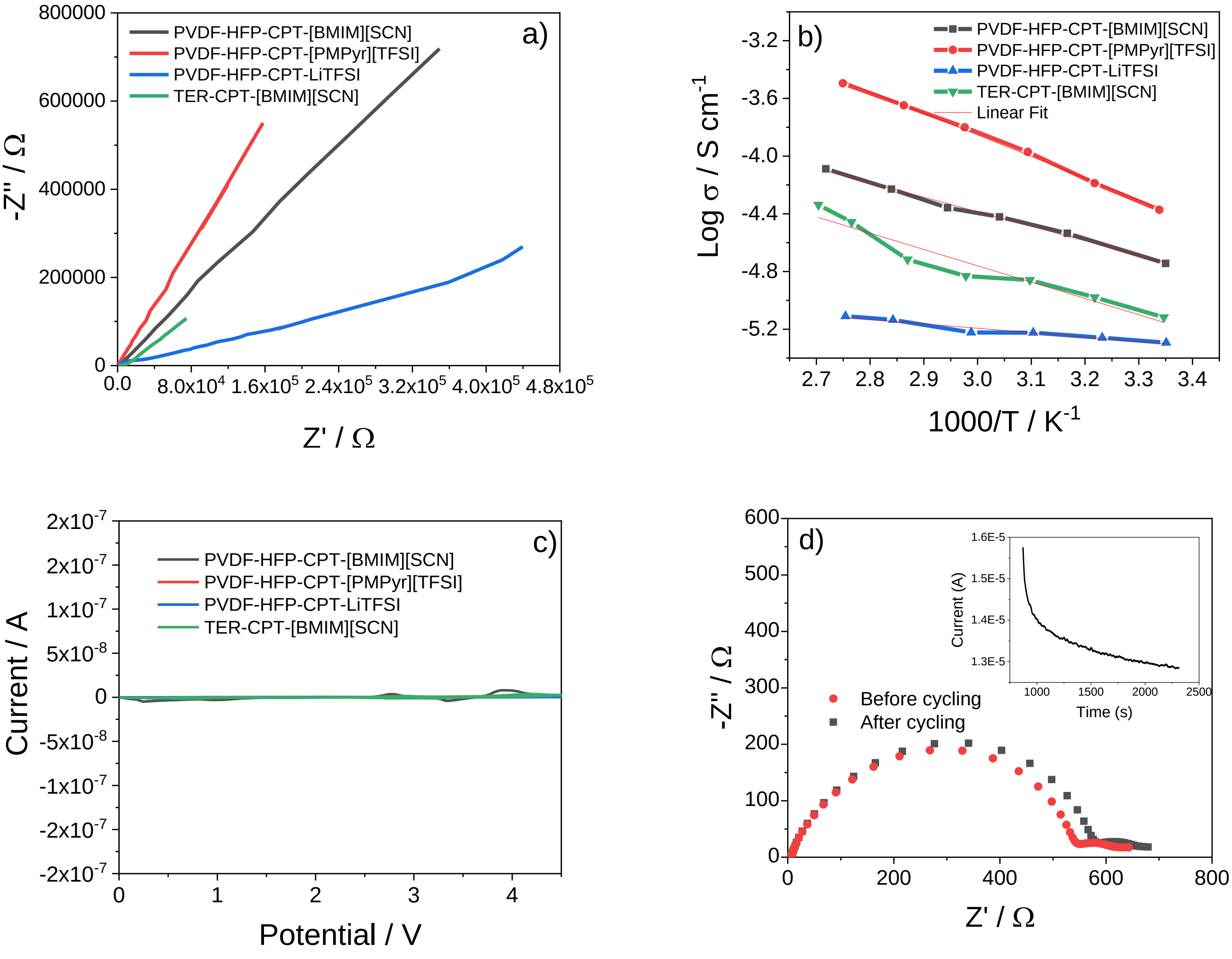

Figure 4.32 – Nyquist plots of the prepared samples at room temperature (a), and ionic conductivity as a function of temperature (b). Cyclic voltammogram of the prepared samples (c); chronoamperometry of the highest Li^+ transference number sample, PVDF-HFP-CPT-[PMPyr][TFSI] sample (d).

In this particular case, the semi-circle is not visible, meaning that the main conduction mechanism in these samples is the diffusion of ions, represented by the straight line, which is attributed to the high number of mobile charge carriers provided by the IL and the Li^+ salt [48]. The ionic conductivity was calculated from the Nyquist plots at different temperatures, and the results are shown in the Arrhenius plots of figure 4.32b. The typical increase of ionic conductivity with increasing temperature is observed due to the higher mobility of the ionic species and of the polymer chains [36]. The levels of ionic conductivity are lower for the PVDF-HFP-CPT-LiTFSI sample due to the salt interaction with the polymer matrix resulting in the complexation of these components, and to a limited number of free charges when compared to the ILs [15]. Also, it is observed that IL type and polymer matrix affect the ionic conductivity due to the electrostatic interaction between the IL cations and anions and the polymer chains. The highest ionic conductivity value of 4.2×10^{-5} S cm^{-1} at room temperature was measured for the PVDF-HFP-CPT-[PMPyr][TFSI] sample. The ionic conductivity values for all samples at room temperature and 60°C are presented Table 4.18.

The samples' thermal activation energy was calculated from the Arrhenius equation, and the results are similar for all samples (Table 4.18) and in line with those reported in literature for related systems [26]. The exception is the PVDF-HFP-CPT-LiTFSI sample, for which the activation energy is lower due to the interaction of the charged species with the polymer matrix.

Further electrochemical analysis was carried out using cycling voltammetry to evaluate the electrochemical stability of the samples at different voltage conditions. There are no significant peaks observed for any sample in the voltage range of battery operation as shown in figure 4.32c, indicating their stability for the application.

Table 4.18 – Obtained values for ionic conductivity at different temperatures, activation energy and lithium transference number, in the prepared samples.

Sample	**Ionic conductivity 25°C (S cm^{-1})**	**Ionic conductivity 60°C (S cm^{-1})**	**Activation Energy (kJ mol^{-1})**	**Li^{+} transference number**
HFP-CPT-BMIM_SCN	$1{,}8\times10^{-5}$	$4{,}4\times10^{-5}$	8.4	0.53
HFP-CPT-PYR_TFSI	$4{,}2\times10^{-5}$	$1{,}6\times10^{-4}$	12.5	0.59
HFP-CPT-LiTFSI	$5{,}1\times10^{-6}$	$5{,}9\times10^{-6}$	2.5	0.32
TRI-CPT-BMIM_SCN	$7{,}6\times10^{-6}$	$1{,}5\times10^{-5}$	9.4	0.42

The lithium transference number was calculated following the Bruce-Vincent method [49], and the obtained values are presented in Table 4.18. There seems to be a correlation between the ionic conductivity and the lithium transference number for the different samples, as they vary in the same way. The highest value of 0.59 is obtained for the PVDF-HFP-CPT-[PMPyr][TFSI], as shown in figure 4.32d. High values near or above 0.5 are a good indicator of the Li+ diffusion capacity in the prepared samples, proving their suitability for application in LIBs.

4.5.4. Battery performance

The prepared samples were assembled in half-cells to study their performance as SPEs for LIBs. The obtained results are presented in figure 4.33. The cycle life tests at C/10 (figure 4.33a) show a good stability for all samples during 50 cycles with values of about 150 mAh g^{-1} and a capacity retention between 85 and 90%, except for the PVDF-HFP-CPT-LiTFSI one that significantly loses its capacity after 30 cycles.

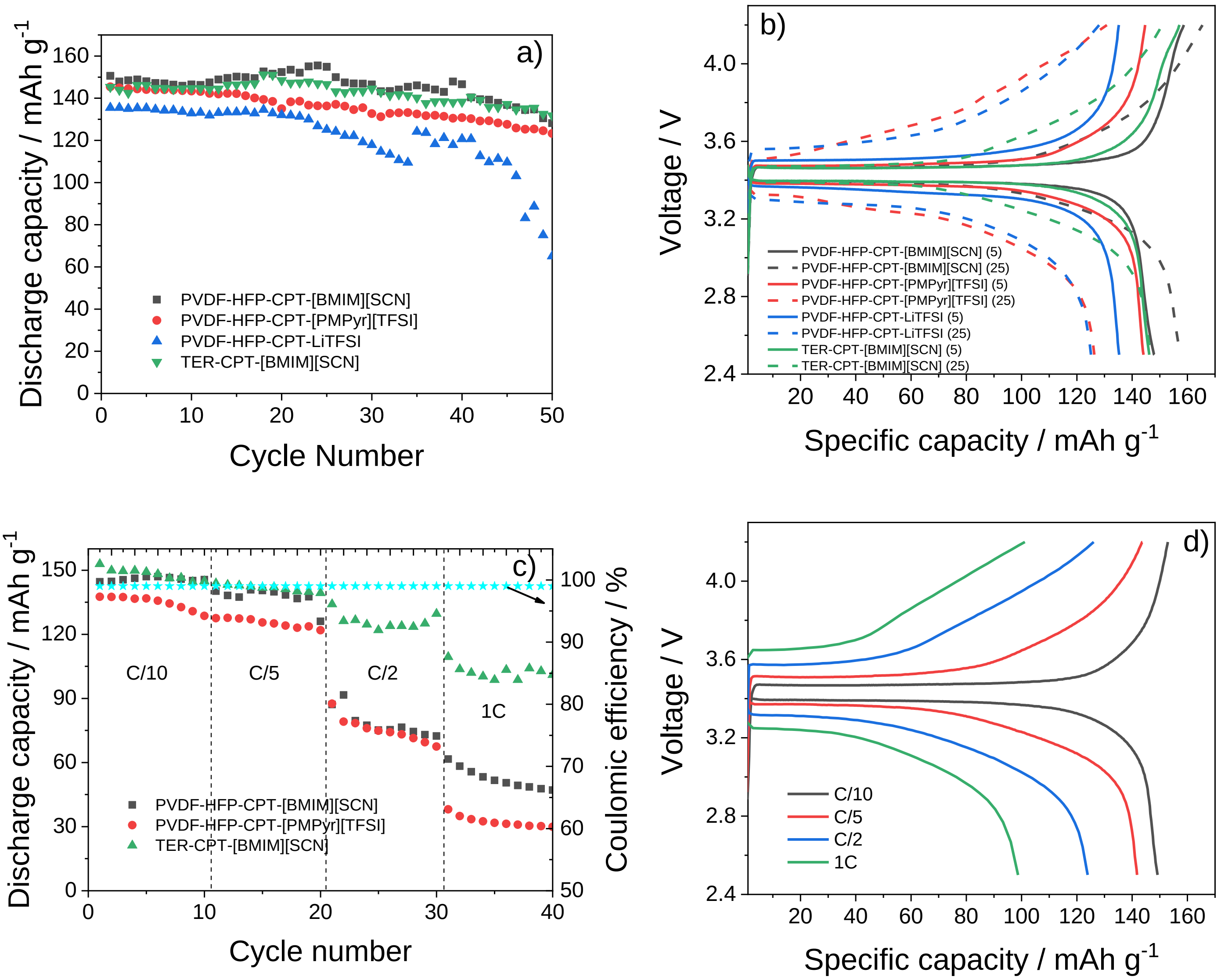

Figure 4.33 – Battery performance at room temperature for the different SPEs (a); charge/discharge profile of the assembled batteries at the 5th and 25th cycles (b); rate performance of the assembled batteries at C/10, C/5; C/2 and 1C rates (c); charge/discharge profile of the TER-CPT-[BMIM][SCN] battery on the 5th cycle of each rate (d).

This is attributed to the strong complexation of the LiTFSI salt with the polymer matrix, [15]. At this scan-rate, the IL and polymer matrix interaction, on the other hand, does not hinder battery performance. A more detailed analysis of the charge/discharge profiles of the assembled batteries between 2.5 and 4.2 V at the 5th and 25th cycle is shown in figure 4.33b. The typical voltage plateau of the LFP active material, attributed to the Fe2+/Fe3+ redox reaction corresponding to the extraction and insertion of Li^+ ions in the structure, is present regardless of the sample [50]. The better performance at the 25th cycle, evident for the PVDF-HFP-CPT-[BMIM][SCN], is attributed to the fact that the system is not fully activated at the 5th cycle. For the other samples, the TER-CPT-[BMIM][SCN] seems to be the most stable one, this effect being ascribed to the use of a high dielectric constant polymer that contributes to increase the battery stability and ionic mobility [28].

Considering the battery performance at the C/10-rate and to evaluate the effect of IL type and polymer matrix, figure 4.33c shows the rate performance tests, where the TER-CPT-[BMIM][SCN] presents an outstanding performance, even at high discharge rates (nearly 100 mAh g^{-1} at 1C rate), which is much better when compared with those of the PVDF-HFP-CPT-[BMIM][SCN] and the PVDF-HFP-CPT-[PMPyr][TFSI] ones, with values of about 50 and 30 mAh g^{-1}, respectively, for the same rate. This behavior is due to the high dielectric constant of this polymer, which promotes ionic dissociation and improves battery performance. The PVDF-HFP-CPT-LiTFSI sample was not able to cycle at high discharge rates, so the results are not presented. The analysis of the charge/discharge profiles of the TER-CPT-[BMIM][SCN] at the 5th cycle of each rate (figure 4.33d) clearly demonstrates its high stability, with values of 149.1, 141.8, 123.9 and 98.7 mAh g^{-1} for the C/10, C/5, C/2 and 1C rates, respectively, which represents 99%, 95%, 83% and 66% of its initial discharge capacity, with a coulombic efficiency of nearly 100% for all cycles. This makes this sample a particularly well-suited candidate for application in fast charging LIBs. The coulombic efficiency, presented in figure 4.33c, related to the reversibility of the process is ~100% independently of the number of cycles and scan rate. The irreversible capacity observed as a function of the cycle number is due to the cathodic decomposition, leading to the SEI formation [51].

The explanation for this behavior can also be hinted by the analysis of the impedance spectroscopy of the batteries before and after cycling (figure 4.34). The increase in the resistance of the TER-CPT-[BMIM][SCN] sample after cycling is not significant when compared with the PVDF-HFP-CPT-LiTFSI one, which indicates that the SEI formation does not have a significant impact on the battery performance in this case [52].

The Nyquist plots obtained before and after cycling (figure 4.34) are described by a semicircle (overall resistance, which is the sum of the ohmic resistance, that represents the contact film resistance and resistance contributions from the charge-transfer reaction resistance) in the high and medium frequency regions, and a straight line (associated of the Li^+ diffusion process) in the low frequency region. Figure 4.34 shows that the overall resistance before and after cycling increases, because of the formation of SEI layer during cycling [52].

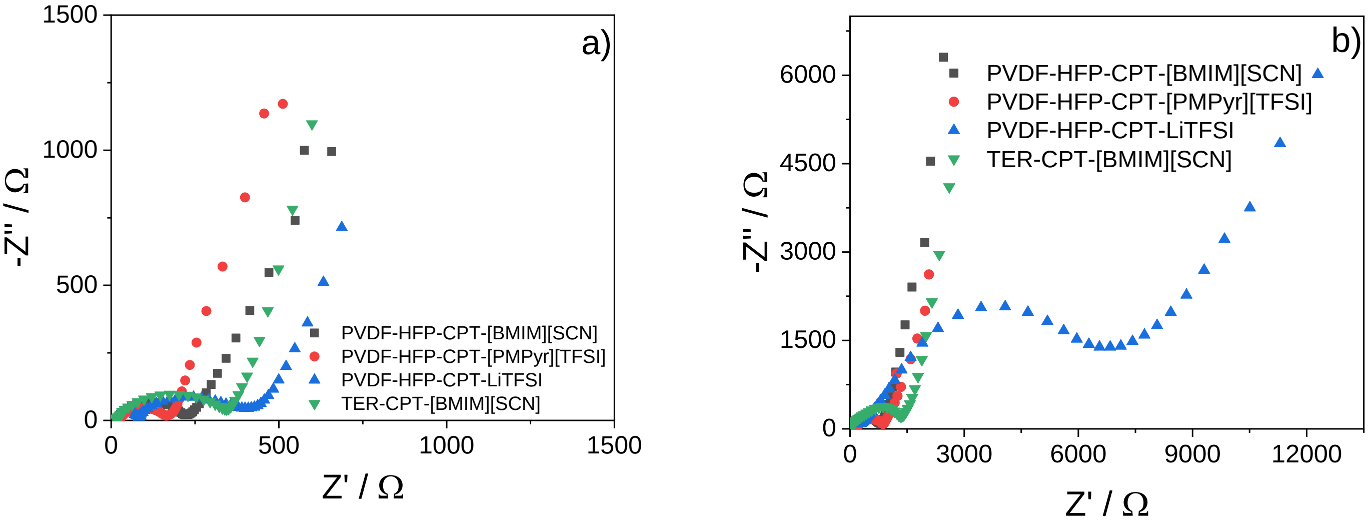

Figure 4.34 – Nyquist plots of the assembled batteries at room temperature before (a), and after cycling (b).

The SPE sample with the lowest resistance is PVDF-HFP-CPT-[PMPyr][TFSI] and the sample with best performance is TER-CPT-[BMIM][SCN], for which the overall resistance before and after cycling is 342 and 1350 Ω, respectively.

This work proves the suitability of the three-component approach as a valid option for the application in LIBs as SPEs. The obtained results are in line or better than those reported in the literature (table 4.19), in particular that concerning TER-CPT-[BMIM][SCN], which possess the best high-rate cycling capacity at room temperature reported up to now.

Table 4.19 – Comparation between the obtained results and those reported in the literature.

Polymer	**Components Doping Agents ou Dopants**	**Ionic Conductivity (S cm^{-1})**	**Li^{+} transference number**	**Battery capacity of LFP batteries (mAh g^{-1})/C-rate**	**Ref.**
PEO	SSZ-13, LiTFSI	5.34×10^{-2} (70°C)	0.85	154 (C/10); 60°C	[5]
PEO	ZYNa Zeolite, LiTFSI	1.66×10^{-2} (60°C)	0.84	152 (C/5); 60°C	[6]
PAES-co-PEG	[PYR][TFSI], LiTFSI	7.2×10^{-4} (25°C)	0.38	139.7 (C/10, 25°C)	[7]
PEGMA, CTA	[PYR][TFSI], LiTFSI	5.24×10^{-3} (25°C)	0.43	125 (C/20, 25°C)	[8]
PVDF	LiClO4, LLTO	5.8×10^{-4} (25°C)	0.80	152 (C/5); 25°C	[9]
PVDF-HFP	IL@UiO-67	4.3×10^{-4} (25°C)	0.45	118 (1C); 25°C	[10]
PVDF-HFP	LiTFSI, LLZTO	8.80×10^{-5} (25°C)	0.27	158.7 (C/10); 25°C	[11]
PVDF-HFP	CPT, [BMIM][SCN]	1.8×10^{-5} (25°C)	0.53	147.9 (C/10) 25°C	This work
PVDF-HFP	CPT, [PYR][TFSI]	1.6×10^{-4} (25°C)	0.59	145.4 (C/10) 25°C	This work
P(VDF-TrFE-CFE)	CPT, [BMIM][SCN]	$7{,}6\times10^{-6}$ (25°C)	0.42	149.1 (C/10) 25°C	This work

In any case, we draw the attention to the fact that all the prepared samples are capable of delivering suitable capacities, which confirms the importance of selecting the right combination of materials, production methods and conditions, in order to optimize battery performance. It is of particular interest that even though the samples prepared in this work show lower ionic conductivity than other samples reported in the literature, the assembled batteries still show outstanding results, meaning that ionic conductivity alone is definitely not the most critical parameter in battery performance, but instead a relevant factor in a more complex system. The important role of polymer selection in the final battery performance is also proved in this work, the high dielectric constant polymer leading to improved battery stability at high discharge rates. When compared to PVDF-HFP, the high dielectric constant P(VDF-TrFE-CFE) polymer presents an increased polymer interchain distance that weakens the intermolecular interactions, supports charge dissociation, and facilitates free charge motion through the SPE, as schematized in figure 4.35 [58].

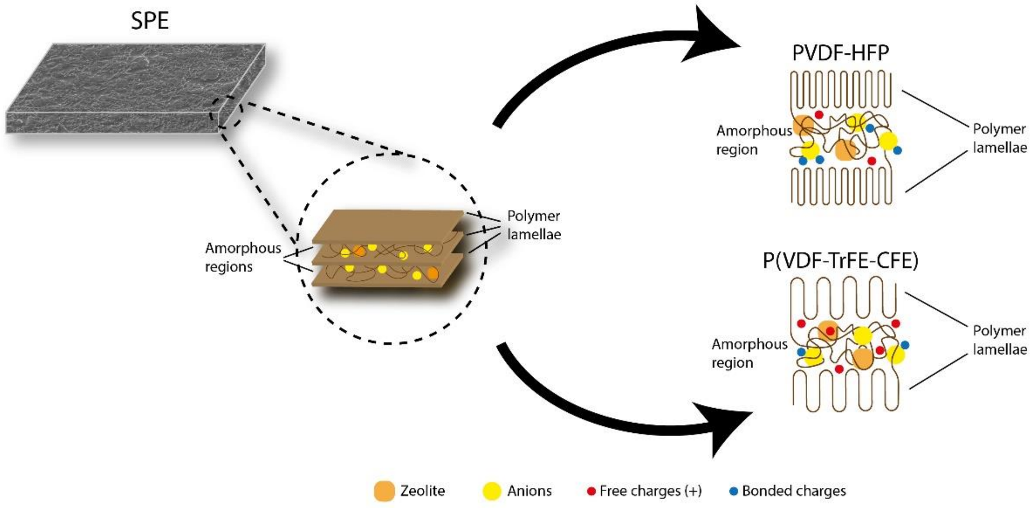

Figure 4.35 - Schematic representation of the polymer/charge interaction in the lower dielectric constant (PVDF-HFP) and higher dielectric constant (P(VDF-TrFE-CFE)) polymers used in the present work.

4.5.5. Conclusion

New solid polymer electrolytes (SPEs) of ternary composites based on poly(vinylidene fluoride-co-hexafluoropropylene) (PVDF-HFP) and poly(vinylidene fluoride-trifluoroethylene-chlorofluoroethylene), P(VDF-TrFE-CFE) as a polymer host, clinoptilolite (CPT) zeolite for stabilizing cycling performance and ionic liquids (IL) (1-butyl-3-methylimidazolium thiocyanate ([BMIM][SCN])), 1-Methyl-1-propylpyrrolidinium bis(trifluoromethylsulfonyl)imide ([PMPyr][TFSI]) and Lithium bis(trifluoromethanesulfonyl)imide (LiTFSI) for improving ionic conductivity, were produced by the doctor blade technique. The effect of the polymer matrix, different ILs and a lithium salt on the SPE morphology, thermal, mechanical and electrical properties was analyzed. The microstructure of the SPEs depends on the polymer matrix and fillers, ranging from compact for PVDF-HFP-CPT-[BMIM][SCN] to porous for PVDF-HFP-CPT-LiTFSI, being determined by the interaction between polymer chains, the fillers and the solvent. The polymer matrix and the different fillers do not have a strong effect on the degree of crystallinity, polymer phase and thermal degradation of the samples. Regarding the mechanical properties, the Young modulus is affected by the IL type, lithium salts and polymer matrix due to the interaction of polymer chains and fillers. The highest ionic conductivity value (4.2×10^{-5} S cm^{-1}) and the highest lithium transference number (0.59) were obtained for the PVDF-HFP-CPT-[PMPyr][TFSI] sample.

The room temperature charge-discharge behavior at C/10 shows excellent battery performance with 150 mAh g^{-1}, regardless of IL type and polymer matrix. For rate performance tests, the highest battery performance was achieved for the poly(vinylidene fluoride-trifluoroethylene-chlorofluoroethylene), P(VDF-TrFE-CFE) SPE due to its high dielectric constant that promotes the dissociation of the ions and consequently the improvement of battery performance. The discharge values of this SPE sample are 149.1, 141.8, 123.9 and 98.7 mAh g^{-1} for the C/10, C/5, C/2 and 1C rates, respectively, which represents 99%, 95%, 83% and 66% or its initial discharge capacity, with a coulombic efficiency of nearly 100% for all cycles

It has been shown that the polymer matrix and filler type used for SPEs development affect the cycling behavior due to compatibility and interaction between IL and polymer matrix, and that a high dielectric constant polymer matrix promotes ions dissociation and allows to improve the performance of room temperature solid-state batteries.

4.5.6. References

1. Zhou, C., et al., *Understanding the Role of Solvents on the Morphological Structure and Li-Ion Conductivity of Poly(vinylidene fluoride)-Based Polymer Electrolytes.* Journal of The Electrochemical Society, 2020. **167**(7): p. 070552.
2. Li, J., et al., *Optimisation of conductivity of PEO/PVDF-based solid polymer electrolytes in all-solid-state Li-ion batteries.* Materials Technology, 2020: p. 1-8.
3. Fu, C., et al., *A Polymerized-Ionic-Liquid-Based Polymer Electrolyte with High Oxidative Stability for 4 and 5 V Class Solid-State Lithium Metal Batteries.* Advanced Energy Materials, 2022. **12**(27): p. 2200412.
4. Pereira, N., et al., *High dielectric constant poly(vinylidene fluoride-trifluoroethylene-chlorofluoroethylene) for capacitive pressure and bending sensors.* Polymer, 2021. **214**: p. 123349.
5. Jamal, H., et al., *Enhancement of the ionic conductivity of a composite polymer electrolyte via surface functionalization of SSZ-13 zeolite for all-solid-state Li-metal batteries.* Journal of Materials Chemistry A, 2021. **9**(7): p. 4126-4137.
6. Jamal, H., et al., *Enhanced compatibility of a polymer-based electrolyte with Li-metal for stable and dendrite-free all-solid-state Li-metal batteries.* Journal of Materials Chemistry A, 2021. **9**(48): p. 27304-27319.
7. Kim, S., A. Le Mong, and D. Kim, *Accelerated ion conduction by co-grafting of poly(ethylene glycol) and nitrile-terminated ionic liquid on poly(arylene ether sulfone) for solid electrolyte membranes for lithium ion battery.* Journal of Power Sources, 2022. **529**: p. 231255.
8. Kale, S.B., et al., *Cellulose-Derived Flame-Retardant Solid Polymer Electrolyte for Lithium-Ion Batteries.* ACS Sustainable Chemistry & Engineering, 2021. **9**(4): p. 1559-1567.
9. Sivaraj, P., et al., *Performance Enhancement of PVDF/LiClO4 Based Nanocomposite Solid Polymer Electrolytes via Incorporation of Li0.5La0.5TiO3 Nano Filler for All-Solid-State Batteries.* Macromolecular Research, 2020. **28**(8): p. 739-750.

10. Liu, L. and C. Sun, *Flexible Quasi-Solid-State Composite Electrolyte Membrane Derived from a Metal-Organic Framework for Lithium-Metal Batteries.* ChemElectroChem, 2020. **7**(3): p. 707-715.

11. Yu, Y., et al., *Zwitterion-containing electrolytes with semi–crystalline PVDF-Co-HFP as a matrix for safer lithium-ion batteries.* Journal of Molecular Liquids, 2019. **282**: p. 340-346.

5. Conclusions and future work

5.1. Conclusions

The relevance of the development of efficient and durable energy storage systems cannot be underestimated, regarding the urgent need to change the paradigms that have driven the economy since the industrial revolution. Lithium-ion batteries (LIBs) are a major player for the energetic transition that is happening nowadays, and they need to be improved in terms of safety, sustainability and cycling stability in order to be able to meet the growing demand for energy storage. Solid polymer electrolytes (SPEs) are one of the most promising battery technological developments, but they still need significant research and improvement to be fully functional and applicable at large scales.

This work was focused on the development of a new ternary system comprising a polymer matrix of poly(vinylidene fluoride-co-hexafluoropropylene) (PVDF-HFP), an ionic liquid (IL) active filler and the clinoptilolite (CPT) zeolite as passive filler for LIB application as room temperature solid polymer electrolyte (SPE). It was the first time that zeolites were applied as a component of these kind of electrolytes and it was proven that the application of this kind of zeolite in a SPE is beneficial, by significantly stabilizing its structure and allowing for a higher number of battery charge/discharge samples without a significant loss in the discharge capacity.

The work focused mainly in the optimization of the proposed system. The study on the zeolites (CPT, ETS-4 and ETS-10) proved the suitability of the CPT as the most effective one, and also the potential of ion exchange to improve the battery stability, with a capacity retention of 70% against 30% after 50 cycles for the samples with and without ion exchange. The study based on the IL type selection ([EMIM][SCN], [BMIM][SCN], [EMIM][NCN$_2$] and [BMIM][NCN$_2$]) showed the best candidate as the [BMIM][SCN] and also highlighted the role of the cation chain length and type of anion in the SPE properties. The processing conditions were also studied, namely at the level of the SPE production temperature, in which it was proved that higher solvent evaporation temperatures (160°C) create a synergistic effect between crystallinity degree and lithium transference number, allowing for higher battery capacities, when compared to lower temperatures (120 °C, 80 °C and room temperature). Finally, the preparation method, focusing on the component addition order to the SPE solution, stated the importance of the methodology chosen for the SPE production, as there are differences in the SPE performance depending on the strength of the interaction between the different components, which can be controlled by the way those components are added, and proved to be most effective with an addition order of IL-polymer-zeolite, when compared to IL-zeolite-polymer and zeolite-polymer-IL.

The results obtained for these works allowed for the production of a SPE with the most optimized conditions, namely using ion exchange CPT, [BMIM][SCN] IL, with an addition order of IL-polymer-zeolite, and with a solvent evaporation temperature of 160°C. Some variations were also evaluated, namely by using some of the most successful materials reported in the literature, as Lithium bis(trifluoromethylsulfonyl)imide (LiTFSI) salts and 1-methyl-1-propylpyrrolidinium bis(trifluoromethylsulfonyl)imide ([PMPYR][TFSI]) IL. The obtained results show an outstanding battery capacity of about 150 mAh g^{-1} at room temperature with minimal capacity losses after 50 cycles, proving the relevance of the previous made works. Also, when the PVDF-HFP was replaced by the Poly(vinylidene fluoride-trifluoroethylene-chlorofluoroethylene) (P(VDF-TrFE-CFE)), a significant improvement in the battery capacity at high discharge rates was verified, suggesting a correlation between the material’s dielectric constant and the battery capacity.

Thus, the main objective of the thesis, the production of three-component SPEs with high room temperature performance and durability, and studying the effect of different materials and procedures in their properties, was achieved as a high performance SPE that works for prolonged life cycle at high discharge rates and with excellent discharge capacity was produced. This work also allowed a better comprehension of the mechanisms involved in the conduction mechanisms of complex systems, hinting that ionic conductivity, despite being important, is not the only factor affecting battery operation. It also reinforced the importance of combining the selection of suitable materials with appropriate processing methodologies in order to optimize their performance.

5.2. Future work

As a perspective, future works should include a deeper understanding on the interactions between the SPE components, as there are still some gaps in this field, such as the role of the interaction between the IL and the zeolite, which seems to be positive to the structure stability at some extent, but it can also reduce the number of free charges in the system, limiting the ion conduction. Also, a more systematical approach to the polymer choice should be taken, as this component was the least studied here, despite its importance being demonstrated through the role of the dielectric constant. However, it is still difficult to find polymers with high dielectric constant without adding other complementary fillers. Other important parameters to take into account regarding polymer properties is the crystallinity degree, as lower crystallinities lead to improved battery performance. Thus, polymers with higher -HFP content and lower molecular weight can contribute to increase the amorphous phase of the polymer. Furthermore, a better tuning of the polymer properties, or even the synthesis of a polymer with the specific desired properties, may allow for even better battery performances, through the crosslinking with polar groups that increase the number of free charges and consequently the overall mobility in the SPE. In this regard, the development of poly(ionic liquids) that combine the mechanical and thermal stability of the polymer with the conductive properties of ILs is also a valid option to improve the system by reducing the number of components without significantly compromise the performance. Finally, a more sustainable approach can also be taken, by trying to replace the used components with green ones, such as natural polymers, thus reducing the overall impact of this system. The main challenge of this approach is to improve the sustainability of the SPEs without compromising their performance, as natural polymers such as cellulose, soy, and carrageenan are not designed specifically for this purpose. Thus it is important to combine these polymers with adequate fillers to mitigate this limitation

6. Annexes

6.1. Annex I: Three-component solid polymer electrolytes based on li-ion exchanged microporous silicates and an ionic liquid for solid-state batteries

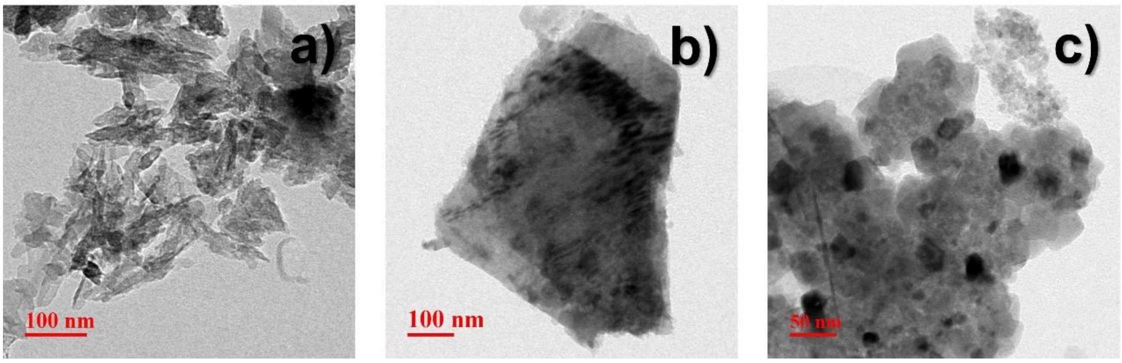

Figure 6.1 - TEM images of CPT (a), ETS-4 (b) and ETS-10 (c) microporous silicates before the IE process.

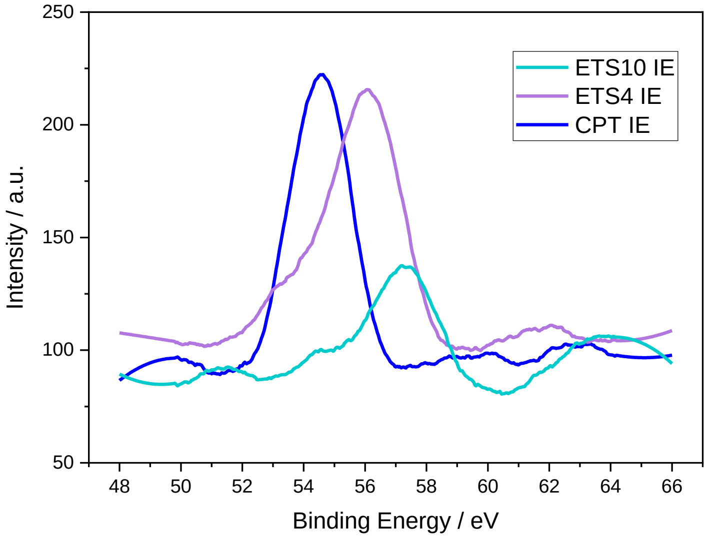

Figure 6.2 - XPS of the ion-exchanged zeolite and titanosilicates powders.

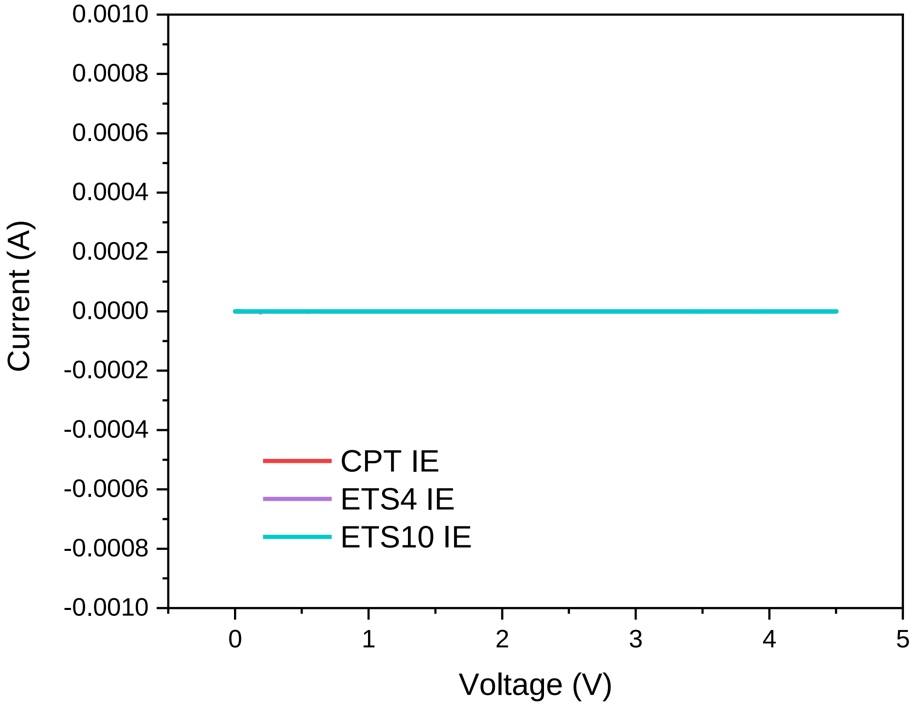

Figure 6.3 - Cyclic voltammogram of the ion-exchanged zeolite and titanosilicate samples.

6.2. Annex II: Three-component solid polymer electrolytes based on li-ion exchanged microporous silicates and an ionic liquid for solid-state batteries

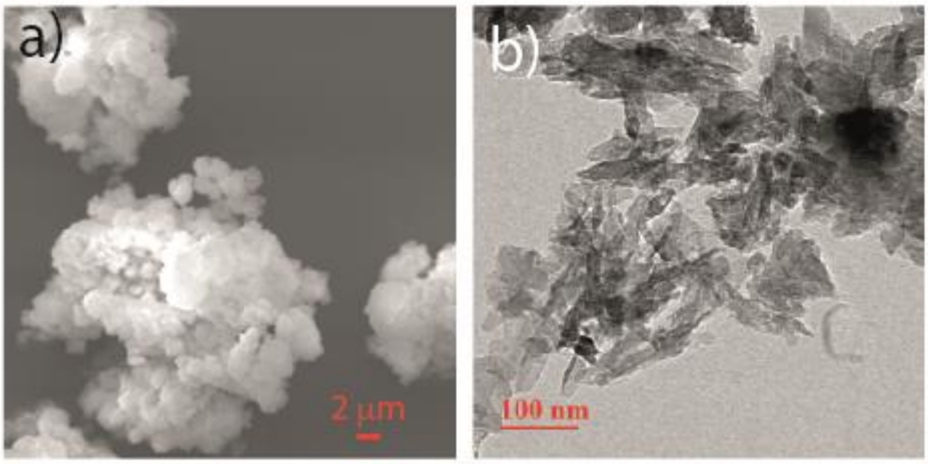

Figure 6.4 – SEM (a) and TEM (b) images of the CPT.

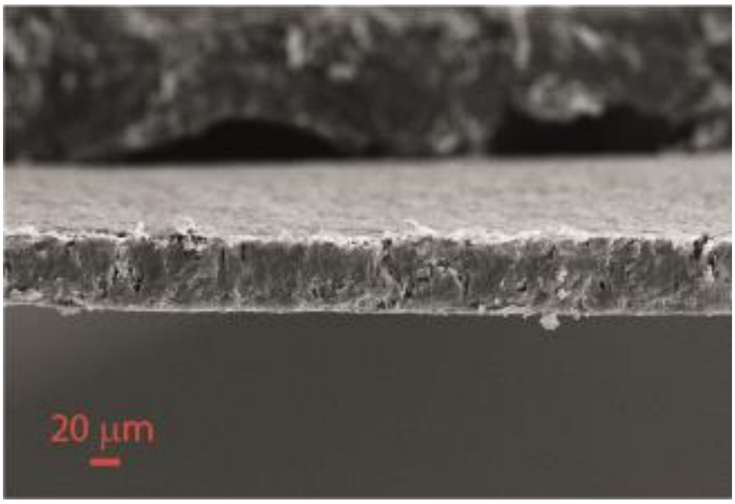

Figure 6.5 – Cross-section image of the SPE.

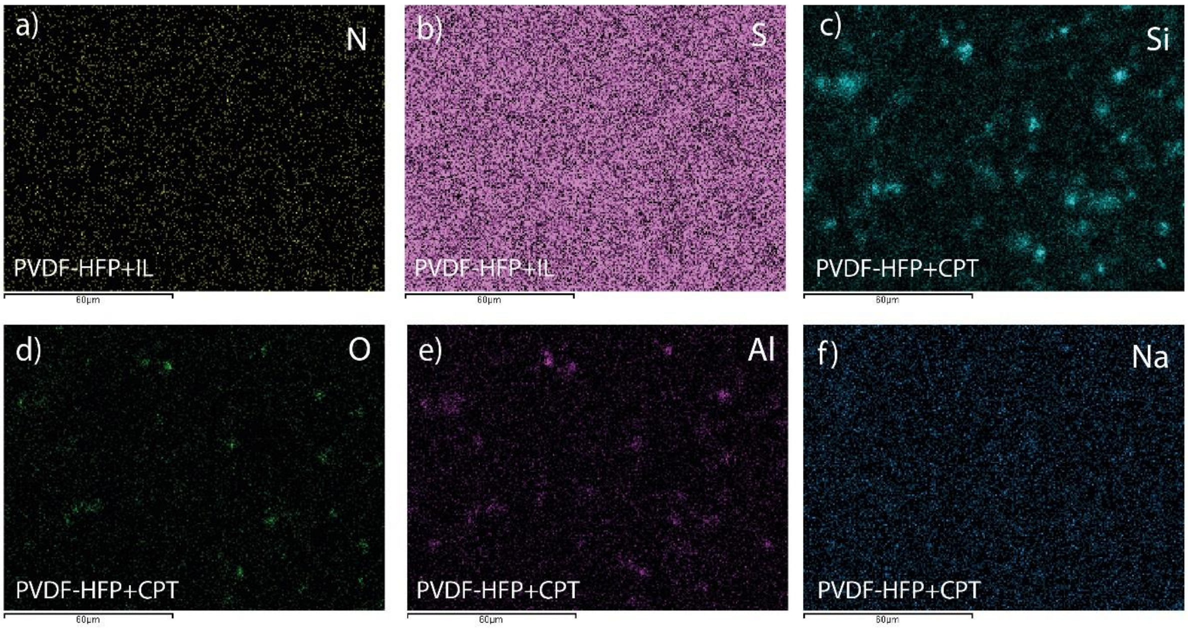

Figure 6.6 – EDX mapping images of the elements N (a), S (b), Si (c), O (d), Al (e) and Na (f) present in IL and CPT.

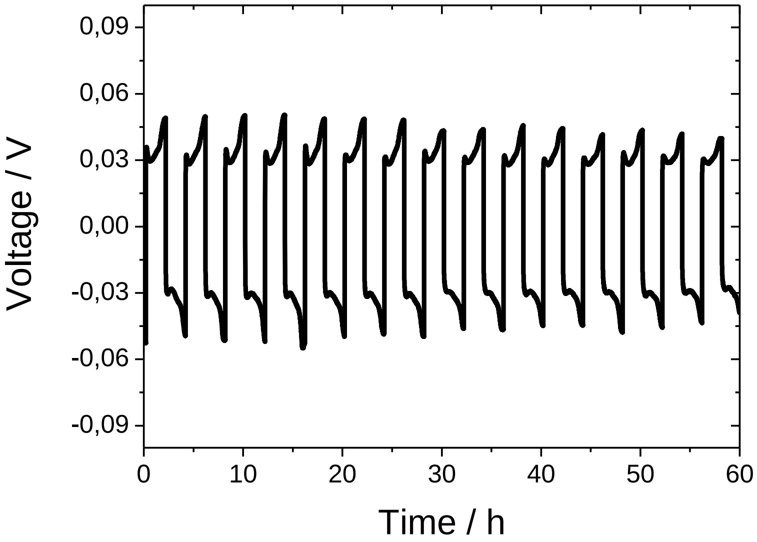

Figure 6.7 - Li compatibility behavior for the IL+PVDF-HFP+CPT sample at room temperature.